Technical Report Documentation Page

1. Report No.	2. Government Accession No.	3. Recipient's Catalog No.
TX-93+932-1F		

4. Title and Subtitle	5. Report Date
OBSERVED BEHAVIOR OF A CONCRETE ARCH CULVERT	*February 1993*
	6. Performing Organization Code

7. Author(s)	8. Performing Organization Report No.
Charles S. Oswald and Richard W. Furlong	*Research Report 932-1F*

9. Performing Organization Name and Address	10. Work Unit No. (TRAIS)
Center for Transportation Research *The University of Texas at Austin* *3208 Red River, Suite 200* *Austin, Texas 78705-2650*	11. Contract or Grant No. *Research Study 3-15D-88/2-932*
	13. Type of Report and Period Covered *Final*
12. Sponsoring Agency Name and Address *Texas Department of Transportation* *Transportation Planning Division, Research Section* *P. O. Box 5051* *Austin, Texas 78763-5051*	14. Sponsoring Agency Code

15. Supplementary Notes

Study conducted in cooperation with the Texas Department of Transportation
Research Study Title: "Monitoring Performance of BEBO Arch Culvert"

16. Abstract

Observations of soil pressures and strains in arch components over a 5-year period indicate that:

(1) The design procedure used for arch segments produced components that have supported imposed soil and environmental forces successfully.

(2) The use of a tension tie reinforcement in the slabs under arches beneath high fill was a wise and proper decision, as the tension strains in the floor indicate that the bars developed significant strains.

(3) Vertical earth pressures exceeded the nominal amount determined for uncompacted density and depth. Measured vertical pressures imply a soil density in the order of 130 pcf.

(4) Creep deformations in concrete must be included in analytic procedures in order to obtain displacement responses corresponding to those measured.

(5) The redundancies associated with soil-structure interaction tend to produce favorable redistributions of resistance to soil loads against the arch.

(6) A sophisticated analytic model of the structural system was shown to produce stress and displacement values very similar to those measured. The analytic model must include specific data regarding soil properties, and creep response time effects for concrete as well as for soil.

17. Key Words	18. Distribution Statement
arch, arch components, soil pressures, strains, arch segments, tension tie reinforcement, bars, density, depth, creep deformations, displacement	*No restrictions. This document is available to the public through the National Technical Information Service, Springfield, Virginia 22161.*

19. Security Classif. (of this report)	20. Security Classif. (of this page)	21. No. of Pages	22. Price
Unclassified	*Unclassified*	*188*	

Form DOT F 1700.7 (8-72) Reproduction of completed page authorized

OBSERVED BEHAVIOR OF A CONCRETE ARCH CULVERT

by

Charles S. Oswald and Richard W. Furlong

Research Report Number 932-1F

Research Project 3-15D-88/2-932
MONITORING PERFORMANCE OF BEBO ARCH CULVERT

Conducted for the

Texas Department of Transportation

In Cooperation with the
U.S. Department of Transportation
Federal Highway Administration

by

CENTER FOR TRANSPORTATION RESEARCH
BUREAU OF ENGINEERING RESEARCH
THE UNIVERSITY OF TEXAS AT AUSTIN

FEBRUARY 1993

IMPLEMENTATION

Results from this study demonstrate that subsequent designs for similar structures can be based on AASHTO recommended practice for strength design of concrete if soil density is taken to be 130 pcf instead of 120 pcf.

The use of steel reinforcement cement in the floor slab, as a tension tie, was shown to be beneficial detail under deep fill (±20 ft.).

The AASHTO CANDE computer code modified for applications in this study can be used for studies of existing as well as proposed new concrete structures in soil. Time dependent deformations and strength stiffness models of concrete have been added to the CANDE code.

Prepared in cooperation with the
Texas Department of Transportation

DISCLAIMERS

Richard W. Furlong, P.E. (Texas No. 17744)
Research Supervisor

PREFACE

The Texas Department of Transportation (TxDOT) in 1987 placed a BEBO arch culvert system under Loop 1604 in San Antonio. The BEBO arch system is a patented set of precast concrete arch segments set into slotted footings. The San Antonio installation involved a rather large opening of 280 sq. ft. under fill depths in excess of 15 ft. A structural engineering consultant was hired to design the arch segments as a tied arch system, and The University of Texas Ferguson Structural Engineering Laboratory was retained to monitor the performance of the arch system over a period of 5 years. This report describes the monitoring effort, the analysis of measured performance, and recommendations for subsequent analytic efforts applied to similar soil-structure interaction concerns.

METRIC (SI*) CONVERSION FACTORS

APPROXIMATE CONVERSIONS TO SI UNITS

Symbol	When You Know	Multiply by	To Find	Symbol
LENGTH				
in	inches	2.54	centimeters	cm
ft	feet	0.3048	meters	m
yd	yards	0.914	meters	m
mi	miles	1.61	kilometers	km
AREA				
in^2	square inches	645.2	millimeters squared	mm^2
ft^2	square feet	0.0929	meters squared	m^2
yd^2	square yards	0.836	meters squared	m^2
mi^2	square miles	2.59	kilometers squared	km^2
ac	acres	0.395	hectares	ha
MASS (weight)				
oz	ounces	28.35	grams	g
lb	pounds	0.454	kilograms	kg
T	short tons (2,000 lb)	0.907	megagrams	Mg
VOLUME				
fl oz	fluid ounces	29.57	milliliters	mL
gal	gallons	3.785	liters	L
ft^3	cubic feet	0.0328	meters cubed	m^3
yd^3	cubic yards	0.0765	meters cubed	m^3
TEMPERATURE (exact)				
°F	Fahrenheit temperature	5/9 (after subtracting 32)	Celsius temperature	°C

NOTE: Volumes greater than 1,000 L shall be shown in m^3.

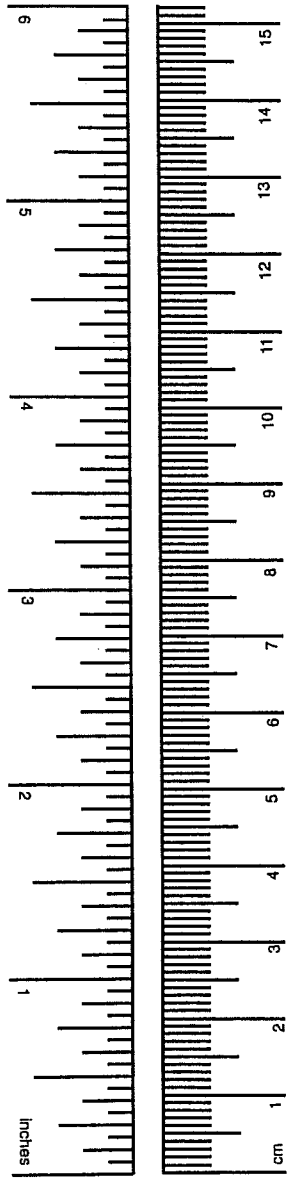

APPROXIMATE CONVERSIONS FROM SI UNITS

Symbol	When You Know	Multiply by	To Find	Symbol
LENGTH				
mm	millimeters	0.039	inches	in
m	meters	3.28	feet	ft
m	meters	1.09	yards	yd
km	kilometers	0.621	miles	mi
AREA				
mm^2	millimeters squared	0.0016	square inches	in^2
m^2	meters squared	10.764	square feet	ft^2
m^2	meters squared	1.20	square yards	yd^2
km^2	kilometers squared	0.39	square miles	mi^2
ha	hectares (10,000 m^2)	2.53	acres	ac
MASS (weight)				
g	grams	0.0353	ounces	oz
kg	kilograms	2.205	pounds	lb
Mg	megagrams (1,000 kg)	1.103	short tons	T
VOLUME				
mL	milliliters	0.034	fluid ounces	fl oz
L	liters	0.264	gallons	gal
m^3	meters cubed	35.315	cubic feet	ft^3
m^3	meters cubed	1.308	cubic yards	yd^3
TEMPERATURE (exact)				
°C	Celsius temperature	9/5 (then add 32)	Fahrenheit temperature	°F

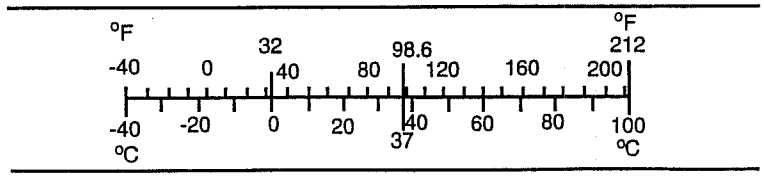

These factors conform to the requirement of FHWA Order 5190.1A.

* SI is the symbol for the International System of Measurements

TABLE OF CONTENTS

LIST OF FIGURES

SUMMARY

Observations of soil pressures and strains in arch components over a 5-year period indicate that:

1. The design procedure used for arch segments produced components that have supported imposed soil and environmental forces successfully.

2. The use of tension tie reinforcement in the slabs under arches beneath high fill was a wise and proper decision, as the tension strains in the floor indicate that the bars developed significant strains.

3. Vertical earth pressures exceeded the nominal amount determined for uncompacted density and depth. Measured vertical pressures imply a soil density in the order of 130 pcf.

4. Creep deformations in concrete must be included in analytic procedures in order to obtain displacement responses corresponding to those measured.

5. The redundancies associated with soil-structure interaction tend to produce favorable redistributions of resistance to soil loads against the arch.

6. A sophisticated analytic model of the structural system was shown to produce stress and displacement values very similar to those measured. The analytic model must include specific data regarding soil properties, and creep response time effects for concrete as well as for soil.

CHAPTER 1

FIELD SETUP AND INSTRUMENTATION OF REINFORCED CONCRETE ARCH CULVERT

In 1987 and 1988 the Texas Department of Transportation (TxDOT) placed a culvert, consisting of a patented system of precast concrete arches, under Loop 1604 in San Antonio, Texas and authorized The University of Texas to monitor the long-term performance of the culvert. A reinforced concrete system was chosen because cold formed corrugated steel arches had failed to support openings of similar size (280 ft.^{2} flow area) in other recent applications beneath fill depths greater than 15 ft. The patented system of precast arches, called BEBO arch culverts, have an ascetically pleasing shape due to a low-rise profile and a relatively large span-to-rise ratio. In this case however, these features raised some concern because the maximum fill height (24 ft.) over the culvert was much larger than previous fill heights placed over BEBO arch culverts. In order to satisfy the concern, two steps were taken. First, a structural engineering firm was employed to design the culvert as a tied arch, using reinforcing steel in the floor slab to resist lateral spreading of the footings, and to design additional midspan flexural steel. Secondly, The University of Texas at Austin was funded to monitor the long-term performance of the culvert. This report describes the results of the monitoring effort and an analysis of the soil-structure system.

1.1 Culvert and Soil Description

In this chapter and the next two chapters the culvert, the surrounding soil fill, and the monitoring system will be described and the measured response of the culvert will be presented and discussed. Figure 1.1 shows a section along the length of the BEBO arch culvert. The arches were precast in eight foot wide segments and the segments were laid side-by-side to form the 536 ft. long culvert. A cross section through the arch culvert describing the steel reinforcement is shown in Figure 1.2. The floor slab and footings were cast in the field and, after they had cured, the precast arches were transported to the culvert site and placed in the blockouts of the footings. Grout was then placed in the blockout around the base of the arch to cause a tight fit between the arch and footing. As Figure 1.1 shows, there are two regions of fill depth over the culvert, a high fill region (24 ft. fill) under the mainlanes, and a low fill region (8 to 10 ft.) under the frontage road. In the regions under high fill, 1 in. diameter reinforcing bars extend from the footings and splice with identical bars in the floor slab which extend to the opposite footing. These reinforcing bars, which are shown in Detail F of Figure 1.2, tie the footings together and resist outward horizontal movement of the footings during vertical loading. The 1 in. diameter bars were not placed in the floor slab in the regions of low fill. In these regions outward footing movement is resisted only by the surrounding soil. The concrete strength of the arch is called out as Class H concrete (minimum compressive strength of 5000 psi). The concrete strength of the footings and floor slab is called out as Class C concrete (the standard Texas Highway Department six sack concrete mix with a minimum compressive strength of 3600 psi). All reinforcing steel is A615 steel with a minimum yield

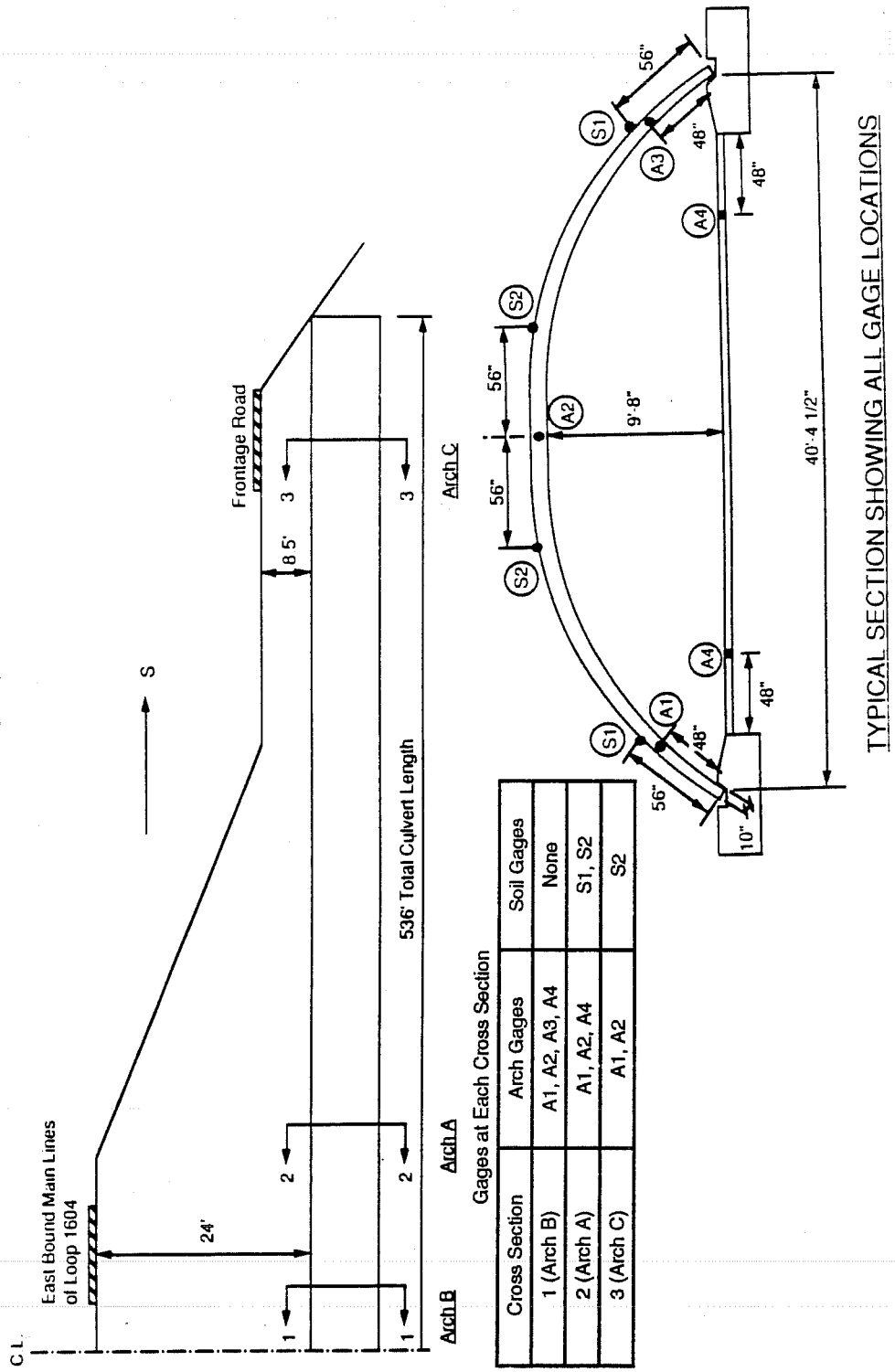

Gages at Each Cross Section

Cross Section	Arch Gages	Soil Gages
1 (Arch B)	A1, A2, A3, A4	None
2 (Arch A)	A1, A2, A4	S1, S2
3 (Arch C)	A1, A2	S2

Figure 1.1 Elevation and section of BEBO arch culvert showing locations of soil pressure and strain gages.

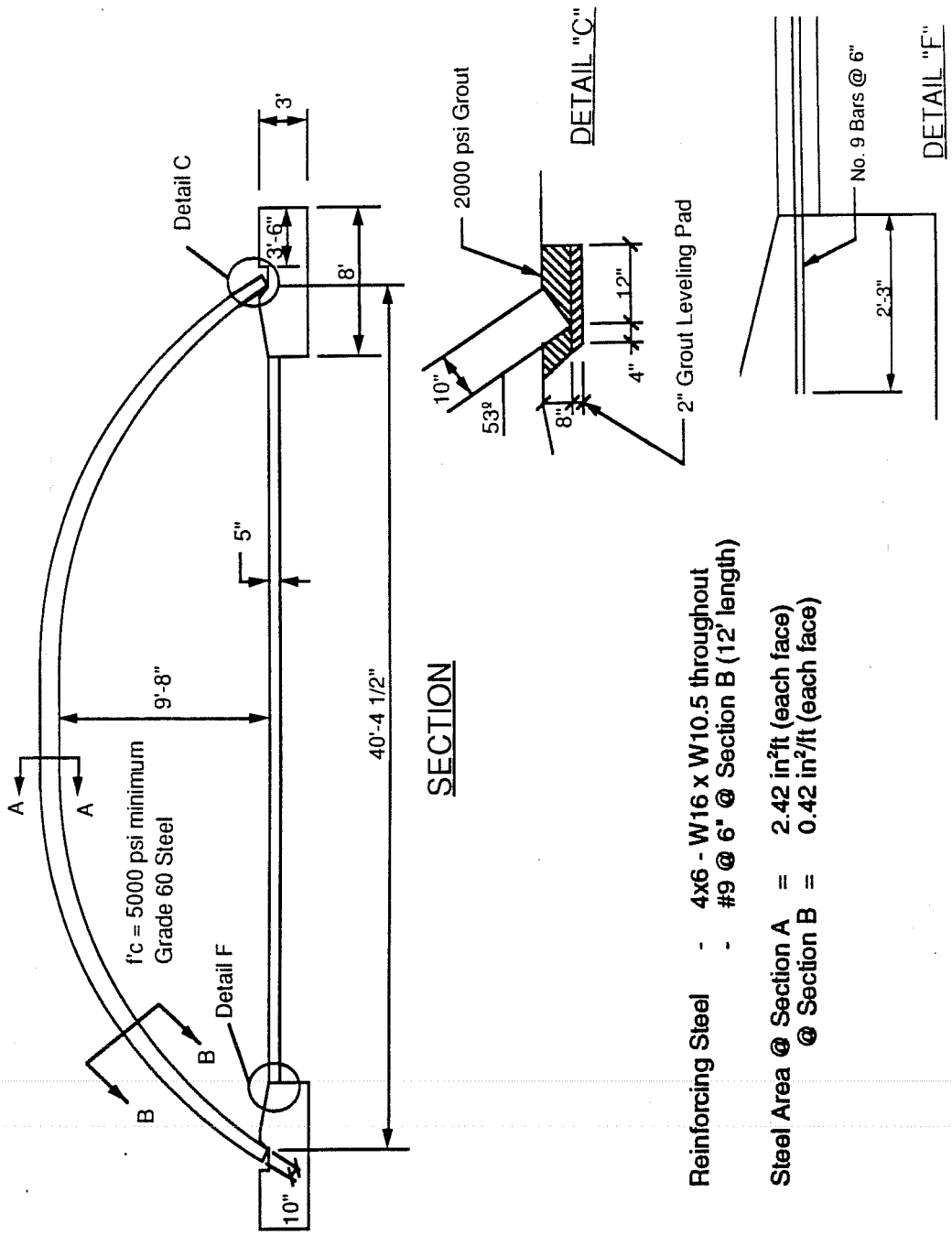

Figure 1.2 BEBO arch details under the high fill

stress of 60,000 psi. The approximate 28-day cylinder compression strength of the culvert concrete is 7000 psi. Due to a mix-up in record-keeping, the exact strength of the concrete in the instrumented culvert sections is unavailable but the 7000 psi strength is a good approximate value based on the available measured strengths for the mix design used for the culvert. The measured strength of the concrete in the floor slab is 6000 psi.

The soil surrounding the culvert consists of a cement stabilized foundation beneath the footings and compacted silty clay in the embankment above and around the culvert. The original brown sandy clay soil beneath the culvert was judged too soft to adequately support the culvert footings. Therefore, it was excavated down to a layer of hard shale approximately 9 ft. below the bottom of the culvert footings, mixed with 3% cement, and replaced as compacted fill. The average dry density and moisture content measured during stabilization of this soil was 128 lb./ft.^{3} and 9% moisture (by weight). This met the required minimum density of 95% of the THD TEX-113-E proctor optimum density of 133 lb./ft.^{3}. The embankment was constructed with compacted tan, silty clay with an average dry density of 111 lb./ft.^{3} and an average moisture of 15% based on nuclear density measurements at several lifts. The corresponding average total unit weight is 128 pcf. This soil also met the minimum density requirement. The high fill region of the culvert near the instrumented sections in Figure 1.1 was placed through an existing embankment. In this region, the existing embankment was excavated down to the previously mentioned shale layer on a 1:1 slope so that approximately 85 ft. of working area was created at the elevation of the arch culvert and this area was then backfilled with cement stabilized soil beneath the culvert and compacted silty tan clay up to the highway grade. This is illustrated in Figure 1.3. There is no description available for the existing embankment soil but, based on field observations, it is similar to the tan silty clay used to backfill around the culvert. No laboratory soils testing was performed on the backfill soil. As the background section indicates, previous studies have shown that knowledge of the exact soil properties is not usually required to achieve a good model of soil-structure response for rigid culverts. It was felt that the limited project financial resources were best spent on purchasing reliable long-term gages and on long-term monitoring efforts.

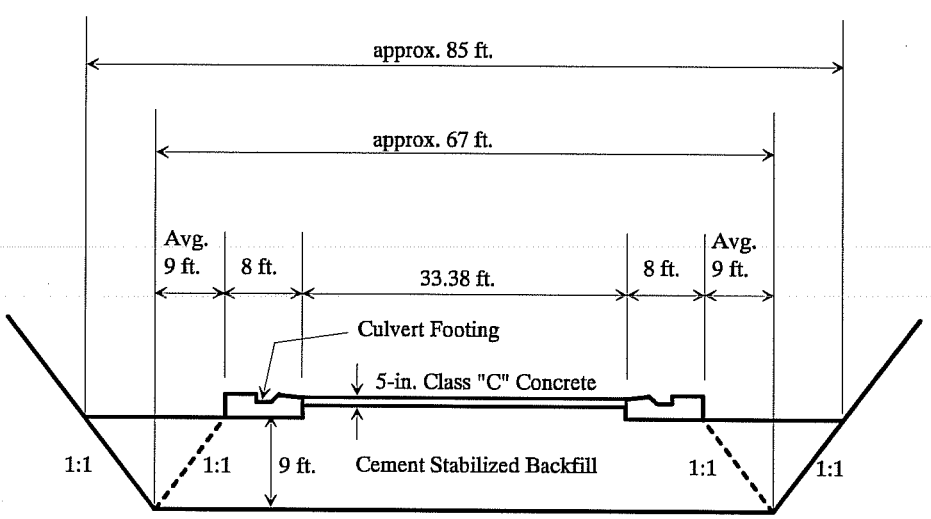

Figure 1.3 Typical section through high fill region showing cement stabilized backfill foundation

1.2 Culvert Instrumentation and Deflection Monitoring System

All the instrumentation was concentrated at the three cross sections called out in Figure 1.1. These cross sections are designated Arches A, B, and C for purposes of identification. The instrumentation consisted of embedded concrete strain gages placed at mid-depth through the culvert thickness and soil stress gages mounted on the outside culvert surface. Figure 1.1 shows the locations in each cross section where strain gages and soil pressure gages were installed. Deflections were also measured at eleven locations marked by nails installed along the inner surface across each instrumented cross section. Gage readings were made during the placement of fill and at least four times each year (once each season) after the fill was placed during the monitoring period of thirty months. After thirty months the wires attached to the strain gages and soil pressure gages had corroded to the point where no further measurements could be made. Except for a few cases, each time gage readings were made, deflections of the arch were also determined by measuring horizontal and vertical angles to the nails on the inside surface of the culvert and using triangulation to calculate the culvert deflections from the angle measurements.

1.2.1 Soil Pressure and Arch Strain Gages. The strain gages and soil pressure gages used to instrument the culvert were purchased from Geokon Inc. in Lebanon, New Hampshire. Figure 1.4 shows a photograph and the dimensions of the Geokon Model VCE-4200 concrete strain gages[22] which were embedded in the culvert. Figure 1.5 shows a photograph of the soil pressure gages (Geokon Model 4800E) that were attached to the culvert surface. A vibrating wire transducer is used in both gages. This transducer is essentially a thin wire, clamped under tension at both ends. The wire vibrates at its lowest natural frequency when it is excited by a dynamic force. The natural frequency of the wire, which is proportional to the square root of the tension in the wire, changes as the clamped ends move relative to each other. A small electrical coil attached to the gage near the midspan of the wire supplies a dynamic electromagnetic force which excites the wire when a voltage pulse is sent through attached wiring. The nonconstant current in the coil causes a changing magnetic field in the coil which momentarily attracts, or excites, the thin metal wire. After it is "plucked" in this manner, the wire vibrates in free vibration at its natural frequency. As the wire vibrates it induces an alternating voltage in the same coil which excited the wire. This voltage signal, which has a frequency identical to the frequency of the gage wire vibration, is transmitted through the wiring attached to the coil to a frequency counter which counts the time required for a set number of cycles. This is illustrated in Figure 1.4. The wiring from the strain gages and soil pressure gages are connected to a readout box each time measurements are made. This box is the source for the excitation voltage pulse and it contains the frequency counter.

The readout box is programmed to calculate the strain in the Geokon strain gages using the vibration frequency and the theoretical relationship between the fundamental vibration frequency of the wire, the tensile strain, and the known vibrating wire properties and gage length. The gage strain is equal to the surrounding concrete strain since movement of the surrounding concrete causes equal movement of the two disks at either end of the gage. Therefore the gage only measures strain along its long axis. The total concrete strain, except for temperature strain, is equal to the change in gage strain after embedment. The gage can only measure concrete movement which affects the elastic strain, or stress, in the vibrating wire. Temperature change causes the vibrating wire length to change by almost the same

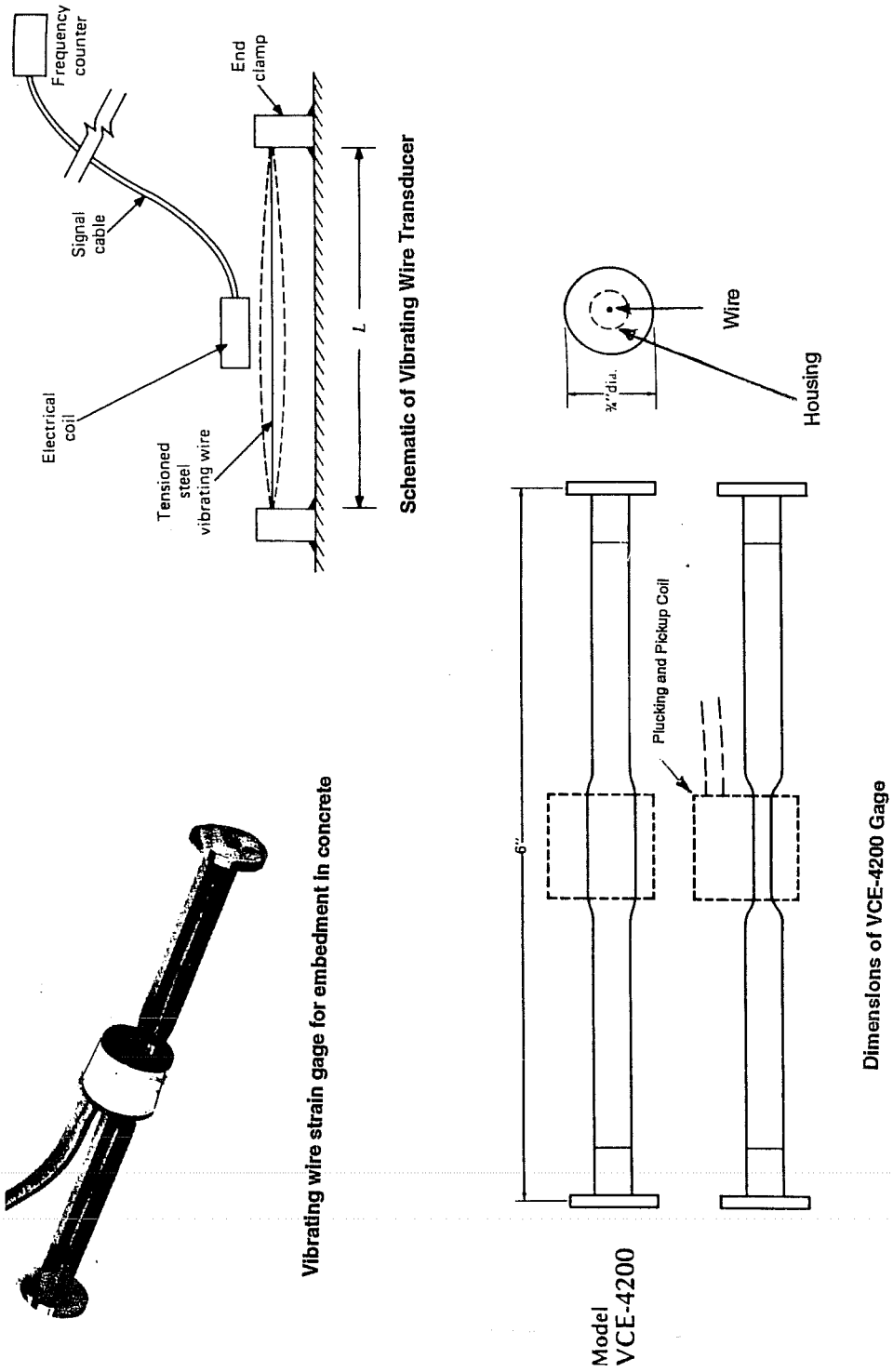

Figure 1.4 Vibrating wire strain gage embedded in culvert

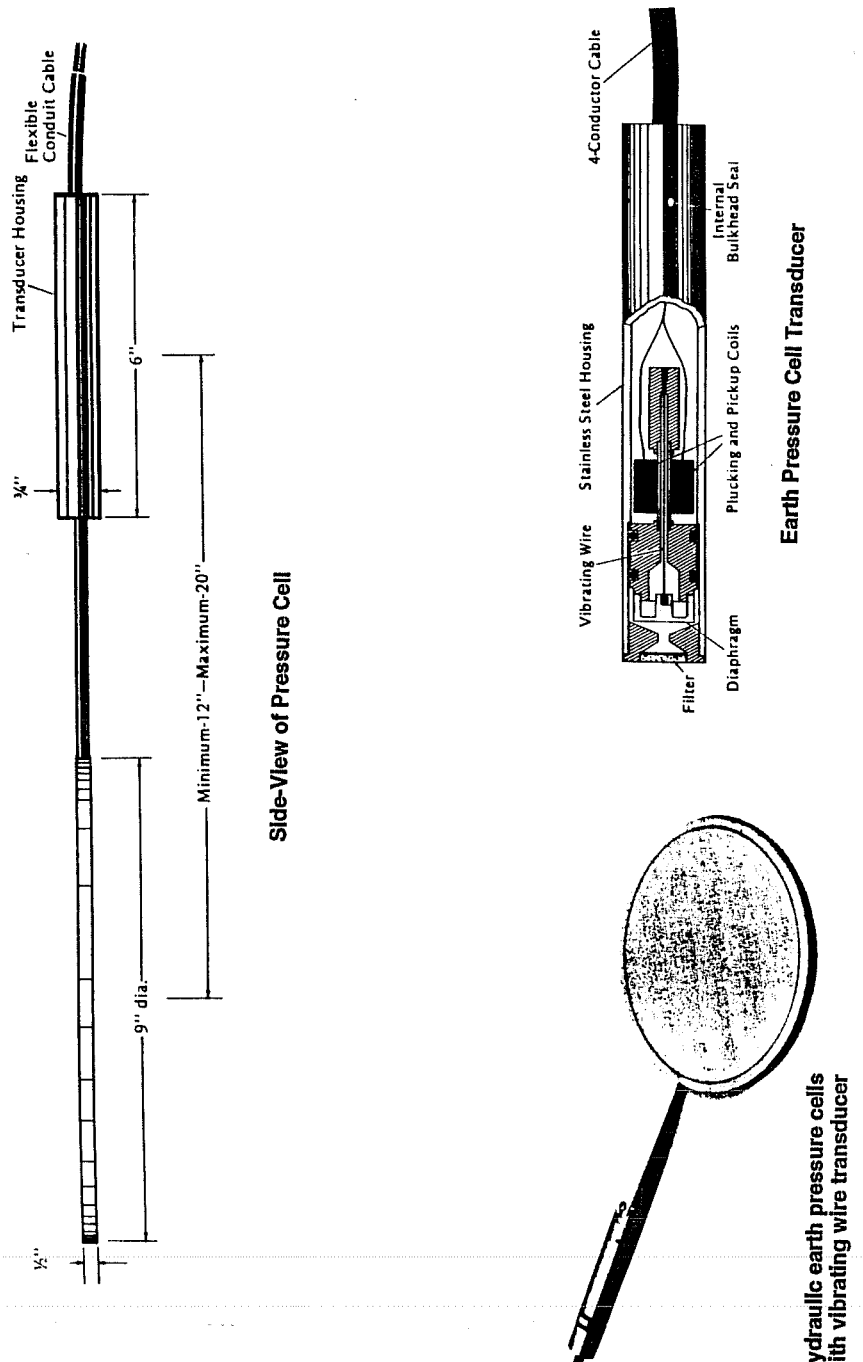

Figure 1.5 Earth pressure cell with vibrating wire transducer attached to culvert

amount as the concrete within the gage length and, therefore, very little change in wire stress occurs. Some temperature induced stress change does occur in the wire since the thermal coefficient of expansion of the vibrating wire is somewhat larger than that of the surrounding concrete. Therefore, the concrete restrains a small proportion of the temperature induced free expansion and contraction of the vibrating wire and this causes a change in the elastic strain of the vibrating wire which must be subtracted out in order to obtain a meaningful measurement. This is discussed in more detail in Chapter 2 in the section on accuracy of the measured strains, but the following example is helpful in understanding this issue. If an unrestrained concrete sample with an embedded vibrating wire gage is uniformly heated, the initial gage reading will indicate that the applied heat has caused a small compressive strain in the concrete. The concrete has in fact expanded, but it has expanded less than the free expansion of the vibrating wire at the given temperature, which causes relaxation of the tension in the vibrating wire, and this is measured as a compressive strain in the concrete. The corrected gage reading, which subtracts out the temperature induced change in wire tension strain, is zero strain change. The vibrating wire strain gage will measure shrinkage, creep, and elastic concrete strains, since it just "observes" these phenomena without reacting to them; it cannot be used to measure temperature effects since the gage itself reacts to applied temperature changes.

Embedded vibrating wire strain gages were placed near the springlines and at the crown of all three instrumented cross sections during construction of the arches at the casting yard. Figure 1.1 shows the locations of the embedded strain gages in the arch and in the floor slab (with the letter "A"). The gages were well tied into the reinforcing steel cage, at mid-depth through the thickness, and oriented with their long axis tangent to the arch profile. The springline gages were placed 4 ft. up from the footings, and measured along the arch profile to avoid measuring edge effects. A strain gage was also placed at the crown, or midspan, of each instrumented culvert section. The placement of concrete in the arch forms and the insertion of vibrators in the forms was supervised by a member of the research team so that no concrete was dumped near the gage locations and no vibrators were inserted near these locations. The wiring attached to the gages was placed in a short length of plastic pipe which was tied flush with the forms during casting. Unfortunately, the short pipe sections were only tied off to one face of the reinforcing cage and therefore rotation of the pipes was not totally prevented. Evidently, pipes containing wiring from gages near the springlines of Arches A and C rotated during placement or vibration of the concrete because they could not be located after the forms were removed. Therefore, Arches A and C were instrumented with only one accessible strain gage near a springline, while Arch B was instrumented with accessible strain gages located near each springline at symmetrical locations.

Figure 1.5 shows a schematic view of the soil pressure gages. These gages are essentially a pair of thin 9 in. diameter metal circular plates welded together around the periphery and separated by a thin layer of antifreeze solution. A change in the fluid pressure changes the tension of the vibrating wire in the transducer attached to the fluid between the plates. Only soil pressure normal to the gage surface is measured since shear stresses on the plate surface will not change the internal fluid pressure. The readout of the signal from the vibrating wire transducer is in terms of strain which is converted to fluid pressure (and thus soil pressure) during data reduction with a gage factor that is determined by the manufacturer during factory calibration of the gages. The vibrating wire transducers in the soil pressure cells, as well as the metal plates, also react to temperature change. Since the temperature effect is primarily confined to the unit itself (i.e. dependent on the expansion of the metal plate volume and the vibrating wire length)

rather than on surrounding in-place material, a temperature correction factor for each pressure cell is determined at the factory. Unfortunately, the temperature dependency is not totally independent of the surrounding material since the pressure cells are bonded to underlying concrete and surrounded by concrete grout as is explained below. It is practically impossible to determine the in-place temperature dependency of the gages without an in-place calibration but fortunately the temperature dependency is very small. This is discussed in more detail in Chapter 3.

Figure 1.1 shows the locations where the soil pressure gages are attached to the exterior of the culvert (with the letter "S"). At Arch A two soil pressure gages were placed at symmetric locations near the crown and two gages were placed at symmetric locations near the springline. The gages near the crown were placed 56 in. off the crown in each direction and the gages near the springline were placed 56 in. up from each footing. At Arch C two soil pressure gages were placed at symmetric locations 56 in. either side of the crown. All dimensions were measured along the arch profile. The gages were epoxied to the concrete surface after the arches were placed in the field. In order to cause a flush surface between the 1/4 in. thick soil pressure cells and the surrounding concrete, high strength grout was placed around each gage flush with the top of the gage and transitioned on a smooth slope down to match flush with the concrete surface over a 18 in. length. All soil stress and arch strain gages were placed along the middle of the 8 ft. width of each instrumented culvert segment.

1.2.2 Deflection Monitoring System. The deflections of each instrumented cross section were calculated from horizontal and vertical angles measured using a triangulation system. Two survey points, or floor points, were embedded in the culvert floor near each instrumented cross section and a theodolite was positioned first over one survey point, and then over the other. Vertical and horizontal angles were read to all eleven nails installed along the inner surface of the instrumented culvert cross sections. The nails were spaced along the inside face of the instrumented cross sections from footing to footing at approximately 5 ft. intervals. The distance between the two floor points at each cross section was measured with a steel tape. This deflection monitoring system, which is relatively "invisible" and does not incorporate any permanent devices which protrude from the inside surface of the culvert, was chosen to reduce the chances that the monitoring system would be destroyed or affected by vandalism.

The vertical and horizontal positions of the nails in the culvert were calculated from the angles measured at the floor points and from the measured distance between floor points using triangulation. This will be briefly explained. The two floor points and each nail form a triangle in the horizontal plane. The measured horizontal angles at each floor point are used to calculate the third horizontal angle in the triangle at the nail of interest. Using the law of sines, the three known interior angles of the triangle, and the known length of the side of the triangle between the floor points, the other two sides of the triangle, which are the horizontal distance from each floor point to the nail of interest, are calculated. In the vertical plane, each floor point is in a separate right triangle with the nail of interest. The vertical position of the nail of interest (relative to the theodolite height) is established at each floor point using the horizontal distance from the floor point to the nail and the measured vertical angle. The vertical position of each nail relative to the theodolite is then converted to a nail height relative to the nail just above the east footing by subtracting the height of each nail from that of this "baseline" nail. Separate heights are calculated for each nail at each floor point and the average of these two heights is used for deflection calculations. The horizontal positions of all nails (in the plane of the instrumented cross

section) are also calculated relative to the baseline nail. Deflections are calculated as the difference between nail positions relative to the baseline nail at any time of interest and that measured prior to placement of fill around the culvert. This measuring system does not detect overall displacement of the culvert considered as a rigid body. Since no benchmark outside the culvert was available, overall displacement or change in location was not measured.

CHAPTER 2

ACCURACY OF THE CULVERT MONITORING SYSTEM

The interpretation and discussion of the measured culvert response is affected by the accuracy of the soil pressure gages, concrete strain gages, and the deflection monitoring system. Therefore, the accuracy of these measurements will be discussed first, in this chapter, and the measured response will be presented and discussed in the next chapter. As the discussion in this chapter shows, the strain gages and soil pressure gages are thought to be more accurate than the deflection monitoring system. Most of the lack of accuracy in the soil and pressure measurements is due to unknowns in the temperature history at the gage locations. As discussed in Chapter 1, corrections must be made to the gage measurements to correct for temperature induced changes in gage properties. The difficulty in siting on the nails embedded in the inside face of the culvert, which function as fixed survey points on the culvert, is thought to be the primary factor affecting the accuracy of the deflection monitoring system. It is almost certain that the error in the measured horizontal deflections is very significant compared to the measured values. The error in the measured strains may also be significant compared to the strains measured at some locations, where only small strains occurred.

2.1 Accuracy of Concrete Strain Gages

The accuracy of both the strain gage and the soil pressure cell are primarily dependent on the accuracy of the vibrating wire transducer. Error in the measured strain in the vibrating wire transducer is introduced by error in the measured vibration frequency, error in the assumed wire properties and gage length, and temperature effects on the vibrating wire which are not accounted for. These sources of error will be discussed in the order they appear above.

The frequency counter in the readout box is very accurate. According to the manufacturer, the readout box can read a frequency of 500 cps (which is at the upper end of the vibration frequencies of the vibrating wire) with an accuracy of 0.001% when compared to standards traceable to the National Bureau of Standards.[22] Since strain is proportional to frequency squared, and the concrete strain is the difference between two measured strains which may both be in error, this corresponds to an accuracy of 0.004% in the measured concrete strain. Therefore, any error in the measured strain due to error in the measured frequency is negligible.

The accuracy of the wire properties and gage length used with the vibration frequency to calculate wire strain are not determined by the manufacturer individually for each gage based on traceable standards. The Geokon company has performed a series of tests on vibrating wire strain gages where gage measurements of strain in a steel member were compared to strains determined from the average of the displacements measured by two precision DCDTs (DC linear variable displacement transducers).[23] The vibrating wire strain gages used in these tests were very similar to the VCE-4200 model except that the two ends of the gages were bolted to the steel member rather than embedded in concrete. These tests

showed that all twelve vibrating wire strain gages used in the study measured strain very accurately compared to the DCDTs at eight different loads. In general, strains from strain gages matched the average measurement made with the two DCDTs within $\pm 0.5\%$.

As a rough check of the ability of the VCE-4200 gages to measure concrete strain under load, one vibrating wire strain gage was embedded in a 12 in. high concrete cylinder which was subjected to a compression test. No high precision equipment, such as the DCDTs used by Geokon, was available to measure the deflection of the cylinder. However strain was measured with the embedded strain gage, stress was calculated based on the applied load, and a realistic Youngs Modulus was calculated (4.7 x 106 psi for 6000 psi strength concrete). Therefore, a gross check was performed on the ability of the strain gage to measure strain in concrete under stresses between 100 and 1000 psi.

Change in vibrating wire properties over time can occur. A reduction in wire tension due to factors such as corrosion, slip, or creep of the vibrating wire is possible. This causes zero drift usually in the direction of decreasing tension (i.e. increase in apparent concrete compression strain and increase in apparent earth pressure). Proper sealing of the vibrating wire and use of high quality clamps and wire reduce the possibility of zero drift. Vibrating wire gages are very good for long-term field measurements in that the output signal is a voltage frequency, as explained in Chapter 1, rather than magnitude of voltage or resistance. The frequency of a voltage output is usually a more reliable measurement than the magnitude of voltage or resistance because the frequency is relatively unaffected by factors such as signal cable resistance, contact resistance, leakage to ground, or length of signal cable, which can significantly affect the magnitude of a measured voltage or resistance.[24]

Since drift due to changing wire properties is known to be a potential problem with vibrating wire transducers, the Geokon corporation has an ongoing, long-term effort which monitors the long term stability of their gages. In one such study they have monitored their Model VCE-4200 and Model VCE-4000 vibrating wire strain gages over an eight year period.[25] The Model VCE-4000 gage is virtually identical to the VCE-4200 gage except it is arc welded to steel members. Figure 2.1 shows results from their investigation. Figure 2.1a shows the strains measured in two Model VCE-4200 vibrating wire strain gages embedded in 5 in. x 9 in. x 2.5 in. concrete test specimens made with 3000 psi concrete and submerged in a water bath. A perfectly stable gage would measure no strain change with time assuming the concrete volume remains constant. Sample gage A shows a peak strain variation of 50×10^{-6} in./in. over the eight year period. Gage B has a peak strain variation of 90×10^{-6} in./in. In both gages there is a gradual drift of increasing measured tension or concrete expansion. For Gage B, where this drift is most noticeable, it is occurring at a rate of about 15×10^{-6} in./in. per year. These specimens were not originally placed in a water bath and therefore substantial initial shrinkage of the concrete occurred. The data in Figure 2.1a shows only data points measured after the test specimens had been inserted in the water baths and were judged to have swelled from the shrunken state to a more or less constant volume. However, some of the change in strain in Figure 2.1a may be due to the continual absorption of water by the concrete specimens and thus continued swelling rather than drift in gage measurements.

Figure 2.1b shows data from a Geokon Model VCE-4000 vibrating wire strain gage welded to a steel I-beam. The VCE-4000 gage has the same vibrating wire transducer used in the VCE-4200

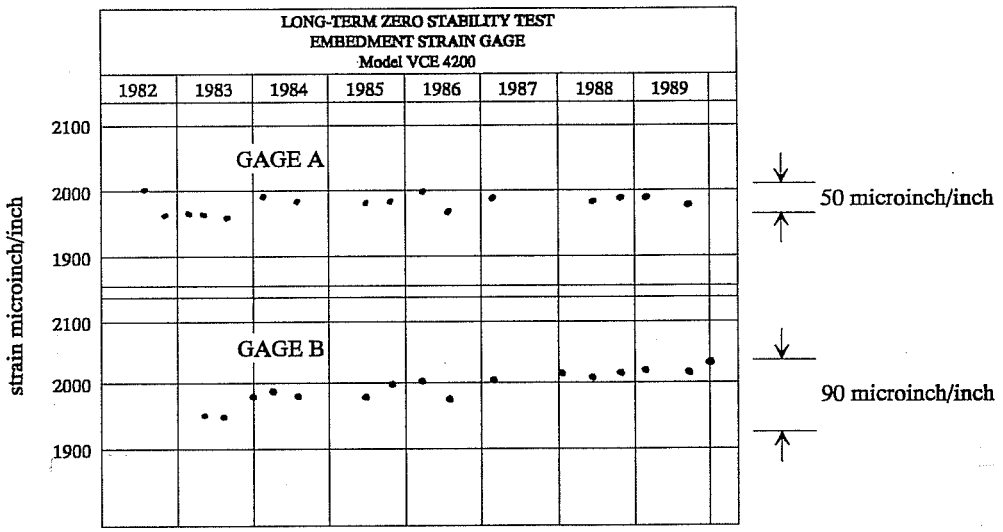

Figure 2.1(a) Measured long-term stability of Geokon Model VCE-4200 Concrete Embedment Strain Gage (Reference 27)

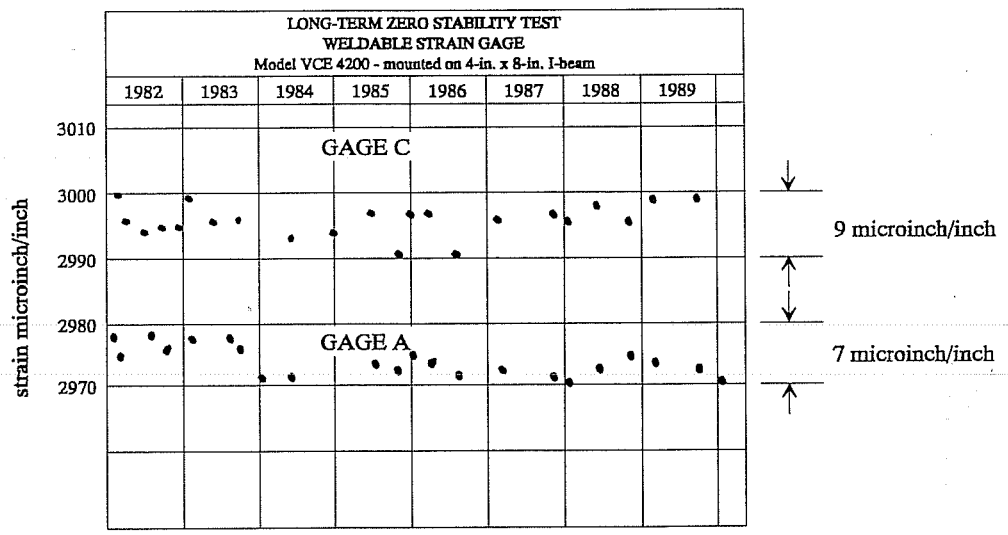

Figure 2.1(b) Measured long-term stability of Geokon Model VCE-4000 strain gage mounted on steel I-beam (Reference 27)

concrete strain gage, and is otherwise almost identical to the VCE-4200, except that it has mounts that can be welded to steel at each end of the gage rather than the disks at either end of the gage shown in Figure 1.4. Since steel is a more stable material than concrete, any variation in measured strain for this case can more confidently be attributed to variation in the gage. As Figure 2.1b shows, the strain variation is much smaller for this gage, only 9 x 10^{-6} over an eight year period for the two gages that were monitored. There is a slight drift of increasing tension in one of the gages and a slight drift of decreasing tension in the other so that, on the whole, the variations seem to be random. This data indicates that the Geokon vibrating wire strain gages are very stable over a time period that is much longer than the monitoring period reported here for the culvert.

A final important variable which affects the accuracy of the measured strains is temperature. Figure 2.2 from Reference 26 illustrates the effect of temperature on measurements made with a vibrating wire transducer. This figure shows the gage reading and the corrected gage reading from a vibrating wire displacement gage that is attached to a steel beam subjected to the temperature history shown in the figure. The beam is subjected only to the temperature change, it not subjected to any stress or restraint. This figure shows the gage reading in terms of its vibration frequency squared, which is directly proportional to the gage displacement. Therefore, a decrease in frequency is equivalent to an apparent shortening of the beam. Figure 2.2 shows that the (uncorrected) gage reading decreases, or becomes more compressive, as the temperature increases, but the corrected gage reading is not affected by temperature change. The large initial drop in the corrected gage reading is thought to be due to creep in the attachments between the gage and steel beam. The corrected reading, which does not include any temperature induced strain in the beam (it would include strain from temperature induced stresses or eigenstresses), corrects for the fact that there is a difference in the thermal coefficients of expansion between the vibrating wire and the steel beam. Based on the data in Figure 2.2, the thermal coefficient

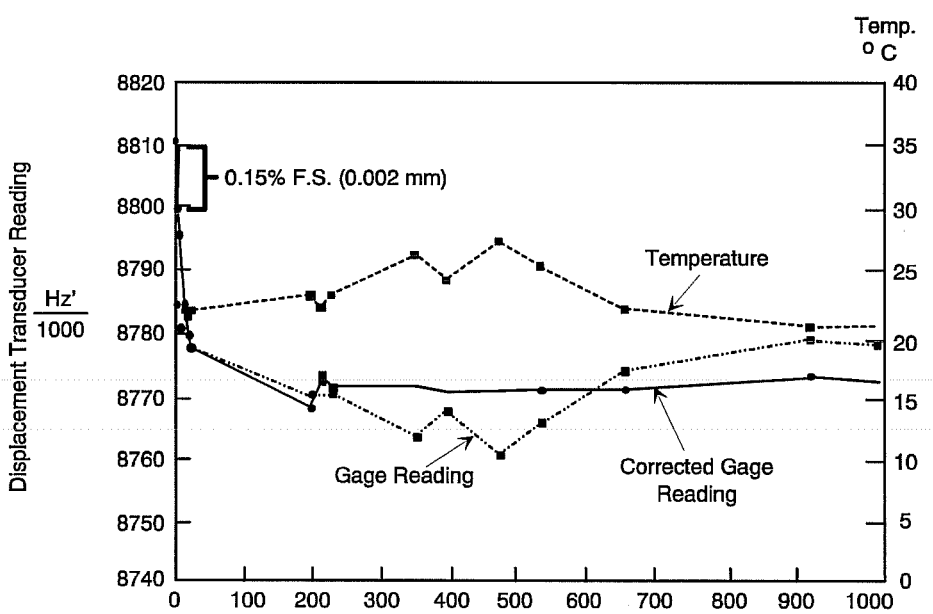

Figure 2.2 Corrected and uncorrected readings from a vibrating wire transducer subjected to temperature change (Reference 28)

of expansion of the vibrating wire in the transducer is greater than that of the steel beam so that the beam restrains the free expansion of the vibrating wire during a temperature rise causing relaxation of the vibrating wire. This is measured as an apparent (false) shortening in the beam prior to correction. The accuracy of the correction factor, and thus the corrected gage reading, is dependent on the accuracy with which the temperature history and material coefficient of expansions are known.

Since the vibrating wire in the VCE-4200 strain gages also has a higher coefficient of expansion than concrete, a temperature rise will cause a similar apparent (false) compression to be measured in the concrete. As discussed above, this temperature induced change in strain is not a measure of concrete temperature strain, since it is due to the differential effect of temperature on the wire and surrounding concrete, and therefore it is an error which must be subtracted out of the measured strain. The corrected strain includes strains due to stress (load induced stress and temperature induced stress), creep, and shrinkage, but not temperature as discussed in Chapter 1. The corrected strain is calculated from the measured strain as shown in the equations below.

$$e = e_m - e_c \tag{2.1}$$

$$e_c = (a_w - a_c) \times (T_1 - T_0) = (a_w - a_c) \times T_c \tag{2.2}$$

where e_m = measured strain,
e_c = correction factor,
a_w = coefficient of thermal expansion for the vibrating wire,
a_c = coefficient of thermal expansion for the concrete,
T_1 = temperature at time strain is measured,
T_0 = temperature at time of initial gage reading, and
T_c = temperature change = $T_1 - T_0$.

Unfortunately, the only variable in Equations 2.1 and 2.2 which is known with a high degree of accuracy is the thermal coefficient of expansion of the vibrating wire (6.7×10^{-6} in./in./°F). However, reasonable ranges for the other variables can be defined based on information in the literature and temperature records from the National Oceanic and Atmospheric Administration (NOAA) measured in San Antonio during the culvert monitoring period.

The thermal coefficient of expansion is discussed for a broad range of concrete types in Reference 27. This reference reports a range of measured thermal coefficients for concrete made with limestone aggregate between 2.0×10^{-6} in./in./°F and 5.7×10^{-6} in./in./°F. The median of this range is 3.9×10^{-6} in./in.°F. This reference also presents a method for calculating the coefficient of expansion based on the aggregate type and the approximate saturation condition. The calculated coefficient of expansion for the concrete in the culvert using this method is 4.6×10^{-6} in./in./°F based on limestone aggregate and assuming the concrete is partially to fully saturated. The presence of the fill on one side of the culvert is assumed to keep the saturation at a higher level than that which would occur in an uncovered outdoor structure, and therefore the lowest saturation range in the methodology, partially saturated decreasing with time to the drier condition, was not used. In order to limit the potential error between the unknown

concrete coefficient of expansion and the assumed value, the median of the measured coefficient of expansions in concrete with limestone aggregate reported in Reference 27 (3.9×10^{-6} in./in.°F) is assumed in the calculated correction factors used to determine the temperature corrected strains reported in the next chapter.

Daily temperature records (high and low temperature) are available from the National Oceanic and Atmospheric Administration (NOAA) which also show the moving 7-day average high and low temperatures.[36] An approximate relationship between air temperature and the temperature near mid-thickness of the culvert where the gages are located can be based in part on data from Reference 28. This reference presents the results of a long-term experimental study of a concrete bridge by Wilson, et al. which shows that the internal temperature of a partially shaded concrete member surrounded by air is virtually constant within a given day (it changed by no more than 10°F on a given day during a two year monitoring period) at a value near the average of the mean daily temperatures over the previous three days. This was true at the two points where temperature was measured, at a distance of 3 in. from the surface and at mid-thickness (15 in. to 20 in. from the surface). Figure 2.3 shows results from the study. Unlike the bridge studied in Reference 28, the culvert is covered with deep soil fill on one side which, at a some distance out from the culvert, remains at a temperature close to the yearly average temperature. The soil temperature is relatively constant at some depth away from the culvert walls and this has a stabilizing effect on the culvert temperature relative to a case where air surrounds the structure. Thus, it is reasonable to expect that the culvert wall temperature responds more slowly to changes in air temperature than the bridge member shown in Figure 2.3. For this reason, it is assumed here that up until the time the culvert has three feet of fill over the top, the concrete temperature at the gage location is equal to the average of mean temperatures from the previous three days. After this time, due to the presence of the fill, it is assumed that the temperature in the concrete near the gage locations is equal to the average temperature over the previous seven days.

Obviously, the lack of certainty in the concrete temperature and thermal coefficient of expansion introduces error in the corrected, or actual measured strain. The error in the correction factor can be calculated with Equations 2.3 and 2.4.

$$e_c' = (a_w - a_c + a')(T_c + T') - (a_w - a_c)(T_c) \tag{2.3}$$

$$e_c' = (a_w - a_c)(T') + (a')(T_c) + (a')(T') \tag{2.4}$$

where e_c' = maximum error in the correction factor e_c,
a' = maximum error in the concrete coefficient of expansion a_c, and
T' = maximum error in the temperature change T_c = twice the maximum error in a temperature measurement.

Assuming the values shown below for a′ and T′, the maximum error in the correction factor is $\pm 8.2 \times 10^{-5}$ in./in. in the summer and $\pm 6.4 \times 10^{-5}$ in./in. in the winter. The value for a′ is based on the

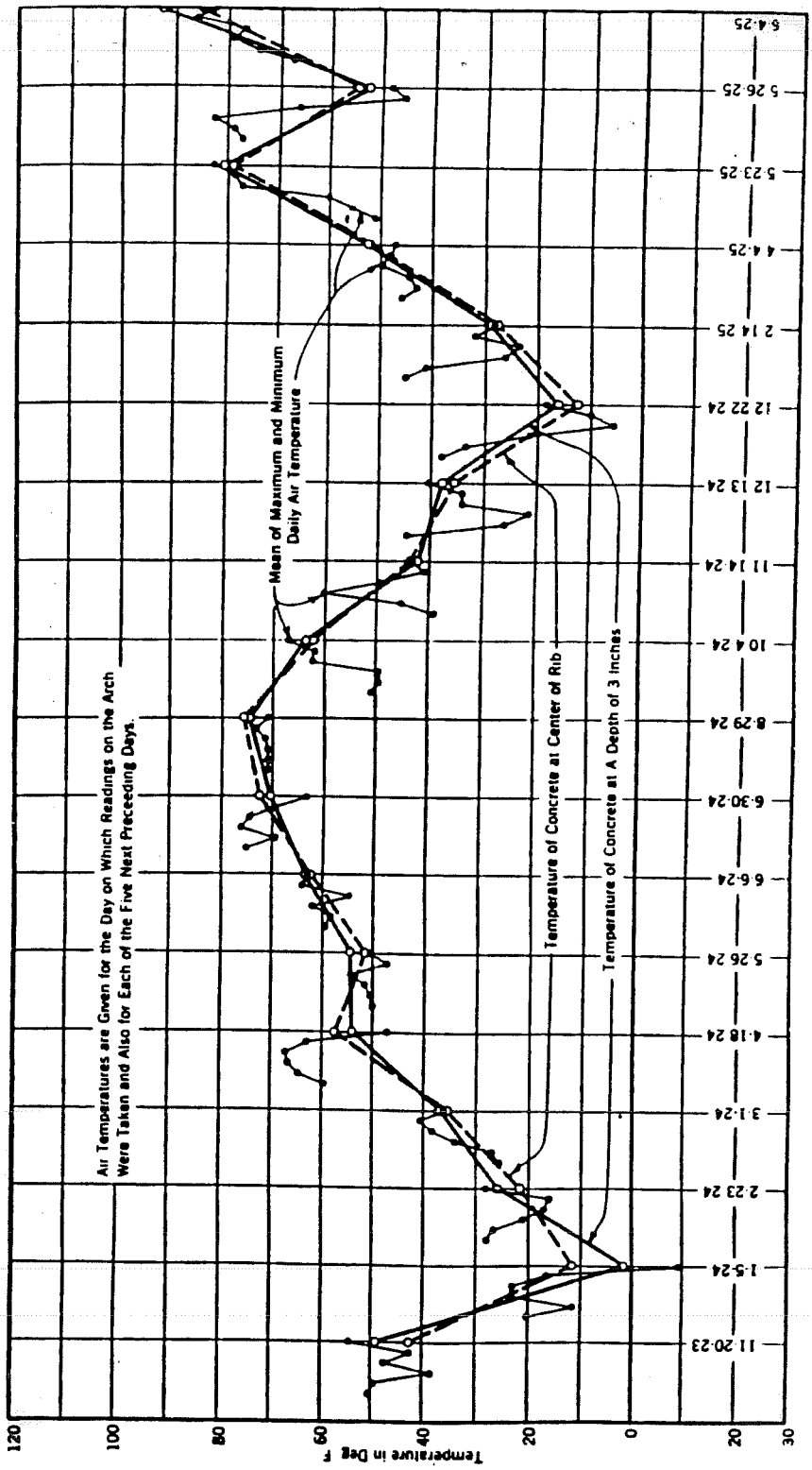

Figure 2.3 Measured temperature history in a partially shaded concrete bridge member (Reference 31)

difference between the extreme measured values of the thermal coefficient of expansion of concretes with limestone aggregate, as reported in Reference 27, and the assumed value. As mentioned above, the assumed value is at the midpoint of the reported range of values. The value for T′ may be too large when considering the maximum values for T_c shown below.

a' = $\pm 1.8 \times 10^{-6}/^{o}F$
T' = $\pm 10^{o}F$
T_c = $+20^{o}F$ (summer) and $-10^{o}F$ (winter) from the NOAA records and the assumed relationship between air and concrete temperature.

If half the estimated values of a′ and T′ above are used, the maximum error in the correction factor is $\pm 3.9 \times 10^{-5}$ in./in. in the summer and $\pm 2.9 \times 10^{-5}$ in./in. in the winter. These latter values, which represent a worst case combination of the assumed errors in temperature and coefficient of thermal expansion, but which assume more realistic bounds on these errors, are considered to represent a realistic upper bound of the error in the measured strain.

The estimated maximum error in the temperature correction factor of 3.9×10^{-5} in./in. adds to any error in e_m, the uncorrected measured strain, to equal the total maximum error in the measured strain. As discussed above, the error in e_m compared to strain measurements with the two precision DCDTs was only $\pm 0.5\%$. Assuming, as a worst case, that this difference is due entirely to error in the vibrating wire strain gages, and noting that the maximum measured strain in the culvert is approximately 0.0012 in./in., the maximum error in e_m is 6×10^{-6} in./in. The possible error in the measured strain due to drift, as measured on the steel beams in Figure 2.1b, is also less than 1×10^{-5} in./in. over an eight year period. Assuming that any error caused by drift over the 2.8 year monitoring period would be less than one-half this much, this source of error is also very small. Therefore, 5×10^{-5} in./in. represents the upper bound on the expected error in the measured strains presented here.

Again it is repeated that the measured strains do not include temperature strains. In future studies it is recommended that the concrete thermal coefficient of expansion be determined in laboratory tests and that additionally, "temperature correction" strain gages be placed in structures along an axis which is not affected by the applied loads to measure the effect of temperature change acting alone on the vibrating wire strain. Since these gages would not be subject to strains from stresses or creep, the measured strains could be used directly to get the correction factor e_c discussed above after the primary effects of shrinkage were assumed to have ended. Finally, knowledge of the concrete thermal coefficient of expansion and the change in vibrating wire strain induced by temperature alone can be used to calculate both the temperature history in the concrete at the strain gage depth and the concrete temperature strains.

2.2 Accuracy of Soil Pressure Cells

As discussed in Chapter 1, the Geokon Model 4800E-100 soil pressure gages used in this field study measure change in the internal fluid pressure, and thus soil pressure, based on the change in tension strain of the vibrating wire in the transducer attached to the gage. This was illustrated in Figure 1.5. The wire strain is related to the fluid pressure by means of a gage factor. The gage factor for each soil

pressure gage was determined by means of a factory calibration at 20 psi increments between 0 and 100 psi. Since all measured pressures in this study were 30 psi or less, the gage factor from the first 20 psi increment is used to convert wire strain to gage pressure. All Model 4800E-100 gages are calibrated to an accuracy of plus or minus 0.25% full scale against standards traceable to the National Bureau of Standards.[22] Since the gages are designed to measure pressures up to 100 psi, this corresponds to an accuracy of $\pm$0.25 psi.

Long-term drift in the measured pressure is also a potential source of error. Since the soil pressure gages use a vibrating wire transducer produced by the Geokon company, the data shown in Figure 2.1, and discussed above, infer that the soil pressure gages are also very stable against long-term drift. The Geokon company has also performed long term testing of their soil pressure cells which is summarized in Figure 2.4. The pressure reading is shown in terms of the vibration frequency of the

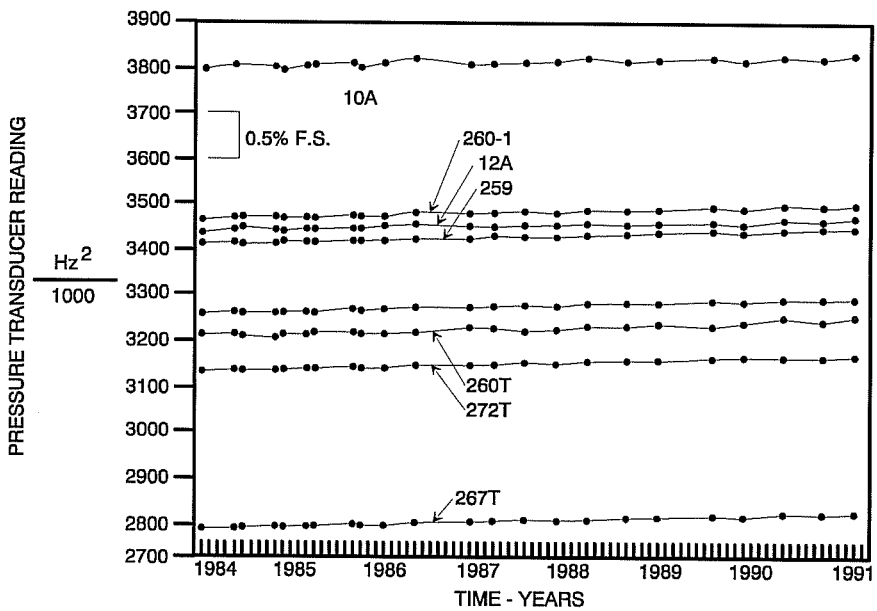

Figure 2.4 Measured pressure in Geokon pressure cells maintained in a stable laboratory environment for seven years (Reference 28)

vibrating wire in the transducer – the gage factor has not been applied. However the pressure is directly proportional to the vibration frequency squared. As would be expected based on the data in Figure 2.1, the pressure cells show very little long-term drift.

The soil pressure cells are also sensitive to temperature change. A temperature correction factor, which is multiplied by the temperature change and added to the measured pressure, is determined by the manufacturer for each gage. This factor corrects for the apparent change in pressure caused by a temperature increase under laboratory conditions. Temperature affects both the tension in the vibrating wire in the transducer and the volume of the pressure cell. The largest temperature correction factor for the soil pressure gages installed on the culvert is -0.027 psi/°F. Using an estimated maximum temperature change of 20°F in the summer, the maximum pressure correction is 0.54 psi. This is a very

small pressure compared to the 100 psi full scale pressure the gage is designed to read and therefore the gages are generally insensitive to temperature. However, 0.5 psi is significant compared to the measured soil pressures under the low fill (3 to 5 psi) and therefore the temperature correction factors have been applied to the pressures presented in the next chapter. The same estimated temperatures used to correct the measured strains for temperature effects were used to correct the measured pressures. Assuming the worst case 10°F error in the estimated temperature used above, the corresponding error in the measured pressure is 0.25 psi. This is equal to the maximum error in the calibration factor and therefore does not represent a significant loss of accuracy. Also, the temperature correction factor was presumably determined in the factory using the same standards as the calibration factor. Therefore, it is subject to a maximum error of 0.25 psi itself.

Another complication that affects the correction factor for temperature change is the fact that this factor, which was determined in the laboratory, does not account for any field constraints on the temperature induced change in the pressure cell volume. In the laboratory, the cell is free to expand and contract during a temperature change. Depending on whether the fluid inside the cell wants to expand more or less than the steel cell, field constraints on the pressure cell expansion could act to increase or decrease the apparent pressure relative to that calculated using the factory determined temperature correction factor.

The "effective" accuracy of any gage is also reduced if the presence of the gage affects the response it is intended to measure. In the case of the soil pressure cells, it is important that the gages do not affect the local distribution of soil pressure on the culvert. The cell is manufactured to be approximately as stiff compared to clay or sandy soil as concrete. For this reason, it is essential that the gages be placed flush with the culvert surface. If the cell protrudes significantly from the concrete surface, it will attract stress from surrounding soil outside the limits of the cell surface area because of the high stiffness of the cell relative to the stiffness of the layer of soil around the gage in contact with the concrete surface. The measured pressure will not be representative of the soil pressure that would occur if the gage were not present. The reverse situation can occur if the gage is recessed from the concrete surface. Since the culvert segments were precast in expensive reusable steel forms, attaching the soil gages or any blockouts to the forms was not an option. Therefore, the soil pressure gages were epoxied to the culvert outer surface and high strength grout was placed up to the top face of the pressure cell over a large area of the structure around the gages to cause the gage face to be flush with the surrounding surface. The grout was sloped down very gradually to the original culvert surface at a distance several cell diameters away from the cell so that no abrupt protrusion would exist on the structure surface.

It is generally a good check on the soil pressure gages to place at least one gage, which is attached to a concrete panel in the same manner the gages are attached on the culvert, at a distance from the culvert where a free field vertical stress is expected. A comparison of the measured pressure with the calculated free field soil pressure can then be used to assess the influence of the gage mounting system on the measured pressures. The culvert was placed near an existing embankment, as shown in Figure 1.3, and there was not any space available between the culvert and the existing embankment where the free field stress could confidently be expected to occur. It was decided that the gages would be placed in symmetrical locations on the culvert so that the total number of available gages could be used to

measure soil pressures on the culvert and a comparison of symmetrically placed gages could be used as the primary means of checking for any significant error due to a disruption of the local soil pressure distribution by the gages. This assumes that if the gage properties, or the manner in which the gage is mounted, influence the measured soil pressures, this influence will cause errors which are not uniform at the different gage locations. Obviously it would be better to avoid relying on such an assumption, but no better, workable option was apparent.

The estimated error of the measured soil pressures is, at worst, ± 0.5 psi based on the maximum ± 0.25 psi error possible in the calibration and the additional error introduced by the temperature dependency of the gages. The lack of a reliable temperature history at the gage location and the lack of a temperature correction factor determined from as-installed testing both contribute to the estimated error due to the temperature dependency of the pressure measurements. Fortunately, the gages are relatively insensitive to temperature change. Finally, it is always possible that the properties of the gage itself are influencing the measured soil properties. However, there is no evidence that this is a significant problem in this study. First of all, a flush surface over the instrumented area of the structure was provided and experience indicates this is the most important requirement for proper placement of a contact pressure cell.[24] Also, the measured pressures presented in the next chapter show that two out of the three sets of symmetrically placed pressure cells measure soil pressures within 20% of each other. Since errors caused by incorrect gage placement are likely to be unequal at each gage location, the close correlation between pressures measured at different locations in this field study adds confidence to the basic accuracy of the measurements. The set of gages which do not measure similar pressures are located in the low fill region very near the top edge of a slope, which may be the cause for the relatively large difference in measured pressures. This is discussed in more detail in the next chapter.

2.3 Accuracy of Deflection Monitoring System

The accuracy of the measured deflections is the most difficult accuracy of the measured parameters to estimate. Since the deflections were measured using a triangulation system as described in Chapter 1, the accuracy of these measurements is dependent on the accuracy of the surveying method. This can be broken into two broad categories: 1) the accuracy of the equipment, which is relatively easy to determine, and 2) the accuracy with which the equipment was used, which is much more difficult to determine. The equipment was quite accurate, especially at the short distances used between surveying points. The basic surveying setup was such that very accurate measurements could be made. However, detailed analysis of the surveying measurements indicates that the overall accuracy is much lower than was originally anticipated. The most likely cause for this is limited accuracy in siting on nails in the culvert wall which were used as survey target points. The equipment and surveying setup will be briefly discussed first and then the problems associated with siting on the nails, and the loss of accuracy caused by these problems, will be discussed in detail.

At different times during the monitoring period, angles were read with several different theodolites, the least accurate of which was a theodolite with markings every 5 arc-seconds. All theodolites were calibrated against the traceable standards typically used by commercial surveying companies for calibration. The lengths between survey points were kept to a minimum by locating the

floor points very close (within 35 ft.) to the nail points. Some of the angles within the triangle in the horizontal plane between the floor points and the nail of interest were small (less than 20°). This is generally discouraged for triangulation since any given error in angle measurement will cause a larger percentage error in the measure of a small angle. However, the distances were much smaller than those normally used for surveying and therefore any error in angle measurement within the resolution of the theodolite could not result in a significant error in nail position (an error greater than 0.02 in.). Also, experienced surveyors were used throughout the monitoring period. Early in the project, a graduate student who was a teaching assistant for a surveying class did most of the surveying and later in the project (after September 1988) a professional surveyor was hired to perform each survey. By September of 1988 it was apparent that the accuracy of the measured deflections was not as high as was desired. In an attempt to improve the accuracy as much as was possible at that time, each horizontal and vertical angle taken during the surveys was read at least twice. After each angle reading the theodolite crosshairs were taken off the target and realigned. If the second measurement was more than 10 arc-seconds different from the previous measurement, which rarely happened, more measurements were taken until it was clear which two measurements were most correct. The two closest measured angles were averaged to get each final measured angle used in the triangulation calculations.

Length measurements were made with a high quality steel tape which was marked off to a one-hundredth of a foot. The lack of precision caused by the relatively large distance between tape markings does seem to have a some effect on the accuracy of the measured deflections. This will be discussed later in this section. The distance between floor points was always measured at least twice, or until two measurements were within 0.005 ft., and then averaged. Two measurements were always sufficient to determine the measured lengths between floor points used in the triangulation calculations.

As mentioned above, it is thought that the accuracy of the deflection measurements is most affected by difficulties in siting accurately on the nail heads. The difficulties are due to at least two primary causes. First, the nails were placed flush, or nearly flush, with the concrete arch surface. Therefore, instead of being perpendicular to the line of site, as is typical for a surveying target, the nail heads were partially parallel to the line of site. A pointer, such as a pencil, was used to locate the approximate center of the nail head and the surveyor focused on the intersection of the pencil point and the nail head surface. The orientation of the arch surface relative to the line of sight made it difficult to focus exactly on the nail-pencil intersection. Also, the relatively slight movements of the pencil point which occurred during the time required to line up the horizontal and vertical focusing screws most probably affected the angle measurements. Secondly, the nail heads, which were approximately 0.2 in. in diameter, did not have any marking on them. During surveying, the pointer was placed at the approximate center point of each nail head. Therefore, the position of the exact same point on the nail head was not measured each time a survey was done. The importance of the head marking was not appreciated until after the nails were installed.

Fortunately there is a means to quantify at least some of the inaccuracies in the deflection measuring system which are probably due to difficulties in accurately siting on the nail heads. As stated above, the vertical position of the nails, relative to the baseline nail near the left footing, were independently calculated from vertical angle measurements made at each floor point. Since the relative height of the nails was constant during each survey, any deviation between the two heights measured from

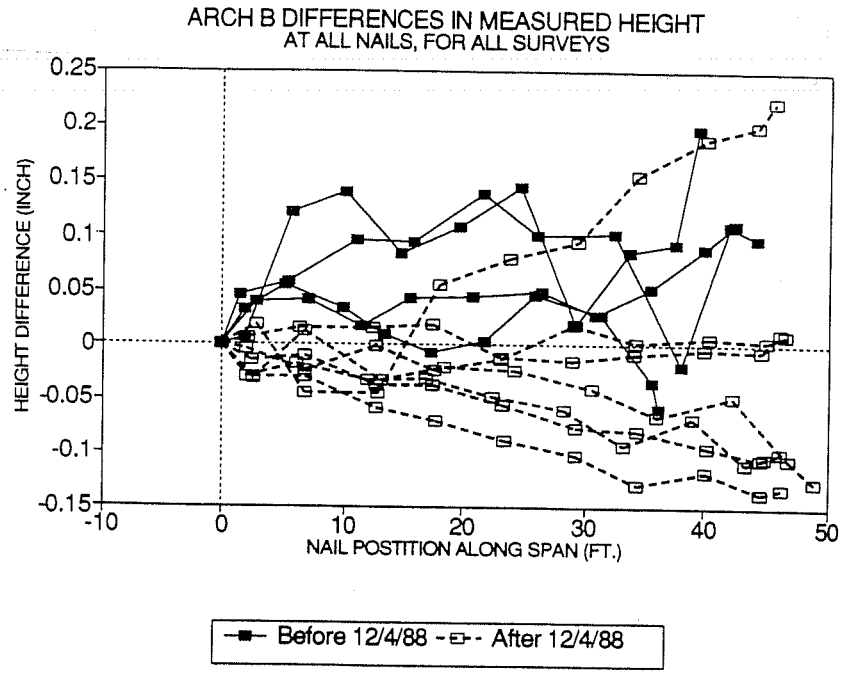

Figure 2.5 Difference in height of target points of culvert measured from two survey points

the two floor points can be attributed to surveying error. Figure 2.5 shows the difference in measured nail heights (relative to the baseline nail as discussed above) across Arch B for each survey. Points corresponding to the same survey are connected with lines. The difference in measured nail heights is similar at the other two instrumented cross sections.

A clear trend can be seen in Figure 2.5 which can be used to help understand a major source of error in the surveying system. The difference between measured heights from the two floor points drifts from a value of zero at the baseline nail (by definition) at the horizontal position 0.0 ft. to a maximum value at the opposite footing, which has a horizontal position of approximately 40 ft., for most of the surveys. This is particularly true after September 1988 when professional surveyors were used. Therefore, the difference in measured heights of a nail from the two floor points, which indicates error in the measurements, is not totally random. A probable cause of the apparent systematic error is illustrated in Figure 2.6. The surveyor's view of the nails near the footings is significantly different from the two floor points due to the large difference in the vertical and horizontal angle of the line of sight from the two floor points to these nails and the relatively steep slope of the arch surface near the footings. The arch surface near the footing is much more nearly perpendicular to the line of sight from the far floor point than to the line of sight from the near floor point. Therefore it is quite possible that the actual point on the baseline nail (Nail #1 in Figure 2.6) which is sited from the closer floor point is not the same as that sited from the further floor point even if the pointer location is kept constant. It is easiest to visualize that the siting from the closer floor point (Point B in Figure 2.6) would tend to be below the siting from the further floor point (Point A) since the line of site from the closer floor point is steeper (in the downward direction) and the nail head is sloped in the same general direction of the line of sight due to the curvature of the arch. This possibility is shown in Figure 2.6. The view of the midspan nail (Nail #6) is practically the same from each floor point since the floor points are placed symmetrically

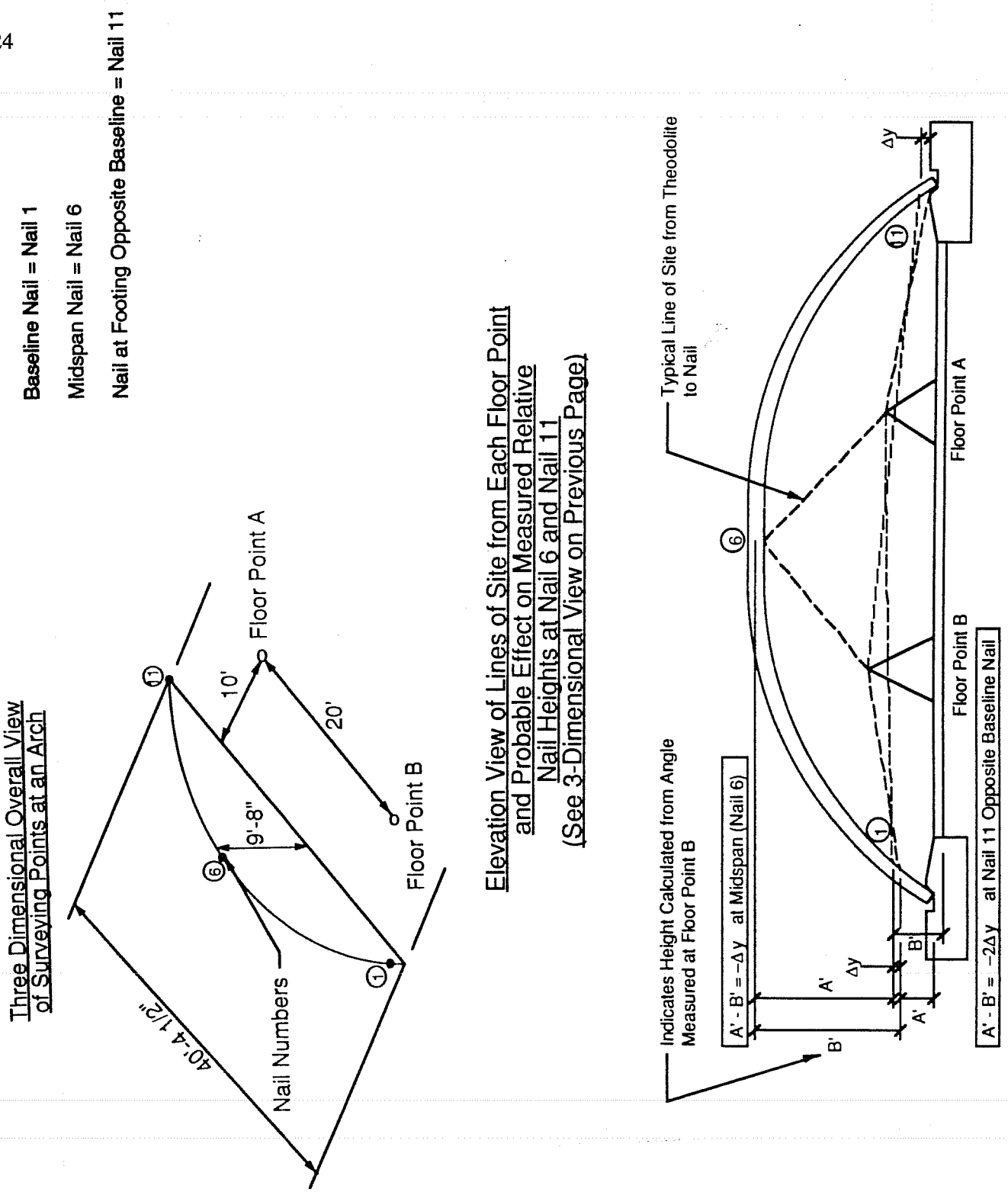

Figure 2.6 Possible effect of differing lines of site from floor points on measured height of targets on arches

about midspan. Therefore it is probable that the vertical siting from both floor points would tend to be on nearly the same point on the midspan nail head. Finally, at the nail opposite the baseline nail (Nail #11), the difference in siting from the two floor points would tend be exactly opposite that stated above for the baseline nail since, for this situation, the locations of the floor points relative to the nail of interest are reversed. This is shown in Figure 2.6 where the siting from the closer floor point (Point A) is below the siting from the further floor point (Point B). Remembering that the "height" of each nail is actually the height relative to the baseline nail, it can be seen in Figure 2.6 that the hypothesized difference in siting can lead to a difference in the measured height from the two floor points equal to $-\Delta y$ for the midspan nail and equal to twice $-\Delta y$ for the nail at the footing opposite the baseline nail. This matches the apparent linear drift in the difference in measured height from the two floor points across the arch span in Figure 2.5. A negative height difference in Figure 2.5 corresponds to a relative height measured from Floor Point B greater than that measured from Floor Point A in Figure 2.3. As Figure 2.5 shows, a trend opposite that shown in Figure 2.3 is also possible, although it only occurred once during a survey by a professional surveyor. Figure 2.5 also indicates that some of the early surveys apparently include a significant amount of random error.

The systematic error described above can be cancelled out by simply calculating the heights of all nails above a line across the arch span from Nail #1 to Nail #11, as shown in Figure 2.6, rather than relative to the height of Nail #1. This causes the heights of both Nail #1 and Nail #11 to be zero and therefore no rigid body rotation of the arch section can be measured. Figure 2.7 shows the difference in measured heights (relative to the base line between Nail #1 and Nail #11) for Arch B for all surveys. The heights of all nails for all surveys at the other two instrumented cross sections have also been calculated relative to a line between the nails nearest the footings. The systematic error is no longer apparent and the average difference in measured heights to each nail from the two floor points is

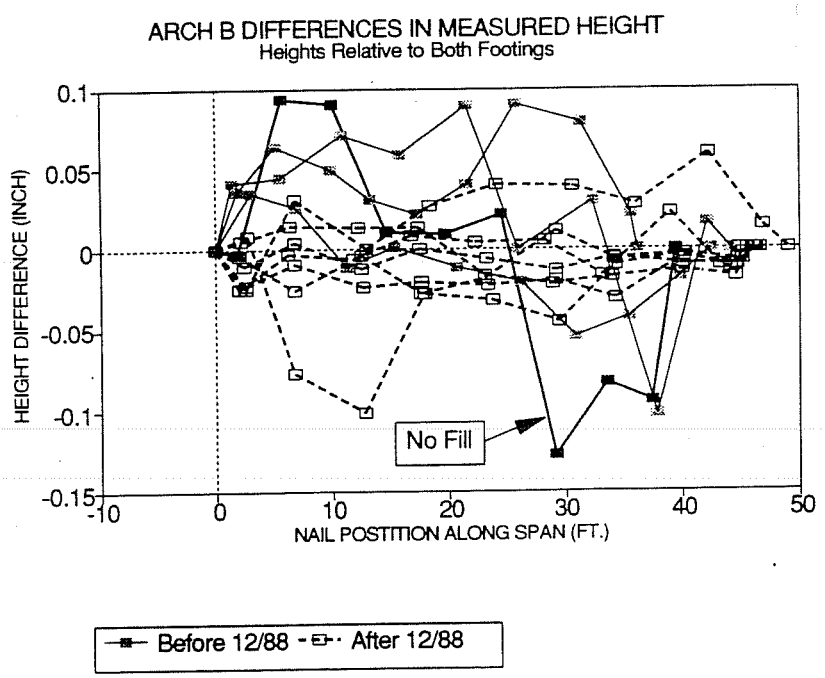

Figure 2.7 Corrected difference in height of target points on culvert measured from two survey points.

significantly reduced. The effect of using a professional surveyor (after December 1988) is also apparent. For all surveys after December 1988 the average measured height difference is approximately 0.02 inches. Prior to December 1988 the average measured height difference is approximately twice this value.

The discussion above has been focused towards understanding some of the cause for the apparent lack of accuracy in the measured nail positions and eliminating as much error as possible. The information in Figure 2.7 can also be used to help quantify the remaining error in the measured deflections. As stated above, the same nail height, relative to the imaginary line from Nail #1 to Nail #11, should be measured from each floor point. Therefore, it is thought that the difference in measured heights from the two floor points shown in Figure 2.7 is indicative of some of the total error in the vertical deflection monitoring system. Figure 2.7 shows that the difference in measured nail heights is not constant. The height difference is less than 0.05 in. for almost all cases for surveys after December 1988. The height difference for the no fill condition is particularly important since deflections are determined by subtracting each nail height at the time of interest from the nail height at the time of no fill. As Figure 2.7 shows, the height difference is less than or equal to 0.1 in. at all the nail points during the no fill condition survey (this survey is shown in Figure 2.7 with a solid line).

The assumed height of each nail for each survey is taken as the average of the two heights measured from the two floor points. If it is assumed that the two heights of each nail measured from the two floor points in some way straddle the actual value that would be measured if there was no unusual siting difficulties, then the averaging results in an error which is at most equal to one-half the difference between the two measured heights shown in Figure 2.7. Dividing the maximum differences in measured heights from the floor points after December 1988 (0.5 in.) and prior to December 1988 (0.1 in.) by a factor of two, the estimated maximum error is 0.025 in. in the measured nail heights after completion of fill and it is 0.05 in. for the no fill measurements. These estimates include error from all sources to the extent which the errors cause a differential in the measured vertical position of the nails at floor points A and B.

The difference in measured heights in Figure 2.7 includes the effect of inaccuracy of the theodolite and lack of surveying skill (as they affect vertical angle measurements only) since the nail heights from each floor point are based on totally separate vertical angle measurements. It also includes difficulties due to siting on the nail heads since this source of error should cause a different height to be measured from each floor point. However, any inaccuracies which cause the same, or a similar, error in the measured nail height at both floor points are not reflected in Figure 2.7. These types of inaccuracies may include inaccuracy in the measured distance between the floor points (the base distance) and inaccuracy in the measured horizontal angles. These two types of inaccuracy can be due to factors such as the resolution of the measuring instrument, the surveying error, and in the case of the horizontal angle measurements, error in horizontally siting on the nails. The horizontal angles and the distance between floor points both affect the measured nail height determined with the triangulation calculations as discussed in Chapter 1.

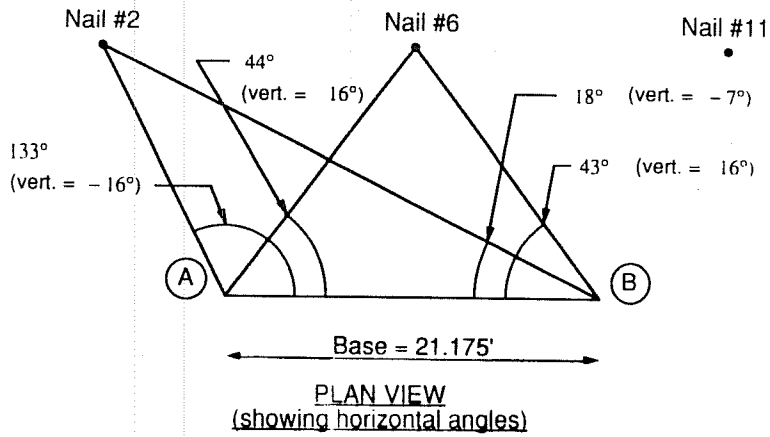

A and B are floor points

Figure 2.8 Effect of hypothesized error in measured angles and baseline on culvert position

Hypothesized Measurement Error				Resulting Change in Nail Position		
Nail	**ΔBase**	**Δ Horz. Angle**	**Δ Vert. Angle**	**Δ Z_A**	**ΔZ_B**	**Δ X**
6	-.0025′	-	-	-.012"	-.012"	-.03"
2	-.0025′	-	-	-.004"	-.003"	-.0025"
11	-.0025′	-	-	-.003"	-.003"	-0.06"
6	-	-5 seconds at B	-	-.0005"	-.0012"	-.0033"
6	-	-	-5 seconds at A	-.004"	0	0
2	-	-5 seconds at B	-	-.0013"	-.005"	-.013"
2	-	-	-5 seconds at A	-.008"	0	0

ΔZ_A = change in nail height from floor point A
ΔZ_B = change in nail height from floor point B
ΔX = change in horizontal measurement to nail

Figure 2.8 shows a limited parameter study which displays the effect of error in the three types of measurements made during the surveys (the distance between floor points, the vertical angle, and the horizontal angle) on the calculated vertical and horizontal positions of a nail near the footing (nail #2), a nail near the crown (nail #6), and a nail near the opposite footing (nail #11). The magnitude of the hypothesized error in measured angles used in the parameter study is taken as 5 arc-seconds, which is the smallest resolution of the theodolite. This is thought to be sufficient to account for error caused by the limited resolution of the theodolite and surveying error caused by slightly moving the theodolite since the surveyor can reasonably estimate the angle accurately to about 3 arc-seconds between the 5 arc-second theodolite markings, and the remaining 2 arc-seconds should be enough to account for surveyors errors since experienced surveyors were used. The hypothesized error in the measured base distance of 0.0025 ft. used for Figure 2.8 assumes that two distance measurements between floor points were made, each accurate to at least 0.005 ft., and they bound the exact value. The fact that the measurements are assumed to bound the exact value and that neither differs from the exact value by more than 0.005 ft. implies that the average does not differ from the exact value by more than 0.0025 ft.. The assumption that the measured values bound the exact value cannot be proven, it simply seems to be a realistic assumption that helps quantify a probable maximum error.

Figure 2.8 shows the changes in measured vertical nail positions (relative to the line between Nails #1 and #11) and change in measured horizontal nail position (relative to Nail #1) caused by the hypothesized errors in measurement of the base line between floor points and angles from the two floor points. The changes in nail vertical position (ΔZ) are shown separately from floor point A (ΔZ_A) and from floor point B (ΔZ_B). These values are shown at Nail #2 and Nail #6 for each given hypothesized angle and distance measurement error. ΔX is also shown at Nail #11 for error in the measured base line distance between floor points, since this error causes a progressively larger error in measured horizontal nail position across the span. Error in nail height will be discussed first. The largest error in measured nail height is equal to 0.012 in. at Nail #6 caused by the hypothesized 0.0025′ error in the measured base line distance between floor points. This error occurs in the nail height measured at both floor points (Z_A and Z_B). The fact that similar error is caused in measurements from both floor points is significant because it implies that the difference in measured nail heights shown in Figure 2.7 does not include error caused by inaccuracies in the measured base line distance. Therefore, error due to inaccuracy in the measured base line distance is in addition to errors implied by the difference in measured nail heights shown in Figure 2.7.

The hypothesized 5 arc-second errors in the horizontal and vertical measured angles cause significantly less error in the vertical nail positions than the hypothesized error in measured base distance. Also inaccuracy in measured angles tends to cause *dissimilar* error in the measured nail heights. This is important because it implies that the difference between measured nail heights from the two floor points shown in Figure 2.7 is affected by inaccuracies in measured angles. Since the information in Figure 2.7 will be used to help determine the total error in the measured vertical deflections, the intent here is to find sources of error, such as error in the measured base line distance, which are not accounted for in Figure 2.7. It is probable that all the error in the nail height shown in Figure 2.8 for inaccuracies in measured angles is accounted for in Figure 2.7 except the relatively small amount (ΔZ_A - ΔZ_B). This amount can be ignored.

The emphasis up to this point has been on the measured nail heights. To get culvert vertical deflections, the measured nail heights from both floor points at the time of interest are subtracted from the average nail height measured when there was no fill over the culvert. Based on Figure 2.7, the maximum estimated error in the average measured nail height is 0.025 in. at times of interest after completion of fill and 0.05 in. at the no fill condition due to difficulties in sighting on the nail heads. Assuming these errors can, as a worst case, be additive, a value of 0.075 in. will be used as a maximum error in the measured vertical deflection due to inaccuracies in siting on the nails. As discussed above, additional error can be introduced into the calculated nail heights due to an inaccurate measurement of the base distance between floor points and this error was estimated to be 0.012 in. As a worst case, error in measured base distance can occur during both the no fill condition survey and any subsequent survey so that the effect of this type of error on the calculated deflections is additive and equal to 0.024 in. Adding 0.075 in. and 0.024 in., the maximum error in the vertical deflections can be taken as 0.1 in. This is an extreme combination of worst case possibilities so that is it more reasonable to estimate the worst case error in measured vertical deflection as some lower value such as 0.07 in. This estimated error in measured culvert deflections is similar to that reported by other researchers.[36]

The error in the measured nail horizontal position is inherently greater than that in the measured vertical positions because there is less averaging of separate measurements. First, the horizontal position of nails is not measured separately from each floor point as is the case for nail height. The measurements from both floor points must be used together to determine the nail horizontal position. Second, the horizontal nail positions must be determined relative to one nail near one of the footings (Nail #1) rather than relative to a line extending between the nails near each footing as is the case for the nail height measurements. This lack of averaging increases the amount of random error included in the measurement. It is assumed that error is introduced into the horizontal nail position measurements by the same phenomena discussed above which affect the vertical nail positions. Error in the parameter study in Figure 2.8 shows that approximately equal errors occur in both the horizontal and vertical nail positions due to a given error in vertical angle measurement (for example, compare $\Delta X = 0.003$ in. to $\Delta Z_A = 0.004$ in. at nail #6 for a 5 arc-second error in the vertical angle measurement). Therefore, it is probable that the errors in the horizontal and vertical nail positions caused by inaccuracies in siting on the nail heads are very similar. Figure 2.5 shows this error for the case of nail heights determined relative to a single nail position. This error is approximately twice that in Figure 2.7. Therefore, after fill is complete the maximum estimated error due to inaccuracies in siting on the nail head in the horizontal nail position (relative to Nail #1) is 0.1 in. (twice the 0.05 in. value used for nail heights based on Figure 2.4) and, for the case of no fill, it is 0.2 in. The error in measured horizontal position is also dependent on the accuracy of the baseline distance between floor points as shown in Figure 2.8. For the previously assumed worst case error of 0.0025 ft. in the base distance measurement, the maximum error in the horizontal position of Nail #11 is 0.06 in. Assuming that these two types of error can add together, the total maximum error in a nail horizontal position measurement made after fill was complete is 0.16 in. and, for the no fill condition, it is 0.26 in. The horizontal deflections are the difference between measured horizontal positions at the time of interest and at the no fill condition and therefore the error in each of these two horizontal measurements at can be additive. Assuming a worst case full addition of these errors, the maximum error in measured horizontal deflection of the spread between culvert footings is approximately 0.4 in. A more realistic estimate of the maximum error would not assume all these errors adding together. Therefore, a more realistic maximum error in the measured

horizontal deflection of the nails furthest from Nail #1 is approximately 0.3 in. The validity of this large estimated error is consistent with the fact that many of the measured horizontal deflections, which are presented in Chapter 3, cannot be explained in terms of normal structural behavior.

The estimated maximum errors in the deflection monitoring system are obviously very dependent on the assumptions that were made. Different assumption would result in different estimated maximum error. The analytical modeling of the culvert discussed in the next chapters will be used to judge if the measured deflections are consistent with the measured strains and soil pressures and this will add some additional criteria for judging the accuracy of the deflection monitoring system. The inherent problem with determining the error in the measured deflections is that a more accurate method is not available to explicitly judge the accuracy of the deflection monitoring system.

CHAPTER 3

MEASURED CULVERT RESPONSE

In this section the soil pressures, culvert strains, and culvert deflections measured at the three instrumented cross sections shown in Figure 3.1 are presented and discussed. Culvert strains and soil pressures were read five times during the 1.5 months it took to place the fill around the culvert. The three instrumented arch sections were surveyed three times during this period. During the 2.5 year period the culvert was monitored after fill was complete, arch strains and soil pressure were read eleven times and the instrumented arch sections were surveyed eight times. Strains and soil pressures were read each time surveys were conducted. An effort was made to monitor culvert response at least once each season of the year. The discussion of the measured culvert response is separated into two main sections: 1) the response during placement of fill; and 2) the response after fill was completed.

3.1 Measured Culvert Response During the Placement of Fill

In this section, each of the parameters measured during placement of fill: soil pressure, arch and floor strain, and deflection, are presented and discussed. They are discussed in this order since, in large part, it seems that the culvert responds to the applied soil pressures and the soil pressures are not, in turn, significantly affected by the culvert response.

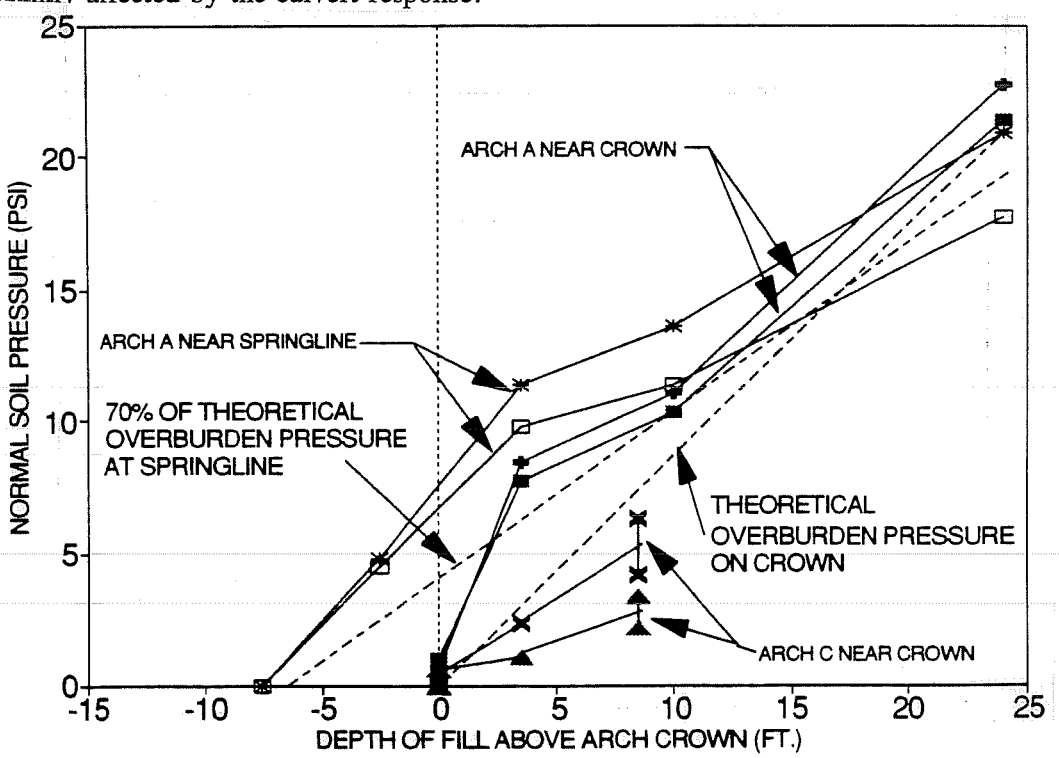

Figure 3.1 Increase in measured soil pressure on culvert with fill depth.

3.1.1 Measured Soil Pressures on the Culvert During Placement of Fill. Figure 3.1 shows the measured soil pressures on the culvert during placement of fill. The fill depth is shown relative to the top surface of the crown of the culvert so that a negative fill depth of -10.5 ft. corresponds to the base of the culvert. The gages near the springline of Arch A are located 7 ft. below the crown (at -7.0 ft.) and all other gages are located near the crown (at 0.0 ft.). A small amount of pressure was measured on the crown at fill heights less than the crown height because some loose soil was mounded over the culvert prior to placement of fill over the crown. The pressures are measured at three "sets" of two pressure gages which are located at the crowns of Arches A and C and at the springline of Arch A as indicated in Figure 3.1. As Figure 1.1 shows, each set of gages are placed symmetrically with respect to the culvert axis of symmetry. The two dotted lines in Figure 3.1 show the theoretical free field relationships between normal pressure and fill depth on the gages near the crown and springline of the culvert under drained soil conditions. The theoretical pressures are based on the measured soil unit weight of 128 pcf. The theoretical free field pressure on the crown is simply the overburden pressure at the crown depth. The estimated theoretical free field normal pressure on the gages near the springline is 70% of the overburden pressure at the gage depth as explained below.

The theoretical free field normal pressure on the gages near the culvert springline is estimated as 70% of the overburden pressure based on the fact these gages, which are tangent to the culvert profile, are oriented at 45° from the horizontal. These gages are shown in Figure 1.1 as the soil pressure gages "S1". Based on the Mohr circle of stress, at 45° from the horizontal, which is the assumed axis of the minor principle stress, the normal soil stress is equal to the average of the major and minor principle stresses. These stresses are assumed to be those on the vertical and horizontal planes in the soil respectively. The free field vertical stress is assumed equal to the overburden pressure. The horizontal free field pressure (ph) in a drained clay backfill is approximated using Equation 3.1 from Reference 29.

$$ph = 0.95\,[\sin(\phi)]\,pv \tag{3.1}$$

where ph = soil horizontal free field stress,
ϕ = drained angle of friction in clay soil, and
pv = soil vertical free field stress.

A typical drained angle of friction for silty clays is 30° based on testing reported by Duncan, et al.[30] Based on Equation 3.1 and a 30° angle of friction, a horizontal free field pressure equal to 45% of the overburden pressure would be expected for a drained silty clay. The average of the horizontal and vertical pressures is 70% of the overburden pressure, which is the theoretical free field normal pressure on a pressure cell oriented at 45° after pore pressures have dissipated. It is difficult to predict the expected pressures prior to the dissipation of pore pressures induced by compaction except to say they would be higher than the drained free field pressures.

Figure 3.1 shows that the measured soil pressure on Arch A generally increases linearly with fill depth at about the same slope as the theoretical curves. However, a more exact characterization of the

pressure increase is that it increases with depth in three "stages" marked by the three slopes in the data in Figure 1.1. Initially, at fill depths near the crown height, the pressure increases with depth at a rate considerably greater than the average rate. This is probably due to the combined effect of compaction induced pore water pressures and soil overburden pressure. At a fill height of 4 ft. over the arch crown, the first change in slope occurs. This second "stage" has the minimum rate of pressure increase with fill depth. The lower rate in the increase in vertical soil pressure with fill depth is probably due to the dissipation of compaction induced pore pressures. The dissipation of these pressures causes some pressure loss to occur simultaneously with the pressure increase caused by additional soil overburden. Therefore, the net rate, or slope, of increase in pressure with fill depth is less than the rate of increase in the overburden pressure with fill depth without simultaneous dissipation of pore pressures. This affects both gages near the springline and near the crown of Arch A. The gages near the springline are also affected by the soil horizontal stress. According to several theories on the effects of soil compaction, the effect of compaction on horizontal soil stress (or any type of overconsolidation) is to "lock-in" horizontal stresses equal to approximately 40% or 50% (for an angle of friction of 30°) of the elevated, compaction-induced, vertical pressure.[31] A high percentage (40% to 90%) of the horizontal stress that develops during compaction remains as a residual stress. Significant increase in the horizontal soil stress does not occur until the overburden pressure increases to a value greater than the compaction pressures which initially caused the locked-in horizontal stress. Therefore, the horizontal soil pressure does not increase with fill depth until the increased overburden pressure equals the original compaction pressures. The measured soil pressures at the springline gages increases slowly with fill height during the "second stage" of pressure increase with fill depth in Figure 3.1 due to both the dissipation of pore pressures against the gages and due to the fact that the soil horizontal stress is increasing very slowly (if at all) with increased fill depth.

At a height of approximately 10 ft. over the crown, the final stage of soil pressure increase with fill depth in Figure 3.1 occurs. At fill heights greater than 10 ft., the measured pressures increase with fill depth at a rate approximately equal to that of the theoretical curves. Therefore, the compaction induced pore pressures have apparently dissipated near the culvert by the time the fill height is 10 ft. over the culvert and the overburden pressure on the culvert is greater than the original compaction pressures. Figure 3.1 shows that, at the final fill height, the measured pressures on the crown and springline of Arch A are approximately equal to the free field pressures in a normally consolidated soil.

Figure 3.1 also shows the measured pressures on the crown of Arch C (under the low fill). Two measured pressures are shown at 8.5 ft. of fill over the crown depth for each gage. The fill over Arch C was difficult to estimate since this location was near a slope that was not really finalized until the end of the construction project. Therefore, the final two pressure measurements that were taken during construction are both shown as occurring at a fill depth of 8.5 ft. The effective fill depth was probably less than 8.5 ft. when the lower of the two measurements shown at this fill depth were taken. Figure 3.1 shows that the pressures on the crown of Arch C increase approximately linearly with fill depth, and that the average of the two measured crown pressures is only about one-half the overburden pressure. This cross section is located at the top edge of a 2:1 slope in the fill, as shown in Figure 1.1, and this fact may be a cause of the low measured pressures. Lefebvre has shown in a three-dimensional finite element elastic analysis of a homogeneous sloped surface (such as a dam) that the vertical stress under the top edge of a 2:1 slope is approximately 25% less than the overburden pressure under the same fill height

with no slope.[32] Also, other researchers have measured lower pressures on culverts near the top edge of a slope than near the middle, or toe, of the slope. Soil pressures reported by Davis and Bacher and by Davis, et al. across the top surface of arch culverts under very deep sloping fills in California show that pressures on the culvert under the top of the slope was approximately one-half the overburden pressure while pressures on a cross section under the middle of the slope was approximately equal to the overburden pressure.[33] Also, for the culvert in this study, there is a concrete abutment above the mouth of the culvert (approximately 15 ft. in front of Arch C) which retains the toe of the soil slope in the vicinity of the culvert. This may cause some additional concentration of vertical soil pressure near the abutment and corresponding reduction in soil pressure at distances further from the abutment such as Arch C. In summary, it seems that the unexpectedly small pressures measured on Arch C can be explained, at least in part, by the presence of the top edge of a slope in the fill directly over this cross section. Also, the effects of the slope and abutment on the soil pressure on Arch C may not be uniform across the width of the culvert and may therefore be the cause of the relatively large discrepancy between the two measured pressures on this cross section.

In summary, at fill heights greater than 10 ft. over the crown, the measured pressures near the crown and near the springline on Arch A under the deep fill correlate reasonably well with predicted free field soil pressures and with pressure measured by other researchers. At lower fill heights the measured pressures on this arch are two to three times greater than the predicted free field pressures. This is most probably due to the effects of compaction. The measured pressures on Arch C under the low fill are approximately one- half the overburden pressure. The fact that Arch C is located under the top edge of a slope in the fill makes the free field pressure at this location very difficult to estimate. However, a computational study indicates that the free field pressure under the top edge of a slope is 25% less than the overburden pressure. Therefore, the measured pressures on this cross section may be near free field values. The measured pressures at this location are consistent with previously measured pressures under the top edge of sloped fills, which were also equal to approximately one-half the overburden pressure.

3.1.2 Measured Strain in the Culvert During Placement of Fill. Figure 3.2 shows the measured strain in Arches A and B (both under the high fill) during the placement of fill. The measured strains can be divided into strains occurring at fill depths less than the crown height (negative fill depths in Figure 3.2) and strains occurring at fill depths over the crown. During fill over the crown, all the measured strains in Figure 3.2 increase approximately linearly with fill depth. However, the rate of strain increase with fill depth is greatest at fill depths near the crown height, just as the rate of the measured soil pressure increase with fill depth was greatest at low fill depths (see Figure 3.1). Plots of arch strain vs. soil pressure on Arch A show that the strains increase nearly proportionally with soil pressure at fill heights over the crown as would be expected. Also, the measured strains are largely the same at similar locations in Arches A and B as would be expected since both cross sections are subjected to the same overburden pressure. The strains measured at the two springline strain gages in Arch B and the one springline gage in Arch A are almost identical at all fill heights. A relatively large difference between the measured strains at the crowns of Arches A and B occurred while fill was placed on the crown. However, the increase in the crown strains at the two cross sections as fill is placed between 4 ft. and 24 ft. above the crown and are almost equal. Similar crown strains were measured at fill heights below the crown.

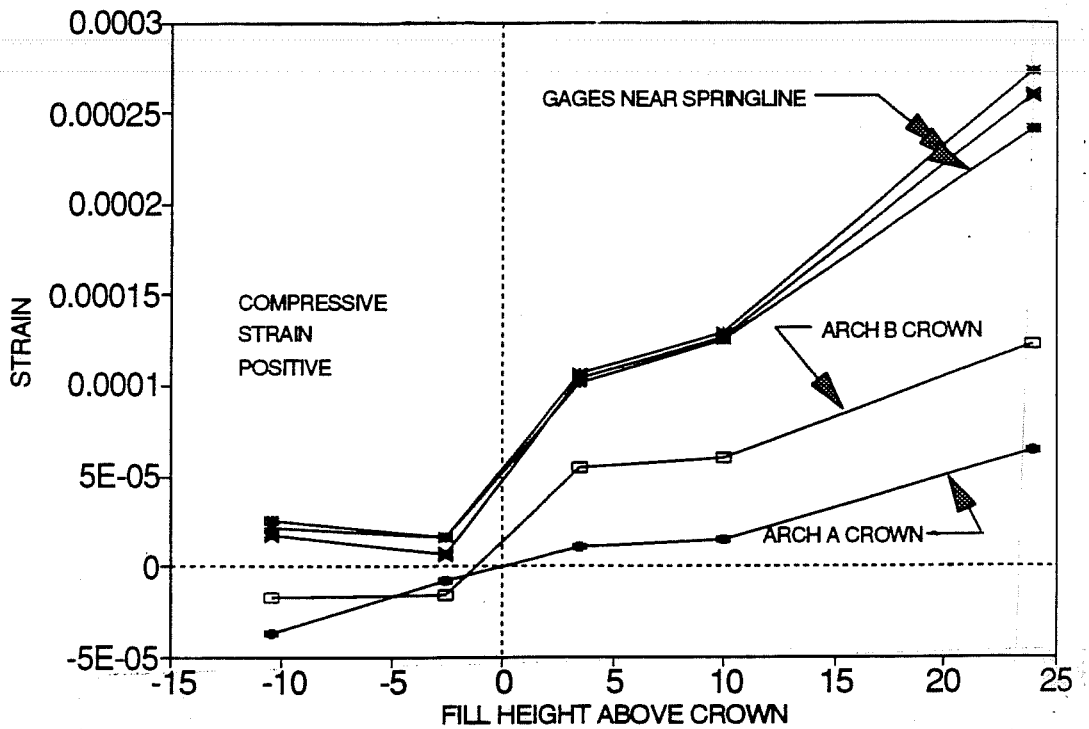

Figure 3.2 Change in measured culvert strain with fill-depth under high fill

All three measured compressive strains near the culvert springline decrease significantly (by a factor of 2) during fill placement below the crown height even though the normal pressure against the culvert springline is increasing at this time. Normal pressure induces compression in the culvert. The strain decrease must therefore be due to shear forces, which are not measured by the pressure cells, that are applied upward along the inclined culvert surface by the soil and cause tension in the culvert below the fill depth. As Figures 1.1 and 1.2 show, horizontal pressures near the springline have a normal component against the culvert surface and an upward shear component along the culvert surface. Since no compaction equipment was allowed within three feet of the culvert, it is very plausible that horizontal pressures caused compaction of soil three feet and more from the culvert, and are the major soil pressure applied to the culvert at low fill depths. Compaction forces applied to the soil near the culvert cause lateral pressures, equal to 45% to 100% of the compaction pressure depending on the degree of soil saturation, which push the soil adjacent to the culvert against the culvert. The measured strains indicate that the inclined shear component of the horizontal pressures, which causes tensile force near the strain gages, affects the thrust near the gages more than the normal component of the horizontal pressure, which causes compression in the culvert cross section.

Figure 3.2 shows that the strains at the crown, which are tensile under self-weight (at -10.5 ft. in the figure), become more compressive during fill placement below the crown depth. This occurs because the same inclined shear forces discussed above cause compression in the culvert above the fill depth. The initial tensile strains prior to fill placement indicates that there is some cracking near the crown under self-weight loading since, in an uncracked section, the bending moment would not affect the mid-thickness strain and the thrust would cause compression. At a fill height just above the crown height, a significant difference between the strain measured at the crown of Arches A and B occurs. The

cause for this difference is not known. Possibly compaction near the top of Arch B caused significant horizontal soil movement near the top surface of the culvert which induced local compression forces in the culvert near the gage location. This possible cause is consistent with the fact that the measured strains at these locations move together at all fill depths except in this one case. In any case, a difference in the strains at the crown of Arches A and B equal to 50 x 10^{-6} in./in. occurs at a fill height just above the crown and remains constant as both strains increase with the fill height. As Figure 3.6 shows (this will be presented later), this difference eventually disappears and the crown strains measured in Arches A and B at the end of the monitoring period are equal. As discussed above, residual horizontal stresses from compaction loads do not tend to dissipate, but the experimental measurements were most probably not continued over a two year period.

Figure 3.3 shows the measured strain vs. fill depth relationship for Arch C under the low fill. The strain in the gage near the springline decreases, and then increases with depth in the same manner as the springline strain measured in Arches A and B. The strains for dead load only near the springline are nearly equal for all gages at all three arches. The measured springline strain in Arch C decreases to a slightly lower value than those in Arches A and B at fill depths below the crown and then increases linearly with fill height at fill heights above the crown. The rate of increase is one-third to one-half the rate the increase in strains in Arches A and B with fill depth. This is consistent with Figure 3.1 which shows that, at a given fill depth, the measured soil pressures at the crown of Arch C increase approximately one-third as fast with fill depth as those measured near the crown of Arch A.

The measured strain in the crown of Arch C is the "oddball" of the measured strains. Evidently, based on the large tensile strain measured at this location under self-weight load only (the measured strain

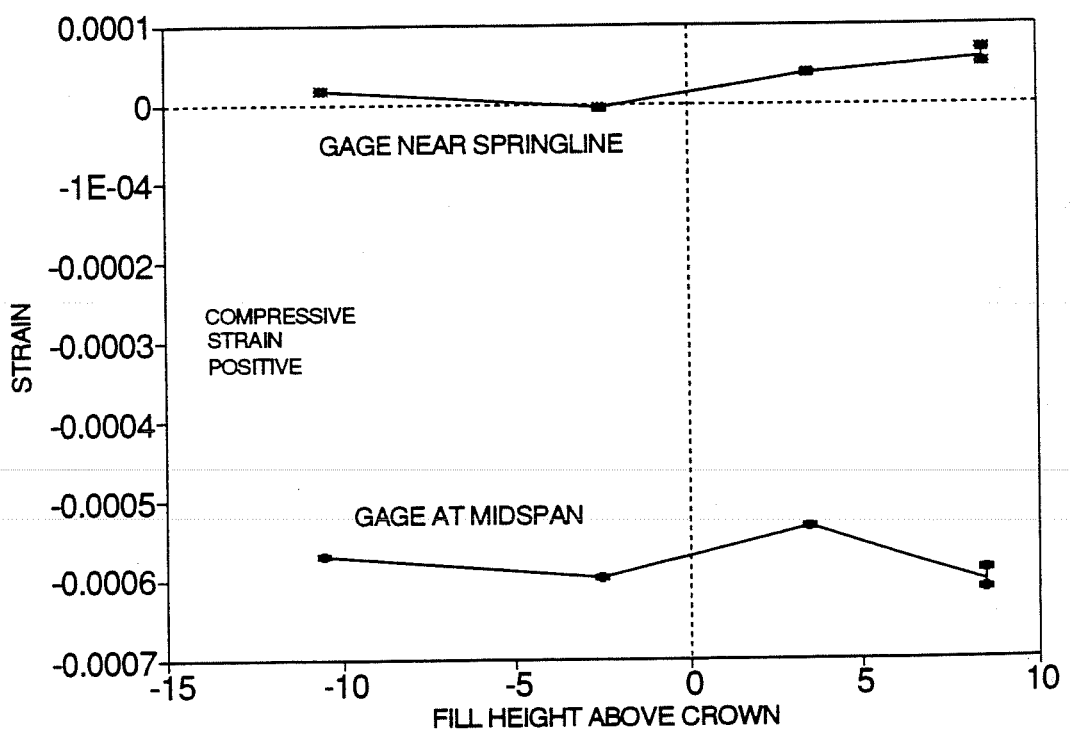

Figure 3.3 Change in measured strain in culvert with fill-depth under low fill

at -10.5 ft. in Figure 3.3), cracking occurred through the mid-thickness of this instrumented arch section during placement, or very soon after placement. As discussed above, cracking also occurred under self-weight loading near the crown at Arches A and B but the measured strains indicate that the cracking is much more severe at Arch C. Two possible causes for the more severe cracking in Arch C are dynamic stresses occurring during the placement of this precast section, and lateral slip along the supports prior to placement of grout in the recesses in the footing around the arch base (see Figure 1.2). Prior to placement of the grout, the boundary conditions at the supports were somewhere between simply supported (no friction between the footing and base of the arch) and fully pinned (sufficient friction between the footing and the edge chamfer of the arch to prevent any lateral movement). The arch bending moment at the crown is very sensitive to the lateral movement of the supports and, for self-weight only, it is very near the yield moment if there is no lateral restraint. For the case where the base is grouted into the footing and lateral restraint is supplied, the moment near the crown is only a relatively small fraction of the yield moment. The fact that no large tensile strains were measured in the crown of Arches A and B is probably due to the fact that these sections were not loaded dynamically during field placement or because there was some unusual condition, such as a grease spill, which prevented friction between the footing surface and Arch C prior to placement of the grout.

During placement of fill the measured crown strain in Arch C remains essentially constant. The largest change in measured strain is 10% of the initial strain due to self-weight only. Evidently the applied soil load over the culvert crown causes compressive thrust and bending moments at the crown which result in offsetting amounts of compressive and tensile strain at mid-thickness. The strain history measured at the crown of Arch C is entirely different from those measured elsewhere throughout the monitoring period. This is not unexpected since the large crack depths that occurred prior to fill placement in Arch C, and which do not occur elsewhere, affect the strain in the culvert caused by applied loads.

Figure 3.4 shows the measured strains in the structural concrete floor slab under Arches A and B in the high fill region. Vertical dead load on the culvert, and the culvert self-weight, tend to spread the arch footings outward and put the floor slab in tension. As Figure 3.4 shows, the strain is almost unaffected by soil fill below the crown and, at most of the gages, the strain increases more or less linearly with fill depth over the crown. It is not known why the horizontal pressures applied to the culvert during fill below the crown depth do not cause measured compression in the floor slab. It may be that phenomena such as tensile creep is also occurring which cancels out the load induced compressive strains, which could be relatively small. Noticeable changes in slope occur as the floor tensile strain increases with fill depth which are similar to the slope changes in the measured soil pressure vs. fill depth and culvert strain vs. fill depth relationships for Arches A and B (see Figures 3.1, 3.2). This is expected since the soil pressure applied to the culvert causes the strain in the culvert and floor slab. The changes in slope in the strain vs. fill depth relationships are not quite as pronounced as they are in the soil pressure vs. fill depth relationship. This fact, and the increase in measures strains after completion of fill, indicate that very significant creep strains occur in the culvert.

Figure 3.4 also shows that there is a very significant variation between the strains measured at symmetrical locations under Arches A and B during placement of fill. As Figure 1.1 shows, all the floor gages were placed at symmetrical locations with respect to the culvert and soil fill geometry, and

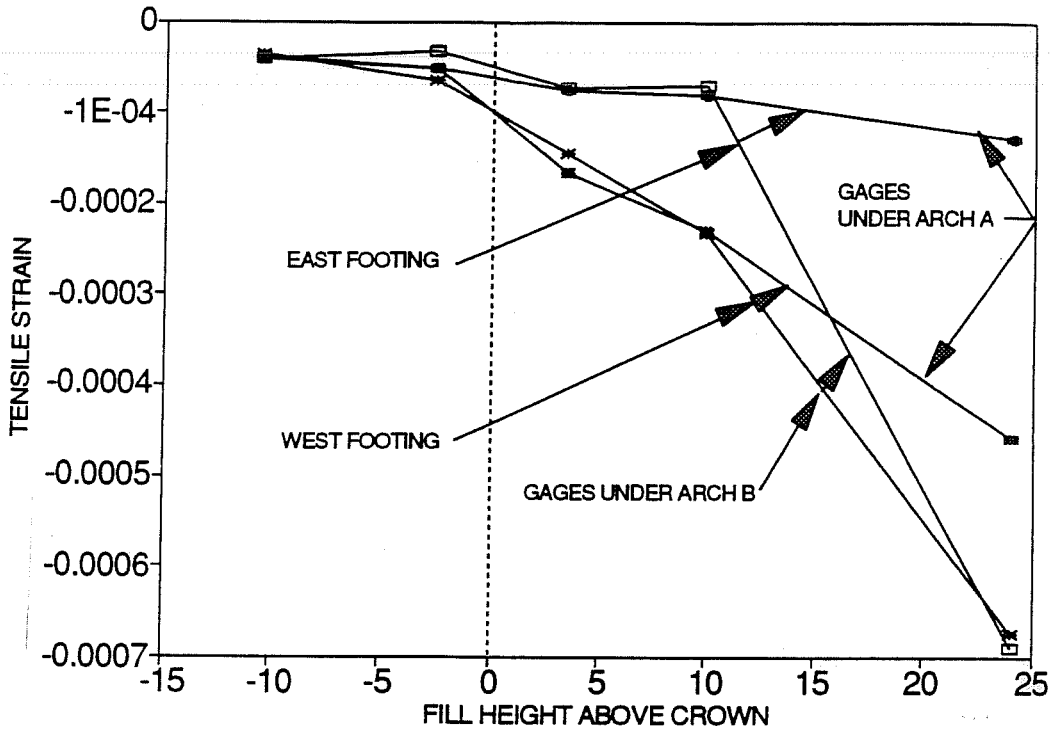

Figure 3.4 Change in measured strain in floor slab with fill-depth under high fill

therefore similar strain measurements were expected. At fill depths less than the maximum fill depth, the two floor strains measured along the west footing are nearly twice as large as the strains measured near the east footing. Therefore the strain distribution in the floors was not uniform across the span but the total spread between the footings under Arch B was probably approximately equal to that under Arch A. Near the maximum fill depth, the opposite trend occurs. The strain becomes more uniform across the span of each arch, but the measured strains indicate that the total lateral spread between the footings under Arch B increases to an amount twice as large as that under Arch A. Since the floor slab is simply a tension element between the two footings, the strain is theoretically uniform throughout the floor. The measured floor strains under Arch B remained twice as high as those measured under Arch A for the duration of the monitoring period. Also, the strains measured under both arches at the completion of fill are very much greater than the theoretical cracking strain, assuming the measured strains consist only of elastic strain, but no cracking was observed.

Factors which may be causing the differences in measured strains at the symmetrical floor gage locations include shear stresses applied across the bottom surface of the floor slab by the foundation and local tensile strains near the gages caused by the transfer of tension from lap spliced reinforcing steel. Figure 3.5 shows a detail of the strain gage placement in the floor slabs and the surrounding reinforcing steel and foundation. Since the concrete fill, which may act compositely with the floor slab, can influence the measured strains at low strain levels, it will be discussed first. The concrete fill will act compositely with the floor slab if there is sufficient normal force and surface roughness to transfer shear stress. This would increase the effective concrete area resisting force in the vicinity of the strain gages, and could easily reduce strain in this local region by a factor of 2 or more. This scenario requires that the dowels transfer some of the dead load reaction from the footings into the floor slab to provide the necessary

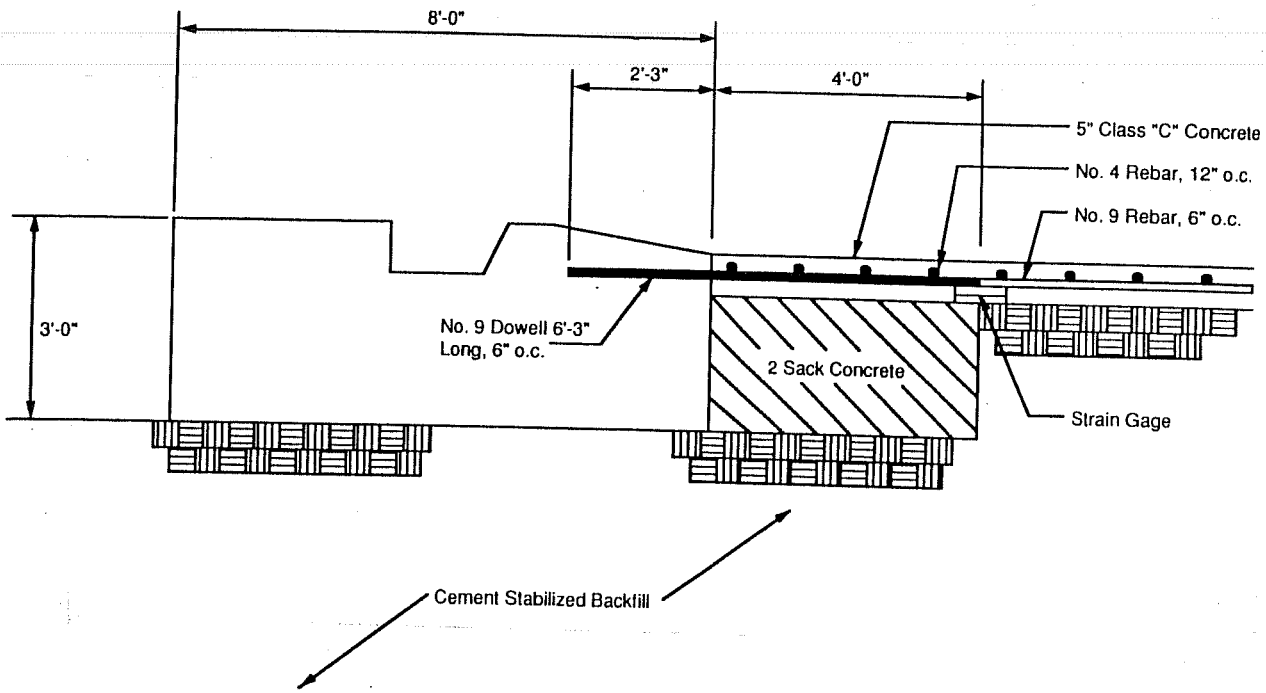

Figure 3.5 Typical section through culvert footing in high fill region.

normal force on the interface. As Figure 3.5 shows, the strain gages are located right at the edge of the limits of the fill. Based on typical construction practices, the limits of fill could easily extend past the gage length on one side of the culvert (the east side) and not extend past the gage length on the other side. Therefore, differing limits for the concrete fill could cause the difference in the floor strain measured at each side of the culvert in Figure 3.4 at the lower strain levels. The disappearance of this east side-west side difference could be due to slip at the interface between the floor and the fill due to larger tensile forces applied to the floor at the larger fill depths.

Between fill depths of 12 ft. and 24 ft., the floor strains under Arch A increase at the same rate as at lower fill heights but the floor strains under Arch B suddenly increase very sharply near both footings. This type of sharp increase in strain during application of loads is typically an indication of a tensile crack that propagates up into the gage length. The measured strains are certainly large enough to justify cracking. However, as mentioned previously, cracking on the top surface was not observed. Photographs of embedded reinforcing steel subjected to tension show that small internal cracks form at the lugs in the reinforcing steel and radiate out a small distance into the surrounding concrete.[34] Therefore, the cracks do not necessarily radiate out to the concrete surface except near failure load of the splice. The extent of such cracking would be expected to increase with the tensile load and thus with the fill height. Therefore, it is possible that, in the floor under Arch B, one of these cracks propagated into the gage length while no such crack propagation occurred near the gages in the floor under Arch A. It is known that cracking typically initiates in a spliced section near the bar cutoff points, which is why the gages are located at this location, as shown in Figure 3.5. The sharp increase in strain in the floor slab under Arch B corresponds with the formation of a 0.003 in. wide crack within the 6 in. gage length, and internal cracks this wide have been measured by researchers.[35] These cracks were not observed on the

surface of the concrete specimen but were consistent with the rebar strain measurements made by the researchers. The increase in strain also corresponds to the formation of several cracks with widths less than 0.003 in. within the gage length. It is odd that such cracking would suddenly occur at both gages under Arch B while not, apparently, occurring at either gage under Arch A. Another possible cause for the sudden increase in measured tensile strain under Arch B is that, at some higher fill depth, slip occurred between the floor slab under Arch B and the foundation causing the portion of the tensile force which had formerly been transferred into the foundation to be suddenly absorbed in full by the floor slab. The only problem with this second hypothesis is that, as analysis in the succeeding sections shows, the very large tensile strains cannot be justified in terms of the applied tensile force and creep strains alone, even if the floor is assumed to resist all the tensile load. An explanation of the very high strain under Arch B seems to require the formation of a tensile crack within the gage length. Most of the hypothesized causes for the difference in measured strains imply that the measured floor strains are to some extent local. Therefore, care must be exercised when using the measured floor strains to calculate the lateral spread of the culvert footings. Only strains which represent an average of the floor slab strain across its 40 ft. will give a good estimate of the lateral spread between footings.

As a point of interest, the design shown in Figure 3.5 is not fully in conformance with the ACI 318 Building Code for Reinforced Concrete which calls for staggered mechanical splices or welds, rather than the non-staggered lap splices, in reinforced concrete tension tie members (Section 12.15.5 in ACI 318-89). It is not generally good practice to count on the concrete to transfer tension load between lapped bars when there is minimum cover and when the large tension forces which must be transferred across the lapped bars can easily crack the concrete through its thickness. In this case, the fact that the culvert was indeterminate, since the surrounding soil could be counted on to provide lateral resistance, may have been taken into consideration by the designers.

It is hypothesized that through-thickness cracking did not occur in the floor slab because the gradually applied loads and the young age of the concrete in the slab allowed creep strains to relieve much of the tension stress (as opposed to strain) in the floor slab. The fact that the measured strains were much larger than the usual assumed cracking strain of concrete (-1.0×10^{-4} to -2.0×10^{-4} in./in. of elastic strain), and yet no surface cracking was observed, indicates that the measured strain includes inelastic strains such as creep strain. Creep strains magnify the elastic concrete strains without causing stress in an unrestrained, unreinforced member. This helps explain the very large measured strains. The tensile creep strains cause secondary compressive stresses to occur in the reinforced floor slab because the creep strains put the steel reinforcement, which does not creep, under additional tensile stress which must be equilibrated within the cross section by an equal compressive force (secondary compressive stresses). This is analogous (though in an opposite sense) to the fact that compressive shrinkage strains cause tensile concrete stresses in an axially reinforced member. Since the net stress includes both the secondary compressive stresses and the primary tensile stresses from applied loads, this may explain why no surface, through-thickness cracking is observed when consideration of the primary tensile stresses themselves would indicate cracking. Also the footings restrain the tensile creep of the floor slab and this causes additional secondary compressive stress in the floor slab. Creep strains often reduce the high stresses which would theoretically result from gradually applied loads, such as gradual support deformations, in concrete structures. The effects of creep are investigated analytically in the following chapters.

Actually, the cracking strain of concrete is approximately five times larger than the strain corresponding to peak tensile stress given above as the usual assumed cracking strain. Usually, in lightly reinforced members, cracking occurs as soon as the concrete is strained above the peak tensile stress because the reinforcing steel must suddenly strain by a relatively large amount to pick up the stress "shed" by the concrete as it strains into the descending, post-ultimate region of its stress-strain curve. It is usually assumed that this dynamic process causes cracking. An analysis which considered the post-ultimate range of the concrete tensile stress-strain curve has shown that tensile stress can be gradually transferred into the reinforcing steel of heavily reinforced tensile members (a steel ratio greater than 6%) and therefore cracking should not occur in these members until the strain reaches 1.0×10^{-3} in./in.[36] It may be possible that, in an indeterminate member such as the culvert, the surrounding soil can temporarily resist some of the tensile load at the time the concrete is straining through its peak tensile stress and prevent the cracking which would otherwise occur at this strain.

3.1.3 Measured Culvert Deflections During Placement of Fill. Figures 3.6 and 3.7 show the deflections in Arches A and B measured at fill heights of 4 ft. over the crown and at the completion of fill (24 ft. fill over the crown). No deflections are shown for Arch C during fill placement because of unusually large apparent errors in the surveying measurements. As explained in Chapter 2, the measured vertical deflections are based on nail heights measured relative to a line extending across the arch span connecting the two nails at the two arch footings. Therefore, the height of the two nails at the arch footings is always zero and any rigid body displacement or rotation of the culvert is not measured. However, such movement is expected to be small because of the 9 ft. deep cement stabilized foundation over hard shale placed beneath the culvert. As discussed above, the estimated maximum error in the measured vertical deflections is 0.07 in. The measured vertical deflections of Arches A and B at the

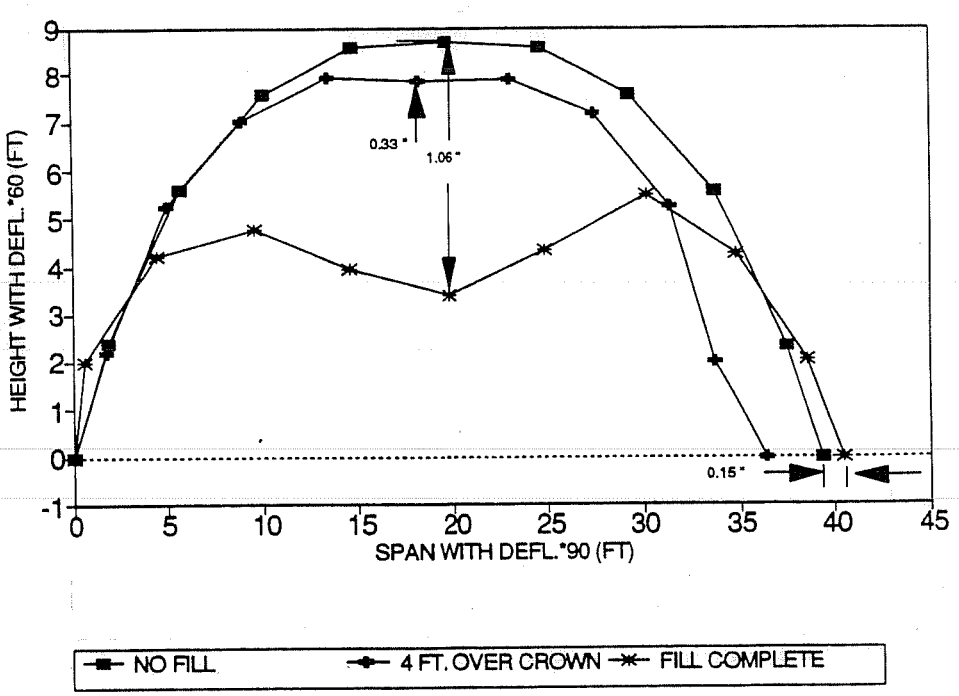

Figure 3.6 Arch A deflections during placement of fill

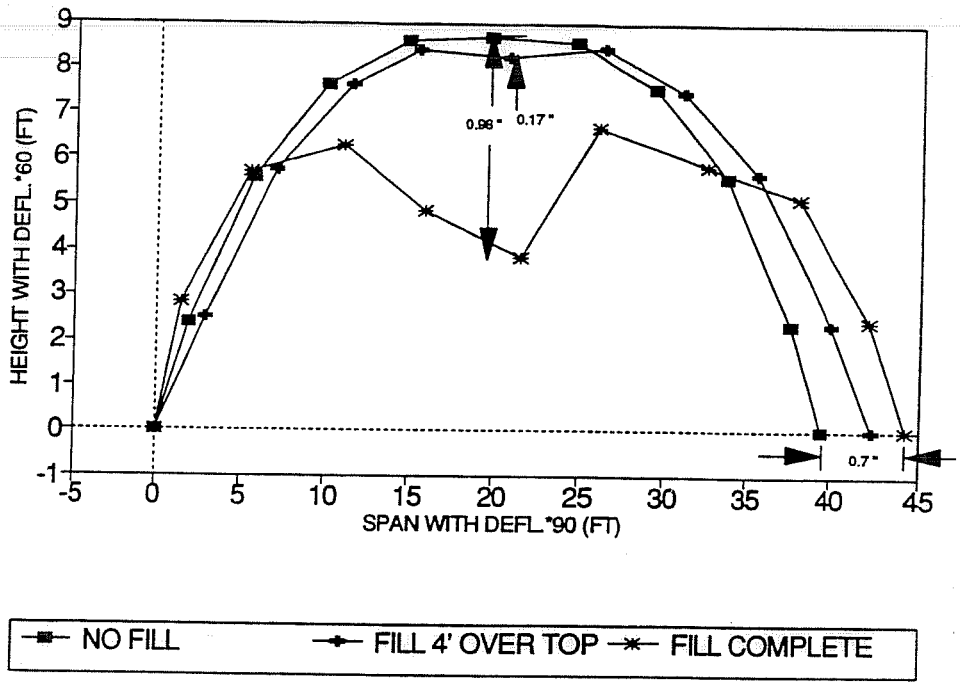

Figure 3.7 Arch B deflections during placement of fill

completion of fill are nearly the same. However, at a fill height of 4 ft. over the crown, the measured deflection of Arch B is only one-half that of Arch A.

The horizontal positions of nails were measured relative to the nail at the left footing (at position 0.0 ft. along the arch span). Therefore all horizontal deflections are zero at this footing and a maximum at the opposite footing. As discussed above, the error in measured horizontal deflections is estimated to be as much as 0.3 in. The measured horizontal deflections of Arches A and B in Figures 3.6 and 3.7 are very difficult to explain except as error in the surveying measurements. It is hard to understand how these two similar culvert sections would displace horizontally at their bases during construction in opposite directions as the surveying measurements show.

If the measured strains in the floor are assumed to be representative of the average strain in the floor, these strains can be used to calculate the spread between culvert footings based on the 40 ft. span of the floor slab. Although this assumption may not be valid, as discussed above, the average floor strains under each cross section indicate that the footings of both Arches A and B had spread outward 0.07 in. when the fill was 4 ft. over the crown. At the completion of fill the measured floor strains indicate that the footings at Arch B had spread outward a total of 0.31 in. and the footings at Arch A had spread a total of 0.14 in. If the hypothesis that the measured floor strain under Arch B is affected by a crack within the gage length, and therefore is not representative of the otherwise uncracked floor slab strain, the total spread between footings estimated from the floor strains under Arch A of 0.14 in. is the best available estimate.

3.1.4 Summary of Measured Culvert Response During Placement of Fill. The measured culvert response during fill placement is characterized by a more or less linear increase in the measured

response parameters with increasing fill depth over the culvert crown. There is also a secondary trend within this generally linear relationship in which the rate of increase in soil pressures and strains increases fastest with fill depth at low fill depths near the culvert, and increases slowest with fill depth at fill depths 5 ft. to 10 ft. above the culvert. The average rate of increase in pressures and strains occurs at large fill depths greater than 10 ft. This trend is probably due to local compaction induced stresses adding to soil pressure on the pressure gages at fill depths near the crown height and dissipating later, so as to partially offset overburden pressures caused by later increases in fill depth. The measured soil pressures on Arch A, under the high fill, correspond well with predicted free field pressures at the completion of fill. The measured soil pressures on Arch C, under the low fill, are significantly lower (about 50% lower) than predicted free field pressures. However, this arch is located at the top edge of a slope in the overlying embankment and, according to the results of computational studies, the presence of the embankment can reduce free field pressures under the top of the embankment by approximately 25%. Measured culvert strains increased nearly proportionally with measured pressures at fill heights above the crown depth. The measured strains in the floor of the culvert, which acts as a tension tie member between culvert footings in the high fill region, are not uniform across the floor width throughout fill placement. Also, although the measured tensile strains in the floor are much larger than the concrete cracking strain, no cracks were observed. These facts indicate that nonuniform shear stresses existed between the floor slab and the underlying foundation during fill placement and that large creep strains occurred in the floor slab during the 1.5 month construction period. Hairline cracks were observed on the inside face of the crown of the culvert. At the completion of fill, nearly equal deflections were measured in the two instrumented sections under the high fill.

Some of the measured parameters during fill placement correlate well with other measured culvert response parameters and some do not. During placement of fill between 4 ft. over the crown and 24 ft. over the crown (complete fill), the midspan deflections in Arch A increase by the same ratio (equal to 3) as the soil pressures, culvert strains, and floor strains in this cross section. This is expected since deflection, load, and strain should be proportional to strain. However, in Arch B, the floor strains increase by a substantially larger ratio than the culvert strains during this same time period. The measured response at similar locations in Arches A and B can also be compared with each other since both cross sections are placed under the same fill and fill height. As mentioned above, Figures 3.6 and 3.7 show that the deflections of Arches A and B are nearly equal at the completion of fill as are the springline strains for these two arches shown in Figure 3.2. However, Figure 3.4 shows a relatively large difference in measured floor strains under Arches A and B at the completion of fill, and Figure 3.2 shows a relatively large difference in measured crown strains. The midspan deflection is the most general indicator of the monitored culvert response parameters since it is affected by the strain and soil pressure at all points on the culvert cross section while the strain gages and pressure gages are only affected by strain and pressure at discrete points. Since the deflections of the two arches are equal, it is quite possible that the large measured differences in crown and floor strain are due to local effects, as hypothesized above, rather than basic differences in the manner in which the two arches are loaded or are responding. Also, the differences between the crown and floor strains measured in Arches A and B do not make sense when considered together unless they are caused by local phenomena. If the footings spread more in Arch B than in Arch A, as is implied by the larger measured floor strains under Arch B at the completion of fill, this would be expected to cause more bending moment, and thus more tensile strain, at the crown of Arch B relative to that in Arch A. However, as Figure 3.2 shows, the strain at

the crown of Arch B is more compressive than that measured at Arch A. In Chapters 4 and 5, which present and discuss the computational analyses of the culvert-soil system, this matter will be discussed further.

3.2 Measured Culvert Response After Placement of Fill

In this section the soil pressures, culvert strains, and culvert deflection measured after the placement of fill was completed are presented and discussed. The response of the instrumented culvert sections was monitored for a period of 30 months after the completion of fill. Although relatively minor changes in soil pressure on the culvert were measured after the completion of fill, substantial culvert structural response (strains and deflections) was measured during this period. The culvert structural response measured after completion of fill was probably due, in large part, to the effects of concrete creep.

3.2.1 Measured Soil Pressure on the Culvert After Placement of Fill. Figure 3.8 shows soil pressures measured on the culvert at Arch A (under 24 ft. of fill) and Arch C (under 8.5 ft. of fill) for 30 months following completion of fill over the culvert. The measured changes in the soil pressure are a small percentage of the total soil pressure. On the average over the 30 month period, the measured pressure on Arch A is approximately 10% greater than that at the end of construction. The peak increase is 20% greater. On the average over the same period, the measured pressure on Arch C is approximately

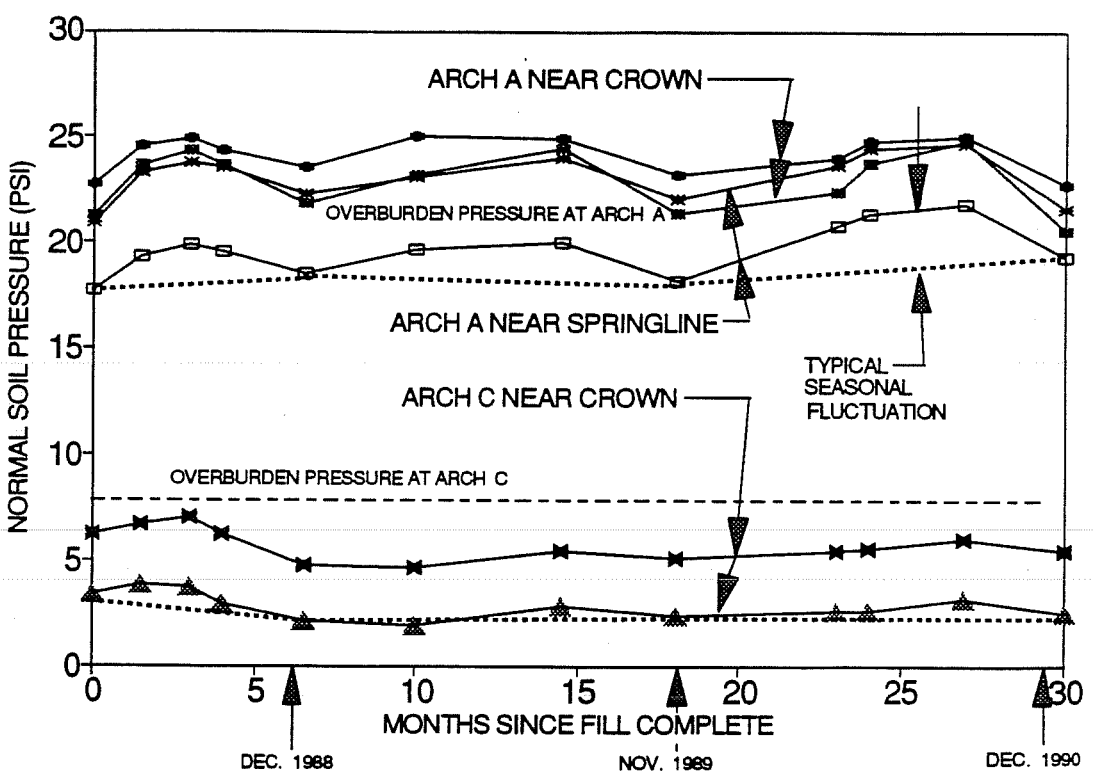

Figure 3.8 Measured soil pressures on culvert after completion of fill.

10% to 20% less than that measured at the end of construction. The peak increase over the pressure at the end of construction on Arch C is 10%.

All the measured soil pressures in Figure 3.8 increase and decrease together in a seasonal pattern. The seasonal fluctuations follow a 12 month pattern beginning with a pressure rise during the summer immediately after fill was completed (time 0 is May 1988) followed by a low pressure 7 months after completion of fill (in December 1988), and continue in this pattern the next calendar year with higher pressures again during the spring and summer and a low pressure the following November (18 months following completion of fill). The last year, from 18 months to 30 months, follows the same trend. The peak soil pressures during each calendar year always occur during the summer and the low soil pressures occur during the winter. The seasonal fluctuations in the measured pressure against Arch A, which average between 2 and 3 psi, are significantly larger than the 0.5 psi maximum error in the pressure gage readings which was estimated in Chapter 2. Therefore, this trend is not due to error in the gage reading.

The probable cause for the seasonal fluctuations in soil pressure is warmer summer temperatures, which cause the culvert to expand into the surrounding soil, followed by cooler winter temperatures, which cause it to contract. In the summer, the culvert expansion is restrained by the stiffness and dead weight of the surrounding soil and, therefore, causes an increase in pressure at the soil-structure interface. In the winter, the culvert contracts and this pressure does not occur. The fact that more seasonal fluctuation occurs in the measured pressures at Arches A and B, under the fill, than at Arch C, under the low fill, is also consistent with this theory. The larger fill depth, and thus larger shear area and dead weight, over Arches A and B causes the overlying soil to exert more resistance against the culvert expansion which causes more interface pressure. At Arch C, the culvert is relatively free to expand and, consequently, there is less interface pressure during temperature induced expansion of Arch C.

*3.2.2 **Measured Strain in the Culvert After Placement of Fill.*** Figure 3.9 shows the mid-thickness strain at the crown and near the springline measured in Arches A and B under deep fill during the 30 months after fill was completed. The measured strains show both a significant overall increase in compressive strain with time, and fluctuations in strain about the overall increase which are largely consistent with the measured fluctuations in soil pressure in Figure 3.8. The overall strain increases at a steadily decreasing rate. Near the springlines of both arches, the overall strain increased 50% during the first seven months, 20% during the second year, and 12% during the final year. Approximately the same percentage increases occur in the overall strain at the crown of Arches A and B, except that during the last year a large strain increase occurs at the crown of Arch A. The overall strain increased by approximately 100% at all gage locations on Figure 3.6 over the 30 month period monitoring period except at the crown of Arch A where more than a threefold strain increase occurred.

As Figures 3.2 and 3.9 show, the measured strain at the crowns of Arches A and B track each other very closely except during the placement of fill at the crown height and during the last year of the monitoring period. During placement of fill at the crown height, the crown strain in Arch B increased relative to that in Arch A by 5×10^{-5} in./in., while during the last year and a half of the monitoring period the strain in Arch A gradually increased relative to that in Arch B by this same amount. It was hypothesized above that the strain difference may have been caused by local compaction induced horizontal stresses near the top surface of Arch A which exerted shear stresses along the top surface of

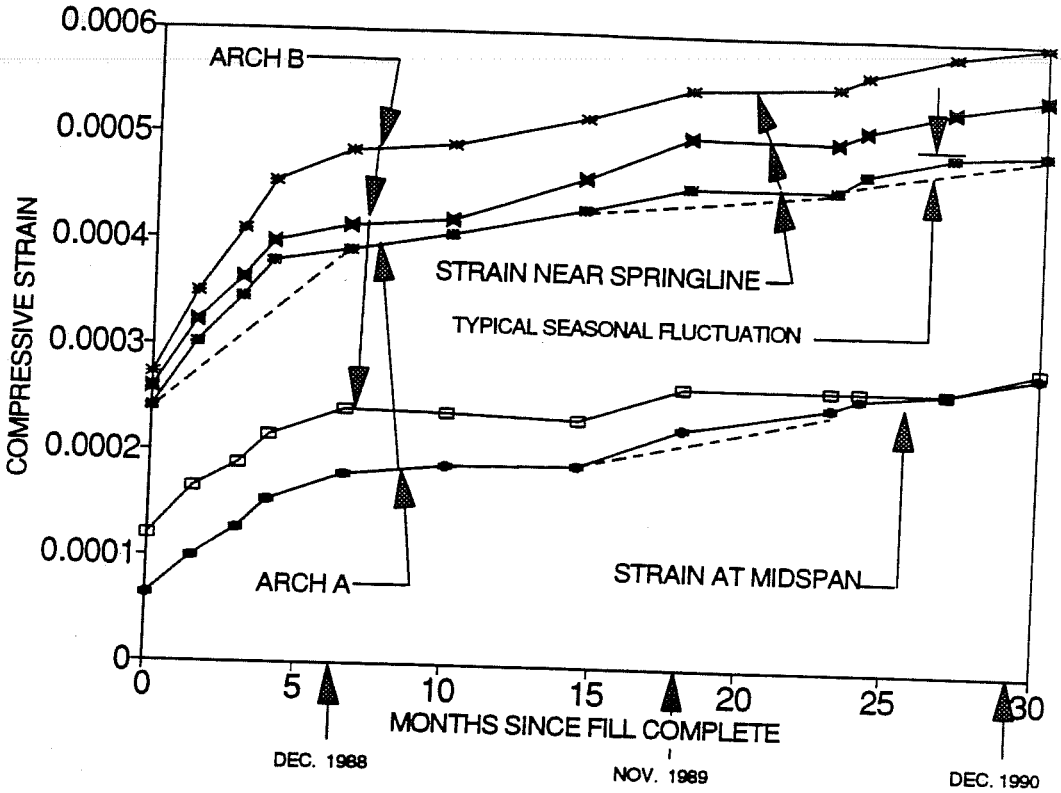

Figure 3.9 Measured strains in culvert under high fill after completion of fill.

the culvert and thereby affected the crown strain in Arch A. Thus the unexpectedly large rise in the crown strain in Arch A during the last year may be due to the dissipation of the local stresses along the culvert surface due to soil creep or slip along the soil-culvert top surface as the culvert was expanding and contracting.

The seasonal strain fluctuation is defined as the difference between a measured strain and that strain which would have occurred if the strain simply increased smoothly throughout the monitoring period. A seasonal fluctuation is illustrated on Figure 3.9. During the first year and last year, the seasonal fluctuations are consistent with the fluctuations in the measured pressure. As mentioned in Chapter 1, the strain gages are not designed to measure temperature strains and the measured strains shown in this chapter do not include any temperature effects except strains due to the stresses caused by restraint of free expansion and contraction of the culvert. A seasonal strain fluctuation pattern characterized by increased compressive strains in the summer is consistent with a temperature induced expansion of the culvert each summer that is restrained by the surrounding soil. Figure 3.9 shows this is the predominant trend but, especially at the crown during the second year, the measured strain can also fluctuate to a less compressive value during the summer. This lack of a totally consistent trend is probably due to the fact that all the seasonal strain fluctuations are significantly less than 5×10^{-5} in./in., which is the maximum estimated error in the strain measurements discussed in Chapter 2.

Figure 3.10 shows the measured strain in Arch C under the shallow fill (8.5 ft. of fill) during the 30 month monitoring period after the completion of fill. The overall compressive strain measured

near the springline increased by the large percentage over the 30 month monitoring period, which is consistent with the large measured strain increases in Arches A and B. However, almost all the increase occurred during the second year, whereas the overall strain increase in Arches A and B was largest during the first year and lower during the successive years. Only a slight overall compressive strain increase occurred at the crown of Arch C. The yearly strain fluctuations at both gage locations in Arch C are very similar to those in Arches A and B under high fill. The overall trend is that the strain fluctuates to a higher compressive value during the summer, but there are also exceptions.

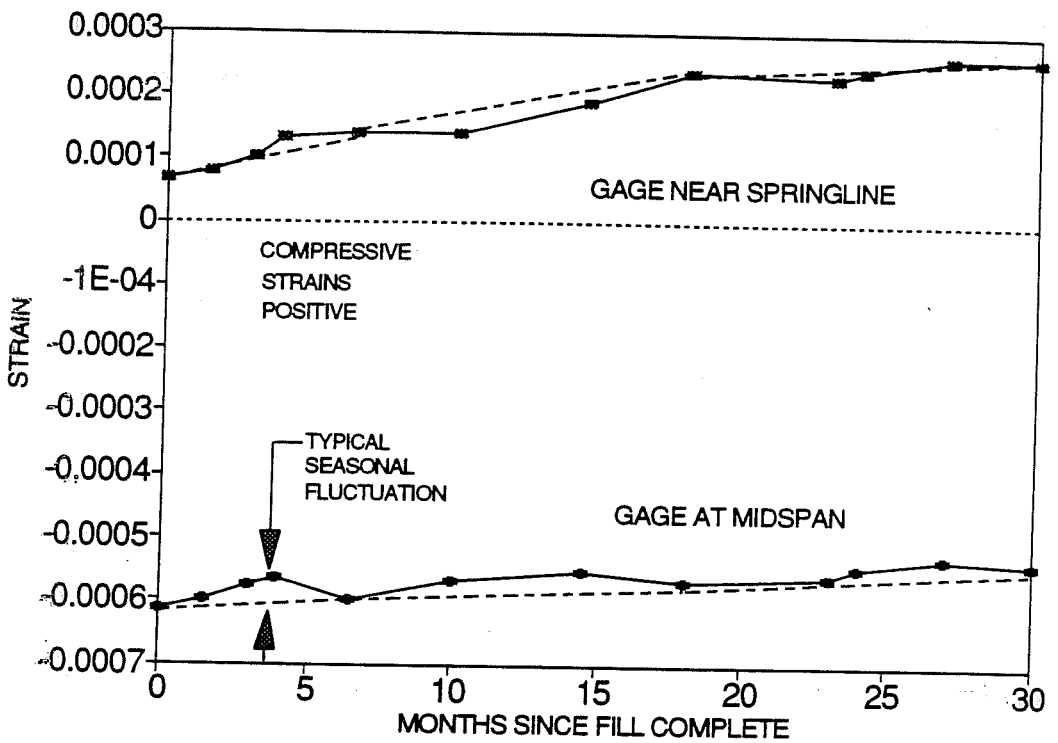

Figure 3.10 Measured strains in culvert under low fill after completion of fill

Finally, Figure 3.11 shows the measured floor strains under Arches A and B in the high fill region during the 30 month period after the completion of fill. Almost all of the trends noted above in the culvert strains also can be seen in the floor strains. An average 100% overall strain increase occurs over the 30 month monitoring period in the strains under each arch. The floor strains generally fluctuate from a minimum amount of compression (or maximum tension) in the winter to a maximum amount of compression (minimum tension) in the summer. This is consistent with a temperature induced expansion of the floor slab during the summer, which is constrained by the footings and surrounding soil, and therefore results in increased compressive strain. It is interesting that the seasonal strain fluctuations are much larger in the floor slab under Arch B than at any other location. The measured tensile strains are also very high compared to those in the floor under Arch A and it was hypothesized above that this may be due to an internal crack within the gage lengths of the gages in the floor of Arch B (which are located right at the cutoff point of the spliced rebar). The unusually large strain change in the floor of Arch B

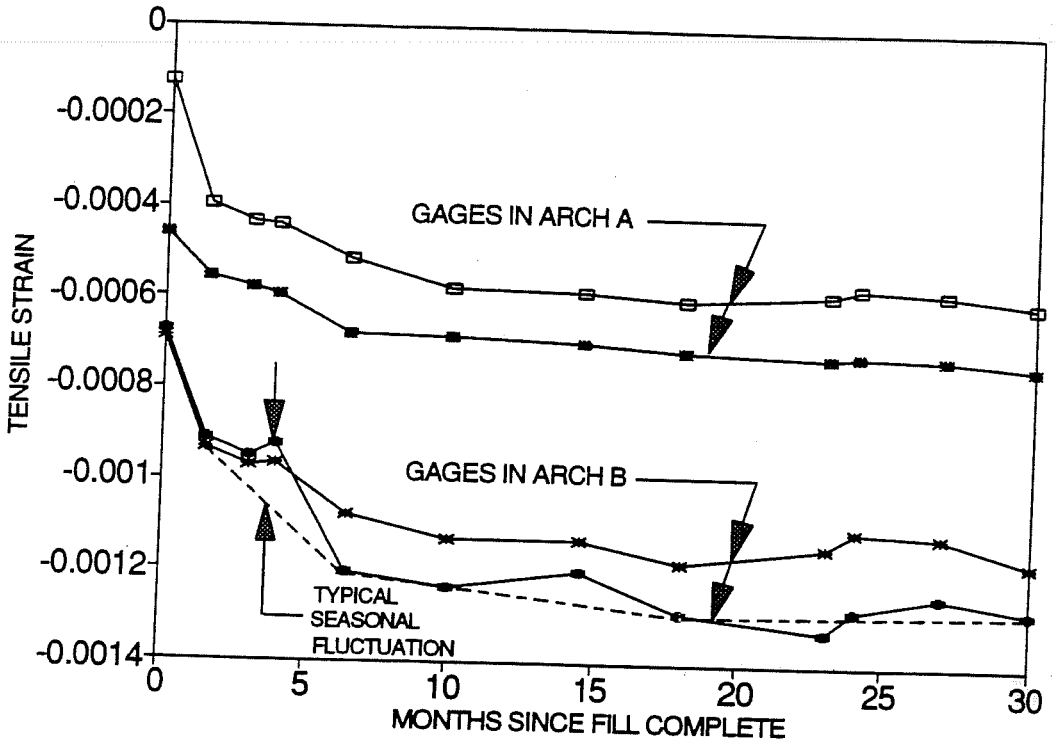

Figure 3.11 Measured strains in floor slab under culvert in high fill after completion of fill

during the summers may be due to the partial closing of these cracks under the seasonal compressive forces.

The floor strains can be used to calculate the lateral spread between footings due to the applied soil pressures as discussed previously. This is based on the assumption that the measured strains are representative of the average strain in the floor slab. Based on the measured floor strains, the total lateral spread of the footings (which are 40.33 ft. apart) at the end of the monitoring period is 0.3 in. at Arch A and 0.6 in. at Arch B. The calculated spread in the footings using the measured floor strains was approximately one-half these values when fill was completed. If there is internal cracking within the gage length of the gages under Arch B as speculated here, the total spread of 0.3 in. based on the measurements under Arch A the better estimate of the spread in the culvert footings.

3.2.3 Measured Culvert Displacements After Placement of Fill. Figure 3.12 shows midspan, or crown, vertical deflections of the three instrumented cross sections measured during the monitoring period after fill was completed. The deflection history of all three arches is characterized by a sharp post-construction increase in the midspan deflection equal to approximately 40% of the deflection at the completion of fill. This increase occurs during the first 7 months following the completion of fill. The change in deflection occurring after this time is negligible except for some seasonal variation. The most substantial seasonal variation in measured deflection occurs in Arch C during the last two years of the monitoring period. However, there is no clear seasonal trend in the fluctuations as there is in the measured strains and soil pressures. The fluctuations are approximately equal to, or less than, the maximum estimated error in measured height of 0.07 in., and therefore it is possible that the surrounding

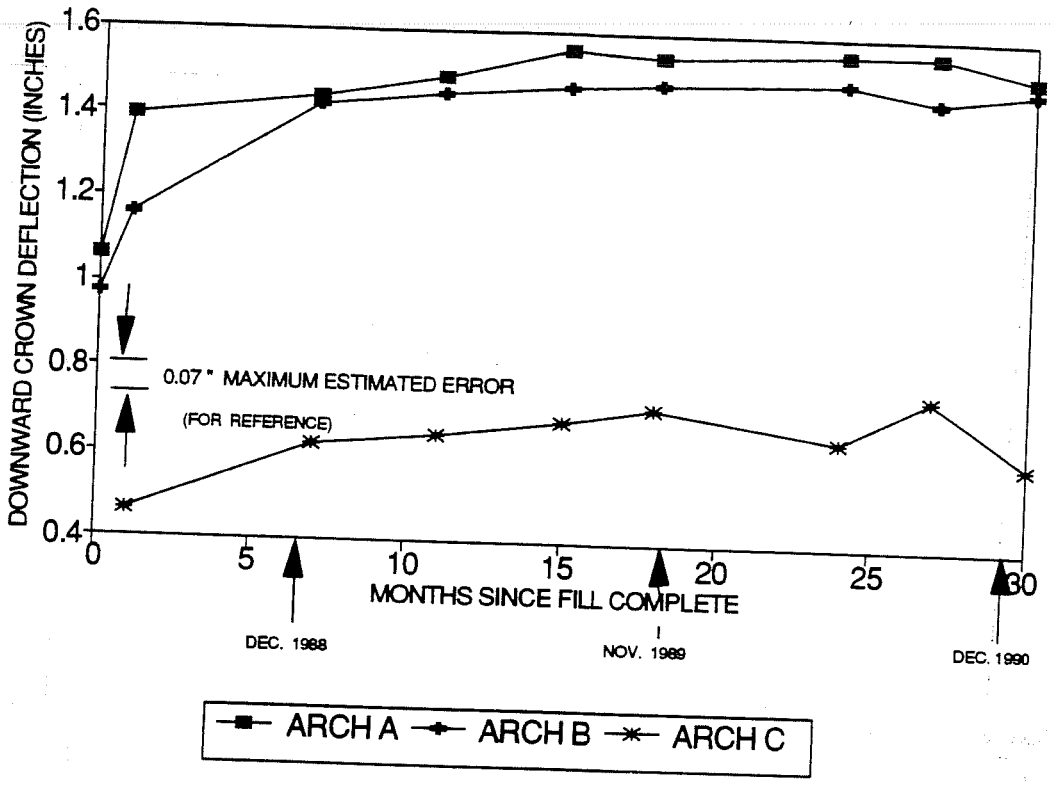

Figure 3.12 Measured culvert midspan deflection after completion of fill

soil constrains the culvert so that the seasonal fluctuations are less than the amount that can be confidently measured.

Figures 3.13, 3.14, and 3.15 show the measured deflections across the cross sections of Arches A, B, and C respectively, at various times throughout the 30 month monitoring period. The vertical deflection patterns for all the arches are similar. Almost all the vertical deflection takes place over the middle five nail points (the middle 20 ft. to 30 ft. of the span). As Figures 1.1 and 1.2 show, the culvert cross section is very flat in this section. The vertical deflections and the measured soil pressures in Figure 3.8 indicate that the high fill arches (Arches A and B) are significantly stiffer than the low fill arch (Arch C). The measured pressures on Arch C are 80% less than those on Arch A but the measured midspan deflection of Arch C is only 45% less than that of Arches A and B. These percentages are approximately constant throughout the monitoring period. This is not surprising since the culvert design is different at Arch A and B than it is at Arch C. The footings of Arches A and B are connected with reinforcing steel while the footings under Arch C are only laterally restrained by the surrounding soil. The effect of the tensile creep strains in the floor is to reduce the effective axial stiffness of the floor and therefore reduce the effective stiffness provided to the Arches A and B by the steel reinforcement in the floor. Also Figure 3.10 shows Arch C is in tension at the mid-thickness of the crown whereas Figure 3.9 shows that Arches A and B are in compression at this location. Therefore, Arches A and B have a significantly greater moment of inertia near midspan, where the bending moments are largest. This is also a contributing factor, perhaps the major factor, to the difference between the stiffness of the two

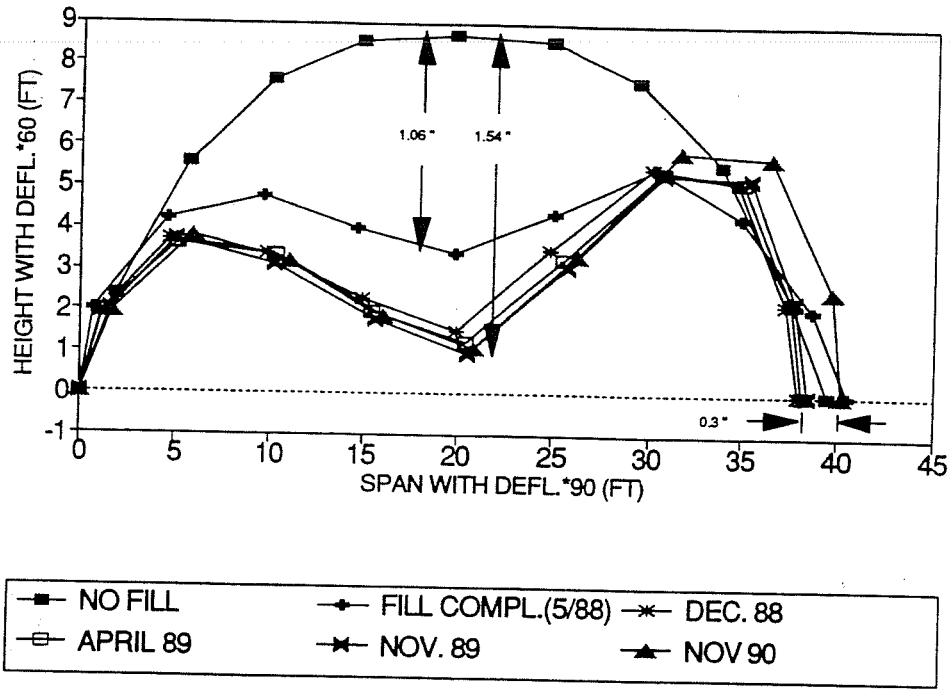

Figure 3.13 Arch A deflections after completion of fill.

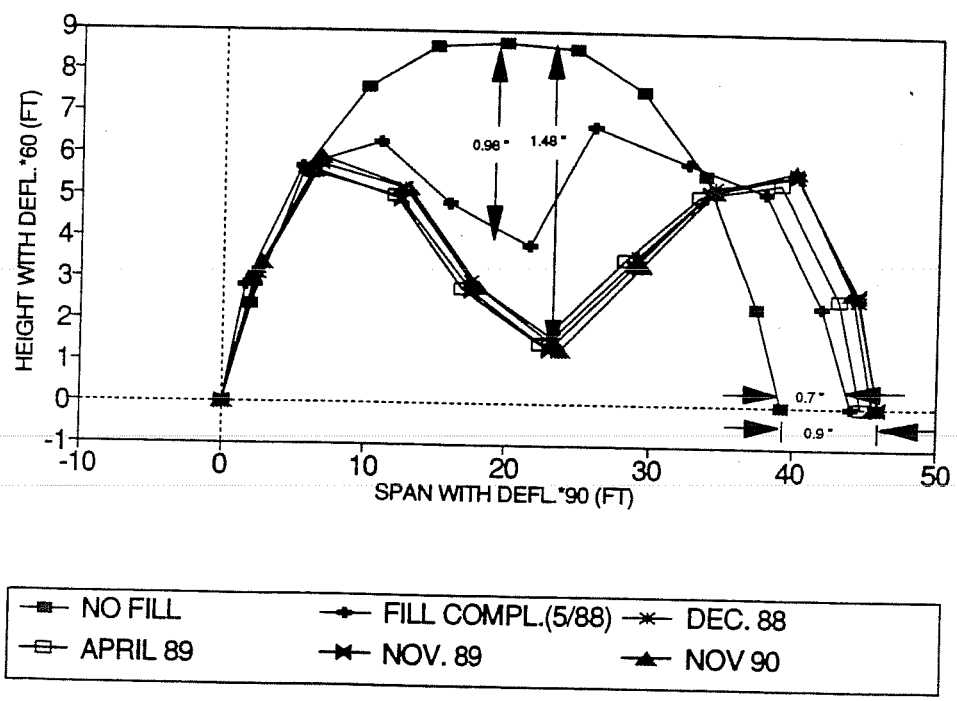

Figure 3.14 Arch B deflections after completion of fill

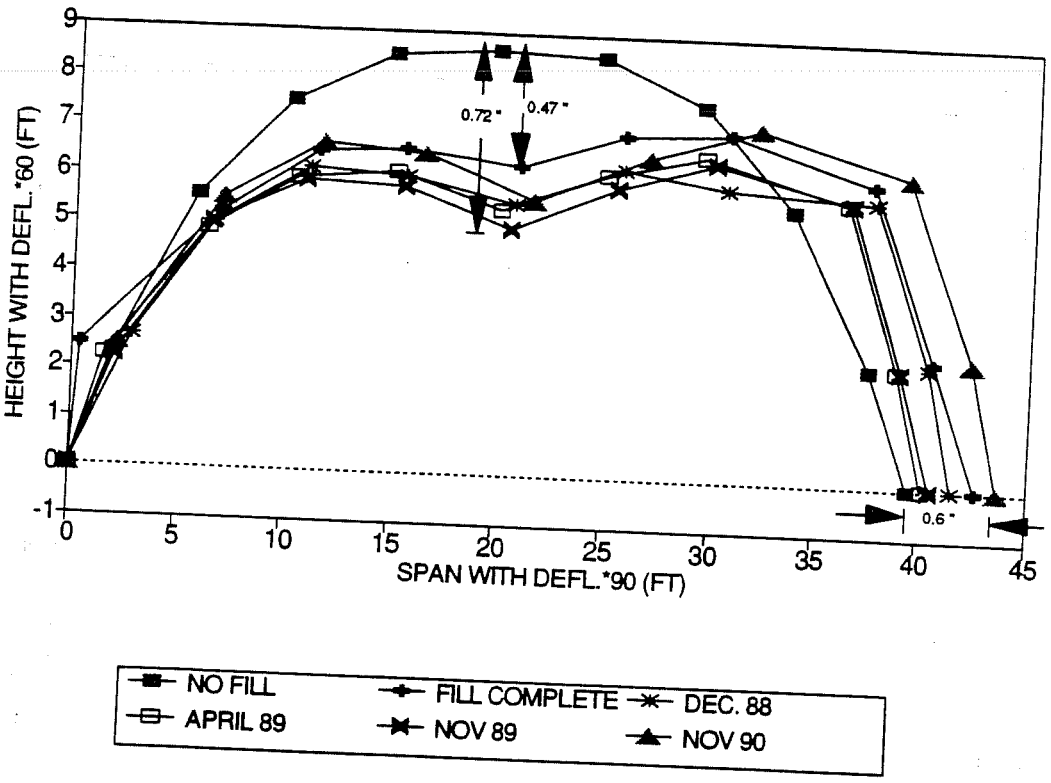

Figure 3.15 Arch C deflections after completion of fill

types of cross section. As Figures 3.2 and 3.3 show, much more cracking occurred in Arch C during the self-weight only condition and this early cracking affects the response of the culvert throughout the monitoring period.

These three figures also show the measured horizontal deflections of the nails across the three instrumented cross sections. The manner in which the measured horizontal spread of the footings of Arches A and C in Figures 3.13 and 3.15 first increases at the completion of fill, then substantially decreases during the ensuing 2 years, and finally increases a large amount during the last survey, is undoubtedly caused by error in the measured values. The very large horizontal spread of the footings of Arch B (Figure 3.14) measured at the completion fill is also suspect since it is twice the value that corresponds to the corresponding measured floor strains.

3.2.4 Summary of Measured Culvert Response After Placement of Fill. Large post-construction increases in strains (more than 100%) and deflections (approximately 40%) were measured over the 30 month monitoring period after fill over the culvert was completed. Only a small, fluctuating increase in the soil pressure on the culvert was measured during the post-construction monitoring period. Relatively small fluctuations also occurred within the general trend of increasing strain. These fluctuations generally occurred on a annual basis where the largest yearly compressive strains, and largest pressures occurred during the summer months and the lowest values occurred during the late fall and winter. It is hypothesized that the fluctuations are caused by temperature induced expansion of the culvert during the summer which is restrained by the surrounding soil. This would result in greater interface pressures during the summer and, since the strain gages do not measure temperature strains, increased compression in the culvert in the summer, which is consistent with the observed trend.

3.3 Consistency of Measurements at Gages Located Symmetrically Within the Culvert Monitoring Setup

A comparison of the measured response at symmetrical gage locations in the culvert is of interest both for general understanding and as an additional criteria for judging the accuracy of the measured strains and pressures. The monitoring system was set up so that there were a number of measurements made at symmetrical locations. As Figure 1.1 shows, pressure gages were located symmetrically with respect to the crown and with respect to the springline of Arch A. Pressure gages were also located symmetrically with respect to the crown of Arch C. Operational strain gages were located symmetrically with respect to the springline of Arch B and with respect to the footings in the floors of both Arches A and B. Lastly, since Arches A and B are virtually identical and are located under the same fill conditions, the gages at corresponding locations and midspan deflections of these two cross sections can be considered symmetrically located.

At the end of the monitoring period, measurements at five out of the six locations which are symmetrical within a cross section were within 20% of each other. Of these five, two were within 10% of each other. Only the measured pressures at the locations symmetrical with respect to the crown of Arch C differed by more than 20% (approximately a factor of 2). Also, at the end of the monitoring period, three out of four measurements at symmetrical locations in Arches A and B were within 20% of each other. In this case only the floor strains measured under the two cross sections differed by a large amount (about a factor of 2). Considering both of these types of symmetrical measurements together, a total of nine out of eleven symmetrical gages measured values within 20% of each other.

At the completion of fill, there was slightly less correlation between symmetrically located gages. Measurements at four out of six symmetrical locations within cross sections were within 20% of each other. Measurements at two out of four symmetrical locations in Arches A and B were within 20% of each other. The good agreement between values measured at symmetrical locations increases the general level of confidence in the accuracy of the measured strains and pressures since it indicates that there are not any general problems with the gages or placement of the gages causing significant random error in the measurements.

CHAPTER 4

MODELING SOIL-STRUCTURE RESPONSE OF CULVERT AND SURROUNDING SOIL FILL

As was mentioned in the first chapter, a combined experimental/analytic approach is used in this study to understand the response of the BEBO culvert and the surrounding soil. The analytic approach consists of modeling the culvert and soil response using the finite element method. Specifically, the CANDE computer code, which is in the public domain and is distributed through the Federal Highway Administration, was used. This code, which was developed at the Naval Civil Engineering Laboratory (NCEL) by M. Katona, et al.[17] in 1976 (and modified in 1980[37]), is "customized" for soil-structure interaction in the sense that it is based on an incremental approach, so that it considers the incremental nature of soil placement around the culvert, and it includes realistic, nonlinear material models for the types of structural components and soils commonly used for underground construction. It also includes interface elements which model frictional behavior and slippage at the soil-structure interface. The primary shortcoming of the code for use in modeling the response of the BEBO culvert is that the material models do not consider time dependent material response. As discussed in Chapter 3, the culvert response is significantly affected by time dependent response, particularly concrete creep and shrinkage, and possibly temperature strains. Therefore, the reinforced concrete material model in the publicly available version of CANDE has been extended to include these types of time dependent response for this study. Also, the limited options available for defining structural boundary conditions in the CANDE code were expanded, and the capability to consider varying material properties within structural components was added.

In this chapter the CANDE code and the modifications which were made to the code are discussed. The inputs used to model the BEBO culvert and the surrounding soil fill are also discussed. In Chapter 5, a comparison of the measured and calculated response of the culvert is presented and discussed, as well as a comparison between the response of a reinforced concrete arch culvert monitored by the State of California and the corresponding response calculated with the modified CANDE code.

4.1 Overall Architecture of the CANDE Code

The existing version of the CANDE computer code is a two-dimensional, static, finite element code which calculates incremental response to loading applied in discrete load steps. Elements can be added to the finite element mesh at the beginning of each load step. This allows the code to model the state of stress and strain caused by the typical incremental placement of soil lifts around underground structures. The summed element stresses and strains calculated with an approach where soil elements are added incrementally to the finite element mesh are much different (usually less severe) than the stress and strain calculated with a one-step analysis which considers the final soil-structure geometry as a single applied load condition. This is, in part, due to the stress-path dependence of the structure and soil stiffness. However, even a fully linear-elastic analysis is affected by the incremental placement of soil because of the presence of the free boundary condition at the surface of the soil during each load step.[15]

The CANDE code includes realistic nonlinear material models for a number of structural components and soils commonly used for underground construction. The material nonlinearity is modeled by using an incrementally linear-elastic approach. In this approach a linear-elastic solution scheme is used within each increment, or load step, which iterates with "trial" solutions of the global system of equations to find the two elastic modulus values for each element which are consistent with the material stress-strain model at the calculated state of stress and strain. When these modulus values have been determined for each element in the finite element mesh, the solution has "converged" for the given load step and the results from this final trial solution are added into the summed results from previous time steps. This approach allows a linear-elastic solution scheme based on Hooke's law to be used during each load step, and also models material nonlinearity by essentially "chording" along the material stress-strain relationship on a load step by load step basis. The penalty imposed on this approach by the nonlinearity of the material stress-strain relationships is the iteration, or multiple trial solutions of the global system of equations, which occur during each load step.

The CANDE material models used in this analysis are: 1) the reinforced concrete model; 2) the Duncan soil model; and 3) the interface element model. The reinforced concrete material model calculates the stiffness parameters used in the stiffness matrix (cross sectional area and moment of inertia) by considering the nonlinear effects of: 1) concrete cracking; 2) a trilinear concrete compression stress-strain relationship which models yield, work-hardening, plastic response, failure, and unload-reload of the concrete; and 3) an elastic-perfectly plastic steel stress-strain relationship. The structure is modeled with beam-column elements with six degrees of freedom. The structural stiffness parameters are calculated assuming plane stress in the in-plane directions, and plane strain in the direction normal (out of the "page") to the two-dimensional plane modeled by the code. This directional coincides with the north-south direction along the longitudinal axis of the culvert in this analysis. All yield, plastic response, and failure criteria of the concrete model are based solely on the one-dimensional, in-plane, longitudinal concrete stresses or strains. The Duncan soil model, which is used to model the soil fill surrounding the culvert, is used to calculate the soil tangent Youngs modulus and tangent bulk modulus as a function of the soil state of stress. The tangent moduli for each load step is the tangent to the stress-strain curve at the average stress calculated from the stress at the beginning and at the end of the load step. In this model, the axial soil stress-strain relationship is assumed to be a hyperbolic curve which is determined for each soil type from curve-fits to triaxial test data. It is a function of both the confining pressure, or the minor principal stress, and the soil deviator stress (the difference between the major and minor principal stresses). The bulk modulus is only assumed to be a function of the minor principal stress. This soil model, as it is implemented into the CANDE code, is applicable for monotonic loading only, but it can be extended to consider unloading as is discussed in Reference 38. The interface elements model relative movement at the soil-structure interface as purely frictional response. Initially, no slip at the boundary is assumed, and slip tangent to the soil-structure interface is allowed when the calculated shear stress along the interface exceeds the product of the normal interface stress and the input friction coefficient. Also, separation is modeled when the normal interface stress exceeds the input interface tensile strength. After any given response state (i.e. slip) is assumed, the response along the interface calculated based on this assumption is checked for compliance with all the conditions assumed for the given state.

4.2 Reinforced Concrete Material Model

Concrete structures are modeled in the CANDE code with beam-column elements with six degrees of freedom consisting of two displacements (in the X and Y directions) and a rotation at each node, or end point. The bending stiffness and axial stiffness used to construct the element stiffness matrix are calculated during each load step using: 1) a value for Youngs modulus of the concrete and steel based on the current state of stress and strain through the thickness and assumed uniaxial stress-strain relationships for each material; and 2) the current effective cross sectional area of the element, which is a function of the state of strain. The effective area is zero if the strain exceeds the concrete cracking strain and the concrete modulus reduces with increasing compression strain at discrete limit strains. The steel modulus is constant up until the yield strain when it effectively reduces to zero. Since the strain generally varies through the thickness, separate modulus and effective area terms are calculated at discrete points through the element thickness, and the overall section properties are determined by integrating over the thickness. The state of uniaxial stress and strain of the reinforced concrete element through the thickness is calculated with the bending moment and thrust at each node, the known cross sectional geometry at each node, the assumed concrete and steel stress-strain relationships, and the assumption that the strain distribution is linear through the thickness. Iteration is necessary because the effective cross sectional area and stiffness must be known in order to calculate the stress and strain but they are also functions of the state of stress and strain. When through thickness stress and strain are calculated which satisfy the equilibrium, stress-strain, and compatibility conditions, this is called "inner" convergence. However, because nodes are not used through the thickness of the structural elements, the relationship between element stiffness and the stress and strain within the element is not explicitly satisfied in the finite element solution. The element stiffness is only affected when the concrete strain exceeds the cracking strain in tension or exceeds a limit yield strain in compression, or when the steel strain exceeds yield. Therefore, the stiffness is often relatively independent of the exact stresses and strains in the element. However, a special convergence check is made after the finite element solution to verify that the stiffness parameters used for the finite element solution are compatible with the through-thickness strain distribution calculated with the bending moment and thrust from the finite element solution. This convergence is called "outer" convergence.

4.2.1 Concrete and Reinforcing Steel Stress-Strain Relationships. The stress-strain relationships used by the CANDE code for reinforcing steel and concrete are shown in Figures 4.1(a) and 4.1(b). Only one-dimensional stresses and strains along the longitudinal axis of the element are considered. Therefore, the material model is applicable when the structural response is dominated by thrust along the longitudinal axis of the structure and flexure and is not affected by stresses perpendicular to the longitudinal axis of the structure. This is not a problem for most structural members used in underground construction, including the BEBO culvert, which usually have depth-to-span ratios greater than five. Plane strain is assumed in the one-of-plane direction (normal to the plane modeled by the CANDE code) and the elastic stiffnesses of both the concrete and steel are divided by $1-v^2$ where v is poissons ratio. All input and output is per unit width in the longitudinal direction where plane strain occurs. The assumed reinforcing steel response is linear elastic in compression and tension up until yield as shown in Figure 4.1(a). Yield occurs at the input yield stress of the steel. The elastic steel stiffness is equal

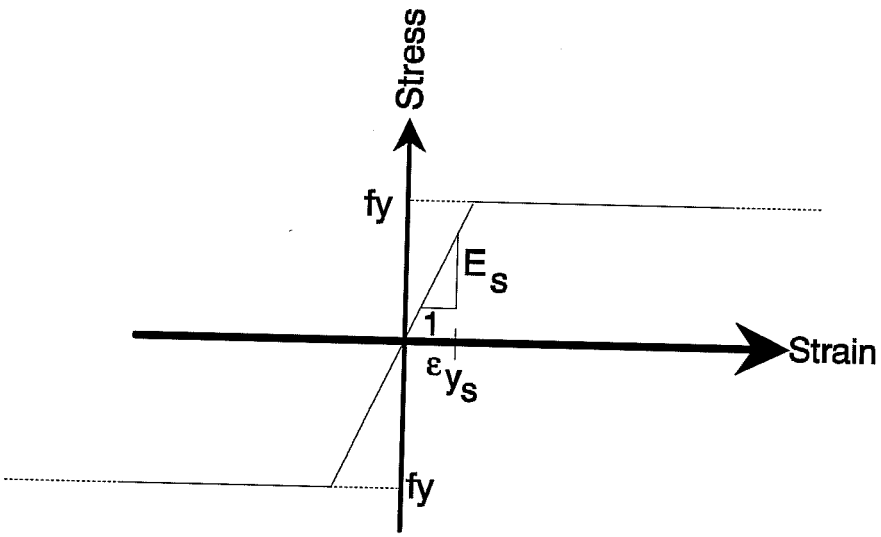

Idealized Stress-Strain Diagram for
Reinforcing Steel

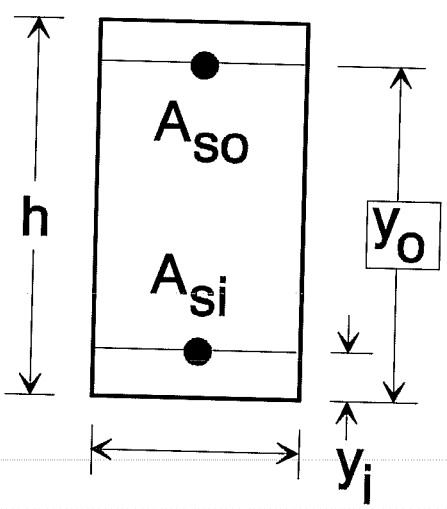

Reinforced Concrete Cross Section

Figure 4.1(a) Stress-strain relationship for reinforcing steel

to the input Youngs modulus (or 29,000 ksi) divided by $1-v^2$. Unloading is elastic with a modulus equal to the elastic modulus. The steel area in the top and bottom steel layers and concrete cover over each steel layer are also input.

For the concrete, a trilinear stress-strain curve is assumed for concrete in compression in the CANDE code as shown in Figure 4.1(b). The first segment of the curve is linear up to the yield strength, which is equal to one-half the input 28-day cylinder compressive strength (f'_c). The modulus in this section is based on an input value for Youngs modulus, or on a default of $57{,}000(f'_c)^{1/2}$ and a poissons ratio (assumed to be 0.17 or input value). The elastic-plastic segment of the assumed stress-strain relationship is also linear, with a reduced slope, up until the onset of plastic response at a strain of 0.002 in./in. Youngs modulus in the elastic-plastic segment is equal to $1/2(f'_c)$ divided by the difference between 0.002 in./in. and the yield strain. The last segment is purely plastic response up to the ultimate strain value of 0.003 in./in. The stress is constant at f'_c and the modulus is equal to a very small value. At strains greater than 0.003, the stress drops to zero. Poissons ratio is assumed constant. Unloading is elastic with a modulus equal to that of the virgin portion of the stress-strain curve. Reloading is elastic with the same modulus until the stress reaches its previous maximum value, after which the concrete response follows the original stress-strain curve. Tension concrete is linear elastic with the same modulus used in the initial portion of the compressive stress-strain relationship up until an input cracking strain. After cracking, the stress drops to zero. Cracked sections can carry compressive stress at a later time, but no tensile stress can develop in a previously cracked section. No tension stiffening is considered.

4.2.2 Iteration Procedures. The heart of the reinforced concrete material model in the CANDE code is the iteration technique used to find the cross-sectional response at each node in the structure which is consistent for the stress-strain relationships for the concrete and steel, the applied thrust and bending moment, and the compatibility condition (linear strain distribution). The incremental strain at each of eleven points through the cross section thickness is calculated with Equation 4.1. The incremental bending moment and thrust are those calculated with the most recent trial finite element solution. The incremental strain is added to the previous sum of strain from all previous load steps to obtain the total strain. The total stress at each point in the concrete is calculated based on the total strain and the stress-strain relationship in Figure 4.1(b). The total strain is compared to the previous maximum strain in order to differentiate between strain along the virgin loading curve or along an unload/reload curve in the stress-strain relationship. The tangent concrete modulus (E_t) at each point through the thickness is equal to the change in total stress at that point since the previous load step divided the change in total strain since the previous load step. This is illustrated in Figure 4.1(c). The tangent modulus associated with a point through the thickness where the strain exceeds the concrete tensile or compressive failure criteria is equal to zero. The depth of cracking is also calculated and printed out. The tangent steel modulus is also calculated at both layers of reinforcing steel using the same basic procedure.

$$e(y) = P/(E_c A') + M \times (y - y')/(E_c I') \qquad (4.1)$$

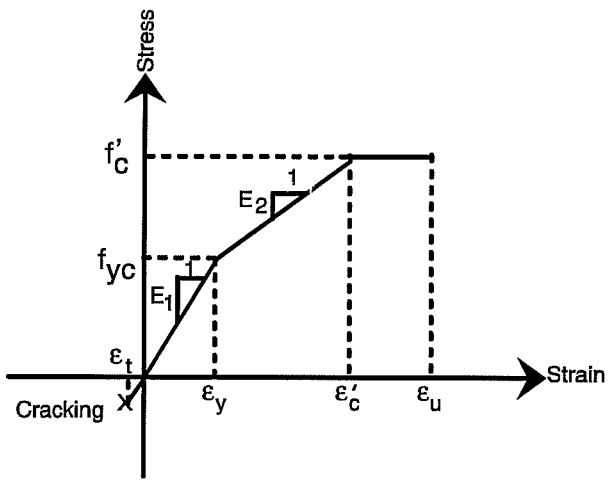

Idealized Stress-Strain Diagram for Concrete

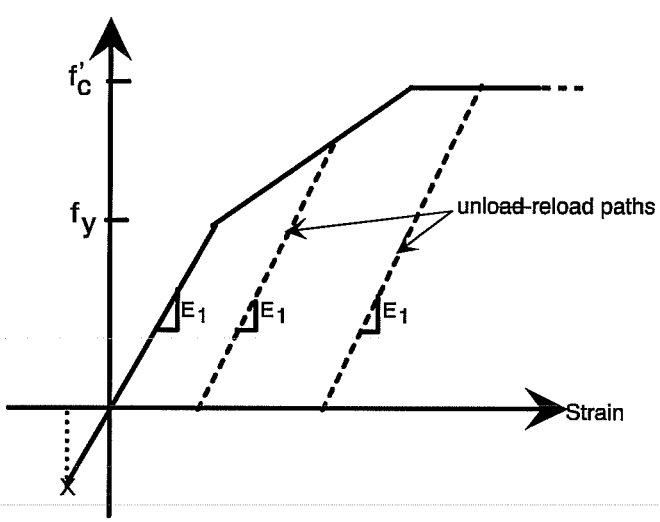

Elastic Unload-Reload for Concrete

Figure 4.1(b) Stress-strain relationship for concrete

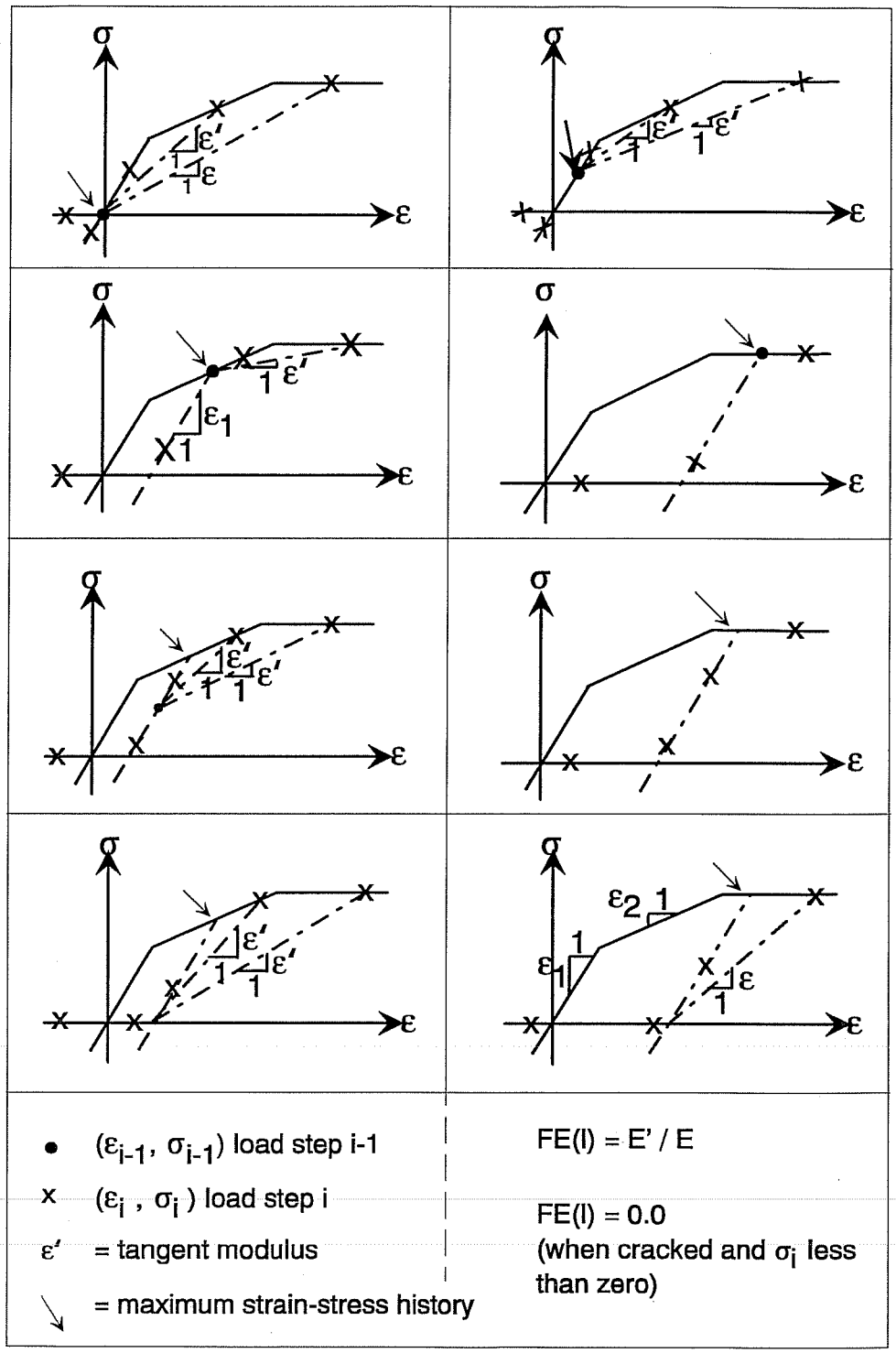

Figure 4.1(c) Modulus function for all possible concrete strain histories at a point in the beam cross section.

where $e(y)$ = strain increment at distance y above bottom surface,
P = incremental axial thrust,
E_c = Youngs modulus for concrete,
A' = effective transformed cross sectional area,
M = incremental bending movement,
y' = height of neutral axis above bottom surface, and
I' = effective moment of inertia based on transformed section.

After the tangent modulus is known at each of the eleven points through the thickness and the depth of cracking is known from the strain distribution, the effective moment of inertia (I'), the location of the neutral axis (y'), and the effective area (A') of the cross section are calculated by numerically integrating over the points through the thickness in the usual manner. However, the ratio of the variable tangent modulus to Youngs modulus (E_t/E_c) is included at each point through the thickness in the integration to account for the nonconstant modulus through the thickness. This also causes the effective area associated with any cracked or yielded points through the thickness to be zero. The transformed steel area, multiplied by the ratio of E_t for the steel divided Youngs modulus for the steel, is also included in the integration.

Inner convergence is achieved when the I' and A' calculated in the integration discussed above are equal to those used in Equation 4.1 to calculate the strain distribution. If inner convergence is not achieved, the new I' and A' terms obtained from the integration are used in Equation 4.1 to calculate a new strain distribution, and the process is repeated until convergence is achieved or until a limit number of iteration is exceeded. The limit is currently set at ten iterations.

The iteration scheme also included an "outer" convergence as discussed above. Outer convergence insures that the stiffness parameters corresponding to the state of stress/strain output from the solution of the global system of equations is consistent with those in the stiffness matrix used in the solution. After outer convergence is achieved, and convergence is achieved for all other elements in the finite element mesh with nonlinear material properties, the incremental strains calculated with Equation 4.1 during the last iteration are added to the sum of strains from all previous load steps. The total thrust and bending moment for each element is also updated. Thus, an incremental approach is used, where the incremental concrete and steel strains due to incremental changes in thrust and bending moment are calculated. However, the state of total stress and strain in the concrete and steel is used to determine the element stiffness matrix and the element sectional properties (I', A', y' in Equation 4.1) which affect the incremental strain.

When an increase in the crack depth occurs, the total stress that was previously carried by concrete which was cracked is redistributed into the remaining effective cross sectional area. This is accomplished by calculating the total force and moment (about the new neutral axis) previously resisted by the stress in the cracked area, and then applying an equal and opposite force and moment to the remaining cross section in Equation 4.1, along with the incremental force and moment from loads applied during the load step. This step is performed after inner convergence, when a new cross sectional area consistent with the previous strain and the additional strain increment from Equation 4.1 is known. Outer convergence is only allowed when the cross sectional properties calculated at inner convergence include

the full effects of any redistribution force and moment caused by increase in the crack depth. However, the inverse of this operation for the case where increased compression forces cause the crack depth to decrease, is not considered in the CANDE reinforced concrete material model. Therefore, if an applied thrust is applied to model post-tensioning of a previously cracked reinforced concrete beam, for example, the decrease in bending stress and decrease in deflection caused by the increase in the effective cross sectional area will not be modeled. Monotonic loading is very typical for underground construction and therefore this limitation would rarely affect the capability of the code to model the response of underground structures. Since the loading is monotonic in this study, and the redistribution of stress in the cross section caused by creep and shrinkage strains is not significant enough to cause compression stress in previously cracked portions of the cross section, this limitation in the model does not affect this study. However, if CANDE was to be used to study repair techniques for reinforced concrete culverts, for example, the existing code would probably require modification.

The publicly available version of CANDE assumes a monolithic structure, such as a pipe or a box culvert, with one set of concrete and reinforcing steel material properties throughout the structure. It does not consider any relative rotation between nodes (no pinned joints within the structure) or pinned structural boundary conditions. Also it considers only one contiguous group of structural elements. Finally, this version of the code allows nodal force and displacement boundary conditions to be prescribed only in two perpendicular directions (rotations are assumed fixed at boundaries and no applied moments are allowed). All enforced displacements are automatically applied during the first load step the element is included in the finite element mesh. These conditions are typically acceptable for simple underground structures but they are too restrictive for this study of the instrumented BEBO culvert cross sections. Therefore, the publicly available version of the code has been modified to allow pinned joints within the structure and at the boundary nodes, to allow the application of moments to structural nodes, and to allow unconnected groups of structural elements. Also, nodal displacements can be applied during any load step and elements can have different sets of concrete and reinforcing steel material properties. The reinforced concrete material model in the publicly available version of CANDE does not consider any long term material response such as creep and shrinkage nor does it consider response to temperature changes. The material model has been modified to include these capabilities, but discussion of these modifications is delayed until later in this chapter.

4.2.3 Structural Model of Field-Instrumented BEBO Arch Culverts. Figure 4.2 shows the cross sections through the BEBO arch culvert which were instrumented in this study. Two sections under the high fill (24 ft. of fill over the culvert crown) were instrumented and one section under the low fill (8.5 ft. of fill over the culvert crown) was instrumented. Figure 4.3 shows the reinforcement in the two sections under high fill (sections 1-1 and 2-2 in Figure 4.2). The reinforcement in the section under low fill, section 3-3 in Figure 4.2, is similar to that shown in Figure 4.3 except that there are no #9 bars at midspan of the arch (section B in Figure 4.3) and no reinforcing steel connecting the arch footings to the slab as shown in detail F of Figure 4.3. Therefore, the culvert has less reinforcing at the crown (where the maximum bending stresses occur) and under the low fill, and the floor slab is not connected into the footings under the low fill. A line of symmetry through the midspan of the culvert and along its longitudinal axis is assumed, as shown in Figure 4.3. The culvert was modeled with 17 nodes (16 elements) in this study, and the reinforcing steel area and location at each node were input into the

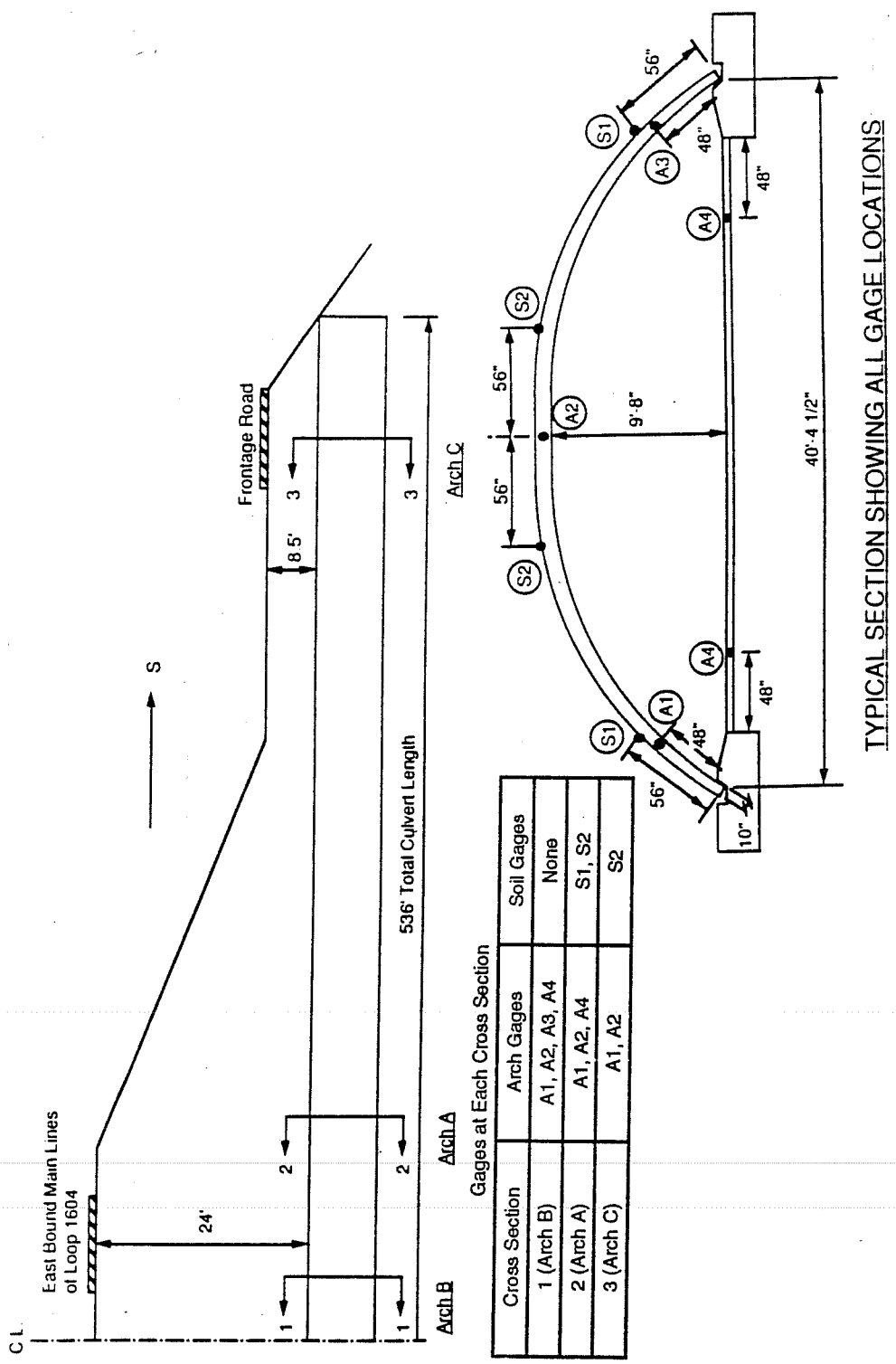

Figure 4.2 Elevation and section showing locations of soil pressure and strain gages

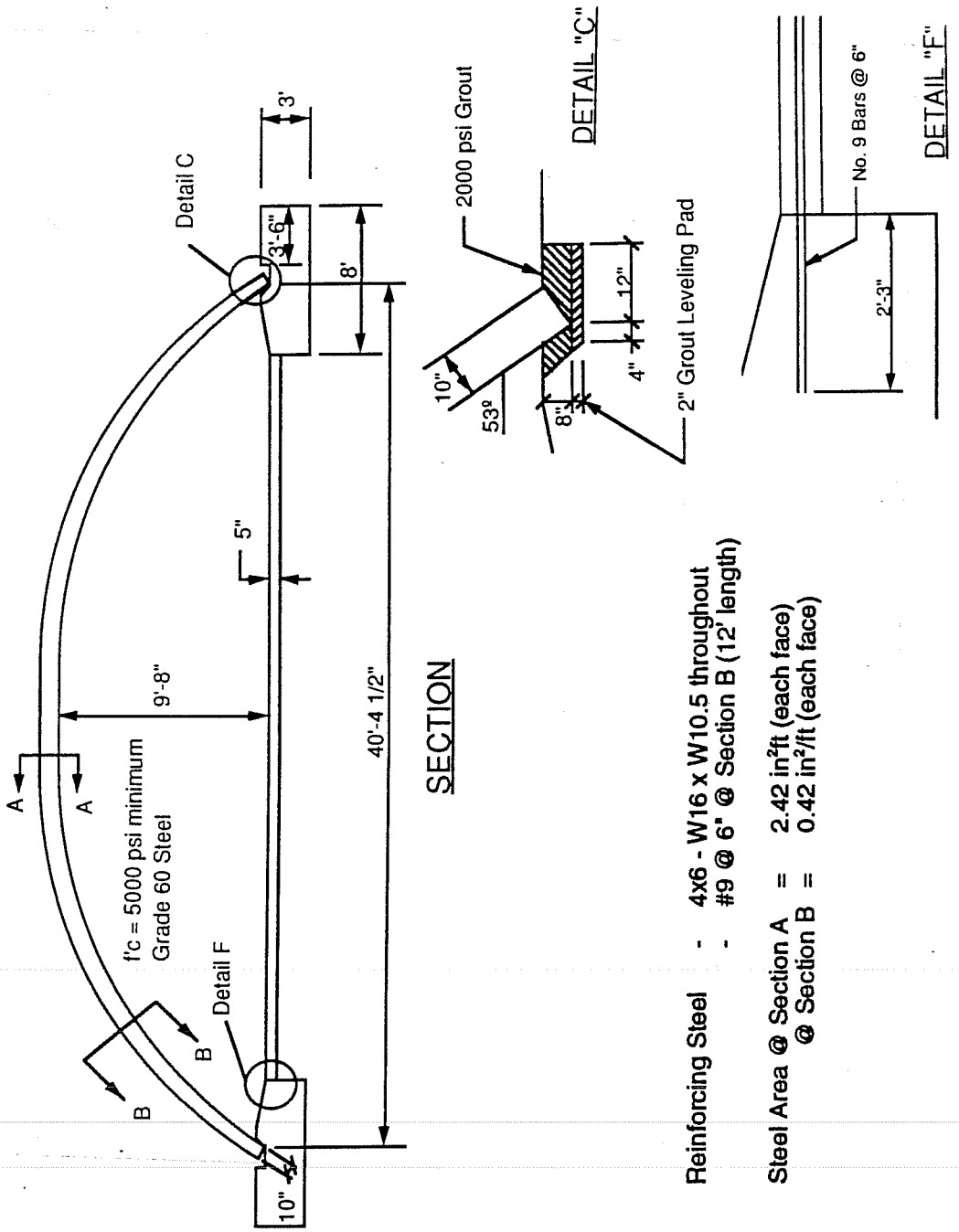

Figure 4.3 BEBO arch details

CANDE code as read off the plans of the culvert. The node at midspan of the culvert, along the line of symmetry, was assumed to have no rotation or horizontal displacement to account for the restraint provided by the symmetry of the structure and loading. The concrete 28-day cylinder compressive strength of the arch is approximately 7,000 psi based on the typical strengths measured from the mix design used for the concrete in the culvert. Due to a mix-up, the strengths for the particular segments of the culvert which were instrumented are unavailable. The mix design is a six-sack Type 3 cement mix (564 lb. of cement per cubic yard of concrete) with proportions of 0.48 (water) to 1.0 (cement) to 2.3 (fine aggregate) to 3.7 (coarse aggregate) by weight. The fine aggregate consists of a 65:35 blend of manufactured aggregate and silica sand. The coarse aggregate is 1-1/4 in. limestone. The assumption of the concrete strength is considered accurate to within 15%, based on the typical spread in the measured concrete strengths made with the mix design. This lack of accuracy does not significantly affect the analysis because the concrete stresses are comfortably less than one-half the compressive strength so that no concrete yielding is thought to occur in the actual structure. The Youngs modulus and cracking strength of the concrete are related to the compressive strength to a power less than 0.67 so that the possible 15% inaccuracy does not have a very significant effect on these variables. The concrete cracking stress is calculated using Equation 4.2, which is a curve-fit to test data. Based on data in Reference 39, this formula fits a large number of data points much better than the formula of 7.5 times the square root of the compression strength which is commonly used. The cracking strain input into the CANDE code for the culvert is equal to the modulus of rupture strength from Equation 4.2 divided by the concrete Youngs modulus.

$$f_r = 2.3(f_c')^{0.67} \tag{4.2}$$

where f_r = modulus of rupture strength (ϕ), and
f_c' = 28-day concrete compressive cylinder strength (ϕ).

At its base, the culvert is grouted into the footings as shown in Figure 4.3. The footings are modeled with two-dimensional elastic elements with a Youngs modulus based on an assumed compressive strength of 3.6×10^6 psi and a poissons ratio of 0.17. Since the footing is primarily in compression, and the stress due to the thrust in the culvert is less than 25% of the compressive strength of the footing concrete, this modeling is considered adequate. Also modeling the relatively complex shape of the footing with reinforced concrete elements would be very difficult with the CANDE code.

In the analytical model, the arch is embedded into the footing elements in a similar manner to that shown in Figure 4.3 This is illustrated in detail later in this chapter during discussion of the interface elements which are used to transmit forces between the base of the culvert and the footing. Trial computer runs with CANDE have shown that a much better match is achieved between measured arch strains and soil pressures when the culvert is assumed to develop some resisting end moment at the top of the footing due to the embedment of the culvert into the footing. Inspection of the details of the arch-footing connection supports this assumption. The culvert is embedded approximately 9 in. along its centerline into the recess in the footing. This is sufficient to develop all or most of the tensile strength of the 4 in. x 4 in. welded wire mesh reinforcing steel (0.42 $in.^2/ft.$) in the culvert at the top of the footing, based on the fact that full development is achieved by embedment of two cross wires (which

requires approximately 7 in. if a cross wire is located along the edge of the mesh) in the mesh below the critical plane. Bearing stresses between the footing, the inner surface of the culvert (near the bottom of the recess), and the outer surface (near the top) transfer resisting moment from the footing into the culvert. Interface elements are used to model these bearing stresses as is discussed in more detail later. The soil pressures beneath the footing resist rotation of the footing and therefore ultimately provide the resisting moment at the support. Since the interface between the footing and the underlying soil is modeled in the CANDE code, the amount of resisting moment provided by the underlying soil is modeled. The finite element mesh, including all the soil elements, is discussed in the next section of this chapter.

The reinforced concrete culvert floor slab affects the structural response of the arches under the high fill (sections 1-1 and 2-2 in Figure 4.2) since, for these cases, the floor reinforcement is spliced into the footings. Section 3-3 floor slab is modeled with a slab made up of three elements with reinforcing steel area and location (at mid-thickness), and thickness based on the culvert construction plans. The concrete in the floor had an average measured 28-day concrete cylinder strength of 6,000 psi and is called out in the construction plans as Class C concrete. The mix design specified for Class C concrete by the Texas Highway Department is a six-sack Type 1 cement mix (451 lb. of cement + 98 lb. of fly ash per cubic yard of concrete) with proportions of 0.49 (water) to 1.0 (cement + fly ash) to 1.94 (fine aggregate) to 3.43 (coarse aggregate) by weight. The fine aggregate consists of a 65:35 blend of manufactured aggregate and silica sand. The coarse aggregate is 1 in. limestone. Since no cracking has been observed in the floor slab, a fictitiously high cracking strain is used in the model to ensure that no cracking occurs in the model. The corresponding stress calculated in the concrete of the floor slab is compared to estimated values of the cracking strength using Equation 4.2 in the next chapter.

In the CANDE model, the floor slab elements are not connected to the underlying soil since the 5 in. thick slab does not have enough weight to allow significant frictional stresses to develop at the soil-structure interface. Based on a friction coefficient of 0.4 with the underlying soil, the maximum interface frictional stress under a normal load equal to the slab weight is less than 5% of the tensile force calculated in the slab with the CANDE program. The floor slab-to-footing connection is modeled as a pinned connection so that only axial tension or compression can develop in the slab. The floor slab of the instrumented arch culvert segment under low fill (section 3-3 in Figure 4.2) is not modeled since it is not connected to the culvert footings.

4.3 Soil Material Model

The CANDE code provides two linear-elastic soil models (isotropic and anisotropic) and several nonlinear (stress-dependent) soil models. As described above, nonlinear soil response is modeled as linear-elastic within each load increment. The magnitude of the stiffness changes from load step to load step depending on the state of stress in the element. Soil failure in compression in the nonlinear soil models is modeled by using a stiffness which is very nearly equal to zero.

Measured soil stress-strain relationships are highly nonlinear; therefore, the nonlinear soil models in CANDE are of primary interest to this study. The nonlinear models available in the publicly available

version of CANDE include: 1) an overburden dependent model, where the elastic stiffness at each load step is calculated based on the height of fill; 2) a modified version of the Hardin soil model, where a variable shear modulus and poissons ratio are calculated based on the hydrostatic stress and the maximum shear stress; and 3) the Duncan soil model, where a tangent Youngs modulus and bulk modulus are calculated based on major and minor principal stress in the soil. Soil type dependent constants, which are essentially curve-fitting parameters based on data, are used in the models. Past comparative studies of the soil models in CANDE have concluded that the Duncan model is the preferred soil model since it combines relatively good accuracy (better, in general, than the other soil models) with a necessary level of simplicity.[40,12] Many of the recent published studies of soil-structure interaction have used the Duncan model, or a modified version of the model, for this reason.[8,10,19,41] For these reasons, the Duncan soil model is also used in this study to model the fill over the arch and the preexisting soil near the culvert. Also, the curve-fit parameters that are necessary to express the tangent Youngs modulus and tangent bulk modulus as a function of the state of stress and the soil type have been experimentally determined for a large number of compacted soils commonly used for fill material at varying dry density and water content and for both drained and undrained conditions.[30,42] This fact makes the model very useful for studies such as this where stress-strain properties of the soil at the site have not been experimentally determined.

4.3.1 Duncan Soil Model. The Duncan soil model determines the tangent value of the soil bulk modulus and the Youngs modulus at a given state of stress (characterized by the major and minor principal stress), for a given soil type, and compacted at a given density relative to the optimum proctor density. In the CANDE program these tangent values are used as the two elastic moduli needed to describe the assumed isotropic linear-elastic soil element stiffness matrices for each load step. An average of the tangent values calculated with the state of stress at the beginning of the load step, before load is added, and at the end of the load step, after the full load has been added, is used to represent the average soil stiffness during the load step. Figures 4.4 and 4.5 show typical stress-strain curves for soils in a typical triaxial soil test where the soil is first loaded isotropicly up to the confining stress, s_3, and then loaded axially thereafter with the deviator stress, s_1- s_3, until shear failure occurs. The deviator stress-axial strain relationship is nonlinear and heavily dependent on the confining stress. In a triaxial test the *change* in the deviator stress is equal to the *change* in the axial stress; therefore, the slope at a given deviator stress in Figures 4.4 and 4.5 is equivalent to the tangent Youngs modulus at that stress level, which is specific to the confining stress and soil type. The fact that the stress-strain relationship is nonlinear is addressed in the Duncan model by simplifying the stress-strain relationships in Figures 4.4 and 4.5 as hyperbolas. Figure 4.6 shows a comparison between a typical deviator stress-axial strain curve from a triaxial test and a best-fit hyperbola. The equation in Figure 4.6 is the equation for the best-fit hyperbola through the actual triaxial test data in terms of parameters defined in the figure. The tangent Youngs modulus is the slope of the hyperbola at the deviator stress of interest and can be determined by differentiating the hyperbolic equation for the stress-strain curve shown in Figure 4.6.

Duncan noted that the initial slope of the deviator stress-axial strain curve for each given soil type varied with confining pressure according to a power law that could be described with a constant "E_i" and an exponent "n", as shown in Figure 4.7. E_i and n are constant for a given soil. He also noted that the horizontal line that the hyperbola approaches asymptotically was approximately equal to the failure deviator stress, or the shear strength, and could therefore be expressed in terms of the cohesion (c) and

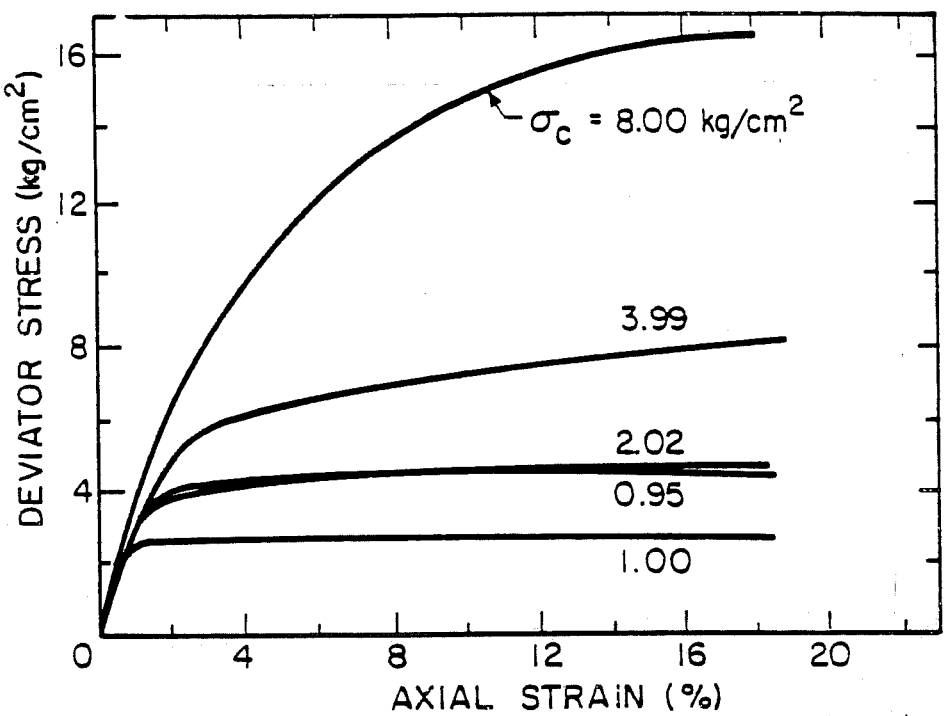

Figure 4.4 Stress-strain curves for CD triaxial tests, Canyon Dam silty clay (CL-29C)

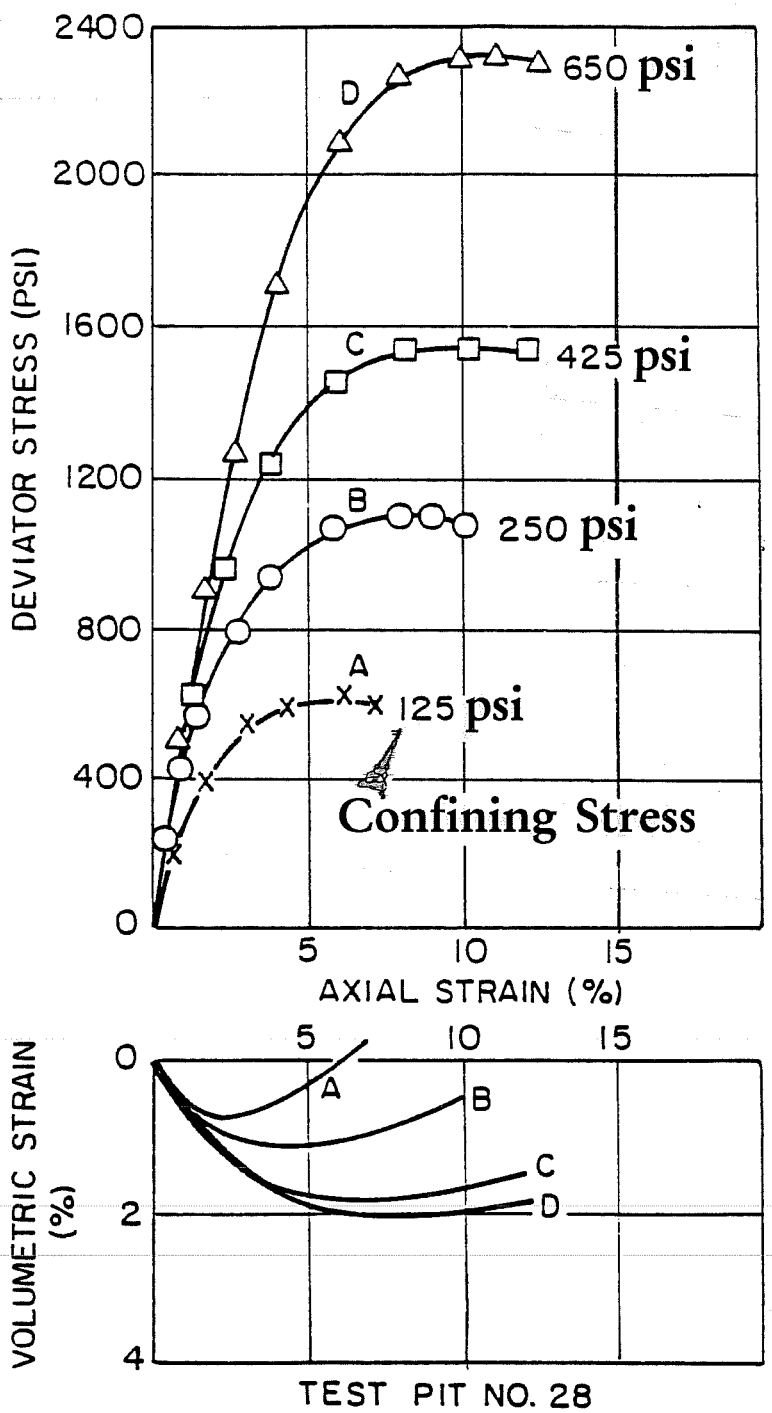

Figure 4.5 Stress-strain and volume-change curves from CD triaxial tests on Oroville Dam shell, silty sandy gravel (GP-6) (Hall and Gordon, 1963)

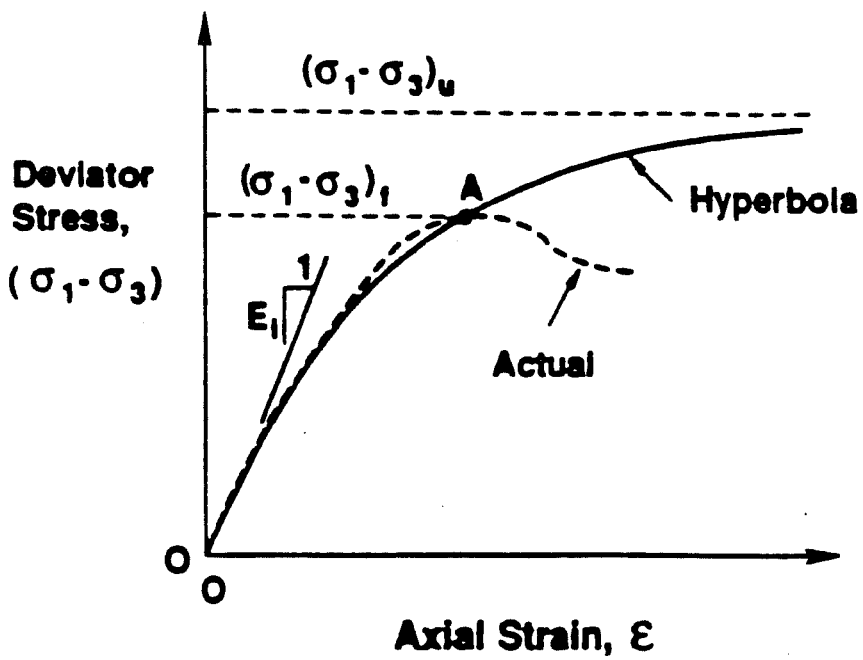

$$\sigma_1-\sigma_3 = \frac{\varepsilon}{\frac{1}{E_i} + \frac{\varepsilon}{(\sigma_1-\sigma_3)_u}}$$

Figure 4.6 Comparison of actual stress-strain curve with hyperbola

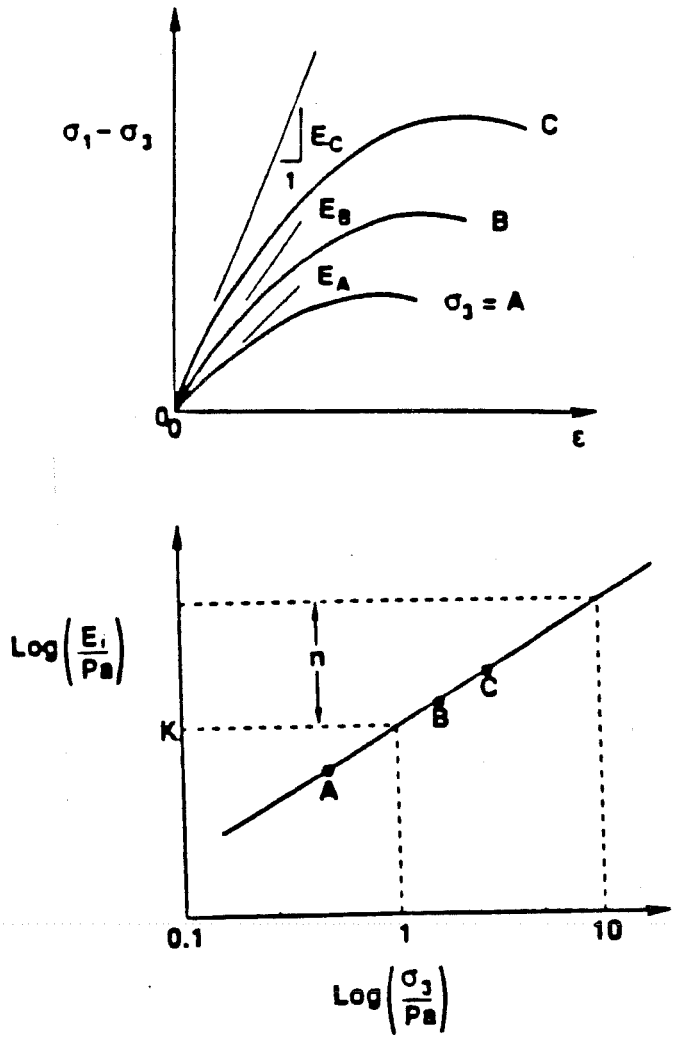

$$E_i = K\, P_a\, (\sigma_3/P_a)^n$$

Figure 4.7 Determination of K and n

the angle of friction (ϕ) commonly used in soil mechanics to describe soil shear strength. However, as Figure 4.6 shows, the asymptotic value of the best-fit hyperbola through a deviator stress-axial strain curve is typically a little larger than the failure deviator stress. Therefore, Duncan assumed that there was a ratio, called a failure ration (R_f), which was a constant for each soil, that relates the failure deviator stress (i.e. shear strength) to the deviator stress along the horizontal asymptotic value of the best fit hyperbola. Finally, Duncan noted that the soil angle of friction, ϕ, which is used to calculate the shear strength of a soil, is not actually constant for a given soil; but, in general, it is related to the logarithm of the confining stress. This relationship can be defined with two constants, ϕ_0 and $\Delta\phi$, which are assumed constant for a given soil, as shown in Figure 4.8. Using all this information, the basic axial stress-axial strain curve shown in Figure 4.6 can be defined for a given confining stress and soil type based on the assumptions above with six constants: E_i, n, ϕ_0, c, R_f, and $\Delta\phi$. The slope of this curve, which is obtained by differentiating the equation in Figure 4.6 and making the substitutions discussed in this paragraph and illustrated in Figures 4.7 and 4.8, is shown below.

$$E_t = \left(1 - R'\right)^2 \times E_i \times P_a \times \left(s_3 / P_a\right)^n \tag{4.3}$$

where E_t = tangent Youngs modulus,
R' = $\{R_f \times [1 - \sin(\phi)] \times [s_1 - s_3]\} / \{2 \times [\cos(\phi) + s_3 \times \sin(\phi)]\}$
E_i, n = see Figure 4.7,
P_a = atmospheric pressure in same units as s_1, s_3, c,
s_3 = minor principal stress
R_f = failure ratio,
ϕ = calculated from ϕ_0 and $\Delta\phi$, see Figure 4.8,
s_1 = major principal stress, and
c = cohesion strength

The six constants are determined by fitting to triaxial data from tests conducted at several confining pressures. Thus, the tangent Youngs modulus is essentially the slope of a six parameter curve fit to experimental uniaxial stress-strain curves measured during triaxial tests. Figure 4.9, 4.10, 4.11, and 4.12 show published comparisons between experimental axial stress-strain curves measured during triaxial soil tests and the Duncan model hyperbola generated with constants determined from the experimental data. Some of these curves also show fits to the relationship between volumetric strain and axial strain, which is based on the bulk modulus predicted with the Duncan model, and are discussed next. It can be seen that an accurate representation of the uniaxial stress-strain curve for a variety of soil types can be attained wit this model. Values for the six constant - K, n, ϕ_0, c, R_f, and $\Delta\phi$ - are available for a wide variety of soils for both drained and undrained soil conditions.

The tangent bulk modulus is equal to the change in mean stress divided by the change in volumetric strain. In a triaxial test, this is equal to one-third the change in the deviator stress divided by the change in volumetric strain. The Duncan model assumes that the bulk modulus is dependent only on the confining pressure. The bulk modulus considered in the Duncan model is determined from triaxial test data by one of two methods, depending on the deviator stress level at peak compressive volumetric

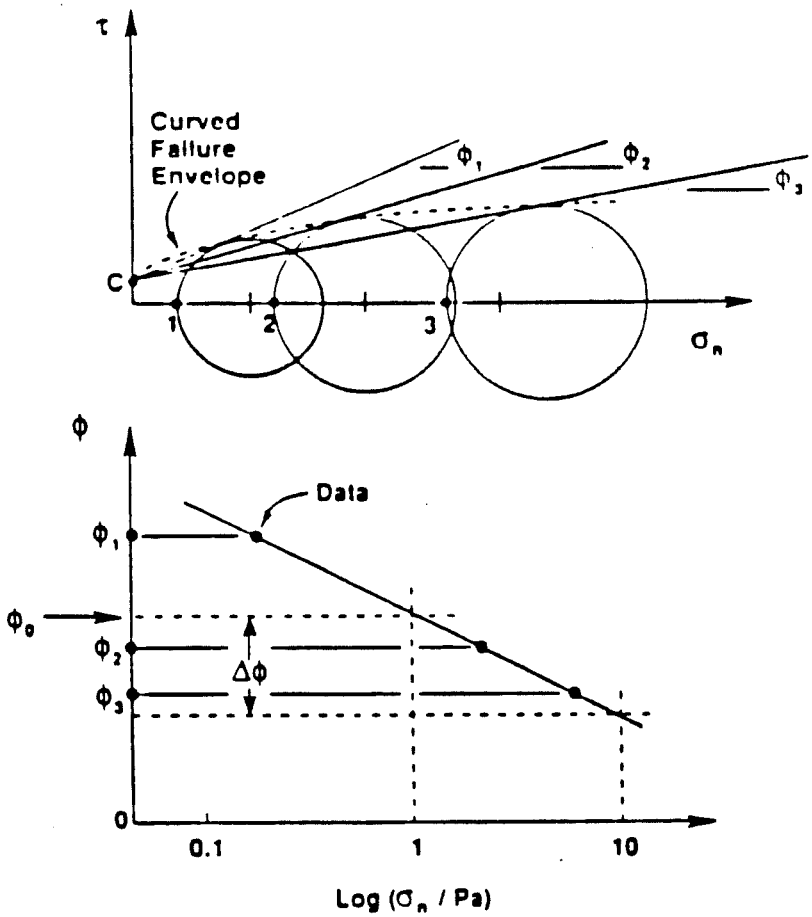

$$\phi = \phi_0 - \Delta\phi \log_{10} (\sigma_3/P_a)$$

P_a is the atmospheric pressure

Figure 4.8 Determination of ϕ_0 and $\Delta\phi$

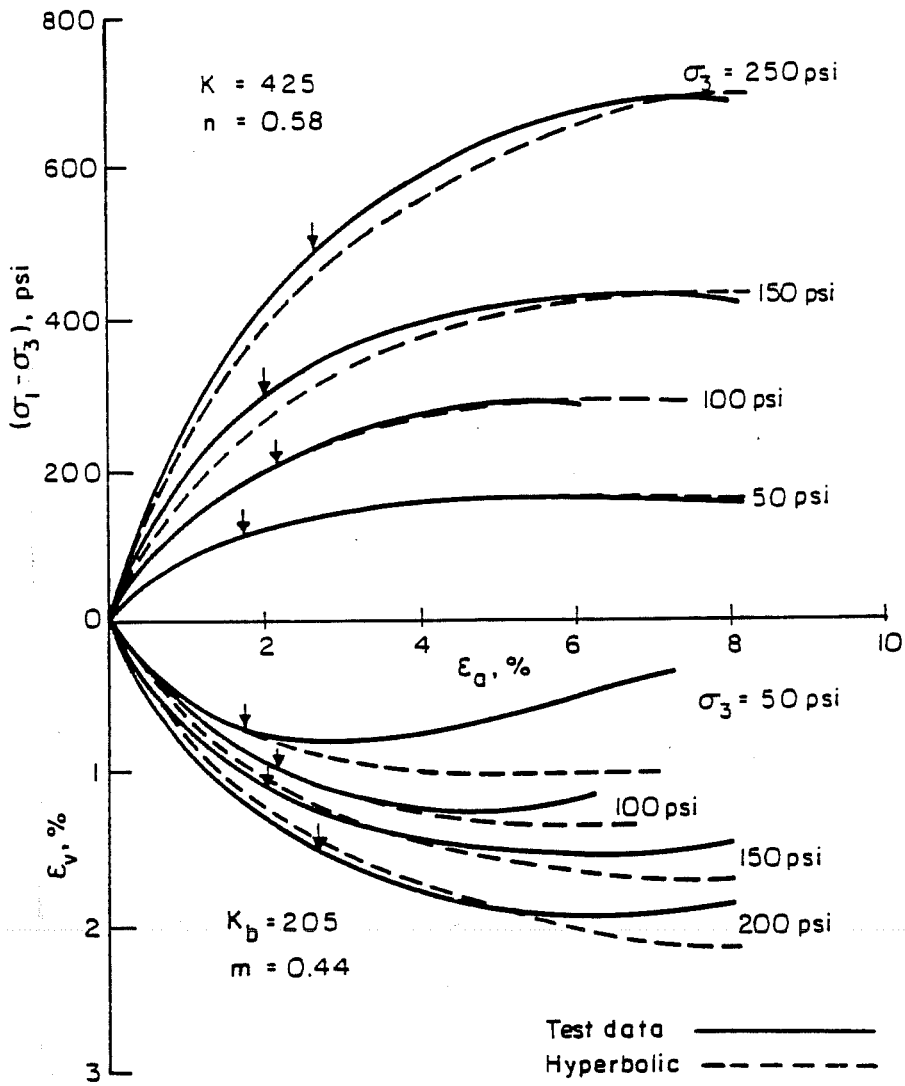

Figure 4.9 Hyperbolic stress-strain and volume change curves for Mica Creek Dam core material (SM-SC-1B)

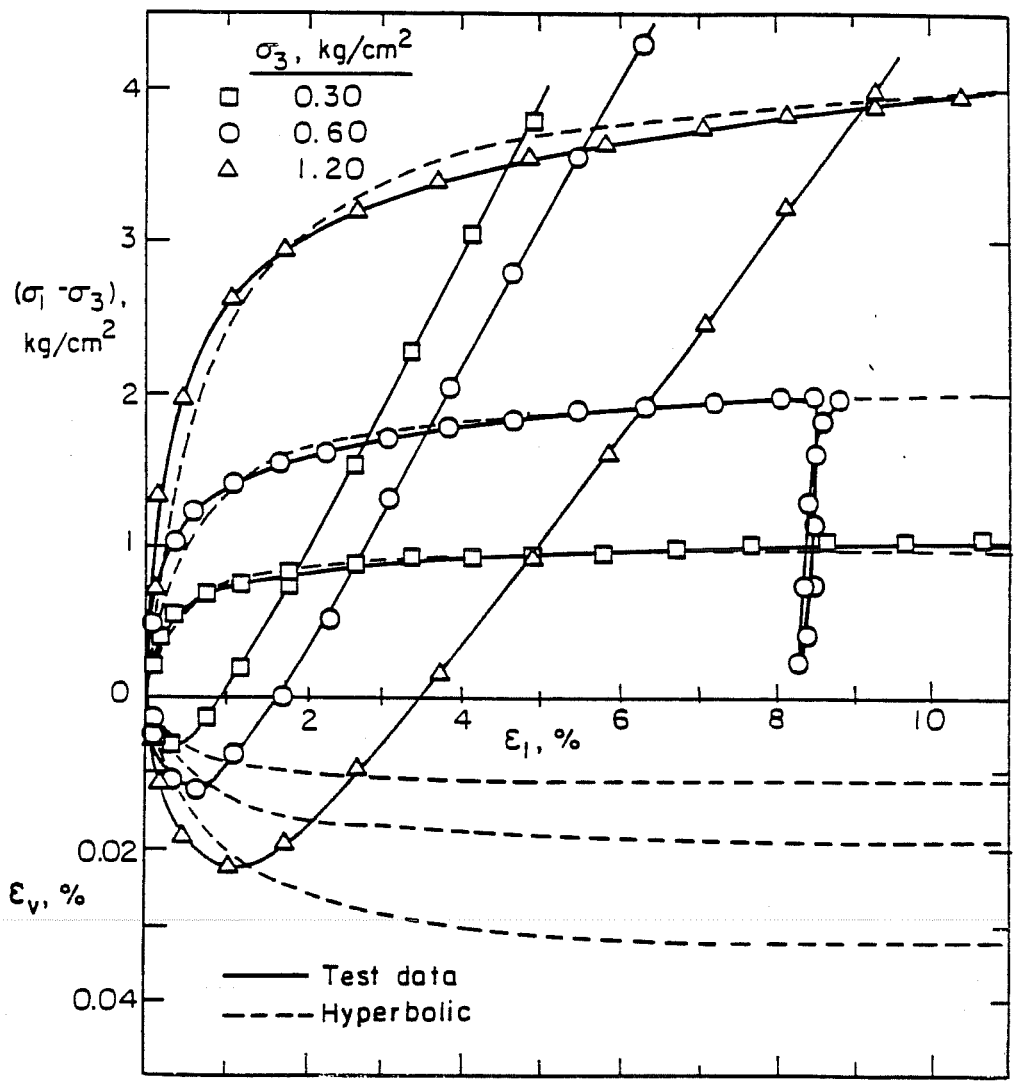

Figure 4.10 Hyperbolic stress-strain and volume change curves for Monterrey No. 0 sand (SP-17B) (Lade, 1971)

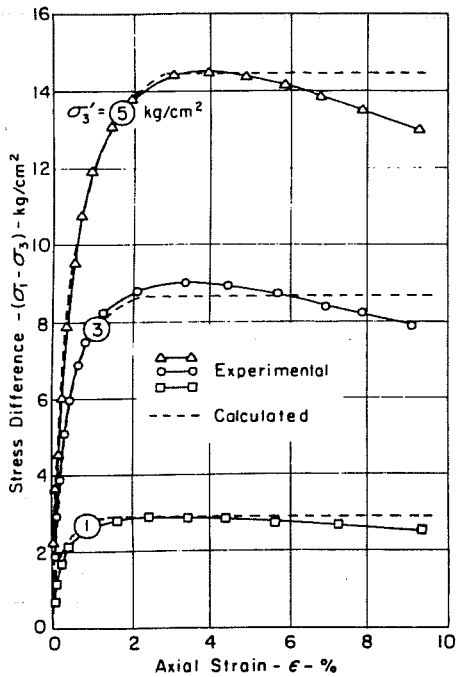

Figure 4.11 Calculated and experimental stress-strain curves for drained triaxial tests on dense silica sand

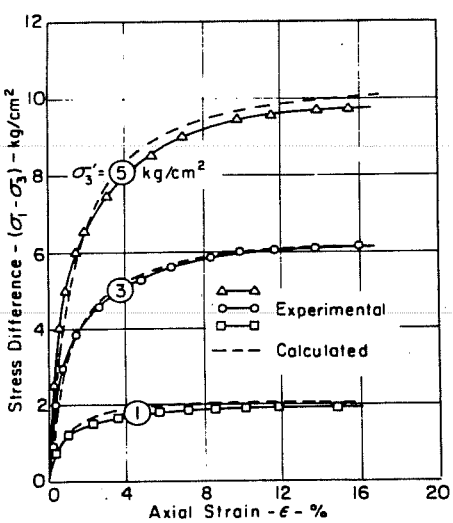

Figure 4.12 Calculated and experimental stress-strain curves for drained triaxial tests on loose silica sand

strain, as follows: 1) if the deviator stress is greater than 70% of the shear strength when the peak compressive volumetric strain occurs, the bulk modulus is equal to 70% of the shear strength divided by the volumetric strain occurring at this deviator stress; otherwise, 2) the bulk modulus is equal to one-third of the deviator stress occurring at the peak compressive volumetric strain divided by that strain. The first case occurs in many clays and silts while the latter case occurs in highly dilantant materials such as coarse sands. Case 1 is illustrated in Figure 4.13. This is a secant bulk modulus for a given confining pressure since only one pair of stress-strain values is used to determine the modulus. However, in a soil-structure analysis, where the confining pressure generally changes during each load step, this bulk modulus can be considered as a tangent value dependent on the current confining pressure.

The Duncan model assumes a power relationship between the confining pressure and the bulk modulus defined in the preceding paragraph (as shown in Figure 4.14). The two parameters which define the power law relationship, K_b, and m, are determined by fitting a line through at least three points defined by corresponding values of confining stress and bulk modulus for a given soil plotted in a log-log space. The power law equation for the tangent bulk modulus is shown below. Because of the manner in which the bulk modulus is defined, this model does not model dilantantcy (and therefore behavior at large soil strains).

$$B_t = K_b \times P_a \times (s_3 / P_a)^m \tag{4.4}$$

where B_t = tangent bulk modulus,
K_b, m = see Figure 4.14,
P_a = atmospheric pressure in same units as s_3, and
s_3 = minor principal stress

The dotted lines in Figures 4.9 and 4.10 show comparisons between volume change versus axial strain curves measured during triaxial tests, and the corresponding computed curves generated using the power law model in Equation 4.4 with K_b and m values determined from the triaxial test data. The volumetric strain is calculated for a given axial strain using the measured deviator stress-axial strain curve to relate axial strain to deviator stress and thus mean stress, and then using the bulk modulus expression in Equation 4.4. Figures 4.9 and 4.10 shows that, over the limited range of volumetric strain used to determine K_b and m, a relatively good approximation of the volume change versus axial strain curves is achieved. Figure 4.10 illustrates how the model does not consider dilantantcy.

Boscardin, et al.[43] have shown that a hyperbolic model predicts the tangent bulk modulus values measured in hydrostatic compression tests much better than a power law model (as is used in the Duncan model). Both the hyperbolic and power law models compared by Boscardin, et al. had two parameters which were determined by fitting to the data. Selig[44] has shown that significantly different hyperbolic bulk modulus curve-fit parameters are required to fit data from the same soil in hydrostatic and triaxial test data. The differences were though to be caused by the presence of shear stresses, and therefore dilantantcy, in triaxial test. In order to determine which set of hyperbolic model bulk modulus parameters (hydrostatic or triaxial) modeled actual soil response better, Selig modeled the response of a flexible metal

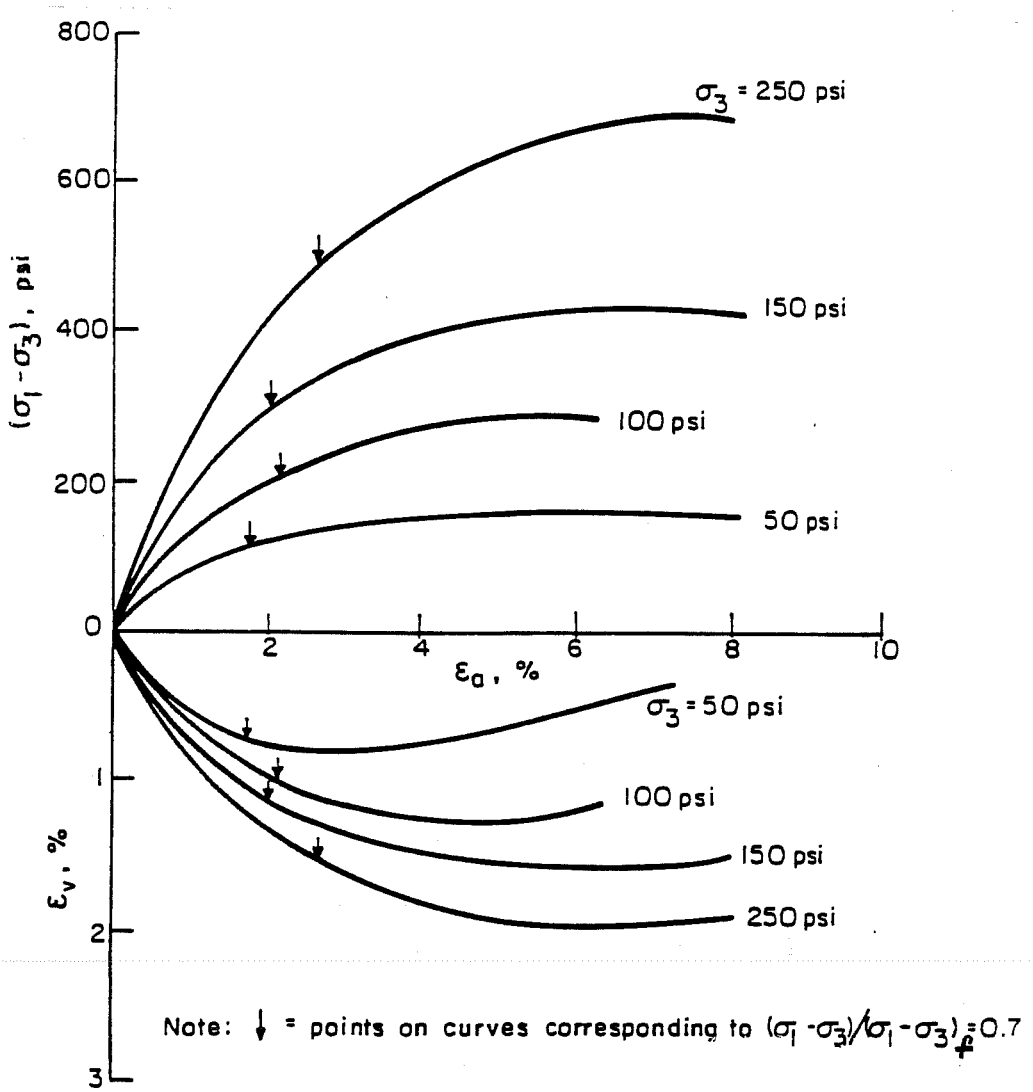

Figure 4.13 Stress-strain and volume change curves for Mica Creek Dam core material (SM-SC-1B) (Insley and Hillis, 1965)

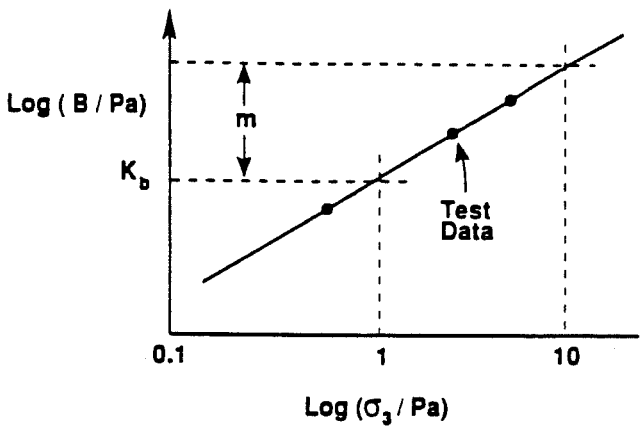

$$B = K_b P_a (\sigma_3/P_a)^m$$

Figure 4.14 Determination of K_b and m

culvert using a finite element analysis program very similar to CANDE. He modeled the soil tangent Youngs modulus with a hyperbolic model very similar to that used in the Duncan model and discussed above, and modeled the tangent bulk modulus with hyperbolic models based on both triaxial and hydrostatic test data. Selig found that when he used the bulk modulus fit to triaxial test data he underestimated measured culvert deflections; when he used the bulk modulus fit to hydrostatic test data, he overestimated deflections. This is consistent with the observed difference between the initial stiffnesses of the two bulk modulus curve-fits. Based on the results of this finite element analysis, Selig has proposed a "modified" hyperbolic model for bulk modulus based on an average between the hyperbolic model fits to triaxial test data and hydrostatic test data.[45] These modified hyperbolic constants for the bulk modulus are available for three broad types of soil at various compaction densities for drained conditions.

It is not known at this time whether a hyperbolic law or a power law provides a better fit to the tangent bulk modulus for the plane strain soil response that typically occurs in soil-structure interaction. The advantage of the power law is that the required curve-fit parameters, K_b and m, have been determined from triaxial test data for a wide variety of soils for both drained and undrained conditions.

4.3.2 Soil Stiffness Calculations in CANDE with the Duncan Soil Model. As described above, the Duncan soil model predicts the tangent Youngs modulus and bulk modulus applicable for each load step using given input parameters dependent on the type of soil, soil drainage, amount of soil compaction, and the calculated state of stress in the soil. Actually, the CANDE program calculates the "secant" values of Youngs modulus and bulk modulus within the load increment since it averages the tangent values calculated at the last converged load step, before any of the current load increment is added, and at the end of the load step, considering the full load increment added during the current load

step. However, these "secant" modulus values are approximately equal to the tangent values at the average state of stress during the load step, and therefore are referred to as "tangent" values. The code iterates during each load step until the tangent Youngs modulus values assumed during a trial solution to construct the stiffness matrix for the finite element mesh is equal (within 5%) to the modulus values calculated with Equations 4.3 and 4.4 using the stresses calculated with the finite element solution. Since the tangent bulk modulus depends only on one of the principal stresses (the minor principal stress), it is assumed to be converged if the tangent Youngs modulus is converged. In general, each soil element has a separate set of linear-elastic tangent bulk modulus and Youngs modulus values which change each load step based on the state of stress during the load step. Based on modifications to the CANDE code made during this study, each soil material can have up to five Duncan model property changes (such as changing from the undrained condition to the drained condition), where the six curve fitting parameters in Equation 4.3 and the two parameters in Equation 4.4 change, during an analysis.

Based on limitations of the Duncan model itself, large strain behavior including drop in post-peak shear stress and dilantantcy, is not modeled by the Duncan soil model. Based on a general lack of curve-fit tangent modulus parameters for soil responding during unloading and relating, only soil behavior during monotonic stress increase is modeled in CANDE. Therefore, the Duncan soil model in the CANDE code is appropriate for soils where the curve-fitting constants are known (or can be approximated based on previous testing of similar soils), where a monotonic increase in deviator stress occurs, and where compressive volumetric strains occur.

The basic soil element is a quadrilateral nonconforming element developed by Herrmann[46] which can be used as a triangle. Herrmann has shown that this element, which has eight external degrees of freedom and nine internal degrees of freedom, has nearly the same accuracy in sample beam bending and plate bending example problems as an eight node (16 degrees of freedom) conforming quadrilateral element. The computational effort for a given level of accuracy is also comparable to an eight noded conforming element. The major advantage is reduced user input effort since only corner nodes need to be input. The nonconforming element violates the displacement continuity condition along element boundaries but it is nonetheless convergent in the sense that solutions calculated with the element converge to the correct solution as the element size goes to zero. Based on this discussion, the soil elements in the CANDE finite element mesh are much more accurate than they "appear" since they only appear to be conventional four noded quadrilateral conforming elements rather than the eight noded conforming elements that they most resemble in terms of their accuracy.

4.3.3 Soil Material Properties Assumed in Model of Field-Instrumented Culverts. Figure 4.15 shows a plot of the 241 element mesh used in this study to model the instrumented arch culvert and surrounding soil under the high fill (Sections 1-1 and 2-2 in Figures 4.2) with 24 ft. of fill over the culvert crown. Figure 4.16 shows a plot of the 203 element mesh under the low fill (Section 3-3 in Figures 4.2) with 8.5 ft. of fill over the culvert crown. The soil and culvert are modeled assuming symmetry about the culvert centerline, and plane strain in the direction out of the page in Figures 4.15 and 4.16. All nodes along the vertical boundaries of the mesh are constrained against horizontal displacement. All nodes along the bottom horizontal boundary are constrained against vertical displacement. The horizontal limits of the finite element mesh extend from the line of symmetry to a

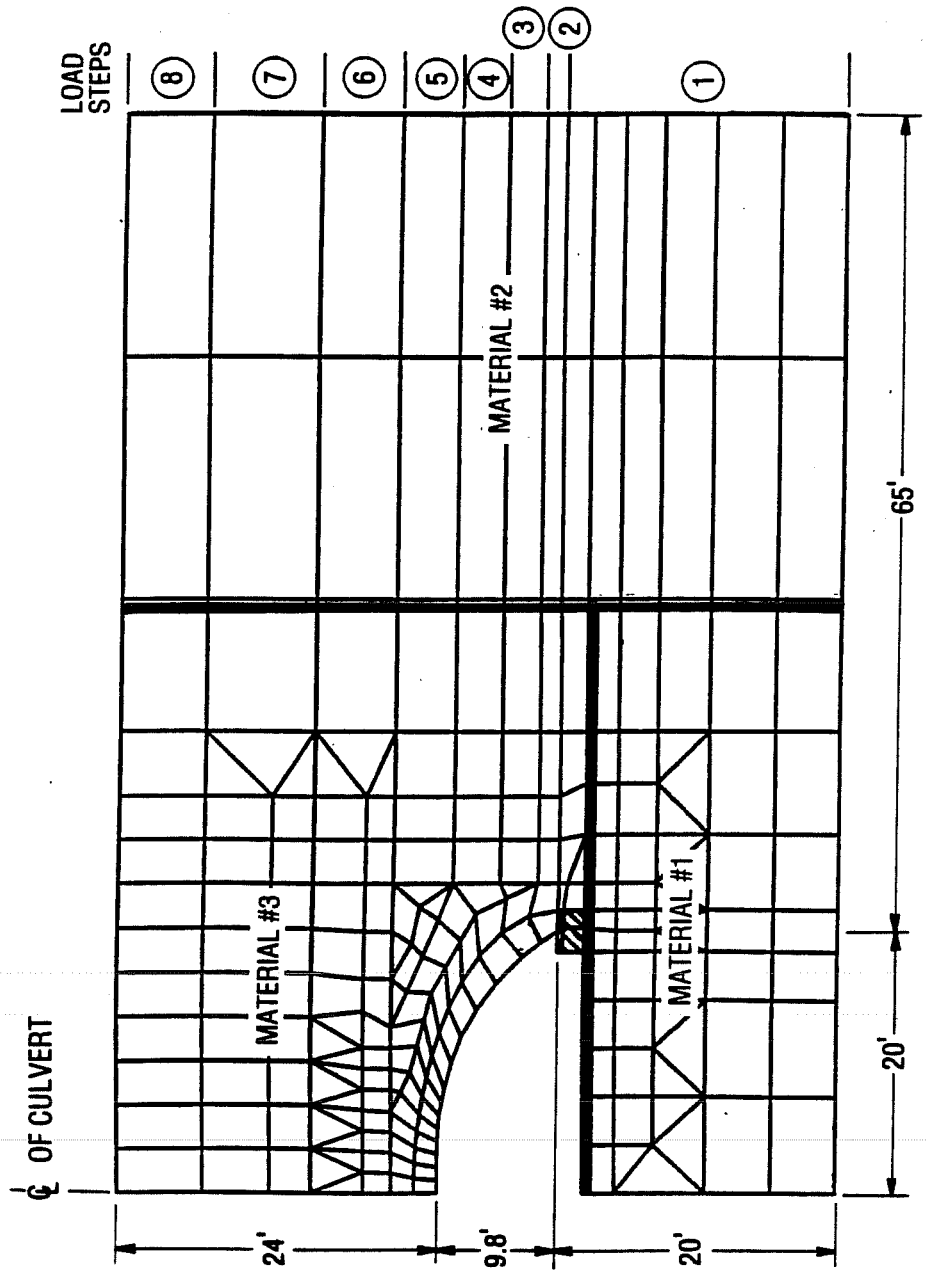

Figure 4.15 Finite element mesh of instrumented arch culvert under high fill

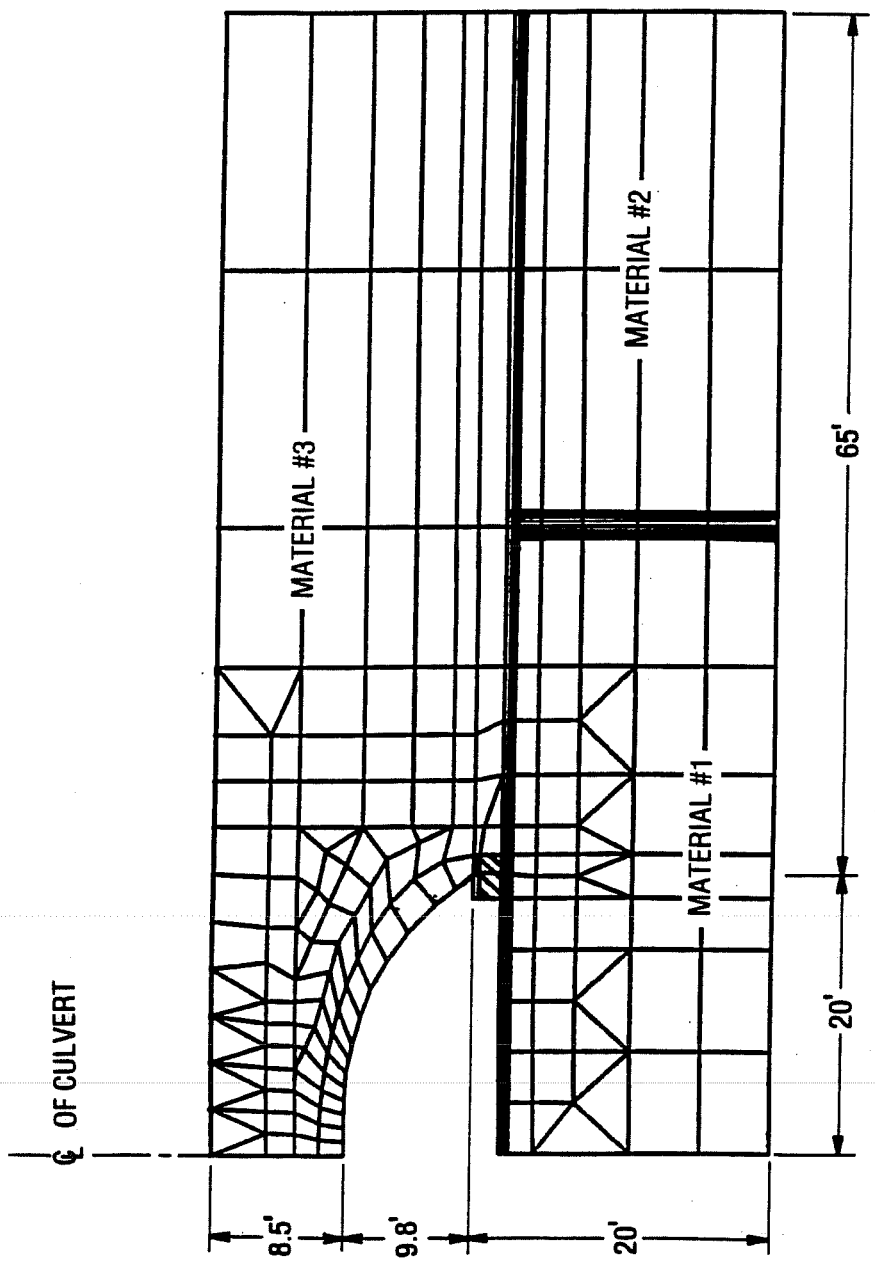

Figure 4.16 Finite element mesh of instrumented arch culvert under low fill

distance equal to four culvert spans (the half-span in the symmetric model) from the line of symmetry based on the past experience of other researchers.[12] The vertical limits extend from a hard shale layer 10 ft. below the culvert footings to the soil surface above the culvert.

The soil elements in the high fill region (Figure 4.15) are entered into the finite element mesh in eight lifts, or eight load steps, and the soil elements in the low fill region (Figure 4.16) are entered in six load steps. Figure 4.15 shows the height of the top surface of soil elements at the end of each load step. In the initial load step, all the structural elements and all the soil elements below the top of the culvert footing are entered into the analysis. In the next four load steps, the soil fill is gradually increased to a depth approximately 1 ft. below the arch crown. In the fifth load step, soil elements are added so that the fill is approximately 2 ft. above the culvert crown. During the sixth load step, soil elements are entered into the mesh up to a height of 8.5 ft. above the crown. This is the height of the soil over the culvert in the low fill region and therefore no additional soil elements are added into the finite element mesh of the low fill region. In the analysis of the culvert under the high fill, the soil height is increased from 8.5 ft. over the culvert to the final height of 24 ft. over the culvert in two additional load steps.

The soil is divided into three soil types as shown in Figures 4.15 and 4.16, a cement stabilized base below the culvert, a compacted silty clay fill over the culvert, and an existing soil beyond the limits of the earthwork of the culvert construction project. The instrumented sections of the culvert under the high fill were within the limits of an existing highway; therefore, there was existing fill from this highway above the elevation of the culvert outside the limits of the earthwork. The limits of the existing highway fill did not extend southward all the way to the instrumented section under low fill. Therefore, all soil above the low fill section was fill placed during the construction project. In both cases, preexisting soil outside the limits of the fill below the culvert footings is included in the mesh. Each soil type is discussed in detail below. Linear-elastic elements are used to model the cement stabilized soil below the culvert and the existing soil outside the limits of the excavation.

Soil #1 in Figures 4.15 and 4.16 is a compacted brown sandy clay stabilized with 3% cement. The original soil below the culvert footing was excavated to a hard shale layer at an elevation approximately 10 ft. below the culvert footings, stabilized with cement, and compacted based on the recommendation of a soils engineer. Figure 4.17 shows typical density measurements after compaction and stabilization of this soil with 3% cement. An average dry density of 128 lb/ft.^{3} and moisture content of 9% was measured, which is more than 95% of the THD TEX-113-E proctor optimum density of 133 lb/ft.^{3} as required. This material is assumed to act linearly elastically within the stress range which develops since the following approximate information indicates that this is reasonable and there is no known nonlinear material model for compacted cement stabilized clay fill. Reference 47 indicates that typical unconfined compressive strengths for cement treated material classified by the AASHTO system as A-5 (silty clays) range from 250 to 600 psi. Bjerrum has recommended that the Youngs modulus for an in-situ soil can be approximated as 200 to 400 times the unconfined compressive strength.[48] Therefore, an approximate Youngs modulus for the cement treated clay in this study is taken as 350 psi x 300 = 1 x 10^5 psi. A lower bound for comparison purposes is a Youngs modulus for a soil with a

NUCLEAR MOISTURE-DENSITY REPORT

PROJECT: Loop 1604 Highway Construction & Lookout Rd. P.O. No. 3261-482337

PROJECT NO.: SA0586-0536

CLIENT: H.B. Zachry Co.

DATE: 3-7-88

CONTRACTOR: H.B. Zachry Co.

TECHNICIAN: JR

REFERENCE: Cement Stabilized Structural Fill

TEST NO.	TEST LOCATION	SOIL TYPE	LIFT NO.	MOISTURE CONTENT (%)	DRY DENSITY (pcf)	PERCENT OF PROCTOR
1	100'N – 30'W of SE Corner of Pad	1	4	10.4	124.2	95.3
2	65'N – 15' W of SE Corner of Pad	1	4	10.6	126.1	96.8
3	65'N – 50'W of SE Corner of Pad	1	4	9.9	125.1	96.0
4	20'N – 30'W of SE Corner of Pad	1	4	10.3	125.6	96.4
5	115'N – 15'W of SE Corner of Pad	1	5	9.9	126.4	97.0
6	115'N – 50'W of SE Corner of Pad	1	5	10.2	125.5	96.3
7	20'N – 50'W of SE Corner of Pad	1	5	10.7	126.3	96.9
8	20'N – 20'W of SE Corner of Pad	1	5	9.8	127.9	98.2

REMARKS: A shot of water was given to the 4th lift after densities were completed.

PERSON NOTIFIED: Mr. Roger Mercado with H.B. Zachry Co.

	SOIL TYPE	OPTIMUM MOISTURE (%)	MAXIMUM DENSITY (pcf)	REQUIRED MOISTURE (%)	REQUIRED DENSITY (% Proctor)
1)	Brown Sandy Clay with some Gravel and 3% Cement	9.8	130.3	9.8 to 12.8	95.0
2)					
3)					

PROCTOR SERIES: THD. TEX-113-E

TROXLER NO.: 26

CONFORMING TEST NOS.: 1-8

NON-CONFORMING TEST NOS.: ----

ASSIGNMENT NO.: 5-130884

PAGE 3 OF 3

Figure 4.17 Typical soil density testing report for cement stabilized clay fill.

"hard" consistency (corresponding to an unconfined compression strength of approximately 60 psi[49]), which is approximately 2 x 10^4 psi based on the assumed 60 psi unconfined compression strength multiplied by 300. An upper bound is the Youngs modulus for a weak rock, which has been estimated as 1 x 10^6 psi.[49] The assumed 1 x 10^5 psi value lies between these two bounds and is therefore reasonable. Reference 47 also reports that cement treated soil can be assumed to have a modulus of rupture equal to approximately 20% of the compressive strength. Therefore, the material probably has a substantial tensile strength (50 psi or more) and it can support significant tensile and the compressive strains as is impled by the use of a linear-elastic material model. A 0.25 value of Poissons ratio is assumed as an "average" between 0.17 for rock/concrete and 0.35 for unstabilized soil.

Material #2 in Figures 4.15 and 4.16 is the pre-existing soil material outside the limits of the excavation. Since this soil is not in the area near the culvert and therefore is not thought to have a large influence on the culvert response, it is modeled with simple linear-elastic elements. Based on available references[12,17] for compacted soil, a Youngs modulus of 3,000 psi and a Poissons ratio of .35 are used in these elements to approximately represent the soil response. In a comparison study, the culvert strain and the soil pressures near the culvert calculated in the high fill mesh, modeling the pre-existing soil elements with the Duncan model using parameters corresponding to a drained silty clay, were only slightly different (less than 5%) than the corresponding values calculated using linear-elastic elements for the pre-existing soil.

Material #3 in Figures 4.15 and 4.16 is the compacted silty tan clay backfill around the arch. The soil backfill was dumped in approximately 1 ft. lifts and compacted to the typical dry densities and water contents shown in Figures 4.18. The soil within 3 ft. of the culvert was tamped with hand-held equipment. The average measured dry density was approximately 111 lb/ft^3 and the average measured moisture content was approximately 15%. The corresponding total unit weight is 128 pcf. This is the only soil material loaded with self weight during the analysis, because it is assumed that all the other soil material had consolidated under self weight prior to placement of the culvert. Duncan soil constants calculated using curve-fits to triaxial tests on silty clays compacted to nearly the same dry density and moisture content as those measured in the BEBO culvert backfill are used in the CANDE program to model the backfill. The constants are published in Reference 30. However, the manner in which the stiffness and the compaction process were modeled requires some detailed discussion.

The stiffness of this soil changes significantly during the time the BEBO culvert was monitored in this study due to changing soil drainage conditions. This complicates the choice of appropriate Duncan soil constants and raises the issue of what approach the CANDE program should use to model soil-structure interaction during the time the soil consolidates. Immediately after it has been compacted, the clay backfill can be idealized as an undrained soil because of its low permeability. Based on report values in Reference 30, compacted silty clays are approximately 85% saturated. At this saturation level, the soil is quite stiff in terms of the ratio of total stress to total strain because the water-filled pores, which absorb much of the stress prior to drainage, are incompressible. As drainage occurs, the soil stiffness reduces significantly because the total stress is absorbed by the soil matrix. Figure 4.19 shows plots of the stress-strain characteristics calculated with the average of the Duncan model soil constants reported in Reference 30 for unconsolidated-undrained (U-U triaxial tests and consolidated-drained (C-D) triaxial tests on silty

NUCLEAR MOISTURE–DENSITY REPORT

PROJECT:	Loop 1604 Highway Construction & Lookout Rd. P.O. No. 3261–482337	PROJECT NO.:	SA0586–0536
CLIENT:	H.B. Zachry Co.	DATE:	4/1/88
CONTRACTOR:	H.B. Zachry Co.	TECHNICIAN:	SW
REFERENCE:	Backfill Operations – Low Profile Arch Culvert	A.S. 7:00 AM D.S. 1:30 PM	

TEST NO.	TEST LOCATION	SOIL TYPE		MOISTURE CONTENT (%)	DRY DENSITY (pcf)	PERCENT OF PROCTOR
	---- APPROXIMATELY 4–FEET BELOW CROWN ----					
1	115'S – 30'E of Centerline	1		14.9	113.2	101.7
2	50'S – 20'W of Centerline	1		15.0	114.8	103.2
3	114'N – 35'E of Centerline	1		14.6	118.8	106.7
	---- APPROXIMATELY 2.5–FEET BELOW CROWN ----					
4	104'N – 16'E of Centerline	1		14.4	113.3	101.8
	----APPROXIMATELY 2–FEET BELOW CROWN ----					
5	168'N – 25'E of Centerline	1	12"	15.2	110.7	99.5
	---- APPROXIMATELY 1–FOOT BELOW CROWN ----					
6	90'S – 14'E of Centerline	1	12"	15.3	108.2	97.2
	---- APPROXIMATELY 2–FEET ABOVE CROWN ----					
7	224'N on Centerline	1	12"	14.2	108.7	97.7

Assignment No. 5–131650

Page 3 of 4

Figure 4.18 Typical soil density testing report for soil fill over culvert

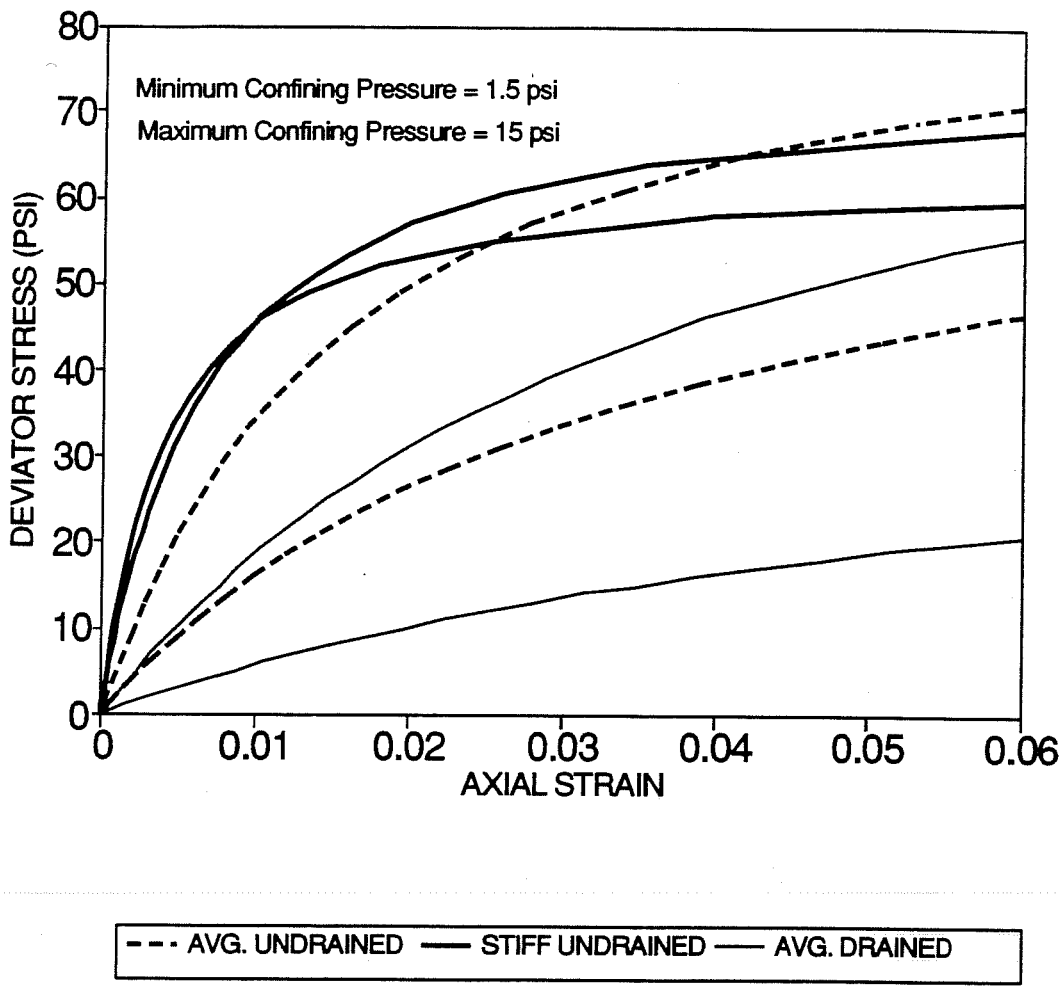

Figure 4.19 Comparison of assumed stress-strain histories considered for silty clay backfill

iclays with similar dry density and moisture content as that measured in the backfill. Figure 4.19 also shows the stress-strain history plotted using the soil constants from the stiffest undrained clay reported n Reference 30 with similar dry density and moisture content as the backfill because of the relatively wide disparity in the reported constants for U-U tests. The initial tangent Youngs modulus and confining pressure is also shown next to each curve for reference. Figure 4.20 shows all the data reported in Reference 30 for silty clays. The data used to get the average soil constants used to plot the stress-strain histories in Figure 4.19 are marked with an asterisk. Figure 4.19 shows that there is a significant difference between drained and undrained stress-strain relationships for compacted silty clay. The confining stresses of 1.5 psi and 15 psi are bounds on the minor principal stress, or confining stress, used in the CANDE analyses to determine the tangent Youngs modulus in the soil near the culvert.

Consideration of the change in soil stiffness that occurs during consolidation, or drainage, can be implemented in a series of steps which include intermediate stress-strain curves for the soil which fit between the curves for the two extremes of drained and undrained conditions. The change in the state of strain and stress in the soil and structure occurring during each soil stiffness change can be calculated with the finite element method using a two-step relaxation method similar to that described in Reference 50. In this method the amount of stress relaxation which would occur if there were no strain during the stiffness reduction accompanying consolidation is calculated and subtracted away from the element stresses in the first step. This causes the state of stress and strain to satisfy compatibility conditions and the new soil stress-strain relationship; but, the new state of stress is not in equilibrium with applied loads. Equilibrium is restored in the second step by applying nodal forces to the finite element mesh which are statically equivalent to the stresses subtracted away in the first step. This step restores equilibrium and causes the displacement that occurs during consolidation. The relaxation stresses in the first step must include relaxation in both principal stresses in the proper ratio so that neither the volumetric strain nor axial strain the element change. This is complicated by the fact that the change, or relaxation in the minor principal stress must be chosen so that the volumetric strain remains unchanged as the bulk modulus is reduced, and the axial strain remains unchanged as the Youngs modulus is reduced. Both strains are affected to a very significant degree of the confining stress, so considerable trial and error can be required.

This discussion in included to show that consolidation can be included in the finite element analysis, if the above approach is programmed into the CANDE code. This additional complexity in the analytical approach is merited if it causes the prediction of the state of stress in the soil and structure to improve significantly at a given time of interest. However, it is thought that the response of the backfill around the culvert can be modeled relatively well by simply assuming undrained soil properties throughout the analysis. This approach will be relatively accurate if: 1) the post-consolidation stress and strain in the soil can be predicted well without modeling the initial undrained state of the soil and the transition of the soil from undrained to drained; and 2) the undrained conditions do not have a significant effect on the structural response prior to dissipation. The validity of the first of these statements was investigated with a parameter study which is described below. The validity of the second statement is dependent on what constitutes a "significant" effect. Here it is probable that an approximate model of the soil stiffness during the time the soil is undrained is acceptable because the CANDE code cannot model other simultaneously occurring factors (particularly compaction) very well. For example, even

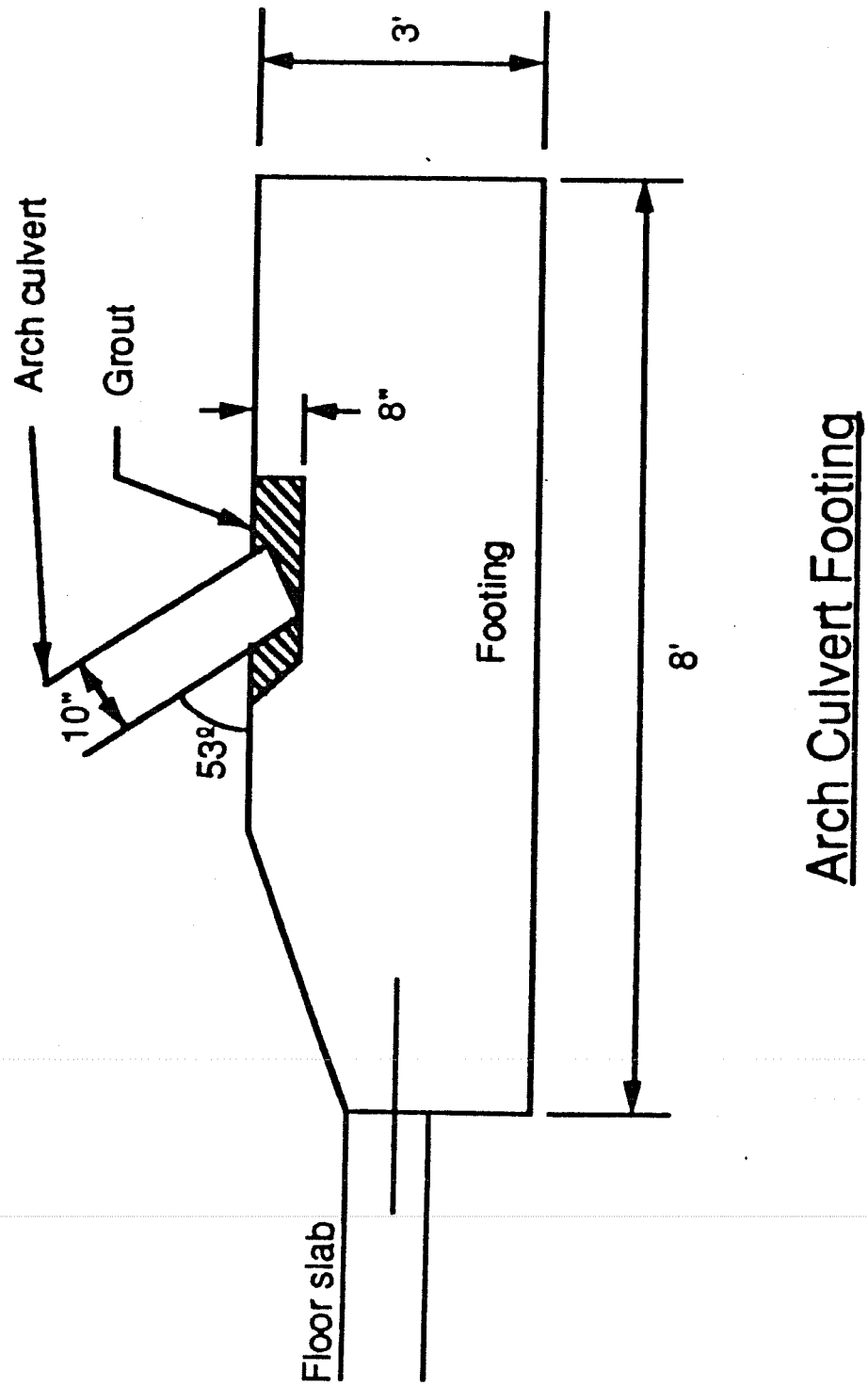

Figure 4.20 Arch culvert footing

if a very accurate model of the undrained soil stiffness was used, this would be overshadowed by inaccuracy in the modeling of compaction-induced inelastic strains which occur during the time the soil is undrained. Very few previous researchers have explicitly discussed the effect of undrained soil conditions on soil-structure interaction. In one exception,[70] it is explicitly stated that structural fill and embankment fill are generally well drained; therefore, the drained soil condition can bemused for analysis.

In an effort to quantify the undrained soil conditions immediately after compaction on the final calculated soil and culvert response, a "parameter" study was conducted using the CANDE program which investigated the effect of the assumed backfill stiffness properties on soil-structure interaction between the BEBO culvert and surrounding backfill in the high fill region. In the first analysis, the Duncan model soil constants for the drained silty clay in Figure 4.19 were used throughout the analysis (for the entire 2.5 year period). In a second comparable analysis, the soil constants for the "average" undrained silty clay in Figure 4.19 were used until the fill height in the analysis was 10 ft. over the culvert (the height of Figure 3.1 where the pore pressures seemed to dissipate) and then the constants for the drained silty clay in Figures 4.19 were used thereafter. Finally, a third analysis was performed similar to the second, except that the Duncan model soil constants corresponding to the "stiff" undrained silty clay in Figure 4.19 were used until the fill height was approximately 10 ft. over the culvert and then the constants for the drained silty clay were used thereafter. These three approaches represent approximate bounds on the actual soil behavior, since the first analysis ignores the relatively undrained condition when the soil stiffness is high, and therefore underestimates the state of stress in the structure and surrounding soil (particularly prior to consolidation). The second two analyses ignore the consolidation process, so that stress relaxation and strain occurring during consolidation is not modeled. Therefore, they probably overestimate the total post-consolidation stress in the soil and culvert.

In the parameter study there was no more than 12% maximum difference between any of the calculated strains, soil pressures on the culvert, or culvert deflections. The results of this parameter study, and the good comparison of the results obtained with the first analysis using only the drained soil stiffness and measured data reported in Chapter 5, indicate that the assumption of drained conditions throughout the analysis is a good simplifying assumption for the case of the BEBO culvert and the surrounding backfill. Therefore, the Duncan model soil stiffness parameters for a drained silty clay, which produce the stress-strain relationship shown in Figure 4.19, were used for the analyses of the BEBO culvert.

The final point requiring some detailed discussion is the manner in which compaction of the soil backfill near the culvert was modeled. The compaction process involves inelastic strains of the soil; therefore, it cannot be modeled explicitly using the Duncan soil model. The soil stresses occurring during the compaction process can be modeled approximately by imposing a surface pressure to each soil layer as it is added to the finite element mesh.[51] Equilibrium is restored during the next load step by applying an equal and opposite pressure to the same nodes. This causes the top layer of soil elements to be in compression during each load step that compaction is modeled. The incremental elastic stress and strain occurring in each soil layer during this load step are summed into the total element stress and strain; therefore, they remain in the element until the last load step when compaction pressure is modeled. After this load step, the surface pressure is removed and there is no corresponding downward pressure on the

overlying soil layer. Therefore, the entire portion of the mesh which has been subjected to the compaction pressure is subjected to an equal "tensile" pressure. It is important to note that this tensile pressure does not put the soil into tension, because compaction pressures are usually not modeled all the way up to the final fill height; therefore, a layer of soil elements is added to the mesh during the load step when the final compaction pressure is removed. The removal of the final compaction pressure models the dissipation of compaction-induced pore pressures. If a layer of soil elements in the mesh is stiffer when the final compaction surface pressure is removed than it was during the load step when the compaction surface pressure was applied to it, then some of the compaction-induced stress and strain will remain "locked-in" the layer of soil.

This method is very approximate for several reasons. First, the stress-strain relationships used in the CANDE analysis are valid models of the post-compaction soil response, but they do not model the inelastic strains which occur during compaction. Therefore, the soil-structure interaction occurring during the compaction process is not modeled well in general. Secondly, the strains caused in this method by the simulated compaction pressure largely disappear (although some may remain "locked-in" as described above) when the final compaction pressure is removed. Therefore, the structure is allowed to rebound from any significant compaction-induced displacement when the final surface compaction pressure is removed. However, the actual inelastic strains occurring during compaction do not disappear when the pore-water pressures dissipate. In an attempt to model this type of behavior for a light corrugated metal drainage pipe, Duncan and Jeyapalan[21] allowed the elastic soil strains caused by compaction surface pressures applied at fill heights below the pipe crown to remain in their finite element analysis after the stresses caused by these pressures were removed. This caused some improvement in their ability to calculate pipe displacements close to those measured. In the case of the BEBO culvert, the effect of these inaccuracies is limited by a relatively large ratio of the structure to soil stiffness, since the culvert is reinforced concrete rather than corrugated metal. Thirdly, the correct magnitude for the surface pressure which best models the compaction process is difficult to estimate.

However, the method outlined above is thought to be worthwhile in spite of its shortcomings because it does model the temporary stresses imposed on the culvert by compaction-induced pore water pressures. Modeling the compaction process in a more accurate, explicit manner is extremely difficult and is a separate research topic in itself. Therefore, in this analysis a temporary 5 psi surface pressure is used to model the soil-structure interaction occurring during compaction. The magnitude of this pressure is chosen to match the observed 5 psi difference between measured pressures and the calculated overburden pressure shown in Figure 3.1. This also matches the compaction pressures estimated by other researchers based on the weight of compaction equipment and measured soil pressures against culverts.[21, 51] Compaction surface pressures are only applied during load steps two through six, since the measured soil pressures against the culvert indicate that the pore water pressures dissipated when the fill height was approximately equal to the height at load step six in the analysis.

4.4 Interface Constraint Elements

In the CANDE finite element mesh, adjoining soil and structural elements are typically not linked directly together in the global system of equations. Rather, the soil and structure elements are defined with unique sets of nodes and the adjoining soil and structure nodes are connected to a common interface

element. The interface elements have three nodes, each with two degrees of freedom, including the adjoining soil and structure nodes (the "soil" node and the "structure" node) and an additional "free" node (the "interface force" node) which is only connected to the interface element. The free node in the interface element does not represent any position in the mesh, it is only included so that two additional degrees of freedom can be added to the solution scheme to represent the unknown normal and shear forces between the soil and structure nodes. The interface element allows full bonding, frictional sliding, separation, and rebonding between the adjoining soil and structure nodes according to criteria based on the normal and shear force and relative displacement between the adjoining nodes.

The interface element is developed based on the method of constraints. Interface elements can also be developed using tangential and normal springs to model the tangential and normal force and relative displacement between adjoining spring and structure nodes.[40] However, the method of constraints does not involve the sometimes difficult process of choosing a normal spring stiffness, which precludes significant penetration without requiring large word lengths to store very small calculated spring displacements under compressive loading. The theoretical development of the interface element stiffness matrix using the method of virtual work is shown in Reference 17. In the development of the interface element, the relative displacements between the soil and structure nodes in the local coordinate system (normal and tangential to the soil-structure interface) are assumed to be controlled by known constraint equations. The general principle of virtual work is used, which includes the work done on constraint forces by virtual displacements not compatible with constraints, and both the interface constraint equations and the interface constraint forces (the shear and normal force across the interface) are included in the set of equilibrium equations which make up the global system of equations for the finite element mesh.

The corresponding element system of equations which is developed for the interface element is shown in Equation 4.5 It is in the conventional form of a loads vector, a displacement vector, and a stiffness matrix relating the two vectors to each other. The first four rows, or equations, cause the incremental interface forces to be in equilibrium with the X and Y direction incremental forces on the adjoining soil and structure nodes in the interface element. The last two rows cause the incremental relative normal and tangential displacement between the adjoining soil and structure nodes to be compatible with the soil and structure node incremental displacements. Therefore, equilibrium and compatibility conditions for the interface element are satisfied. The incremental interface forces and the relative displacements within the interface element must jointly satisfy the conditions of admissible interface "states" in a manner similar to the way in which the stress and strain of a nonlinear elastic element must jointly satisfy the stress-strain relationship. These states are discussed in the next paragraph. Constraints between the adjoining soil and structure relative displacements are enforced by setting values for a_n and a_s. Known interface forces are enforced in the same manner as known displacements are normally enforced in the finite element method system of equations. Thus the known interface forces are added into the appropriate locations in the loads vector, and the constraints equations in the last two rows of Equation 4.5 are eliminated from the finite element system of equations. This implies that whenever the interface forces are known, the adjoining soil and structure nodes are free to displace separately from each other.

$$\begin{bmatrix} 0 & 0 & 0 & 0 & -\cos(a) & \sin(a) & u_s & Ps_x \\ 0 & 0 & 0 & 0 & -\sin(a) & -\cos(a) & v_s & Ps_y \\ 0 & 0 & 0 & 0 & \cos(a) & -\sin(a) & u_t & Pt_x \\ 0 & 0 & 0 & 0 & \sin(a) & \cos(a) & v_t & Pt_y \\ -\cos(a) & -\sin(a) & \cos(a) & \sin(a) & 0 & 0 & Fn & a_n \\ \sin(a) & -\cos(a) & -\sin(a) & \cos(a) & 0 & 0 & Fs & a_s \end{bmatrix} \qquad (4.5)$$

where

a	=	angle of interface surface normal with respect to X axis,
u_s	=	incremental X displacement of structure node,
v_s	=	incremental Y displacement of structure node,
u_t	=	incremental X displacement of soil node,
v_t	=	incremental Y displacement of soil node,
Ps_x	=	incremental X direction force on structure node,
Ps_y	=	incremental Y direction force on structure node,
Pt_x	=	incremental X direction force on soil node,
Pt_y	=	incremental Y direction force on soil node,
Fn	=	incremental normal interface force (positive for tension),
Fs	=	incremental shear interface force (positive when 90°) counterclockwise from interface surface outward normal,
a_n	=	incremental relative normal displacement between soil and structure nodes, and
a_s	=	incremental relative shear displacement between soil and structure nodes.

The permissible states which can exist in the interface element are: (1) complete bond between the adjoining soil and structure nodes; (2) slip between the adjoining nodes along the soil-structure interface; and (3) separation between the adjoining nodes. Initially complete bond is assumed. When this state is assumed, a_n and a_s, in Equation 4.5 are set equal to zero so that no relative displacement between the adjoining soil and structure nodes is calculated. The incremental interface forces Fs and Fn are calculated in the solution of the system of equations for the finite element mesh and added to the total from previous load steps. Complete bond is the only admissible state until either the calculated total normal interface force exceeds the input tensile adhesion force or the calculated total shear force along the interface exceeds the product of the total normal interface force and the input friction coefficient along the surface. After each trial solution of the system of equations for the finite element mesh, the current calculated total shear and normal forces are checked to see if the state of complete fixity is still the valid state. If so, then the trial solution is considered valid.

If the total normal interface force exceeds the input adhesion value, the state of separation is valid. The basic conditions of this state are that no net force exists between the adjoining soil and structure nodes and that these nodes are free to displace independent of each other. These conditions are satisfied by setting Fs and Fn in Equation 4.5 equal and opposite to the total shear and normal interface forces from the previous load steps. Because Fs and Fn are treated as known displacements in the finite

element solution, they are added to the loads on the adjoining soil and structure nodes in the loads vector, which causes the net total interface forces between the adjoining soil and structure nodes to become zero, and the constraint equations between the adjoining soil and structures nodes in Equation 4.5 are eliminated. Separation remains the admissible state until either the calculated incremental normal relative displacement between the adjoining soil and structure nodes becomes negative indicating overlap, or until penetration of one element (either the soil or structure element) into the other element. After each trial solution of the system of equations for the finite element mesh the current calculated total relative normal displacement across the interface element is checked to see if the state of separation is still the valid state. If so, then the trial solution is considered valid. If not, then the state of fixity is assumed and a_n and a_s in Equation 4.5 are set equal to any values which will cause the total soil node and structure node displacements to be flush with the interface surface.

If the calculated total shear interface force exceeds the production of the total normal interface force multiplied by the input surface friction constant (S), the state of sliding becomes valid. The basic conditions of this state are that the relative normal displacement between the adjoining soil and structure nodes is zero, the adjoining soil and structure nodes can slide along the interface independently of each other, and the total tangential force on the adjoining soil and structure nodes is equal to S. These conditions are satisfied by setting Fs (which is an incremental value) in Equation 4.5 equal to the difference between S and the sum of the incremental interface shear forces from all previous load steps. Because Fs is treated as a known displacement in the finite element solution, it is added to the loads on the adjoining soil and structure nodes in the loads vector, which causes the net total interface shear force on the adjoining soil and structure nodes to equal the shear force during sliding, and the constraint equation in Equation 4.5 between the adjoining soil and structure nodes relative tangential displacement is eliminated. Sliding remains the admissible state until either the calculated total normal interface force exceeds the input tensile adhesion force, or the calculated incremental shear relative displacement between the adjoining soil and structure nodes changes sign, indicating that assumed interface shear force S is overcome by forces resisting sliding. After each trial solution of the system of equations for the finite element mesh the current calculated total relative normal displacement across the interface element is checked to see if the state of separation is still the valid state. If so, then the trial solution is considered valid. If not, then the state of separation or fixity is assumed based on the calculated response.

Convergence of each interface element is required for each load step in the same way convergence is required for each soil and structure element. Convergence requires that the calculated relative displacements between the soil and structure nodes and the calculated total normal and shear interface forces are compatible with the same state which was assumed to construct the interface element stiffness matrix and loads vector in Equation 4.5. All interface elements must converge before the load step can reach a converged condition. However, a maximum value of iterations (10) per load step is also input by the user so that an infinite number of iterations cannot occur.

The soil-structure surface of the BEBO culvert is modeled in the CANDE code with interface elements between each of the sixteen structure nodes and the corresponding soil nodes. An input friction coefficient of 0.3 is used for these interface elements. This coefficient is slightly less than the 0.35 values recommended in basic soil mechanics references[21] for calculating the sliding resistance of a concrete retaining wall on silt, and for calculating the downward vertical force along the vertical faces of a

retaining wall with granular backfill from the lateral soil force. In the latter case, the frictional constant is usually expressed as a 20° angle of "wall friction." Since the backfill contains some clay and therefore has a somewhat lower drained angle of friction than granular materials, the value of 0.3 ranter than 0.35 is used. However, the results or the finite element analysis are not sensitive to small changes of 0.05 to 0.1 in the friction coefficient. One shortcoming of the interface elements in the CANDE code is that a slip resistance based on the cohesion of clay soils cannot be considered. Since a drained silty clay has a relatively high angle of friction (approximately 30°) and no slip is calculated by the code at low fill heights while the soil is undrained, this is probably not an issue. Zero adhesion, or tensile strength, is input between the soil and structures nodes along the culvert-soil interface.

Interface elements are also used to attach the springline of the arch culvert to the footing and to attach the concrete floor to the footing for the culvert section under high fill. The interface elements simulate bearing forces in the footing and a pin connection between the footing and floor slab. It is assumed that the flexibility of the long slender floor slab prevents any significant moment from being transferred through the splice between the reinforcing steel in the footing and the floor slab. The input tensile adhesive strengths are chosen to ensure that the connected structural components do not separate. Figure 4.20 shows a drawing of the culvert to footing connection and footing to floor slab connections. The precast arch culvert was set into the 18-in. wide x 10-in. deep recess in the footing, and grout with a 2,500 psi 28-day cube compression strength was then placed in the recess around the arch. This is modeled as shown in Figure 4.21. Interface forces are allowed to develop between the footing and the arch at the interface elements at the top and bottom of the 8-in. deep recess into the footing. A friction coefficient equal to 1.0 is assumed as suggested in the ACI building code for concrete placed against hardened concrete. These forces can exert a couple about the end of the arch and therefore induce an end moment in the arch. The amount of moment that can develop is limited by yielding in the steel in the arch below the top level of the recess and the amount of rotation of the footing into the underlying soil. The 4-in. x 4-in. welded wire fabric, which is the tensile steel in the springline of the culvert, can be considered developed below the embedment of the arch in the footing recess since more than two perpendicular wires frame into the tension steel at an elevation below the top of the footing. Grout failure can also influence the end moment but the grout is highly confined by the surrounding concrete footing and 34-ft. of overlying fill. Finally, the rotation of the footing is directly modeled by the analysis since there are three nodes across the bottom of the footing, and the soil elements below the footing and the soil elements can deform in a nonlinear strain field (similar to conforming 8 noded elements). It is therefore reasonable to expect the CANDE model to calculate the actual end moment in the culvert within the accuracy of the assumed soil and structural stiffness models. A moment of 22,000 lb.-in./in. was calculated at the top of the footing in the arch culvert under the high fill arch. This is approximately one-half the calculated maximum positive moment at midspan for this culvert.

4.5 Creep and Shrinkage Strain Prediction in the Concrete Material Model

The measured long-term deflectios and strains of the culvert indicate that creep and shrinkage are strongly affecting the response. Therefore, the reinforced concrete model in the CANDE code has been expanded during this study to model the effects of these two phenomena. Creep and shrinkage comprise

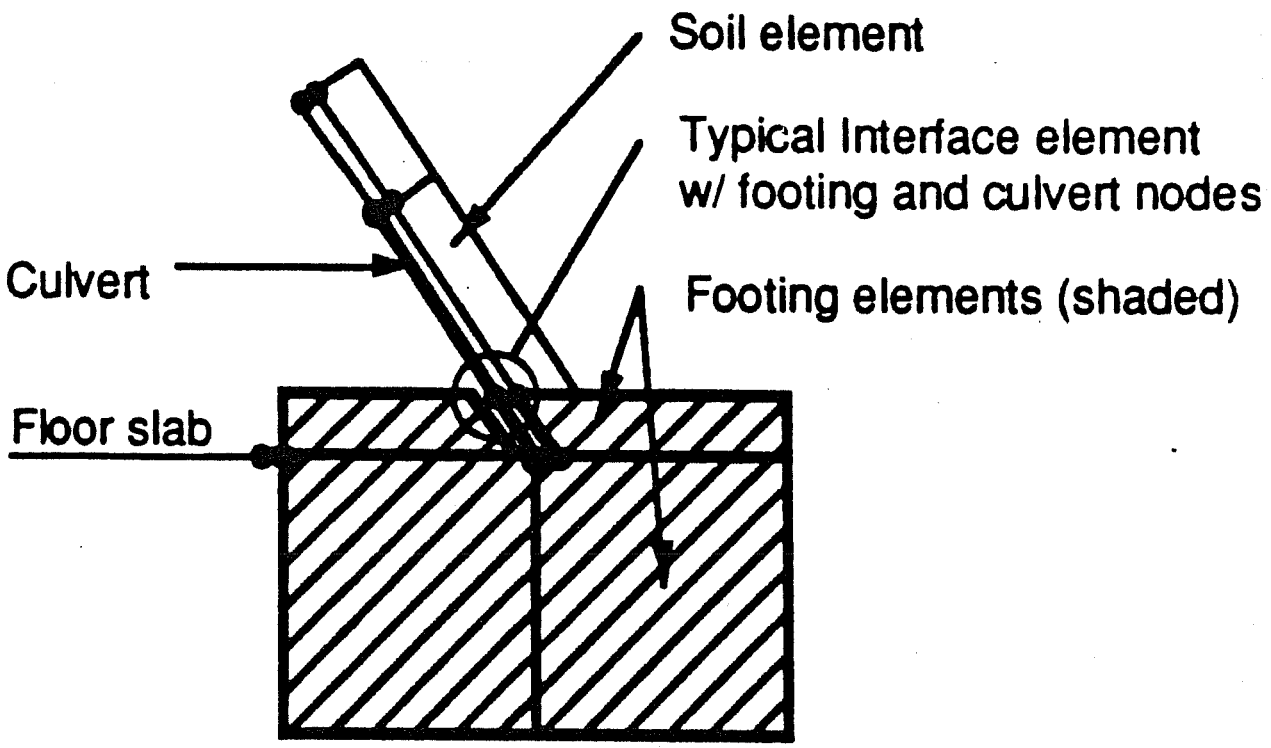

FEM Model of
Arch Culvert Footing

Figure 4.21 FEM Model of Arch Culvert Footing.

the stress dependent and stress independent portions, respectively, of time dependent concrete response which occurs in the absence of temperature and stress change. Creep acts to increase or enhance the initial elastic strain, whereas shrinkage is always compressive. These two types of inelastic strain, which can be several times greater than the elastic strain occurring immediately after stress is applied, cause a gradual change in the deflections of a concrete member, a redistribution of stress between the concrete portion and the steel portion of the reinforced concrete cross section, and a redistribution of internal loads (moments and thrusts) in indeterminate concrete structures. The deleterious effects of creep and shrinkage are typically not calculated explicitly in practical design situations. They are accounted for where necessary from a practical point of view with empirical factors on the elastic strains and deflections calculated with an elastic analysis, with minimum requirements on reinforcing steel and the spacing of control and expansion joints. The stress redistribution caused by creep and shrinkage is roughly accounted for with other more complex variables in the strength reduction factors or other safety factors used in the design.

However, this detailed study, which is intended to predict measured long-term reinforced concrete response well, must explicitly consider creep and shrinkage. Creep is thought to occur as the bonds which hold chains of molecules in the hardened concrete paste fail under stress and rebond. Shrinkage is thought to occur because of the increase of solid surface tension and capillary tension due to drying.[52] Although the mechanisms causing creep and shrinkage are not understood very well, an empirical understanding of the factors which influence creep and shrinkage has been developed based on available test data. These factors include concrete composition, degree of hydration, pore humidity, pore water content, temperature, and age of first loading (creep). The pore humidity and water content are influenced by the size of the member, the number of surfaces exposed to drying, the ambient relative humidity, the curing process, and the amount of cracking. The creep strain is also heavily dependent on the amount of elastic strain. The available prediction methods for creep and shrinkage strains are curve-fits of differing degrees of complexity through various sets of creep and shrinkage data. Based on an inspection of the creep prediction methods, creep is influenced primarily by elastic strain, age of first loading, effective member size, relative humidity, curing time, concrete composition, and concrete compressive strength. The effective member size is the ratio of the volume to the surface area over which drying occurs. In the simpler prediction methods, creep is assumed directly proportional to the elastic strain. Shrinkage is most affected by effective member size, relative humidity, curing time, and concrete composition. Finally, creep and shrinkage strain both increase nonlinearly with time after loading or curing, where most of the strain increase occurs relatively early in time.

Creep strain is usually characterized in terms of a creep coefficient, which is the creep strain per unit of constant elastic strain occurring between the time of loading and a given time of interest. The product of the creep coefficient and the total elastic strain is equal to the total creep strain. Figure 4.22 shows typical graphs of the creep coefficient versus time for several loading ages. These curves qualitatively show the importance of the age of loading on the creep coefficient (and thus on the creep strain) and show the characteristic decreasing slope of the creep curves as the elapsed time since loading increases. The creep coefficient is also a function of the other previously discussed variables which influence creep.

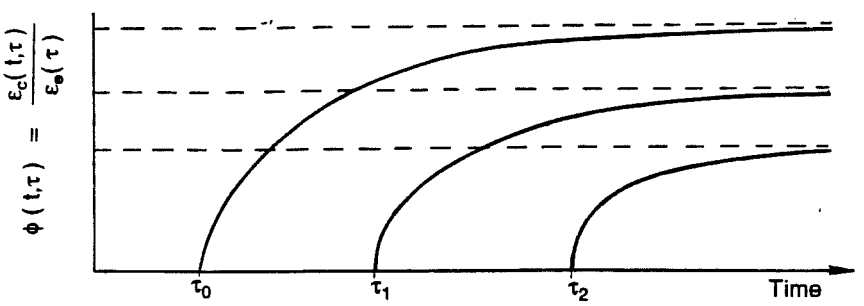

Effect of age at first loading on creep

φ (t, τ) = creep coefficient at time t for load applied at time τ

ε_c (t, τ) = creep strain = φ (t, τ) ε_e (τ)

ε_e (τ) = elastic strain caused by load applied at time τ

τ = age of first loading

ε_t (t, τ) =Total strain = ε_e (τ) (φ (t, τ) + 1)

Figure 4.22 Creep Coefficient

4.5.1 Available Creep Prediction Models. There are at least seven different methods in use in design codes around the world or recommended in codes of practice for predicting creep and shrinkage as well as variations on these methods and a number of lesser known methods. All the methods are based on curve-fits of varying degrees of complexity to various sets of creep and shrinkage data. These methods often give widely differing results for the same conditions and when compared to any given set of data, often none of the available methods predict observed creep and shrinkage well.[56] Therefore, some thought is required to choose the "best" prediction model for this study and the calculated creep and shrinkage must be considered as approximate regardless which method is chosen. Figures 4.23a and 4.23b illustrate the variability in the complexity creep prediction methods. Figure 4.23a shows the creep prediction method formulated by Branson and recommended by ACI committee 209.[53] ACI 209 method may be the most accurate "simple" creep and shrinkage prediction method available.[55] The product of the last three multiplication factors in Figure 4.23a, which are dependent on the concrete slump, entrained air, and fine aggregate to total aggregate ratio, respectively, is often assumed to be 1.0. This assumption simplifies the ACI 209 creep prediction method further. Figure 4.23b shows the creep prediction method formulated by Bazant and Panula (the BP method).[54] This method, which is based on a computer generated curve-fit to eighty different sets of creep and shrinkage data, is one of the most complex creep prediction methods. The creep compliance function J(t, t′), which includes both the elastic and creep strain, is used in the BP method rather than a creep coefficient in order to avoid the problem of designating the time at which "elastic" strain stops occurring and creep strain begins occurring. However, the creep compliance function is often converted into an equivalent creep coefficient using the static Youngs modulus as is shown in Figure 4.23b for convenience, since most creep analysis is based on a separate elastic strain and creep strain. The final shrinkage strain and shrinkage square half-time terms in Figure 4.23b are defined in Figure 4.28b in the next section where the BP shrinkage prediction method is presented. Factors within the BP method can also be used to account for temperature effects and pulsating loads, but these are not included in Figure 4.23b since these factors are not considered relevant to this study.

The large difference in complexity between the simplified ACI 209 method and the more complex BP method is due to a number of factors. A primary factor is that simple creep prediction models implicitly assume that the time shape of the "basic" creep curve and "drying" creep curve are the same. This is true because the effects of humidity and member size, which only affect drying creep, are introduced into the creep prediction method by multiplication factors which scale the total creep curve vertically.[54] Basic creep is the creep that occurs in a sealed specimen (no moisture loss) and drying creep is the difference between the basic creep (i.e. a sealed specimen) and the observed larger amount of creep in an identical specimen exposed to drying. The two types of creep can be considered more accurately by having separate terms which add and can therefore have independent time shapes determined by the specific variables affecting each. This, of course, adds considerable complexity. The more complex methods also make the choice to use more curve-fitting variables so as to explicitly consider more of the numerous factors known to affect creep.

There is sometimes, but not always, a difference in the accuracy between simplified and complex creep and shrinkage prediction methods and large sets of test data. In their comparison of three widely used creep prediction methods using approximately 30 different sets of data, Bazant and Panula found

creep function $\phi(t,\tau) = \dfrac{(t-\tau)^{0.6}}{10 + (t-\tau)^{0.6}}\ \phi^{*}(\tau)$

where τ is the age of the concrete at first loading (in days); $t - \tau$ is the duration of loading (in days); $\phi^{*}(\tau)$ is the final creep coefficient and is expressed as

$$\phi^{*}(\tau) = 2.35\ \gamma_1\ \gamma_2\ \gamma_3\ \gamma_4\ \gamma_5\ \gamma_6$$

γ_1 to γ_6 are empirical correction factors which account for many of the parameters which affect the magnitude of creep.

γ_1 accounts for the age of concrete at the time of first loading, τ.

For moist cured concrete: $\gamma_1 = 1.25\ \tau^{-.118}$ for $\tau > 7$ days

For steam cured concrete: $\gamma_1 = 1.13\ \tau^{-.094}$ for $\tau > 3$ days

γ_2 includes the effect of variations in the relative humidity, λ (in percent):

$$\gamma_2 = 1.27 - 0.0067\ \lambda \quad \text{for } \lambda > 40$$

γ_3 accounts for the size and shape of the member. Two alternative methods are given for the estimation of γ_3, one based on the average thickness h_o (equal to 4V/S, in mm) and the other based on the volume to surface ratio (V/S).
When $h_o \leq 150$ mm, γ_3 is obtained from

h_o (mm)	50	75	100	125	150
γ_3	1.30	1.17	1.11	1.04	1.00

When $150 \text{ mm} < h_o < 380$ mm:

$$\gamma_3 = 1.14 - 0.00092\ h_o \quad \text{when } t - \tau \leq 365 \text{ days}$$

$$\gamma_3 = 1.10 - 0.00067\ h_o \quad \text{when } t - \tau > 365 \text{ days}$$

and when $h_o \geq 380$ mm :

$$\gamma_3 = \frac{2}{3}\left[1 + 1.13\ e^{-0.0213\ V/S}\right]$$

γ_4 to γ_6 depend on the composition of the concrete:

$$\gamma_4 = 0.82 + 0.00264\ s$$

where s is the slump of the fresh concrete in mm.

$$\gamma_5 = 0.88 + 0.0024\ \psi$$

where ψ is the ratio of the fine aggregate to total aggregate by weight (in percent).

$$\gamma_6 = 0.46 + 0.09\ a < 1.0$$

where a is the air content in percent.

Figure 4.23(a) ACI Creep Prediction Method

$$J(t, t') = \frac{1}{E_0} + C_0(t, t') + C_d(t, t', t_0)$$

$J(t, t')$ = creep function = strain at time t caused by a unit sustained uniaxial stress acting since time t':

The standard creep coefficient is obtained from

$$\varphi(t, t') = E(t')J(t, t') - 1.$$

$E(t')$ = the conventional static modulus

Basic creep

$$C_0(t, t') = \frac{\varphi_1}{E_0}(t'^{-m} + \alpha)(t - t')^n.$$

$$\varphi_1 = \frac{10^{3n}}{2(28^{-m} + \alpha)}.$$

$$\alpha = \frac{1}{40\, w/c}, \qquad m = 0.28 + \frac{1}{(f'_c)^2},$$

$$n = 0.115 + 0.0002\,(f'_c)^3$$

$$\frac{1}{E_0} = 0.09 + \frac{1}{1.7 z_1^2}, \qquad z_1 = 0.000\,05\,\rho^2 f'_c,$$

in which ρ = unit mass of concrete in lb/ft^3 (= 16.03 kg/m^3), f'_c is the 28 day cylinder strength in ksi (= 6.895 N/mm^2) and $1/E_0$ is in 10^{-6}/psi (= 145.0×10^{-6} per N/mm^2). When substituted in equation (12), this formula can be also used to calculate $E(t')$. The resulting values are in good correlation with the familiar ACI formula ($57\,000\sqrt{f'_c}$);

DRYING CREEP

$$C_d(t, t', t_0) = \frac{\varphi'_d}{E_0} t'^{-m \cdot 2} k'_h \varepsilon_{sh\infty} S_d(t, t'),$$

$$\varphi'_d = \left(1 + \frac{t' - t_0}{10\,\tau_{sh}}\right)^{-1\,2} \varphi_d.$$

Time shapes (similar to shrinkage):

$$S_d(t, t') = \left(1 + \frac{10\,\tau_{sh}}{t - t'}\right)^{-c_d n}.$$

τ_{sh} = shrinkage square half-time $\qquad c_d = 2.8 - 7.5n.$

for $r > 0$:

$$\varphi_d = 0.008 + 0.027u, \qquad u = \frac{1}{1 + 0.7 r^{-1.4}}$$

for $r \leqq 0$: $\varphi_d = 0.008$.

$$k'_h = 1 - h^{1.5}$$

h = relative humidity of the environment

$$r = 56\,000 \left(\frac{s}{a} f'_c\right)^{0.3} \times \left(\frac{g}{s}\right)^{1.3} \left(\frac{w/c}{\varepsilon_{s\infty}}\right)^{1.5} - 0.85$$

Here n = exponent given in Part II (equation 17): f'_c = 28-day cylinder strength (ksi); w/c = water-cement ratio; g/s = gravel-sand ratio: s/a = sand-aggregate ratio (all by weight): $\varepsilon_{s\infty}$ = final shrinkage in 10^{-6} given in Part I

Figure 4.23(b) Bazant-Panula Creep Prediction Method

the two-sided 90% confidence limits on their model are 35% whereas the same limit on the ACI 209 model is 49%, and on the complex 1978 CEB method it was 41%.[55] This implies that there is only a 10% probability that a creep strain prediction made with the BP model would vary from the actual measured creep by more than 35% if all the concrete properties needed for the BP model were correctly measured. Based on this information, which is the most comprehensive comparison that was located in the literature, the additional complexity in the BP method is accompanied with significantly more accuracy. Some references advise that no method is very reliable and therefore it is usually most practical to choose one of the simpler methods.[56] Reference 53 presents a moderated version of this opinion by stating that the simplified methods, such as the ACI 209 method, work best for structures which are not too massive that are in a drying environment because the BP method compares much better to data than simplified methods for the more unusual cases such as thick structures (12 in. or more) which dry more slowly, creep duration greater than 10 years, very small or large ages of first loading (<10 days or >10 years). This is echoed by Bazant and Panula to the extent that they state that the increase in accuracy of their method for predicting creep relative to that of the ACI 209 method is greatest for thicker structures loaded at later times.[55]

Figure 4.24 shows a comparison between three methods for predicting creep for a given set of hypothesized initial conditions. The top plot on the figure shows a comparison between two simple creep prediction methods; the method in the Australian Design Code AS-3600 and ACI 209 method, and the Bazant-Panula (BP) method. The large difference between the creep coefficients calculated with these different prediction methods in Figure 4.24a is quite typical of the wide variation in creep predicted with different methods.[56] Figure 4.24b shows the basic creep and drying creep predicted with BP method separately, where the total creep is the sum of the two. The total creep predicted by the ACI 209 method in Figure 4.24a is shown for reference. The different shape of the basic creep and drying creep curves is evident. It is also apparent that the shape of the ACI 209 method curve is approximately a "smeared" version of the drying creep and basic creep curves, more like the basic creep curve early in time and very much like that of the drying creep curve late in time. The same is true of the shape of the creep curve predicted with the simple AS-3600 method.

In the modification to the CANDE program the ACI 209 method, the Australian Code method, and the Bazant-Panula method for predicting creep are incorporated. The user can indicate which predictive method is to be used in the input deck. Figure 4.25 shows a comparison between the creep coefficients (the creep strain per unit elastic strain) predicted with the AS-3600 method, the ACI 209 method, and the Bazant-Panula method for the BEBO culvert arch segment and floor slab. The stress history is not constant for either member but, for comparison purposes, a constant stress history is assumed applied at the times shown in the figure. These times are equal to the ages of both members when fill over the culvert was complete. Both members are also assumed to be "drained," or to allow drying, on one side of the culvert for the comparison. This causes the effective thickness of the culvert and floor slab to be twice their actual thicknesses of 10 in. (for the arch) and 5 in. (for the floor slab). A constant 65% relative humidity is assumed at the surface exposed to drying based on the average of measurements made four times a day over the 2.5 year culvert monitoring period by the National Oceanic and Atmospheric Administration in San Antonio. The concrete properties presented above for the concrete in the arch segment of the culvert and in the floor slab are used in the comparison. The

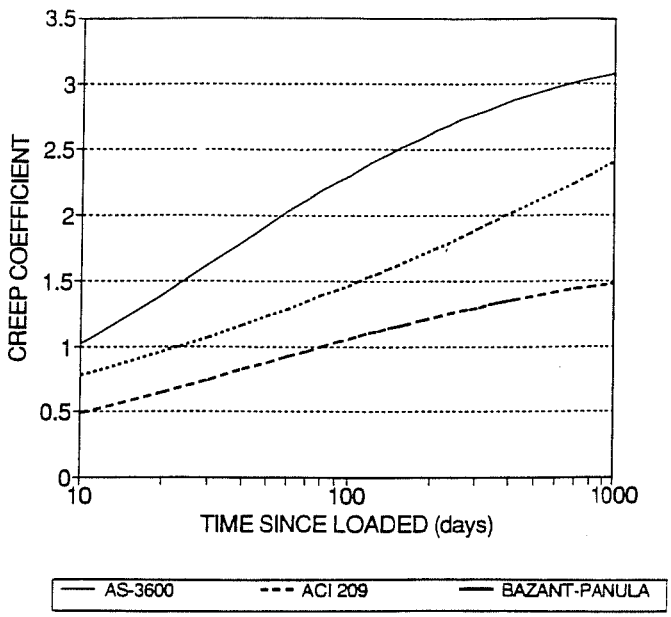

(a) General comparison between creep prediction methods

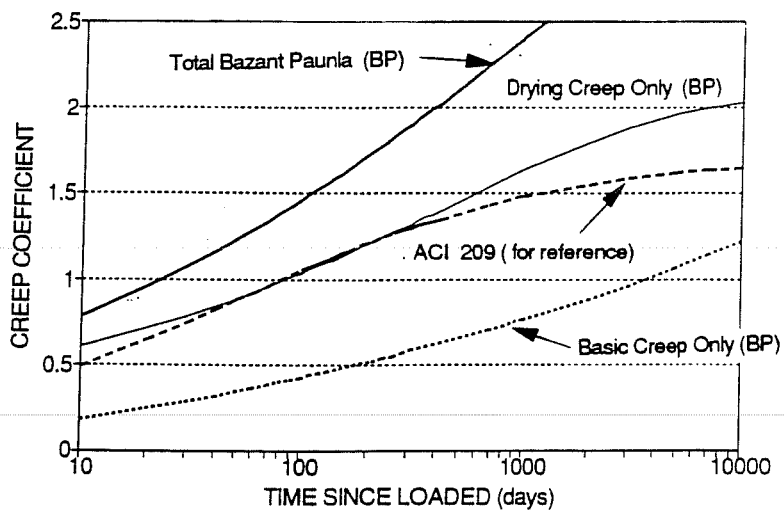

(b) Drying creep and basic creep in Bazant-Panula (BP) Method

Figure 4.24 Comparison of creep prediction methods for a standard 4000 psi strength concrete cylinder loaded at 28 days in 65% relative humidity

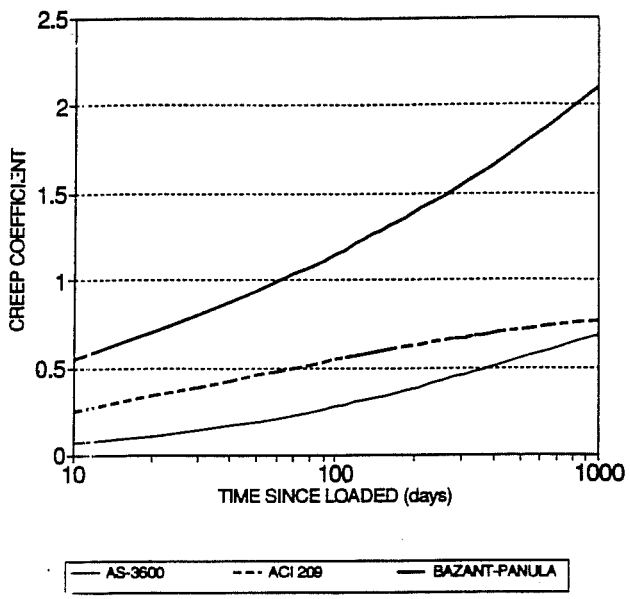

(a) Comparison of creep prediction methods for culvert arch

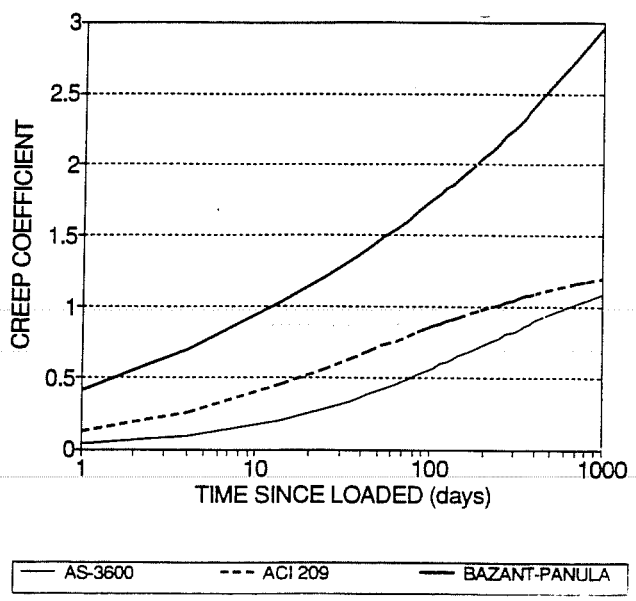

(b) Comparison of creep prediction method for culvert floor slab

Figure 4.25 Comparison of creep predicted with different methods for the BEBO culvert

comparison shows that the creep predicted with the Bazant-Panula method is approximately twice that predicted with the larger of the other two simplified methods. Figure 4.26 shows a comparison between measured creep in specimens exposed to drying, and the complex CEB method and the ACI 209 method (with the dotted lines) that is taken from Reference 55. It can be seen that it is not unusual for the ACI 209 method to underestimate measured creep by a factor of two.

4.5.2 Factors Affecting Creep in the Culvert not Considered in the Available Creep Prediction Methods. There are several other complexities which are not considered in the creep prediction methods, but which significantly affect creep in the culvert and must be considered. First, the stress in the culvert is not constant. The creep coefficient predicted by all creep prediction methods is based on a constant stress over a given time interval. This problem is usually accounted for in creep analyses by assuming the principal of superposition. According to this assumption, the creep due to a number of stress increments applied at different times is the sum of the creep strains caused by each of the stress increments considered separately. The discretization of an arbitrary stress history into separately applied stress increments is shown at the top of Figure 4.27. The elastic strain history can be discretized similarly. Based on the principle of superposition, the incremental creep strain due to a series of N elastic strain increments applied at times t_1 through t_N is shown below in Equation 4.6. This approach for calculating incremental creep strain fits very well into an incrementally based analysis such as that in the CANDE code.

$$e_c(t_N) - e_c(t_{N-1}) = \sum : ([c(t_N, t_i) - c(t_{N-1}, t_i)][e_e(t_i)]) \quad \text{for } i = 1, N \tag{4.6}$$

where $e_c(t_N) - e_c(t_{N-1})$ = creep strain occurring between time t_N and time t_{N-1},
$c(t, t')$ = creep coefficient for constant unit elastic strain applied at time t' until time t, and
$e_e(t')$ = constant elastic increment strain applied at time t'.

The principle of superposition has been found to predict observed creep relatively well for cases of monotonically increasing stress.[57] This is especially true for stresses less than one-half the concrete yield stress. For cases where the stress decreases, the assumption of superposition overpredicts the reduction in creep since only part of the creep strain is recoverable. The lower half of Figure 4.27 shows comparisons between measured total strain histories (elastic and creep strain) caused by simple non-constant stress histories, and corresponding strain histories calculated by superimposing the strain histories measured under two constant applied stress increments applied at different times.

The creep prediction methods also do not consider the fact that cracking occurs in the culvert or that the culvert is exposed to different levels of humidity on the air-side and soil-side surfaces. Cracking was observed over a 6 ft. to 8 ft. wide area on the inside surface culvert near the crown during backfill and may also have occurred on the soil-side of the culvert in the negative moment region. The effect of cracking is to increase the rate of drying and therefore increase the rate of drying creep. For example, data is available[58] which shows that the observed time required to achieve a given amount of moisture

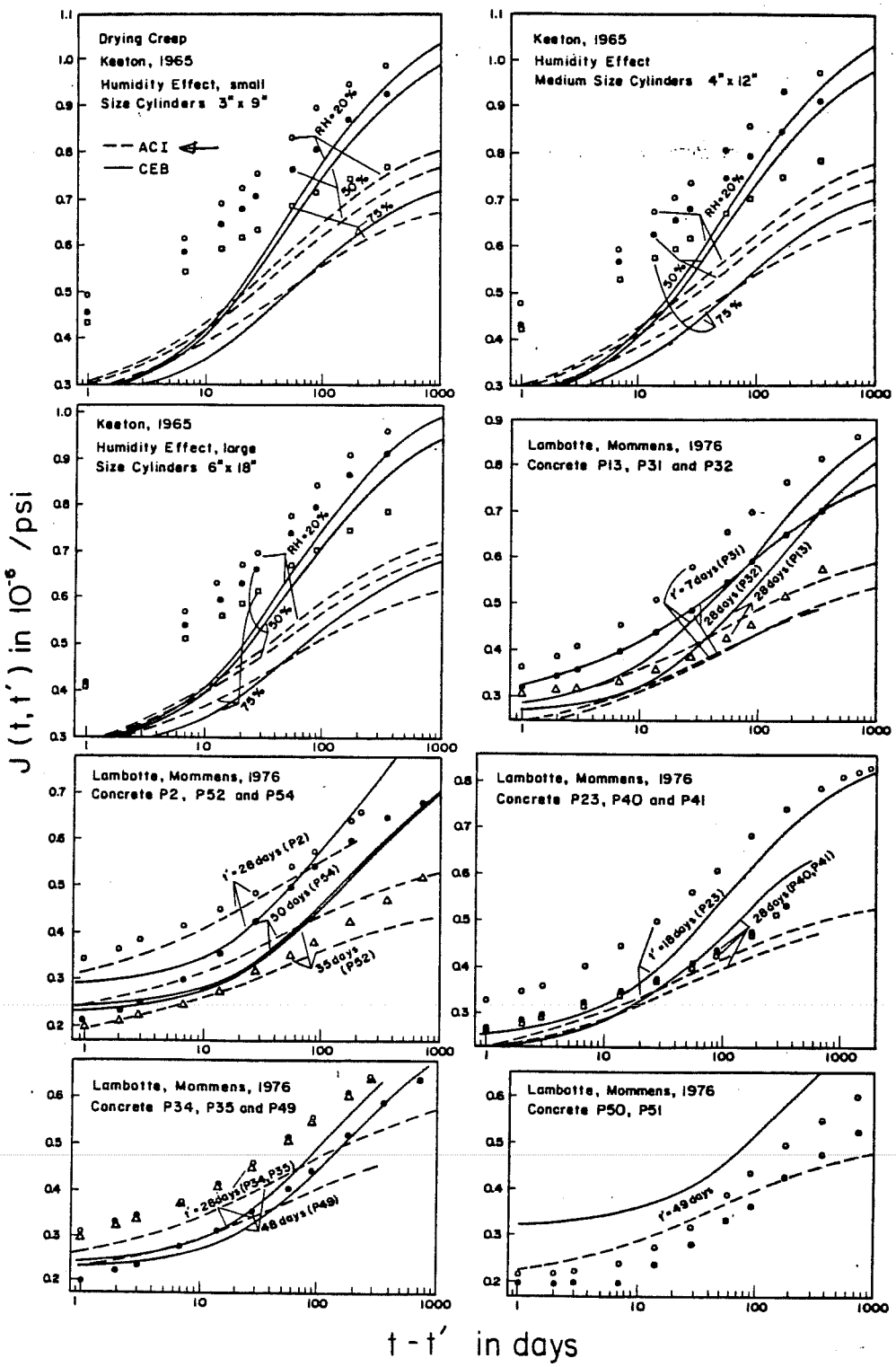

Figure 4.26 Comparison of ACI 209 and CEB-FIP creep prediction methods to data

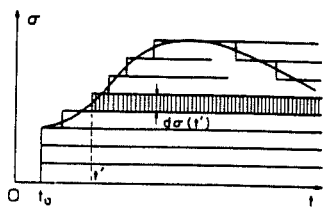

a) Stress Increments

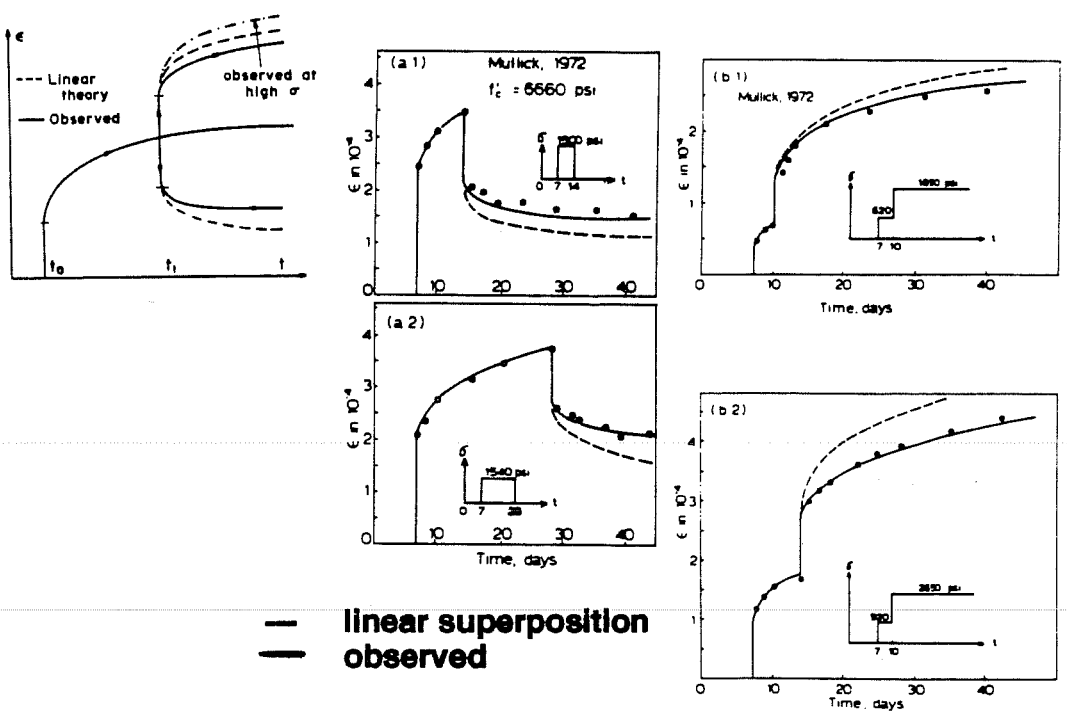

Figure 4.27 Superposition principle as applied to concrete creep (from Reference 29)

loss in uncracked reinforced concrete samples was approximately 2.25 times longer than that required for similar cracked concrete samples subjected to a constant bending moment. Therefore, the effect of cracking on drying is substantial. Unfortunately, there is no data available on the magnitude of the increase in creep due to concrete cracking. Since shrinkage is also very dependent on the rate of drying, it is also increased relative to predicted values by the presence of cracking.

The humidity on the air-side is assumed equal to 65% relative humidity based on the average of measurements made four times a day over the 2.5 year culvert monitoring period by the National Oceanic and Atmospheric Administration in San Antonio. The relative humidity on the soil-side of the culvert is thought to be considerably greater than that on the air-side due to the presence of the soil. Thus, it is probable that much more drying takes place at the air-concrete surface than at the soil-concrete surface. However, the exact value of the relative humidity on the soil-side of the culvert is unknown and some significant amount of drying may take place at this surface especially early in time when the culvert concrete pore moisture content is relatively high. Also, the floor slab was subjected to rewetting on the air-side due to large amounts of wet mud that flowed into the culvert during heavy rains and were not removed for several weeks. The creep prediction methods are based on constant levels of known relative humidity; therefore they cannot take into account complexities such as these well.

Finally, the creep prediction methods discussed above are based strictly on creep measured during compression. However, at low moment regions (i.e. uncracked regions) the concrete in the arch below the neutral axis, the stress tensile, and the floor slab is assumed to be in pure tension. There has been limited measurements of creep strains occurring during flexural response or pure tension. The available test data indicates that creep in tension is on the same order of magnitude as compression creep, and that tensile creep is influenced by age of loading, its rate decreases with time, and it is influenced by drying in a similar manner as compression creep.[56] Usually, tensile creep is predicted using the same methods as those discussed above for prediction of compression creep.[56,59]

4.5.3 Prediction of Creep in the CANDE Model of the BEBO Culvert. In the study of the culvert response that is presented in the next chapter, the Bazant-Panula method was used as the creep prediction method. This choice was based on several considerations. First, as was stated in the discussion presented earlier, there seems to be increased accuracy that can be gained with the BP method relative to that of the simplified methods, such as the ACI 209 method and the AS-3600 method. Secondly, the numerous trial computer runs which were made with the modified version of the CANDE code, which includes the consideration of creep and shrinkage, showed that a relatively large creep coefficient was needed to match the measured culvert response well. In fact, it was found that a moderate increase factor had to be applied to the BP method to achieve a close match between predicted and measured culvert response.

The fact that the stress history in the culvert was not constant was taken into account by using the principle of superposition as implemented in Equation 4.6. This is explained in more detail in the next section. The effect of cracking on the creep coefficient is very difficult to consider. Basically, this is accounted for with a trial and error approach where different multiplication factors were placed on the drying creep in order to see which value caused the calculated response to best match measured values. This is explained more in the next chapter.

The culvert is idealized as having only one drainage surface, with a relative humidity of 65%, and as having two drainage surfaces with this humidity level. These two extremes represent bounds on the amount of drying creep, as it is affected by the drying surface area of the culvert, which is thought to occur in the culvert. In separate computer runs with the CANDE program, which differ only in the number of drainage surfaces (one or two), the calculated strains, including both creep and shrinkage strain, typically only differed by about 10%. Therefore, this variable is not very significant.

The increased creep due to the additional drying which occurs in cracked regions of the culvert is approximately accounted with a user input multiplier which was programmed into the CANDE computer code because this creep is not predicted with the creep prediction model. This multiplier is applied to the drying portion of the creep in the BP method which is predicted at load/time steps after cracking occurs at any node on the inside surface of the culvert. Since the amount of drying is thought to be significantly less on the soil-side of the culvert, the multiplier on the drying creep is not applied to nodes where cracking occurs on the outside surface of the culvert. The use of this multiplier did not cause a significant increase in calculated creep strain, however, because drying creep is a low percentage of the total strain. The unknown factors affecting drying creep do not have a very significant affect on this study because of the relatively low importance of drying creep. Finally, creep strain is predicted in uncracked regions of tensile stress in the CANDE program using the BP method with no modification. No stress is assumed to exist in cracked regions and therefore no creep is calculated.

4.5.4 Prediction of Shrinkage in the CANDE Model of the BEBO Culvert. Shrinkage strain, which is stress independent, is usually predicted as a total strain. Both simplified and relatively complex methods exist for predicting shrinkage strains. Figure 4.28a shows the ACI 209 prediction method,[21] which is a relatively "simple" method, and Figure 4.28b shows the Bazant Panula method, which is somewhat more complex.[54] The four parameters in the ACI 209 method which are dependent on the concrete slump, air content, aggregate content, and cement content can be assumed equal to one with relatively little error (usually less than 15%). Bazant and Panula made a comparison between these two prediction methods and approximately 30 different sets of shrinkage data. They found the two-sided 90% confidence limits on their model are 27% whereas the same limit on the ACI 209 model is 87%.[55] This implies that there is only a 10% probability that a shrinkage strain prediction made with the BP model would vary from the actual measured shrinkage by more than 27% if all the parameters needed for the BP model were correctly measured. Based on this information, the BP method is significantly more accurate than the ACI method. Figure 4.29 shows a comparison of the shrinkage predicted for the culvert arch and floor slab using three shrinkage prediction methods: the AS-3600 method, the ACI 209 method, and the BP method. A relative humidity of 65% and the concrete properties presented above for the concrete in the arch segment of the culvert and in the floor slab are used in the comparison. The comparison is in terms of "delta shrinkage," which is the shrinkage at the time of interest minus the shrinkage at the reference time. Since all comparisons between calculated and measured culvert response in the next chapter are in terms of response after initial placement of the culvert in the field, the reference times in the comparison in Figure 4.29 were chosen to correspond to the approximate drying ages of the arch and floor slab at the time the culvert was placed in the field. The long-term shrinkage predicted with the BP method is, on the average, similar to those predicted with the ACI 209 and somewhat less than that predicted with the AS-3600 method.

Shrinkage:

The shrinkage strain at time t measured from the start of drying is given by

$$\text{For moist cured concrete:} \quad \varepsilon_{sh}(t) = \frac{t}{35 + t}\,\varepsilon_{sh}^{*} \tag{2.45a}$$

$$\text{For steam cured concrete:} \quad \varepsilon_{sh}(t) = \frac{t}{55 + t}\,\varepsilon_{sh}^{*} \tag{2.45b}$$

where ε_{sh}^{*} is the final shrinkage at time infinity and is given by

$$\varepsilon_{sh}^{*} = 780\ \gamma_2'\ \gamma_3'\ \gamma_4'\ \gamma_5'\ \gamma_6'\ \gamma_7'\ \gamma_8 \tag{2.46}$$

γ_2' accounts for the effect of relative humidity, λ, and is given by

$$\gamma_2' = 1.40 - 0.01\,\lambda \quad \text{for } 40 \le \lambda \le 80 \tag{2.47a}$$

$$\gamma_2' = 3.00 - 0.03\,\lambda \quad \text{for } 80 < \lambda \le 100 \tag{2.47b}$$

γ_3' accounts for the size and shape of the member and depends on the average thickness h_o (= 4V/S). When 50 mm $\le h_o \le$ 150 mm , γ_3' is given by

h_o (mm)	50	75	100	125	150
γ_3'	1.35	1.25	1.17	1.08	1.00

(2.48)

When 150 mm < $h_o \le$ 380 mm:

$$\gamma_3' = 1.23 - 0.0015\,h_o \quad \text{for } t \le 365 \text{ days} \tag{2.49a}$$

$$\gamma_3' = 1.17 - 0.0011\,h_o \quad \text{for } t > 365 \text{ days} \tag{2.49b}$$

and when h_o > 380 mm:

$$\gamma_3' = 1.2\ e^{-0.00472\ V/S} \tag{2.50}$$

where the volume to surface ratio V/S is in mm.

The correction factors for slump s (mm), ratio of fine aggregate to total aggregate content ψ (percent), air content a (percent of volume) and cement content c (kg/m^3) are γ_4', γ_5', γ_6', and γ_7', respectively:

$$\gamma_4' = 0.89 + 0.00161\,s \tag{2.51}$$

$$\gamma_5' = 0.30 + 0.014\,\psi \quad \text{for } \psi \le 50\% \tag{2.52a}$$

$$\gamma_5' = 0.90 + 0.002\,\psi \quad \text{for } \psi > 50\% \tag{2.52b}$$

$$\gamma_6' = 0.95 + 0.008\,a \tag{2.53}$$

$$\gamma_7' = 0.75 + 0.00061\,c \tag{2.54}$$

Finally, γ_8 accounts for variations in the period of initial moist curing T_c (in days) and is given by

T_c	1.0	3.0	7.0	14.0	28.0	90.0
γ_8	1.2	1.1	1.0	0.93	0.86	0.75

(2.55)

For concrete which is steam cured for a period of between one and three days, $\gamma_8 = 1.0$.

Figure 4.28(a) ACI-209 Shrinkage Prediction Method

$$\varepsilon_{sh}(\hat{t},\, t_0) = \varepsilon_{sh_\infty} k_h S(\hat{t}); \qquad \hat{t} = t - t_0;$$

square-root hyperbolic law in time:

$$S(\hat{t}) = \sqrt{\frac{\hat{t}}{\tau_{sh} + \hat{t}}};$$

humidity dependence:

$$\left.\begin{array}{ll} \text{for} & h \leqq 0.98: \quad k_h = 1 - h^3: \\ \text{for} & h = 1.00: \quad k_h = -0.2. \end{array}\right\}$$

size-dependence (of diffusion type):

$$\tau_{sh} = 600\left(\frac{k_s}{150} D\right)^2 \frac{C_1^{\text{ref}}}{C_1(t_0)}, \qquad D = 2\frac{v}{s};$$

age-dependence:

$$C_1(t) = C_7 \cdot (0.05 + \sqrt{6.3/t}),$$

Here ε_{sh} = shrinkage strain; t = time (in days), representing age of concrete, t_0 = age when drying begins. $\hat{t}$ = duration of drying, ε_{sh_∞} = ultimate shrinkage. E = Young's modulus, h = relative humidity of the environment ($0 \leqq h \leqq 1$), τ_{sh} = shrinkage square half-time, D = effective cross section thickness in millimetres. v/s = volume-to-surface ratio, C_1 = drying diffusivity of nearly saturated concrete at reference temperature T_c (chosen as 23°C for all data).

$C_1^{ref} = 10$ mm/day

k_s = shape factor which equals 1.0 for a slab, 1.15 for a cylinder, 1.25 for a square prism, 1.30 for a sphere, 1.55 for a cube

The following empirical dependence on strength and the composition parameters of concrete mix has been identified:

Reference diffusivity (mm^2/day):

$$C_7 = \frac{1}{8}\frac{w}{c} c - 12;$$

$$\left.\begin{array}{ll} & \text{if } C_7 < 7 \text{ set } C_7 = 7, \\ \text{and} & \text{if } C_7 > 21 \text{ set } C_7 = 21. \end{array}\right\}$$

Final shrinkage (in 10^{-6}):

$$\epsilon_{sh_\infty} = (1330 - 970y)10^{-6}$$

$$y = (390z^{-4} + 1)^{-1}$$

$$z = \sqrt{f_c'}\left[1.25\sqrt{\frac{a}{c}} + 0.5\left(\frac{g}{s}\right)^2\right] \times \left(\frac{1 + s/c}{w/c}\right)^{1/3} - 12$$

if $z \geqslant 0$, otherwise $z = 0$

Here c = cement content in kg/m^3, w/c = water-cement ratio, a/c = aggregate-cement ratio, g/s = gravel-sand ratio, s/c = sand-cement ratio (all ratios by weight), and f_c' = 28-day cylinder strength in ksi (1 ksi = 6.895 N/mm^2). Sand is defined as aggregate of less than 4.7 mm size (sieve No. 4), the rest being considered as gravel.

Figure 4.28(b) Bazant Panula Shrinkage Prediction Method

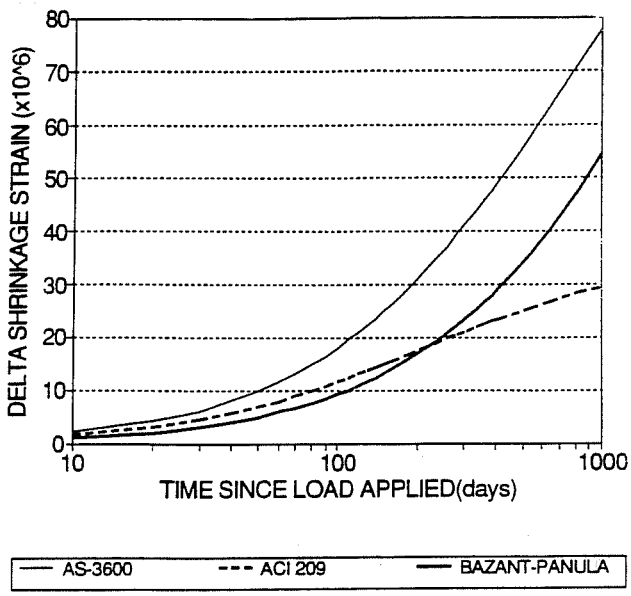

(a) Comparison of shrinkage prediction methods for culvert arch

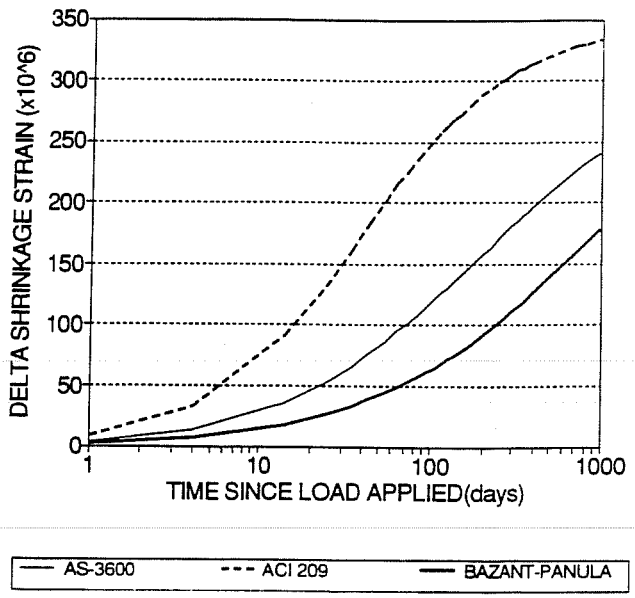

(b) Comparison of shrinkage strain prediction methods for culvert floor slab

Figure 4.29 Comparison of shrinkage strain since reference time (time culvert placed in field) predicted with different methods

The BP method is used to predict shrinkage in the analysis of the culvert with the modified CANDE code due to its greater accuracy. The shrinkage prediction is affected by the same factors discussed above for creep which are not considered by the prediction models, namely concrete cracking and the difference in relative humidity on the soil-side and air-side of the culvert. Another factor affecting shrinkage in the floor slab was the presence of a thick layer of mud on the floor slab during parts of the first year after construction when large amounts of mud tended to wash into the culvert during rainstorms and remain there for several days to weeks afterwards. This effectively rewetted the floor slab, reversing earlier shrinkage, and "resetting" the drying process. There are also some low spots in the culvert floor slab near the instrumented arch sections where water tends to pond and gradually evaporate after rains have caused flow through the culvert. In the floor slab tensile creep occurs, so that shrinkage and creep cause opposite strain. The rewetting process most probably reduces the shrinkage strain which would otherwise occur and therefore increases the amount of measured tensile strain. Since there are no known methods to calculate shrinkage and creep taking into account the changing moisture conditions on the culvert floor, a 65% moisture content with no rewetting is used in the CANDE model. The creep and shrinkage strains are stored separately in the modified CANDE program so that the shrinkage strains can be subtracted out of the calculated strains to get the approximate strain assuming that the periodic rewetting of the floor slab has virtually negated all shrinkage.

4.6 Structural Response to Creep, Shrinkage, and Temperature Strains

Methods for predicting creep and shrinkage of concrete predict the "free" creep of an unrestrained, unreinforced block of concrete. In reinforced concrete, the no-slip condition between the concrete and the steel reinforcement causes the reinforcement to be stressed by concrete creep and/or shrinkage strains. Equilibrium requires that corresponding stress change must occur in the concrete so that there is no net change in the internal force (thrust and moment) in the cross section. This results in an internal stress redistribution which causes either a gradual increase or decrease in the steel stress and a corresponding decrease or increase in the concrete stress. Creep strains generally cause the stress in the steel reinforcement to increase and the concrete stress to decrease since the creep strains which deform the reinforcement are usually in the same direction as the load-induced strain. The concrete stress change that occurs during internal stress redistribution also causes creep strains which are called "secondary" creep strains. These creep strains, which develop simultaneously with the "primary" creep strains, generally act opposite the primary creep strains since the redistributed stresses in the concrete generally act to reduce the initial load-induced stress.

In an statically indeterminate structure, the boundary constraints typically restrain creep and shrinkage strains. The change in restraining forces which develops at the reactions causes the internal forces (thrust and moment) in the structure to change. In soil-structure interaction problems, where soil pressures are partially a function of structural deformations, creep and shrinkage induced deflections can also cause changes in internal forces. Internal stress redistribution and internal force redistribution are discussed separately in the next two subsections.

The effects of temperature strains on the concrete structure are also considered in the modified version of the CANDE code. The free temperature strain is calculated assuming the same thermal

coefficient of expansion for both the steel and concrete, equal to 5.5 x 10^{-6} in./in./°F. The thermal coefficients for the two materials differ by approximately 15% using average values for their respective coefficients of expansion reported in Reference 60. A larger variation may occur due to the fact that the concrete in the culvert is made with limestone aggregate as discussed in Chapter 3. However, even if the steel thermal coefficient is assumed to be a factor of two larger than the concrete coefficient and a maximum 20°F temperature change is assumed, the small ratio of steel area to concrete area in the cross section causes the steel to induce only approximately a 60 psi, or 15 x 10^{-6} in./in. tensile strain in the concrete. This is small enough to be outside the accuracy of this analysis considering the lack of information on the actual temperature changes and concrete thermal coefficient of expansion. The temperature is assumed constant over the thickness of the cross section. Based on these assumptions, there is no internal stress redistribution causes by thermal strain since both the concrete and steel are assumed to respond identically to temperature change. Internal force redistribution will occur if indeterminate structural boundary constraints and the surrounding soil stiffness restrict the free temperature strains.

4.6.1 Internal Stress Redistribution. The internal stress redistribution due to creep and shrinkage occurring during a given time interval, which will be referred to as the "current" load/time interval, can be calculated from the free creep and shrinkage strain of the concrete and the cross section geometry using the relaxation method proposed by Bresler and Selna.[61] In this two step method, the moment and thrust required to restrain the free creep and shrinkage distribution over the concrete portion of the cross section are calculated first. These are referred to as the restraining forces and they can be calculated using Equations 4.7 and 4.8. Normally, concrete section properties are calculated about the centroidal axis of the transformed section. However, in a time analysis which considers the effects of creep and shrinkage, the centroidal axis of the transformed section changes with time if the section is unsymmetrically reinforced or there is concrete cracking. Therefore, it is convenient to choose a fixed reference for the strain distribution and internal forces such as the top (loaded) face of the section as is done in Equations 4.7 and 4.8. The free creep strain distribution during the load/time step of interest is assumed equal to the elastic strain distribution, which is defined in terms of the strain at the top of the section and the curvature, multiplied by the change in the creep coefficient over the current load/time step of interest. The change in the creep coefficient is the difference between the creep coefficient at the end of the current time step and that at the beginning of the time step. Since the creep coefficient is a function of the time at which a stress (or elastic strain) is applied, the free creep during the current load/time step is calculated as the sum of the creep strains from each elastic strain applied during a previous load step. This assumes the principle of superposition shown in Equation 4.6. The change in the free shrinkage strain is the difference between the shrinkage strain at the end of the current load step and that at the beginning of the load step. The shrinkage strain is assumed constant over the uncracked concrete area.

$$N=E_m[A_c(\sum_{i=1,N} [c(t_N,t_i)-c(t_{N-1},t_i)]e(t_i))-B_c(\sum_{i=1,N} [c(t_N,t_i)-c(t_{N-1},t_i)]K(t_i))+e_sA_c] \qquad (4.7)$$

$$M=E_m[-B_c(\sum_{i=1,N}[c(t_N,t_i)-c(t_{N-1},t_i)]e(t_i))+I_c(\sum_{i=1,N}[c(t_N,t_i)-c(t_{N-1},t_i)]K(t_i))-e_sB_c] \quad (4.8)$$

where

N = restraining thrust during current load/time step,

M = restraining moment about top concrete surface during current load/time step,

$\Sigma_{i=1,N}[c(t_N,t_i)-c(t_{N-1},t_i)]e(t_i)$ = total creep strain at top fiber of concrete surface occurring during current load/time step due to elastic strain increments applied during all previous time steps and the current time step. This is the summation shown in Equation 4.6 where the current load step extends from t_{N-1} to t_N,

$c(t_N,t_i)-c(t_{N-1},t_i)$ = change in the creep coefficient from a stress applied during load/time step i during current load/time step,

$e(t_i)$ = elastic strain at top surface applied during load/time step i,

$\Sigma_{i=1,N}[c(t_N,t_i)-c(t_{N-1},t_i)]K(t_i)$ = total creep curvature occurring during current load/time step from elastic curvature applied at all previous time steps and current time step,

$K(t_i)$ = elastic curvature applied during previous load/time step i, NOTE: $\Sigma(y)=E_{top}+KY$, $y=0$ at top fiber,

A_c = area of current uncracked concrete section (without reinforcing steel),

e_s = change in shrinkage strain during current load/time step,

B_c = first moment of the current area of concrete section about the top surface of the section, and

I_c = second moment of the current area of concrete section about the top surface of the section.

$$E_m = E_c/[c_c(t_N, t_{N-1/2})+1] \quad (4.9)$$

where

E_m = effective concrete modulus during current load/time step,

E_c = elastic concrete modulus at the middle of the current time step, and

$c_c(t_N,t_{N-1/2})$ = creep coefficient during current load/time step N for stress applied during middle of current load/time step.

The secondary creep caused by elastic concrete strain created by internal stress redistribution is included in the summed creep from each load/time step. Stresses from internal stress redistribution are assumed to be suddenly applied midway through each time step although they develop gradually in response to the gradual creep and shrinkage during each time step. This approach is accurate as long the creep strain occurring during each time step is small enough. Usually six to ten time steps is adequate to accurately calculate the long-term stresses and strains caused by creep and shrinkage.[56] Time steps which are equal in log space are suggested since the creep strain increases with time as approximately a logarithmic function as illustrated in Figure 4.22.

The modified, or effective concrete modulus (E_m) is used in Equations 4.7 and 4.8. Based on Equation 4.9, and the definition of the creep coefficient in Figure 4.22, this modulus is the ratio of an applied constant stress to the total amount of corresponding strain which develops in the concrete over a given time interval. Therefore, the effective modulus accounts for both the immediate elastic strain and the creep strain caused by the applied stress. This modulus is used rather than E_c in Equation 4.7 and 4.8 because the restraining forces cause elastic and creep strain over the time step which both offset the free creep and shrinkage strains. The restraining forces in Equations 4.7 and 4.8 are constant forces applied halfway through each load/time which produce creep and elastic strain at the end of the time step equal to the total free creep and shrinkage strain that develops in the concrete during the time step.

In the second step of the relaxation method, equilibrium is restored by applying "restoring" forces to the full transformed cross section, which are equal and opposite to the restraining forces in Equations 4.7 and 4.8. The restoring forces represent the effects of creep and shrinkage strains in the concrete on the full cross section. The change in the strain distribution caused by the restoring forces can be calculated using Equations 4.10 and 4.11. The total change in the strain distribution is the sum of the change in strain occurring during both steps. Since no change in strain was allowed during the first step, the strain distribution calculated with Equations 4.10 and 4.11 is the total change in the strain distribution caused by creep and shrinkage in the concrete. This includes the actual creep and shrinkage strains after the restraining effect of the steel reinforcement is accounted for and the elastic strain in the concrete caused by internal stress redistribution between the reinforcement and the concrete. The effective transformed section properties in Equations 4.10 and 4.11 are the transformed section properties calculated using E_m as the concrete modulus rather than E_c. The force applied by the steel reinforcement which resists creep and shrinkage is accounted for implicitly, since it is included in the cross sectional stiffness which resists the applied relaxation forces. This simplifies the calculations, especially when there are several layers of reinforcing steel in the cross section. Note that if Equations 4.7 and 4.8 are substituted into Equations 4.10 and 4.11 for an unreinforced concrete section (so that $A_c=A_e$, $B_c=B_e$, $I_c=I_e$), the strain distribution calculated with Equations 4.10 and 4.11 is equal to the free creep and shrinkage strain distribution.

$$e_0 = (B_e M + I_e N)/[E_m(A_e I_e - B_e^2)] \tag{4.10}$$

$$k_0 = (A_e M + B_e N)/[E_m(A_e I_e - B_e^2)] \tag{4.11}$$

where e_0 = change in strain in top concrete fiber during current load/time step due to creep and shrinkage,

B_e = first moment of the area of the effective transformed section about the top surface during current load/time step,

M = restraining moment from Equation 4.7,

I_e = second moment of the area of the effective transformed section about the top surface during current load/time step,

N = restraining thrust from Equation 4.8,

A_e = area of the effective transformed section during current load/time step, and

k_0 = change in curvature during current load/time step due to creep and shrinkage.

After the strain distribution is known, the change in the force in each layer of steel reinforcement in the section during the current load/time step due to creep and shrinkage can be calculated using Equation 4.12. The total change in the force is equal to the force developing during each load step, and, since no concrete strain occurred during the first step, no steel stress occurred during this step. Finally, since the cross section must remain in equilibrium, the change in the concrete stress distribution during the current load/time step due to creep and shrinkage can be calculated by applying the change in the steel force in each layer of reinforcement as an internal load located at the depth of reinforcement layer in the section, to the concrete portion of the cross section. Equation 4.13 is the concrete stress distribution which is in equilibrium with a thrust equal to -Tn and a moment about the top surface of the section equal to $-T_n d_n$. A linear stress distribution is assumed since creep is rarely a concern near ultimate load when the concrete stress distribution is nonlinear. The total change in the concrete stress distribution during the current load/time step due to creep and shrinkage is the sum of the stress distribution in Equation 4.13 for all layers of steel reinforcement in the cross section. The internal stress redistribution during the current load/time step is the stress change in the reinforcement calculated with Equation 4.12 and the change in the concrete stress distribution calculated with Equation 4.13. The deflection caused by creep and shrinkage during the current load/time step can be calculated by integrating the strain distributions at each cross section along the component length calculated using Equations 4.10 and 4.11.

$$T_n = A_{Sn}(e_0 - d_n k_0) \tag{4.12}$$

$$s(y)_n = [-(B_c - yA_c)d_n T_n + (I_c - yB_c)T_n] / (A_c I_c - B_c^2) \tag{4.13}$$

where T_n = change in force in steel area at layer n during current load/time step due to creep and shrinkage,
A_{Sn} = reinforcing steel area in layer n,
d_n = distance from top of concrete section to reinforcing steel in layer n, and
$s(y)_n$ = change in concrete stress at distance y from top of concrete surface due to the effect of creep and shrinkage during current load/time step on reinforcing steel in layer n (total change in concrete stress is the sum of $s(y)_n$ for all values of n.

The internal stress redistribution occurring during long-term creep and shrinkage can also be considered with a single time analysis by using the entire free creep and shrinkage strain in Equations 4.7 and 4.8 and using an "age-adjusted" effective modulus (AEEM) for E_m. The AEEM is calculated by using $t_{N-1/2} = t_0$ and $t_N = t_f$ in Equation 4.9 and multiplying c_c by an "aging coefficient" which accounts for the fact that significant secondary creep, caused by the concrete stresses from internal stress redistribution, develops during the long-term single load step which acts opposite of the primary creep strains caused by the restraining forces T and M in Equations 4.7 and 4.8. The creep strain caused by T and M is overestimated if the full creep coefficient c_c is used in Equation 4.9. The values of t_0 and t_f are the times at which load is applied and the final time of interest respectively. Values of the aging coefficient for various load duration, time of loading, and long-term creep coefficients, have been

backcalculated using the results from a multi-step analysis similar to that described approach by a number of researchers.[56] When the age of loading exceeds 5 days and the long-term creep coefficient is between 1.5 and 3 (which are all typical conditions) the aging coefficient can be assumed equal to 0.8 with little loss of accuracy. The single step method using the aging coefficient is valid when the applied load is constant or when the applied load changes at the same rate as creep develops such as the case of constrained axially loaded column where the stress relaxation. However, when the load changes arbitrarily during the time of interest, then the multi-step approach must be used.

If the maximum tensile stress exceeds the cracking stress during shrinkage or creep, the calculation method is similar to that described above except that creep, shrinkage, and internal stress redistribution only occur over the uncracked portion of the concrete cross section. Therefore only I_c, B_c, A_c, I_e, B_e, and A_e in Equations 4.7 through 4.13 change. As the last example case in Figure 4.30 implies, internal stress redistribution caused by creep from bending stresses tends to cause internal stress redistribution resulting in compressive stress at the original neutral axis. In a cracked member with assumed zero tensile strength, this implies that internal stress redistribution will cause more of the beam to go into compression and will shift the neutral axis downward. In a more realistic case, where some of the concrete below the neutral axis is carrying tension, the location of the neutral axis is not typically affected by internal stress redistribution because the additional compression from stress redistribution at the crack tip does not exceed the cracking strength and therefore the crack depth and the neutral axis remain constant. If cracking occurs at some time after the application of any significant amount of stress, then a multi-step creep analysis must be performed to obtain reasonable results.

4.6.2 Internal Force Redistribution. In addition to internal stress redistribution, creep and shrinkage cause the reaction forces to change with time in a statically indeterminate structure. This causes redistribution of internal forces (thrust and moment) in the structure and corresponding changes in stresses in the structure. The stress changes also cause creep strains. During a load/time step of interest, the change in reaction forces is equal to the boundary forces required to maintain equilibrium and compatibility conditions in the structure, as the creep and shrinkage induced strains calculated with Equations 4.10 and 4.11 occur. Calculation of the change in boundary forces can be accomplished in a manner similar to that used to calculate the initial redundant boundary conditions immediately after the loads are applied. The same redundant boundary conditions are established, and released in order to obtain the same determinate, "primary" structure. Then the change in the strain distribution caused by creep from the initial stress distribution in the structure and shrinkage over the time interval of interest is calculated at each cross section in the primary structure using Equations 4.10 and 4.11. These strain distributions are then integrated over the primary structure to obtain the deflections/rotations at each of the released boundary constraints. The change in boundary forces at the redundant boundaries are the forces on the primary structure required to restrain the deflections/rotations at each of the released boundary constraints. The change in the internal force distribution is that caused by applying the calculated redundant boundary forces to the primary structure as applied loads. The method is the same as that commonly used to calculate the internal force distribution due to applied loads, except that the primary structure deflections are calculated from the inelastic strains caused by the applied loads rather the elastic strains. Also, the effective modulus (E_m) is used to calculate the forces on the primary structure required at the redundant boundary conditions to enforce the boundary conditions because these

forces create both elastic and creep strains which offset the deflection/rotations calculated in the primary structure at the redundant boundaries.

If a single step analysis is used, the age-adjusted effective concrete modulus is used to calculate both the change in strain at each cross section from creep and shrinkage in the primary structure and the boundary forces on the primary needed to maintain the redundant boundary conditions. The internal force redistribution can lead to additional cracking in the structure. This can cause significant error in a single step analysis since an implicit assumption of this approach is that the elastic stresses caused by the applied loads are constant over time.

In a situation where the loads and structural deformation are coupled, such as soil-structure interaction, the loads are also affected by creep and shrinkage. In this case, additional internal force redistribution can occur if the soil pressure applied along the soil-structure interface changes as creep and shrinkage induced structural deformations take place. In this situation a multi-step analysis is necessary in order to obtain accurate results. During each time step, an iterative method must generally be used which ensures that the calculated internal force redistribution and corresponding displacements comply with equilibrium, the stress-strain relationships for both the soil and structure (including both elastic and inelastic strains), and compatibility requirements.

4.6.3 Method Used to Calculate Structural Response Including the Effects of Creep, Shrinkage, and Temperature Strains in the Modified CANDE Code. This general background of structural response to creep and shrinkage leads to the discussion of how the modified version of CANDE calculates soil-structure interaction including the effects of creep and shrinkage. The multi-step method discussed above is used for calculating structural response to creep and shrinkage in the CANDE code. Superposition of creep from stress increments applied at different times is also assumed. Since CANDE is based on a load step approach, the program is structured in a manner that can easily consider the multi-step approach.

The revisions to CANDE include revisions to the input and revisions to the calculation scheme. The CANDE input has been changed so that structural geometry and environmental factors which affect creep and shrinkage are read in for each member of the structure. These inputs define the structure geometry at each node and all the material parameters which influence creep and shrinkage required by the ACI 209, the Australian AS-3600, and the Bazant-Panula creep and shrinkage prediction methods. An input flag is used to define which prediction method for free creep and shrinkage strains will be used in the analysis. The CANDE input has also been changed so that there is a input time and temperature associated with each load step and an input time for casting and curing of each member of the structure. Time steps are defined by the times associated with each load step.

The basic calculation scheme of the revised CANDE code which includes the effects of creep and shrinkage is described below. It is based on the previously discussed concepts of the multi-step approach for determining structural response to creep and shrinkage. All descriptions of the basic elastic reinforced concrete CANDE model in Section 4.2 of this chapter are maintained in the material model also. Some basic parts of the original algorithm were rewritten since stress is not related to strain by a single constant

(the elastic modulus) in this revised version of the material model which invalidates some of the previous calculation procedures.

1) At the beginning of each load/time step, the incremental "free" creep distribution that occurs during the current time step due to incremental stresses, or elastic strains, applied during previous time steps is calculated at each structural node. Also, the free temperature strain in both the concrete and steel and the change in the concrete shrinkage strain during the current time/load step is calculated. In the CANDE structural beam-column elements, each node represents a cross section through the structure. Equation 4.6 is used to calculate the incremental free creep strain. The incremental free shrinkage and temperature strains are the difference between the strains calculated at the end of the time step and at the beginning of the time step. The inelastic strain distribution is assumed linear over each cross section since creep is proportional to the elastic strain and both shrinkage and temperature strains are assumed constant over the cross section.

2) Also, at the beginning of the load/time step, the effective concrete modulus (E_m) for the time step for each concrete member is calculated using Equation 4.9. The elastic modulus (E_c) used in Equation 4.9 is calculated taking into account aging of the concrete.

3) At the beginning of the iteration process for each time step, the incremental elastic strain distribution at each node of the structure is calculated from the thrust and moment caused by the soil loading during the current load/time step and the current elastic transformed section. The soil loads are those from the most recent trial solution of the global system of equations of the entire soil-structure system. The current value of the elastic concrete modulus E_c is used for this calculation. The creep caused by the stresses occurring during the current load step could be considered more simply by using the effective modulus E_m in this step. This approach would cause both the elastic strain and the creep strain to be calculated together. However, the concrete material model is programmed in CANDE so that all yield criteria are strain-based. Therefore, rather than reprogram this portion of the model, all strain in the material model is separated into elastic strain (the stress divided by the elastic modulus) and inelastic strain (the total strain minus the elastic strain). The creep strain caused by stress from the applied loads and any internal force redistribution is calculated explicitly in Step No. 4.

4) The incremental free creep strains caused by the elastic strains from the applied loads and any internal force redistribution occurring during the time step (from Step No. 3) are calculated. These elastic strains are assumed to be applied as a step function half-way through the time step. The applied loads are assumed to be gradually applied during the time step to simulate the gradual placement of soil over the structure in the field. A zero time step can be input for immediately applied loads.

5) The relaxation method is used to calculate the effects of creep and shrinkage at each node or cross section of the structure. First, Equations 4.7 and 4.8 are used to calculate the force and moment required to restrain the summed free creep and shrinkage distributions that occur during the current load/time step at each structural node. The cross sectional properties in Equations 4.7 and 4.8 are calculated using only the current uncracked portion of the concrete cross section. These equations

are modified slightly in that the thrust and moment required to resist the free temperature strain in both the concrete and reinforcing steel in the cross section are added in with the restraining thrust and moment calculated with Equations 4.7 and 4.8. The effective modulus is used in this calculation since it is also used in Equations 4.10 and 4.11 to calculate the total strain distribution. No internal stress redistribution is created by temperature strains since the concrete and steel are assumed to have the same coefficient of expansion. However, it is important to include these strains in the total strain distribution calculated in the next step so that the effects of these inelastic strains are included in the solution of the global system of equations for the finite element mesh.

6) In the second step of the relaxation method, the total strain increment induced by creep and shrinkage is calculated by applying the force and moment calculated in Step No. 5 to the effective transformed cross section at each structural node using Equations 4.10 and 4.11. The change in the reinforcing steel force is calculated using Equation 4.12 and the change in the concrete stress distribution is calculated using Equation 4.13. The change in steel stress is calculated using the change in steel force in Equation 4.12. The free temperature strain is subtracted out of the total strain before calculating the steel force in Equation 4.12. The change in the elastic concrete strain is calculated by dividing the change in the concrete stress calculated using Equation 4.13 by the concrete elastic modulus E_c. The creep plus temperature plus shrinkage strain is the difference between this elastic strain and the total strain calculated using Equations 4.10 and 4.11. The effective modulus is used to calculate internal stress redistribution as shown in Equations 4.8 through 4.11 so that the "secondary" creep strains, which are caused by the concrete stresses from internal stress redistribution during the time step, are implicitly included in the calculated creep strains.

7) The total strain distribution induced by creep, shrinkage, and temperature strains from Step No. 6 and the elastic stiffness parameters at each node are used to calculate the applied moment and thrust corresponding to the total strain distribution at each node. These internal forces are stored as a "pseudo" force vector. Elastic section properties (based on the concrete elastic modulus, not the effective modulus) are used in this step since elastic structural stiffness parameters calculated in Step No. 3 are used in the global stiffness matrix and the pseudo force vector will be used to impose the creep, shrinkage, and temperature strains, as well as the elastic strains from internal stress redistribution in the global system of equations.

8) The applied X and Y direction loads which cause the thrust at each node in Step No. 7 are calculated and these loads and the moment from Step No. 7 are stored in a "pseudo" load vector. These are the loads which, when applied to the elastic structural stiffness matrix, cause the total strains (and therefore deflections) associated with creep, temperature, and shrinkage during the current time step in a determinate structure. The external loads applied during the load/time step are also included in the loads vector.

9) The global system of equations for the finite element mesh is solved with updated elastic stiffnesses for soil and structural elements and updated states for interface elements. The pseudo loads vector from Step No. 8 is added into the global loads vector so that the deflections associated with creep and shrinkage will be included in the calculated deflections.

10) The internal forces in the structural elements are calculated based on the calculated deflections and the elastic element stiffness matrices. The pseudo force vector from Step No. 7 is subtracted out from these internal forces because none of the strains used to calculate the pseudo loads (i.e. creep, shrinkage, temperature, and elastic strains from internal stress redistribution) directly affect the internal loads. In a determinate structure, the internal forces are not affected by the additional deflections/rotations caused by the pseudo loads in the loads vector, and the "real" internal forces which remain after the subtraction of the pseudo forces are the same as those which would have been calculated in an analysis which ignored inelastic strains. If indeterminate boundary constraints restrain the deflections/rotations caused by the pseudo loads, or soil loads are affected by these deflections, then the internal forces which remain after the subtraction of the pseudo forces are different than those which would have been calculated in an analysis which ignored inelastic strains.

11) The incremental internal forces at each structural node (the moment and thrust) from Step No. 10 are sent to the subroutine calculating the elastic strain distribution and effective concrete area at each node in Step No. 3. The incremental elastic strain from applied loads (including soil loads) and internal load redistribution that occurs during the current load/time step are calculated. The elastic strains calculated from the internal stress redistribution in Step No. 6 are included in the logic used in this subroutine to determine the effective (uncracked) concrete area and the elastic concrete and steel tangent modulus.

12) The convergence check, that normally occurs after each iteration in the CANDE code, is made. Based on the incremental stress and strain calculated in each structure and soil element, the tangent modulus is calculated for each element and compared to that assumed at the start of the iteration to construct the global stiffness matrix. If the stiffnesses for all elements do not converge within the convergence criteria, the iteration is repeated. In this case the incremental elastic strains from Step No. 11 are used to calculate creep strains in Step No. 4 and the succeeding steps are repeated.

13) When convergence is attained, incremental elastic strains that developed during the load step, including the strains from internal stress redistribution, are stored and used to calculate the free creep occurring during subsequent load steps. Also, the total elastic, total creep, shrinkage, and temperature strain distributions are updated at each node. The program continues in the same manner with all subsequent time steps included in the input deck. Time steps were chosen to coincide with dates when the culvert response was monitored.

The output of the CANDE code has been modified to output the elastic strains, the creep strains, and the total strains at the top and bottom surface and at mid-depth of each structural node. The change in temperature strain and the total accumulated shrinkage strain since the first load/time step are also printed out for each structural member. The CANDE code also outputs internal forces at all structural nodes, the X and Y direction deflections at all nodes, the X, Y, and X-Y direction stress and strain in the soil elements, the principal stresses in each soil element, the deflections of the structure and soil nodes in each interface element normal to the soil-structure surface and tangent to the structure surface, the interface forces in each interface element, and the state (i.e. fixed, slip, etc.) of each interface element.

4.6.4 Structural Analyses by Other Researchers Which Consider the Effect Creep and Shrinkage Strains. The multi-step method of determining creep and shrinkage strains, using the principle of superposition to determine the creep strain produced by a nonconstant stress history, has been used to calculate the response of reinforced concrete structures in finite element analyses by a number of researchers. Several of these analyses have calculated the response of frame members taking into account such variables as concrete cracking,[62] temperature stains and large displacement effects,[63] prestressed members,[63] and concurrent creep of wood shoring prior to removal of the concrete formwork.[64] The response of shell structures subject to creep and shrinkage, such as HP cooling towers and nuclear reactor containment structures,[57] have been investigated with this approach. This approach has also been used to study the effects of creep and shrinkage on the stress distribution of a masonry system consisting of an axially loaded masonry block wall, an outer brick wall, and the mortar collar joint connecting the two walls.[65] A variety of creep and shrinkage prediction models have been used in these analyses ranging from the Bazant-Panula method, to the ACI 209 Committee method, to the CEB-FIP method, to curve-fits of specific measured data.

There are also a number of structural analyses in the literature where the response reinforced concrete response subjected to creep and shrinkage is calculated using a single-step analysis, either the age-adjusted modulus method or a similar simplified approach.[66,67,68] These cases consider constant applied loads and investigate the effect of creep and shrinkage on a variety of structural members including prestressed concrete tanks and composite beams where a concrete deck is connected to a steel beam with shear studs. A single-step analysis has also been used to determine the effects of creep and shrinkage on buried prestressed concrete pipe.[69] However, in this analysis the effect of soil load was not included since the aim of the study was to determine the effects of creep and shrinkage on the prestress forced in the pipe.

In large part the analyses mentioned have been studies intended to calculate the probable effects of creep and shrinkage on design – particularly the effects of stress redistribution caused by shrinkage and creep strains. There are very few cases of reported comparisons between measured structural response and long-term response calculated taking into account creep and shrinkage. In one published comparison in Reference 63, the midspan deflection of a simply-supported prestressed concrete beam subjected to constant load was calculated using a time-stepping finite element analysis which included the effects of creep and shrinkage and compared with data measured over a seven year period. The calculated and measured deflections under two different applied loads both matched within 10%. Free creep and shrinkage strains were predicted using the ACI 209 Committee method. The nonconstant stress history (due to internal stress redistribution) was considered in the analysis using an approach based on the principle of superposition of creep strains. In another comparison, in Reference 69, there was good agreement (within 10 - 15%) between the calculated and measured stress in the prestressing wire of prestressed concrete pipe stored above ground at 70% relative humidity without applied load. The tests were conducted over a twenty-five year period. The ACI 209 method was used to calculate the free creep and shrinkage, and an empirical formula was used to account for stress relaxation in the prestressing wire and a single-step structural analysis. The effective modulus method was used in the analysis, but evidently no aging coefficient was used.

In summary, the basic method used to modify the CANDE code so that it will calculate structural response, including the effects of creep and shrinkage strains, has been used by a number of previous researchers. However, no case was found in the literature where this method was used to investigate the influence of creep and shrinkage strains on soil-structure interaction. It is also evident that there has been little comparison between long-term measured structural response and calculated response considering the effects of creep and shrinkage. The few comparisons which were located in the literature reported good agreement for simple structural systems.

4.7 Validation of the Modified CANDE Code

Four validation cases were used to validate the calculation scheme in the modified CANDE code for determining structural response including the effects of creep and shrinkage strains. In each validation case a constant load was applied to a reinforced concrete beam. The type of response, the number of redundant supports, and the amount of cracking in the beam varied in each validation case as indicated below.

Validation Case #1: The total strain distribution (including creep and shrinkage strains) and internal stress redistribution in a determinate reinforced beam subjected to creep from a constant load and shrinkage with no concrete cracking is calculated at the cross section with maximum stress.

Validation Case #2: The total strain distribution is calculated for a case identical to Case #1 except that the applied load causes concrete cracking in the cross section.

Validation Case #3: The deflections in a cracked determinate beam subjected to creep and shrinkage is calculated.

Validation Case #4: The internal force redistribution in a cracked indeterminate beam subjected to creep and shrinkage is calculated.

In each of these cases calculated results were compared to solutions to the same problems presented in Reference 56. In Reference 56 the problems are worked using a single-step analysis with the age-adjusted elastic modulus method as discussed in Section 4.6.1. Since this analysis approach results in relatively little error compared to more complex, multi-step analyses for these types of problems,[56] they are used here to validate the modified CANDE code. The creep and shrinkage predicted with CANDE were forced to match those used in Reference 56 so that the calculated results could be directly used to check the validity of the new structural analysis approach in the modified CANDE code. The computer coding of the free creep and shrinkage prediction methods into the modified CANDE code was checked with direct comparisons between the free creep and shrinkage strains predicted with CANDE and those calculated with identical input conditions using a spreadsheet. Figures 4.31 through 4.34 describe each validation problem and show the comparison of the solution from CANDE to that in Reference 56.

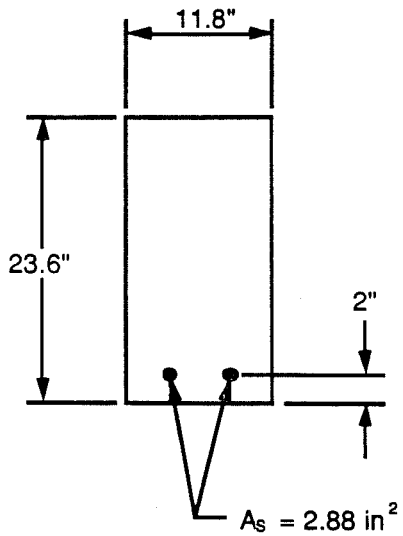

Applied Bending Moment = 30 kip-ft

φ = creep coefficient

ε_{sh} = shrinkage strain

t_o = concrete age when load applied = 28 days

t_m = maximum concrete age = 10,000 days

Case 1 $\varphi(t_m, t_o) = 3.0$ $\varepsilon_{sh}(t_m) = 6 \times 10^{-4}$

Case 2 $\varphi(t_m, t_o) = 3.0$ $\varepsilon_{sh}(t_m) = 0$ (No Shrinkage)

Comparison of Strains Calculated with CANDE Program to Reference 58*

	Initial Loading	Case 1		Case 2	
	@ t_o	Ref. 58 @ t_m	Calculated @ t_m	Ref. 58 @ t_m	Calculated @ t_m
Top Elastic Strain	82	110	107	70	71
Top Total Strain	82	1025	1010	287	286
Bottom Elastic Strain	-74	-138	-133	-45	-47
Bottom Total Strain	-74	81	77	-197	-196
Steel Strain	-60	160	155	-155	-155

*Note: All Strains ($x10^{-6}$), compression positive

Figure 4.30 Validation Case 1

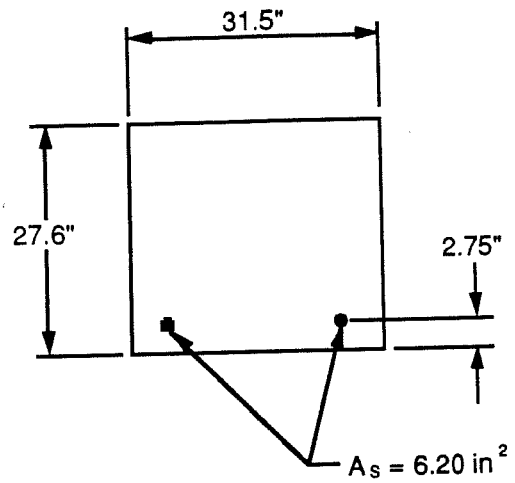

SECTION A-A

Applied Bending Moment = 221 kip-ft

φ = creep coefficient
ε_{sh} = shrinkage strain
t_o = concrete age when load applied = 28 days
t_m = maximum concrete age = 10,000 days
$\varphi(t_m, t_o)$ = 3.0
$\varepsilon_{sh}(t_m)$ = 5×10^{-4}

Comparison of Strains Calculated with CANDE Program to Reference 58*

	Initial Loading @ t_o	Reference 58 @ t_m	Calculated @ t_m
Top Elastic Strain	261	210	204
Top Total Strain	261	1370	1330
Bottom Total Strain	-750	-886	-869
Steel Strain	-648	-655	-650

Note 1: All Strains ($x10^{-6}$), compression positive
Note 2: In CANDE analysis neutral axis gradually changes from 20.5" above bottom face at t_o to 17.5" @ t_m. No such change occurs in one-step calculation in Reference 58

Figure 4.31 Validation Case 2

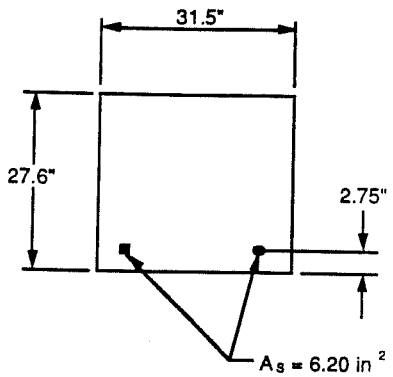

SECTION A-A

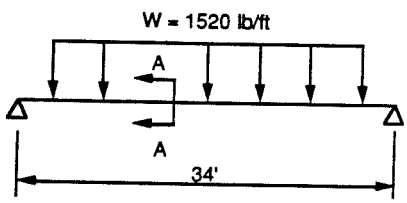

φ = creep coefficient
ε_{sh} = shrinkage strain
t_o = concrete age when load applied = 28 days
t_m = maximum concrete age = 10,000 days
$\varphi(t_m, t_o)$ = 3.0
$\varepsilon_{sh}(t_m)$ = 5×10^{-4}

Comparison of Midspan Deflection Calculated with CANDE Program to Reference 58

	Initial Loading @ t_o (Inches)	Reference 58 @ t_m (Inches)	Calculated @ t_m (Inches)
Midspan Deflection	0.63	1.52	1.42
Cracked Depth	20.5	20.5	15.6

Figure 4.32 Validation Case 3

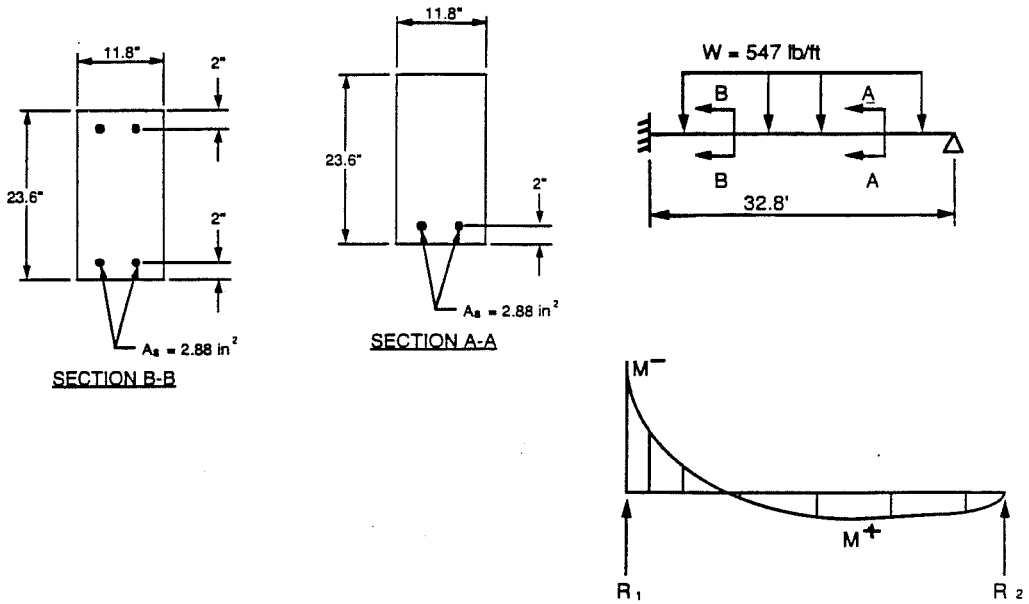

φ = creep coefficient
ε_{sh} = shrinkage strain
t_o = concrete age when load applied = 28 days
t_m = maximum concrete age = 10,000 days
$\varphi(t_m, t_o)$ = 2.5
$\varepsilon_{sh}(t_m)$ = 6×10^{-4}

Comparison of Internal Forces Calculated with CANDE Program and Reference 58

	Reference 58			Calculated		
	@ t_o	@ t_m	% change	@ t_o	@ t_m	% change
M^+ (kip-ft)	45.0	31.3	-30	48.0	33.4	-31
M^- (kip-ft)	-64.4	-102.5	+59	-66.8	-107.2	+60
R_1 (kips)	10.9	12.1	+11	11.0	12.3	+11
R_2	7.1	5.9	-17	6.9	5.64	-18

Figure 4.33 Validation Case 4

In Validation Case #4 it was not possible to match the moment and reaction force distribution from the applied load (prior to creep and shrinkage) reported in Reference 56 exactly with the CANDE code. The solutions in Reference 56 were made using hand calculation methods rather than a finite element analysis. In the hand solution, the cracked depth and beam length over which cracking occurs were assumed based on the stresses in the uncracked member. However, the iterative method in the CANDE program ensures that the stress distribution calculated with the final thrust and moment distributions and the stress distribution assumed to calculate the structural stiffness parameters are identical. Therefore, the final thrust and moment distributions are calculated taking into account all concrete cracking. In spite of this, a close approximation of the initial internal force distribution (prior to creep and shrinkage) was achieved with the CANDE validation run, as shown in Figure 4.34, and the change in the internal force distribution due to creep and shrinkage strain calculated in Reference 56 is closely matched by the output from the modified CANDE code.

In general, the comparisons in Figures 4.30 through 4.33 show that the elastic strains, total strains, internal forces, reaction forces, and deflections predicted with CANDE match those from Reference 56 quite well. All compared values are within 5% of each other except for the following two cases. In Validation Case #2 the elastic strains after internal stress redistribution at the original neutral axis location differ by 20%. In Validation Case #3 the deflections differ by 7%.

These differences are attributed to the fact that the solutions in Reference 56 were made using the age-adjusted elastic modulus method discussed above (a single step solution method) rather than with the step-by-step solution method incorporated into CANDE. Because of this difference, the solutions from Reference 56 do not consider any change in cracked depth with time while CANDE does consider this change. Internal stress redistribution in Validation Cases #2 and #3 causes the neutral axis to change with time during a creep analysis as indicated in Figures 4.31 and 4.32. Since T and M in Equations 4.7 and 4.8 are calculated primarily from creep strains in the area of concrete above the original neutral axis where all concrete stress from the applied load exists, and the effective area in Equations 4.10 and 4.11 includes all concrete area which is effective during the current load/time step, the downward movement of the neutral axis reduces the magnitudes of the strain, and therefore the redistributed stress in the concrete relative to that which would be calculated assuming no movement of the neutral axis. For Validation Case #2, where creep and shrinkage cause an small increase in the steel tensile force, the gradual downward movement of the neutral axis causes the increase in concrete compressive force that offsets the increase in the steel force to be distributed over a larger area and thus has a smaller magnitude than that calculated with the single-step analysis in Reference 56.

In Validation Case #3 the downward movement of the neutral axis in the CANDE analysis gradually increases the moment of inertia, thereby reducing the calculated deflection caused by later time creep compared to the deflection calculated with the single-step analysis in Reference 56 which assumes a constant location for the neutral axis. A larger difference would have been calculated if the CANDE code considered the effect of the increased effective concrete area on the deflection caused by loads applied during previous load steps (see Section 4.6.1). Validation Case #4 also includes concrete cracking but a realistic (nonzero) cracking strain was assumed for this case and the internal stress redistribution did not cause the concrete stresses near the crack tip to become compressive and thus close

the crack. The increased negative moment caused by creep and shrinkage did cause a slight reduction in the effective concrete area in the CANDE analysis.

CHAPTER 5

COMPARISON OF MEASURED SOIL-STRUCTURE RESPONSE PARAMETERS WITH VALUES CALCULATED WITH THE MODIFIED VERSION OF CANDE

In this chapter, soil and structure response parameters measured in two long-term field investigations of soil-structure interaction are compared with values calculated with the modified version of the CANDE code. In both cases, relatively detailed structural response measurements were made in a reinforced concrete culvert surrounded by an embankment fill. In the first comparison, values of strain, deflection, and soil-structure interface pressure measured on the instrumented cross sections of the BEBO culvert and reported in Chapter 3 are compared with calculated values. The finite element model of the culvert and the surrounding soil, and material properties used in the computer model, have also been explained in Chapter 4.

In the second part of the chapter, a similar comparison is made between soil pressures on the culvert, internal culvert strains, and culvert displacements measured in an arch culvert under fill depths ranging from 70 ft. to 150 ft. by the California State Department of Transportation (CALTRANS) and calculated values. The finite element mesh and material models used in the CANDE model are presented first in this section and followed by comparisons between reported measurements and calculated values.

5.1 Comparison of Measured Values in the BEBO Arch Culvert and Calculated Values

Figure 5.1 shows a typical instrumented cross section through the BEBO culvert. The figure shows the locations of the gages used to make measurements which are compared to calculated values. Crown deflections, mid-thickness strains at the crown and near the springline (or base) of the culvert, strains in the floor slab, and interface soil pressures near the crown and near the springline were measured at the two instrumented segments of the arch culvert under the high fill (24 ft.). An average of measurements made at similarly located points in the two arches is compared to calculated values except for cases where such values differ significantly (by more than 25%) from each other. Similar measurements were made at the one instrumented segment of arch culvert under the low fill (8.5 ft.), except no floor strains were measured since the floor slab under the low fill was not tied into the culvert footings.

Figures 5.2 through 5.11 show comparisons between measured BEBO culvert response and calculated values. In general, there was poor agreement between measured and calculated values using the original version of the CANDE code. A very marked improvement was achieved by using the modified version of the CANDE code with the creep and shrinkage prediction model. However, there were still some measured values where the agreement between measured and calculated values differed by a significant amount. Better agreement was achieved in a final set of analyses when the measured floor strains under the high fill and the measured soil pressure on the culvert sections under high and low

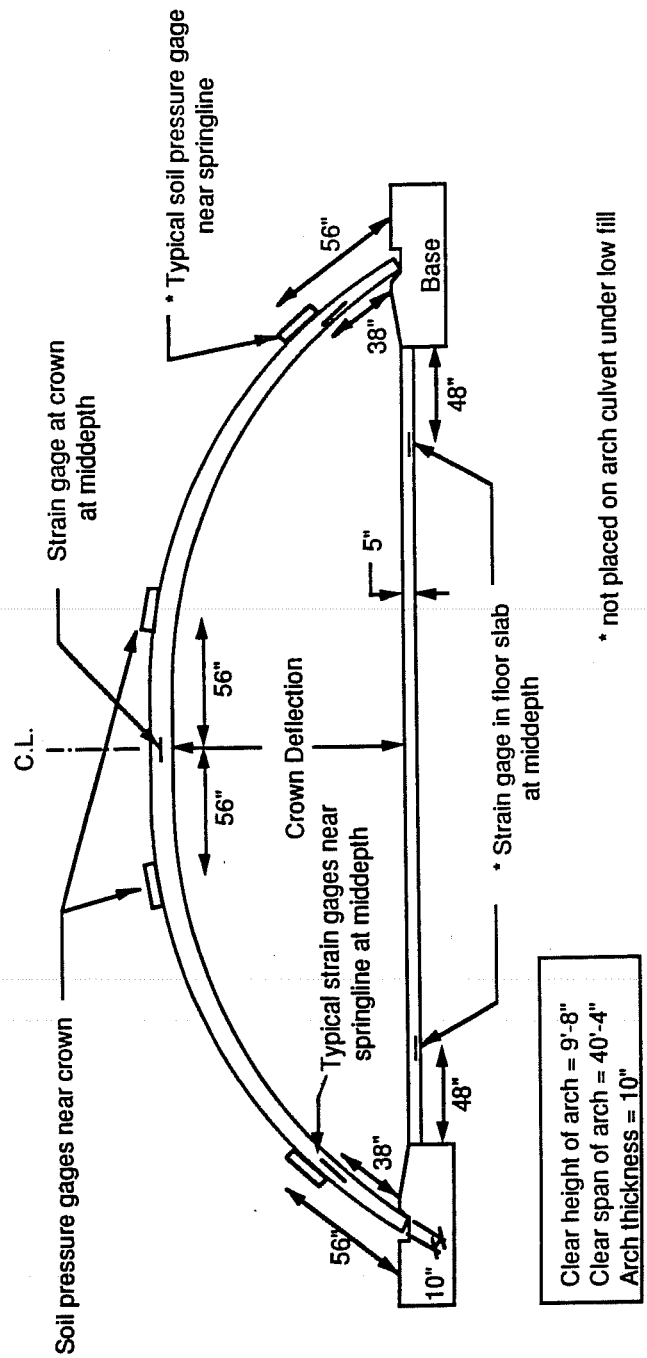

Figure 5.1 Location of soil pressure gages and strain gages in culvert

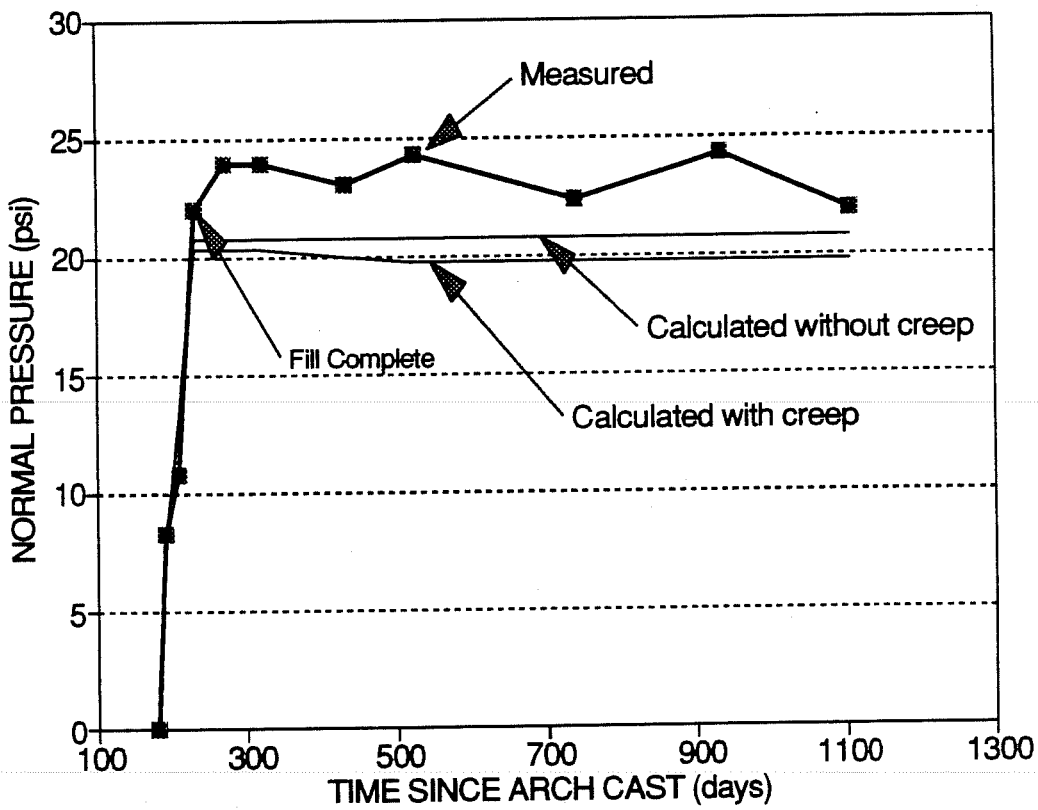

Figure 5.2 Comparison of calculated and measured soil pressure near crown of culvert under high fill

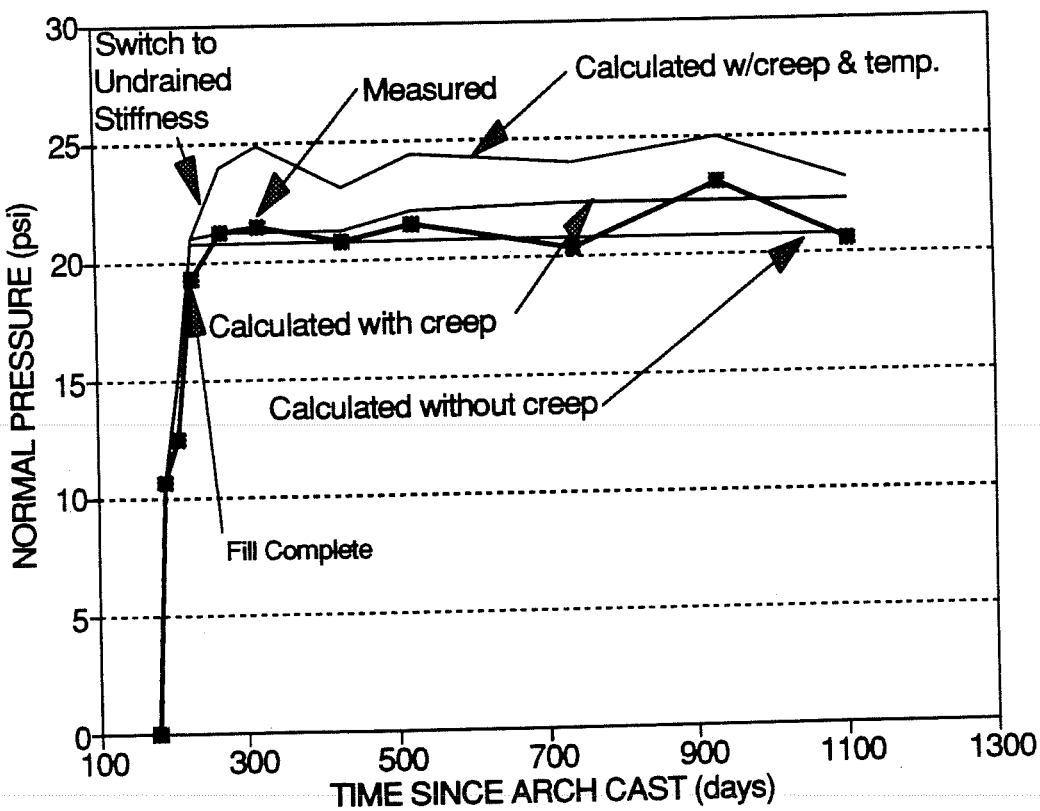

Figure 5.3 Comparison of calculated and measured soil pressure near springline of culvert under high fill

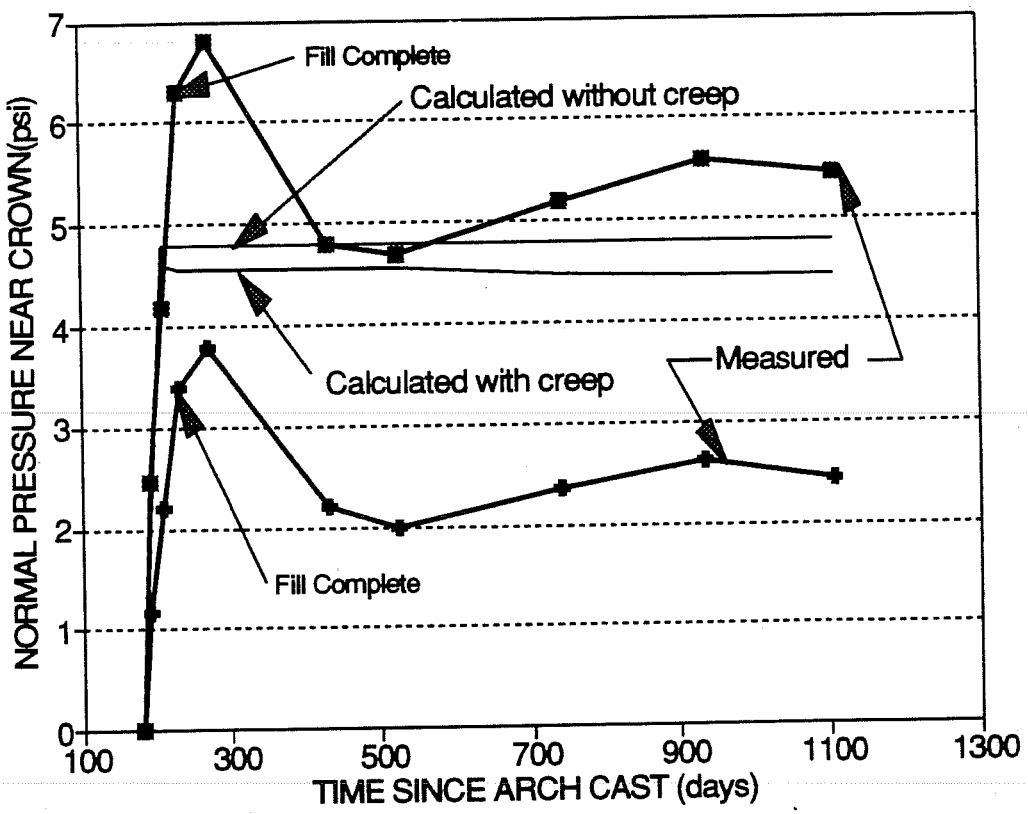

Figure 5.4 Comparison of calculated and measured soil pressure near crown of culvert under low fill

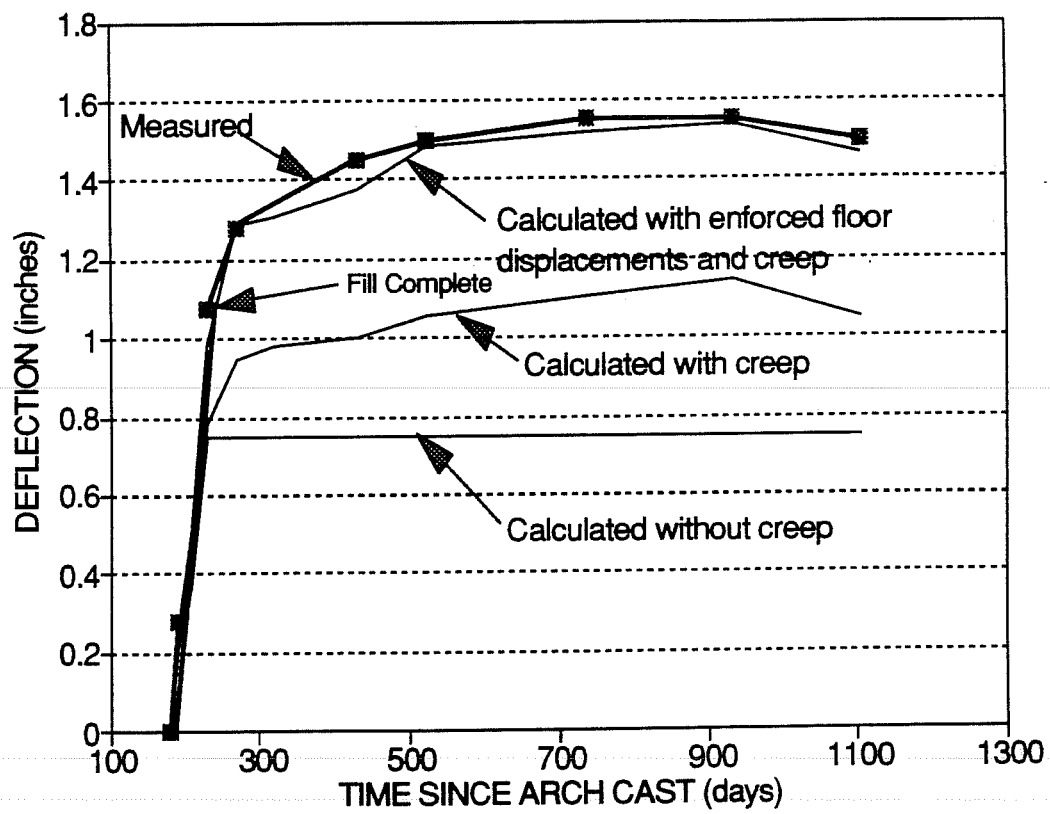

Figure 5.5 Comparison of calculated and measured crown deflection of culvert under high fill

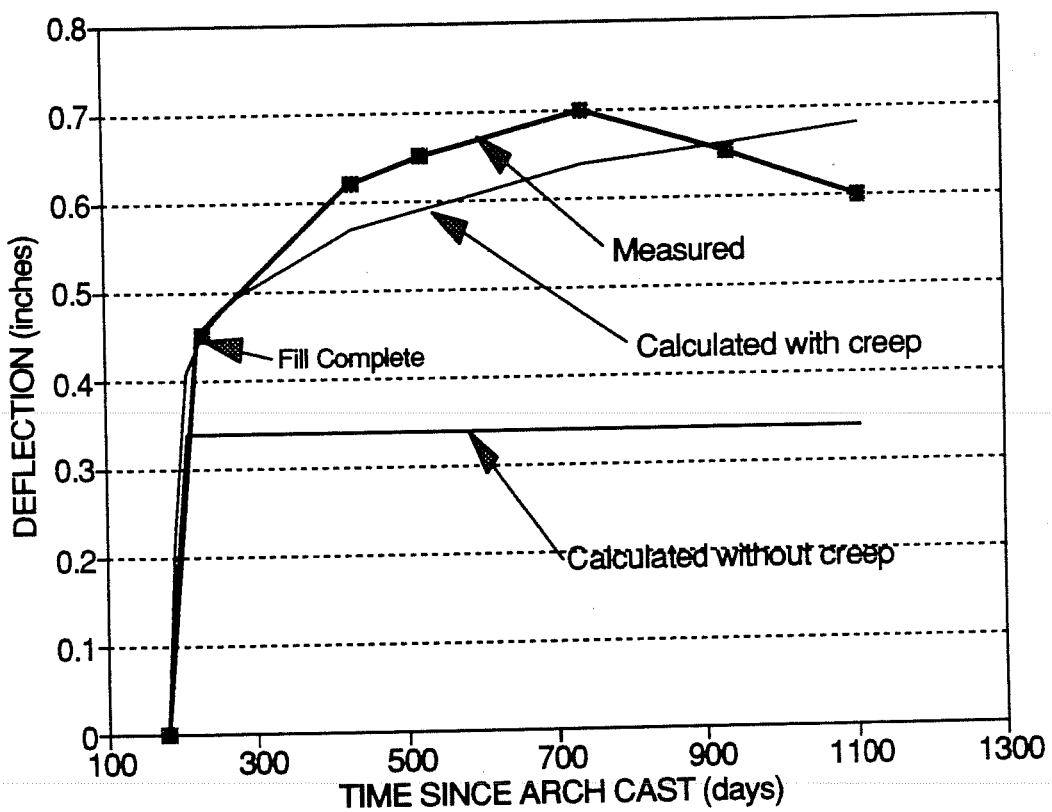

Figure 5.6 Comparison of calculated and measured crown deflection of culvert under low fill

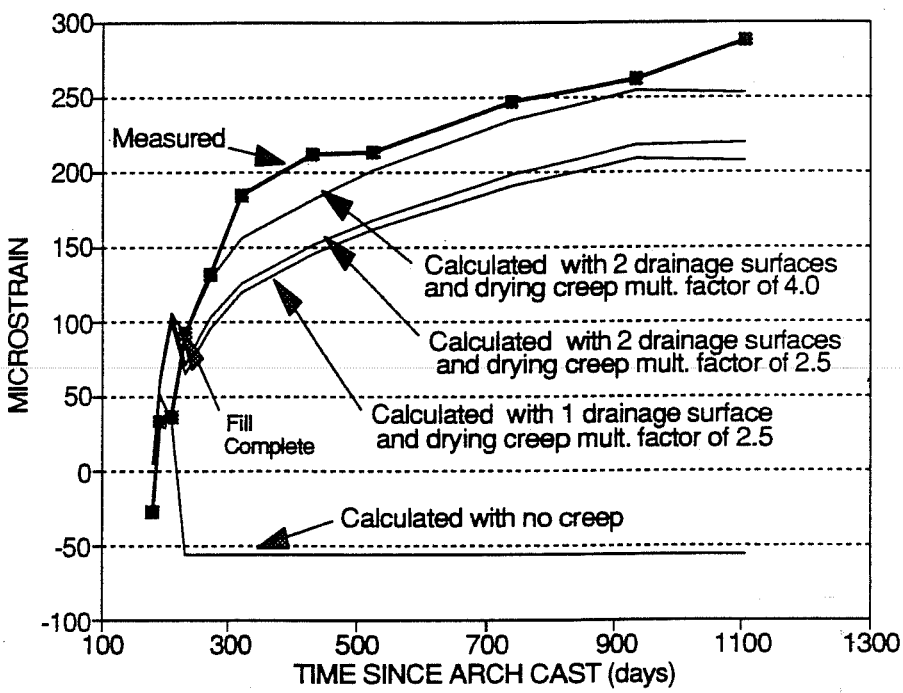

Figure 5.7 Comparison of calculated and measured mid-thickness strain at crown of culvert under high fill

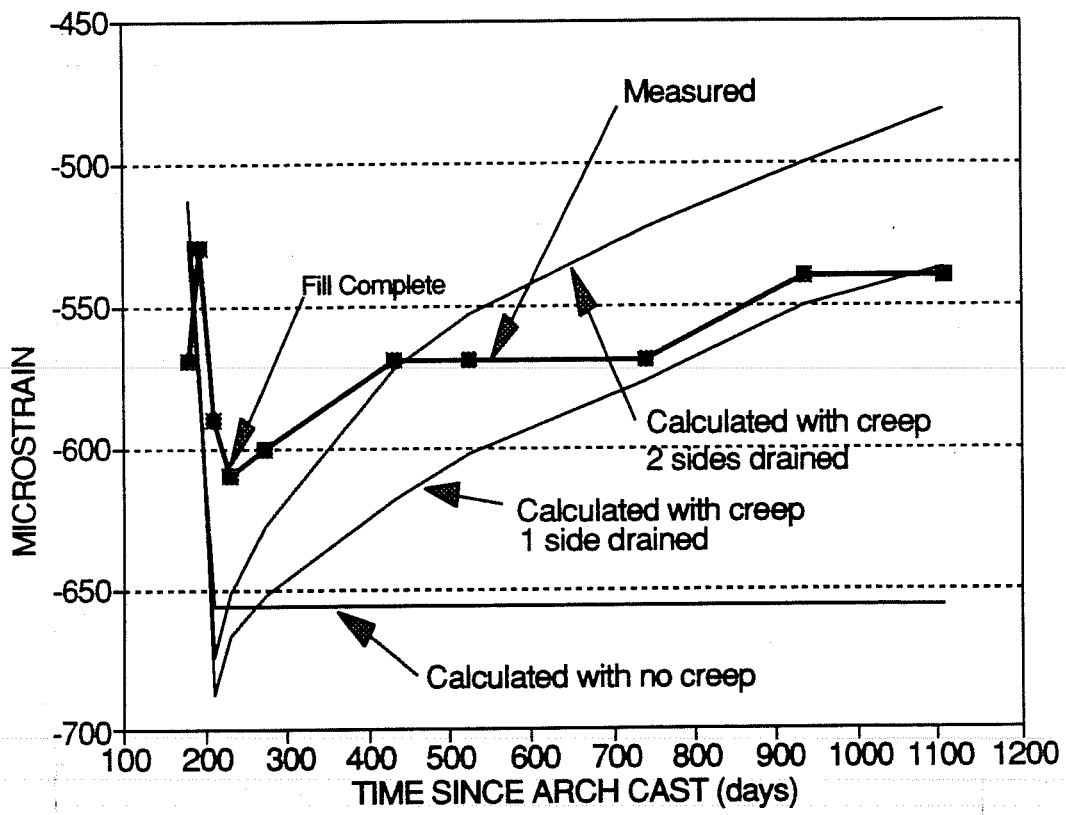

Figure 5.8 Comparison of calculated and measured mid-thickness strain at crown of culvert under low fill

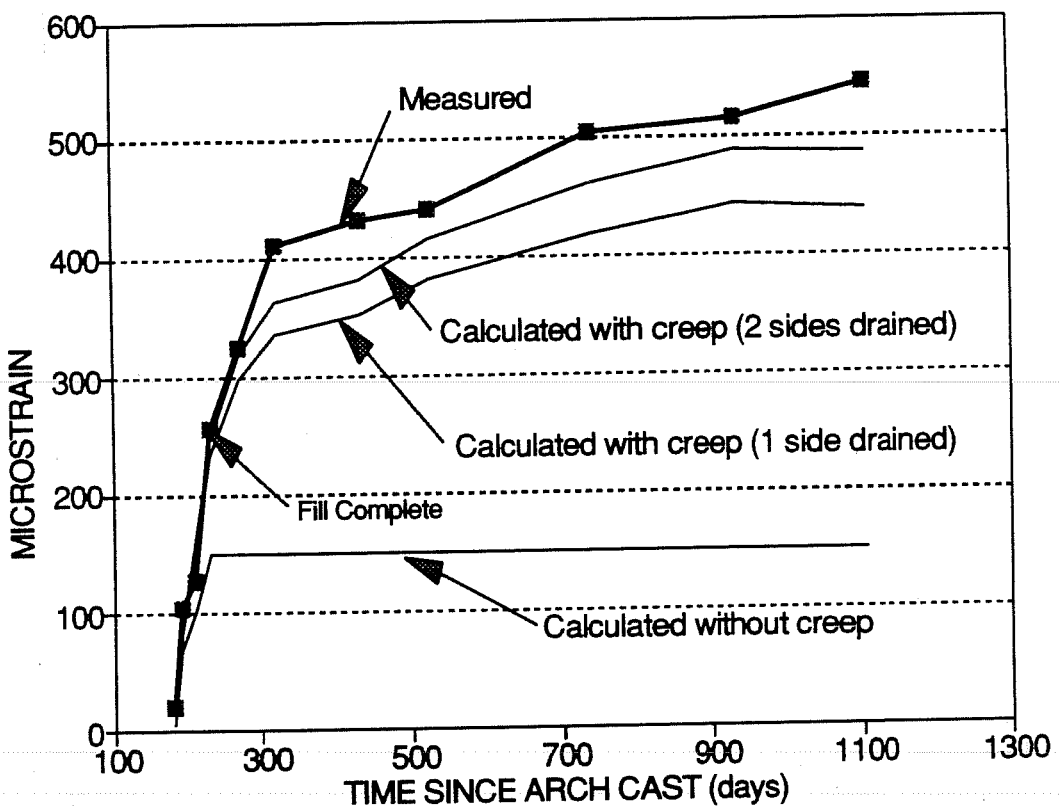

Figure 5.9 Comparison of calculated and measured mid-thickness strain near springline of culvert under high fill

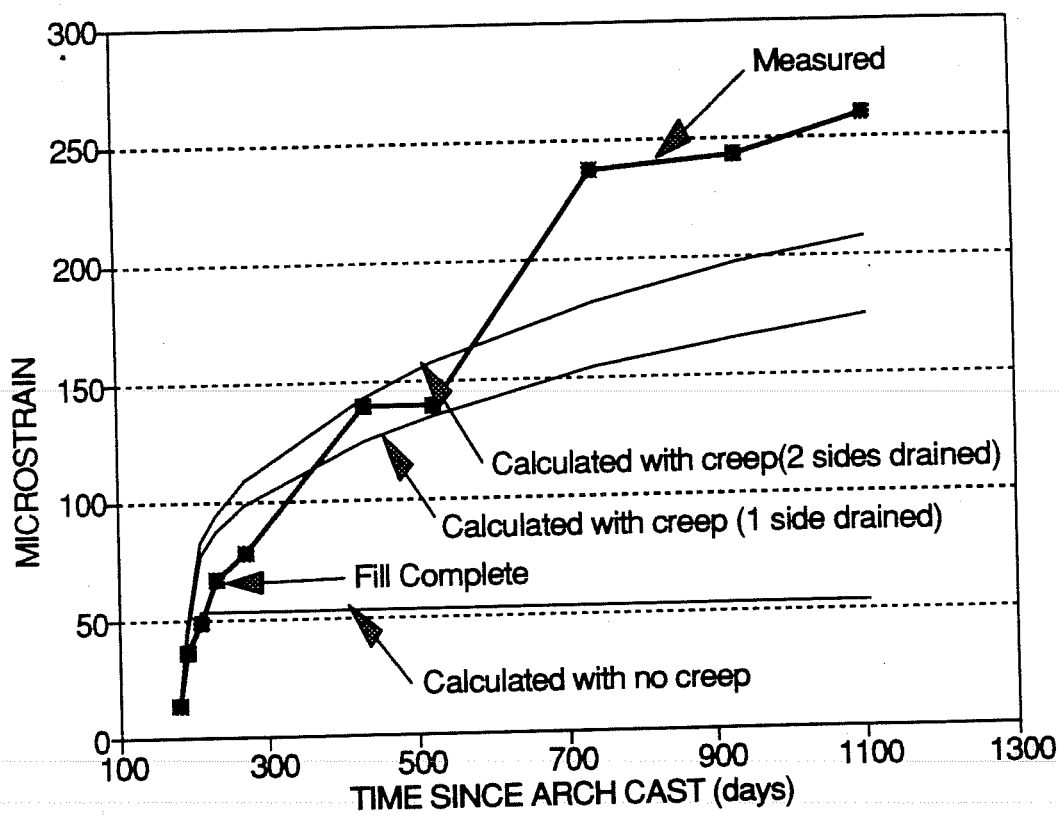

Figure 5.10 Comparison of calculated and measured mid-thickness strain near springline of culvert under low fill

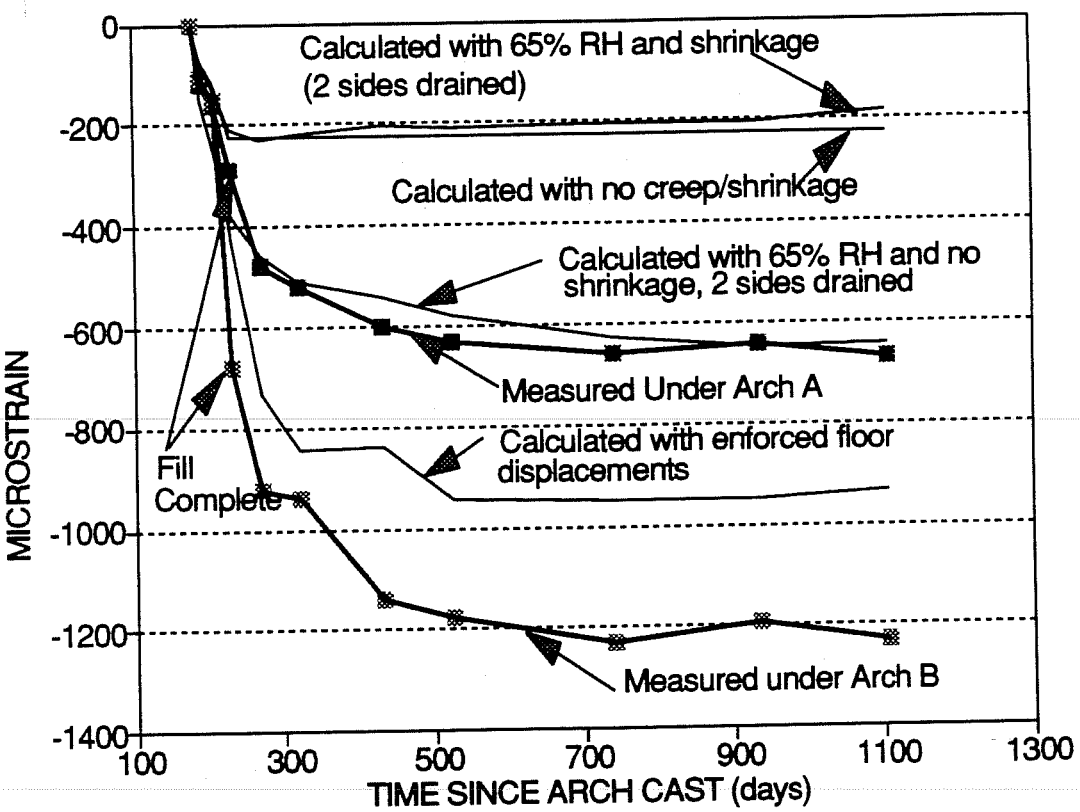

Figure 5.11 Comparison of calculated and measured mid-thickness strain in floor slab of culvert under high fill

fill were enforced. The measured values of these two parameters were enforced in order to judge how well the CANDE code calculated the culvert strains. The calculated values with, and without, the enforced floor strains and soil pressures are discussed in the following sections.

Free creep and shrinkage strains were predicted with the Bazant-Panula (BP) method as discussed in Chapter 4. The difficulties involved in modeling the effect of concrete cracking and drying at the soil-side surface of the culvert on creep were also discussed previously. The effect of concrete cracking on drying creep was approximated using the CANDE code by applying a multiplication factor of 2.5 on drying creep only at the nodes where cracking occurred on the inside face of the culvert. However, it was found that this had little effect because most of the creep in the culvert was basic creep and therefore the multiplier was only applied to a small percentage of the total strain and then only after cracking occurred. The effect of drying at the outside surface of the culvert in contact with the soil was investigated by running separate cases with only one culvert surface exposed to drying (or drained) in a 65% relative humidity, and with both culvert surfaces exposed to drying in a 65% relative humidity. These two cases are upper and lower bounds on the actual case since some drying occurs at the outside culvert surface but at a humidity which is probably significantly greater than 65%. The results from the two cases are not very different from each other because of the relatively small part of the total culvert strain caused by drying creep. However, the results from these two cases are shown on some of the comparisons where there is a noticeable difference.

The times shown in the figures are times since the precast culvert arch segments were cast. The floor slab was five days old when the arches were placed. The arches were placed at day 180 on the figures. The first measurements after the high fill was completed were made on day 229 and the first measurements after the low fill was completed were made on day 209. However, the slope in the low fill region shown in Figure 1.1 was not finished until approximately day 229.

5.1.1 Comparison of Measured and Calculated Soil Pressures on the BEBO Culvert. Figures 5.2 and 5.3 show a comparison of calculated and measured soil pressures on the culvert under high fill. Figure 5.2 shows the comparison at the soil pressure gages near the crown and Figure 5.3 shows the comparison at the gages near the springline, or base of the culvert. These gage locations are shown in Figure 5.1. The calculated pressures near both the crown and springline under the high fill compare relatively well to measured values regardless of the assumptions used to calculate the soil pressures. All the analyses used the temporary 5 psi surface pressures discussed in Chapter 4 to model compaction-induced soil pressures on the culvert. The measured and calculated soil pressures match very well at the first set of non-zero points in Figures 5.2 and 5.3 where the fill height is 2 ft. over the crown. At the second set of points, where the fill height is 9 ft. over the crown, the measured pressures are overpredicted by about 20%, since pore water pressure dissipation occurs gradually between these two fill heights in the field, whereas dissipation is assumed to occur suddenly after the fill height is 9 ft. in the analyses. The third set of non-zero points in Figures 5.2 and 5.3 shows that the calculated and measured soil pressures at the completion of fill are in good agreement (within 10%).

The post-construction portion of the pressure histories plotted on Figures 5.2 and 5.3 show that the measured seasonal fluctuations in soil pressure were not modeled by the CANDE code at the crown and were only modeled at the gages near the springline with some special assumptions. The measured

seasonal fluctuation consisted of a rise in the measured soil pressure occurring during summer months and a fall in pressure during winter months as discussed in Chapter 3. Since these fluctuations are not large compared to the total pressure, the calculated soil pressures are always within 20% of the measured soil pressures.

It was hypothesized in Chapter 3 that the measured post-construction pressure fluctuation may be due to the restraint provided by the surrounding compacted soil against temperature-induced expansion of the culvert. This possibility was modeled with the CANDE code by applying a temperature history based on the average temperature over the three days prior to the soil pressure measurement as discussed in Chapter 3. However, this only resulted in a small fluctuation in the culvert displacements and no appreciable increase in the interface pressure when the Duncan model soil stiffness parameters for a drained silty clay were used throughout the analysis as is the usual assumption as discussed in Chapter 4. In order to investigate this issue further, another CANDE run was made where the soil stiffness parameters were switched from those of the drained clay to those of the "stiff" undrained clay (shown in Figure 4.20) after the completion of fill because it was reasoned that the soil may respond as undrained during the relatively short duration (two to three months) of temperature-induced culvert deflection. This increase in soil stiffness and the corresponding fluctuation in calculated soil pressure at the gage location near the springline are shown in the top curve in Figure 5.3. The results from this analysis in Figure 5.3 show that, with an upper bound soil stiffness, the fluctuation, or change in measured soil pressure over time at the springline, is modeled relatively well as a temperature-induced phenomena. The large gradually increasing tensile strains measured in the floor were enforced in all the time-dependent analyses plotted in Figures 5.2 and 5.3 and, in the case where the post-construction soil stiffness was increased in Figure 5.3, this structural displacement caused an unrealistically large increase in springline pressure. A more realistic analysis would consider the soil stiffness against the creep-induced floor movement to be based on drained conditions, while the soil stiffness against the shorter duration temperature-induced culvert displacement to be based on undrained conditions. However, such an analysis can only be accomplished if consolidation is explicitly considered.

No results from an analysis considering the effects of temperature are shown in Figure 5.2 because no fluctuation in the calculated soil pressure near the crown occurred in analyses using either the drained or the undrained Duncan soil stiffness parameters. The interface pressure resulting from expansion or contraction of the culvert is totally dependent on the restraint caused by the soil stiffness, which, in turn, is heavily dependent on the soil state of stress. The fact that very low lateral stresses (some of which were tensile stresses) are calculated in the soil above the crown, while higher confining pressures (10-15 psi) are calculated in the soil near the springline, is probably responsible for the difference in the soil pressures caused by temperature-induced culvert movement at these two locations. The stresses calculated in the soil under the high fill are shown in Figures 5.12 through 5.14 and are discussed later in this chapter. The very low lateral soil stresses calculated near the crown do not include any lateral stresses in this soil "locked-in" by the compaction process since this process is not explicitly modeled. Therefore, the CANDE code may not be calculating any temperature-induced change in the interface pressure near the crown because it does not consider the actual soil state of stress in this region and thus underestimates the actual soil stiffness.

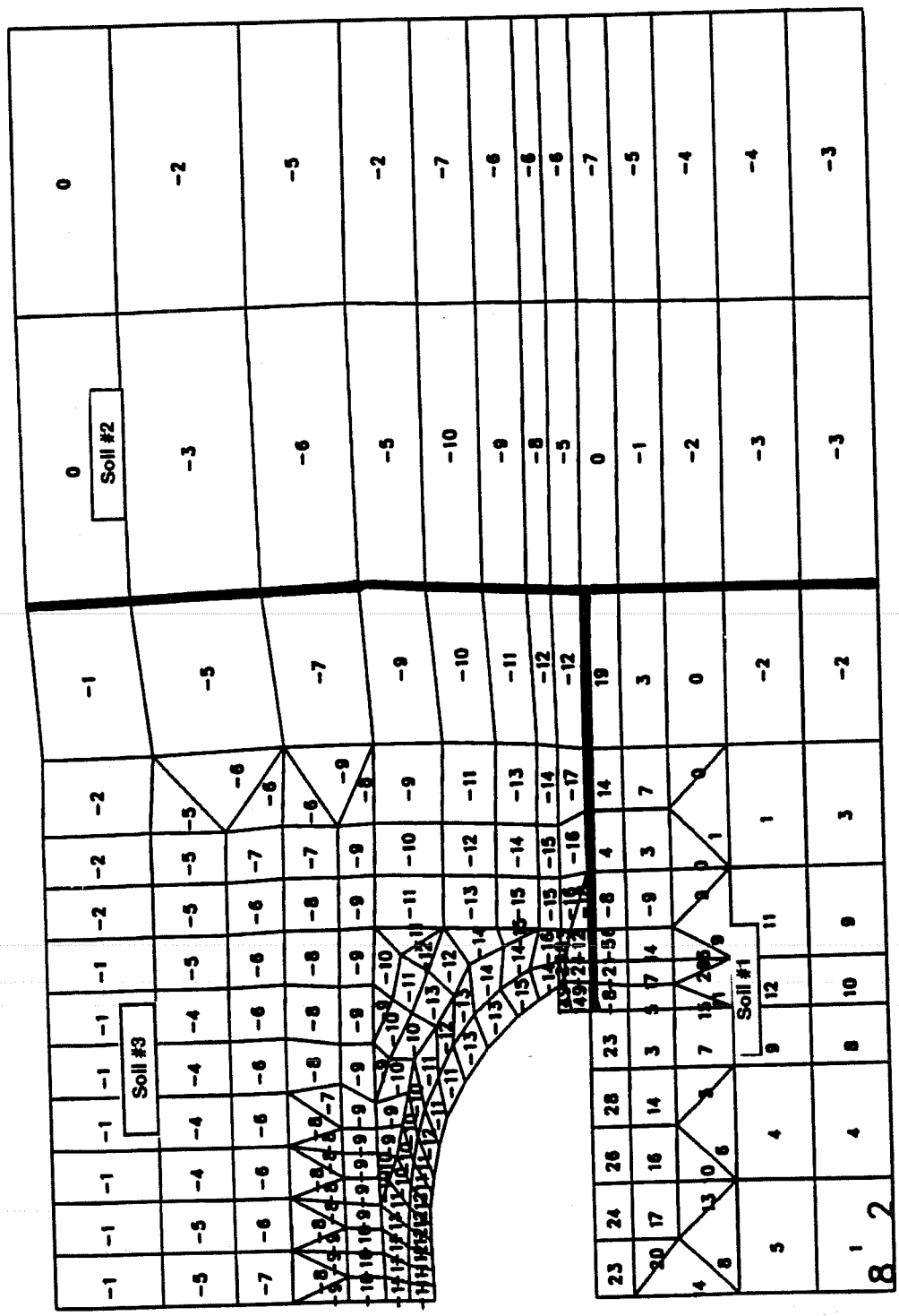

Figure 5.12 X-direction stresses in soil in high fill region

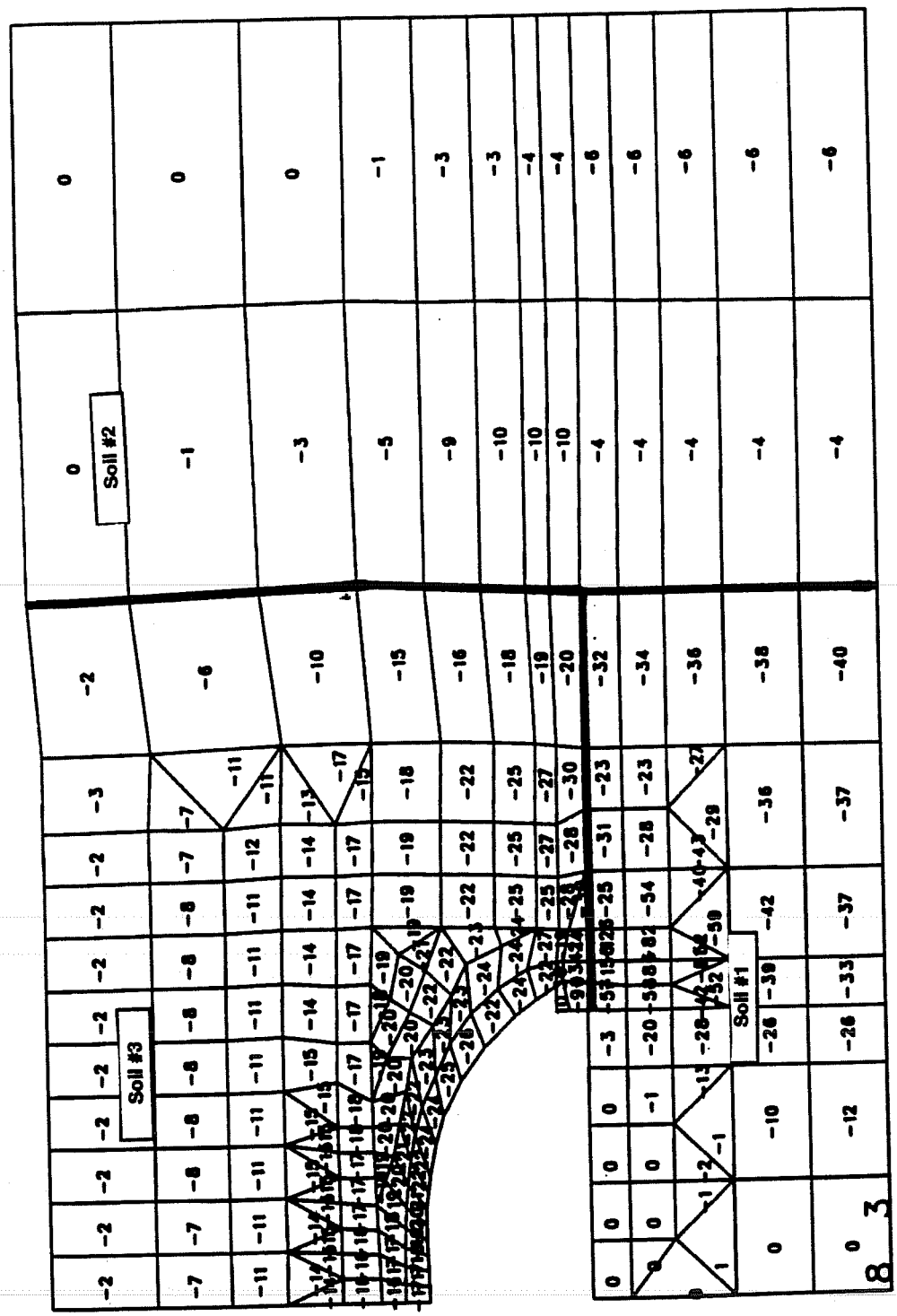

Figure 5.13 Y-direction stresses in soil in high fill region

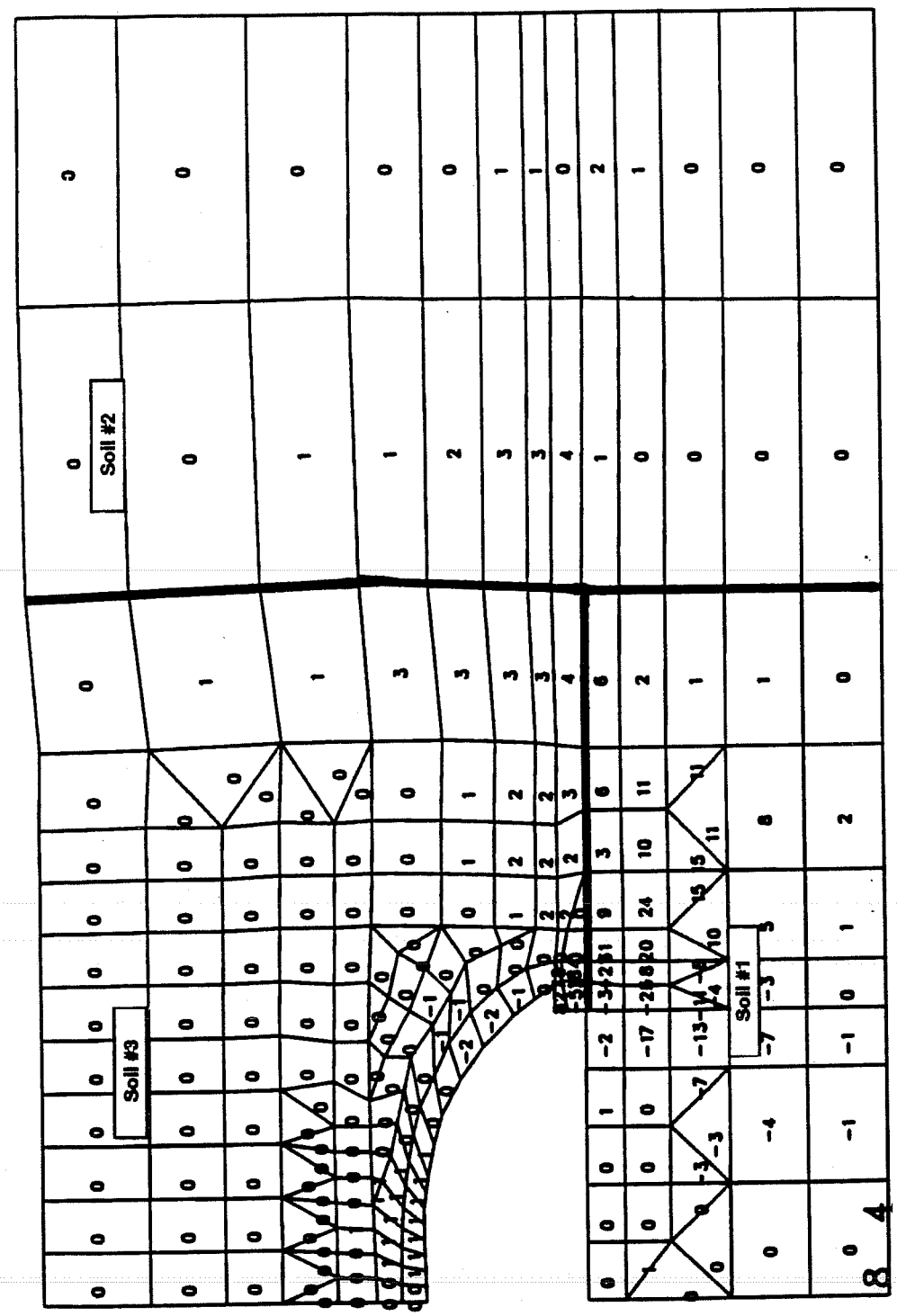

Figure 5.14 Shear stresses in soil in high fill region

The discussion above indicates that the measured post-construction pressure fluctuations in the soil pressure history are not well modeled with the CANDE code. Since all culvert response is dependent on the applied soil pressure, the measured post-construction soil pressures are enforced in the subsequent CANDE analyses which are compared to measured strains and deflections in the culvert by applying and removing an intermittent 2 psi surface pressure to the finite element mesh. This is discussed in more detail in the next section.

Figure 5.4 shows a comparison between measured and "calculated" soil pressures at the gages near the crown of the culvert under low fill. An effective soil density of 75 pcf was used in the analysis of the low fill region because the average measured soil pressure at the top of the culvert in this region was approximately one-half of that corresponding to the overburden pressure calculated with the measured soil density of 128 pcf. The effective soil density of 75 pcf was used so that the CANDE code would calculate a pressure on the culvert crown near the average of the peak measured values as shown in Figure 5.4. Temporary compaction pressures, or post-construction surface pressures, were applied during the modeling of the low fill region for two reasons. First, there was no obvious increase in the measured soil pressure against the instrumented culvert cross section in this region during the placement of fill which could be attributed to compaction; and second, the fluctuation in the long-term measured soil pressure is relatively small (less than 1 psi over most of the monitoring period).

Possible reasons why the measured soil pressure at the low fill culvert is much less than the overburden pressure, and therefore less than calculated pressures using the full measured soil density, are discussed in Chapter 3. It is hypothesized that the presence of a slope along the direction of the flow through the culvert (out of the page in Figure 5.1) over the instrumented segment of the culvert is the cause for the low soil pressure on the culvert.

The data in Figures 5.2 and 5.3 show that soil pressures on the culvert under the high fill are not significantly affected by creep and shrinkage. Both the analysis and the measured culvert response show this. The difference between soil pressures calculated considering the effects of creep and shrinkage and neglecting these effects is less than 10%. Also, the change in measured post-construction soil pressure is very slight (less that 10% ignoring the fluctuations) in spite of the fact that a large change in measured culvert deflection (50% increase) and elongation in the floor slab occurred. The data in Figure 5.4 for the culvert under the low fill, which also undergoes significant post-construction crown deflection, shows that there may be some reduction in crown interface pressure caused by increased long-term structural displacement for this case although it is still small (approximately 20% ignoring fluctuations) compared to the change in midspan deflection (nearly 100%). It is also possible that the change in soil pressure in the low fill region was influenced by gradual movement of the nearby slope. These facts indicate that the soil pressures on the BEBO culvert are not very sensitive to structural deflections or structural stiffness for the range of deflections occurring in this study. This is consistent with the data reported by other researchers who have investigated soil-structure interaction between reinforced concrete structures and a surrounding compacted backfill.

5.1.2 Comparison of Measured and Calculated Midspan Culvert Deflections. Figures 5.5 and 5.6 show comparisons of the calculated and measured culvert deflection history at the crown under high and low fill respectively. The deflection is that which occurred after the initial placement of the culvert

and therefore is the deflection caused by the placement of the soil fill. The factors affecting the deflection of the culvert under high fill include creep and shrinkage strains, especially the relatively large post-construction displacement of the floor slab, and the applied soil pressure. The displacement of the floor slab is important because, under the high fill, the floor slab, which is tied into the culvert footings, acts to prevent spreading of the culvert footings and corresponding downward deflection of the culvert crown. Tensile creep in the floor slab allows the culvert footings to spread more and therefore allows more deflection of the culvert near the crown. The measured fluctuation in soil pressure on the culvert under the high fill was enforced with applied surface pressures for all cases shown on Figure 5.5 except for the case where no time effects (no creep) were considered. A 2 psi surface pressure was applied soon after fill was completed (at time 250 days in Figure 5.2), the pressure was reduced by 1 psi at time 433 days, increased back to 2 psi at time 527 days, and reduced to zero for the final time since the last measured soil pressures are close to those measured at the completion of fill.

Figure 5.5 shows that modeling creep (and shrinkage) in the culvert and floor slab cause the calculated deflections to compare much better to measured values than the analysis which did not consider creep and shrinkage. As stated above, the measured soil pressure fluctuation was also included in the analyses considering creep and shrinkage but it only affects the calculated displacements by about 0.1 in. However, the deflections calculated with the creep and shrinkage strains predicted by the CANDE code and the measured soil pressure fluctuation were still about 40% less than measured values. The creep and shrinkage model in the CANDE code only predicts approximately one-fifth of the total long term tensile strain measured in the floor slab. This is discussed later in this section. Therefore, an analysis was performed where the measured floor strains were enforced and, as Figure 5.5 shows, the comparison improved significantly. However, the calculated deflection history was still approximately 5 to 10% less than the measured deflection history. The calculated culvert strains were also approximately 10 to 15% less than the measured strains. Therefore, a final analysis was performed where the creep strains in the culvert were multiplied by a 1.4 increase factor. This caused the calculated strains to match the measured values better and also caused the calculated crown deflection history to match the measured deflection history very well.

Figure 5.6, which compares calculated and measured crown deflection in the culvert under low fill, shows some of the same trends as Figure 5.5. Figure 5.6 shows that including creep (and shrinkage) in the calculated culvert response causes a very marked improvement in the ability of the CANDE code to model the measured culvert deflections. The calculated culvert deflections in Figure 5.6, which include the effects of creep and shrinkage, are within 10% of the measured values. This is good considering the difficulties involved in modeling the applied soil pressures. The 1.4 increase factor on the calculated creep strains causes the displacements to be overestimated by a small amount (10% to 20%). For most of the monitoring period the analysis with the creep and shrinkage calculated by the BP model and the analysis with 1.4 times the calculated creep provide lower and upper bounds respectively on the measured displacements. The response of the floor slab in this region is not important because the culvert footings are not restrained by the floor slab. As mentioned above, an "effective" soil density of 75 pcf was used for all analyses of the culvert under the low fill and no "fine-tuning" of the calculated soil pressure with applied surface pressures was attempted.

5.1.3 Comparison of Measured and Calculated Strain at the Crown of the BEBO Culvert. Figures 5.7 and 5.8 show comparisons of measured and calculated strain at mid-depth through the thickness at the crown of the culvert under the high fill and low fill. Compressive strains are positive. The calculated total strains, which include all elastic, creep, temperature, and shrinkage strains, are compared to the measured values. Calculated temperature strains were very small (less than 10×10^{-6}). The figures show strains calculated for four cases: 1) no creep or shrinkage included in the analysis with CANDE; 2) creep and shrinkage calculated with the BP model considering the culvert drained on surface only; 3) creep and shrinkage calculated with the BP model considering the culvert drained on both surfaces (which affects the amount of drying creep); and, 4) shrinkage and 1.4 times the creep calculated with the BP model considering the culvert drained on both surfaces. There is little difference (less than 10% for both culverts) between cases two and three because the drying creep strain is not a very large percentage of the total strain. Also, the strains were calculated in analyses where the measured floor strains were enforced with displacements. This causes a small (approximately 5%) decrease in the calculated strains compared to strains in analyses where only the floor strains predicted by the CANDE code are present.

Figure 5.7 shows that the strains at the crown of the culvert under the high fill are bounded by the analyses considering the creep and shrinkage calculated with the BP method and considering 1.4 times the calculated creep. Without the 1.4 multiplication factor, the calculated strain underestimates the measured strain by about 15%. The effect of creep and shrinkage on the calculated mid-thickness crown strain is very dramatic. Figure 5.7 shows that the strain becomes tensile after cracking occurs in the analysis which does not consider the effects of creep and shrinkage, while the analyses which do consider creep and shrinkage, and the measured strains, are always compressive. The effect of cracking on the strains calculated in the analyses, which include creep and shrinkage, can be noted at the time of 229 days. Due to its long span and flat shape in the center (see Figure 5.1) the culvert is in bending at the crown. The calculated bending moment at the crown of the culvert under the full high fill changes with time but is approximately 42,000 lb.-in./in. while the thrust is approximately 6,500 lb./in. Although it is difficult to see in Figure 5.7, the measured strains indicate that the cracking occurred in the culvert under high fill at a time near 200 days, when the fill was 5 ft. to 10 ft. over the top of the culvert. This is also when cracks were first observed in the culvert. This may have some effect on the analysis since the strains calculated with the BP model (no multiplier on the creep strain) in the analyses considering creep and shrinkage overestimate measured strains before cracking is calculated in the culvert, and underestimate the measured strain thereafter.

Figure 5.8 shows a comparison between calculated and measured tensile strain at mid-depth through the thickness of the instrumented segment of the culvert under low fill. A large tensile strain was measured prior to placement of the backfill, indicating that this segment of the culvert was cracked during placement in the field or by some enforced lateral deflection at the base of the culvert. In order to produce a similar strain in the model prior to placement of the backfill, a force of 400 lb./in. was applied at the culvert crown during the first time step in the analysis. This causes a tensile strain of 500×10^{-6} which matches the measured strain prior to placement of backfill relatively well. Figure 5.8 shows that the measured strain has a high initial tensile value, it increases as fill is placed over the culvert, and then gradually decreases with time. The CANDE analysis which does not consider creep and shrinkage does not predict the long-term decrease in the measured strain. The analyses which consider creep and

shrinkage tend to overestimate the long-term strain decrease. The assumptions which result in the largest calculated creep strains (i.e. a multiplier on the calculated creep stain and two drainage surfaces) overestimate the measured long-term tensile strain reduction. All analyses overestimate the strain rise during placement of soil fill.

The measured long-term reduction in tensile strain is thought to be due to stress redistribution caused by restraint of creep and shrinkage in the top uncracked portion of the cross section by the top layer of steel. The restraining force of this steel reduces tensile strain near the neutral axis in spite of the fact that it acts on the cross section as a tensile force because it is applied above the neutral axis. The fact that the calculated reduction in tensile strain is too high may indicate that some tensile creep, which causes some tensile strain, is occurring in the cracked portion of the concrete near the strain gage. The CANDE code does not model any tensile creep in the cracked section since the stress is assumed to be zero. However, concrete continues to carry at least some tension stress after cracking by a phenomena usually referred to as tension stiffening because concrete can support tension stress between cracks, especially in regions where cracking is slight.[56] The fact that both the values calculated with CANDE and the measured strain decrease gradually with time indicates that creep and shrinkage affect the culvert strain at this location in the basic manner predicted with the CANDE code. Also, the measured strains are predicted relatively well except for the case where the multiplication factor is applied to the calculated creep strain.

5.1.4 Comparison of Measured and Calculated Strain near the Springline of the BEBO Culvert. Figures 5.9 and 5.10 compare calculated and measured strains at the strain gage locations near the springline, or base of the culvert at mid-depth through the thickness. These gages are located approximately 3 ft. up from the top of the footing. At this location the bending moment is relatively small, the entire cross section is in compression, and there is no concrete cracking. Figure 5.9 shows that the measured strains near the springline of the culvert under high fill are predicted well with the CANDE model when the effects of creep and shrinkage are included in the analysis. The measured strains are bounded by the strains from the analyses with creep and shrinkage calculated with the BP model and with shrinkage and 1.4 times the creep strain. The strains near the springline are insensitive to the enforced floor displacements and are increased approximately 5% by the application of the surface pressures which model the long-term fluctuation in the measured soil pressure on the culvert.

Figure 5.10 shows that the measured strains near the springline of the culvert under low fill are also predicted well with the CANDE model when the effects of creep and shrinkage are included in the analysis. The measured strain does not increase very uniformly, and an unusually large strain increase occurs relatively late in time between days 600 and 700 in Figure 5.10. The calculated strains do not show any such large late-time strain increase. The strains calculated without the multiplier on the creep strain predict the measured strains best prior to the large late-time measured strain increase, and the strains calculated with the multiplier on the creep strain predict the measured strain best thereafter.

5.1.5 Comparison of Measured and Calculated Strain in the Floor Slab of the BEBO Culvert. Figure 5.11 shows a comparison between the measured and calculated strains in the floor slab of the culvert under the high fill. The reinforcing steel in this region of the floor slab is spliced with steel extending from the footings causing the floor slab to function as a tension tie between the two footings.

The two calculated strain histories with the smallest magnitudes in Figure 5.11 show that the strains calculated including creep and shrinkage as predicted with the BP method are not significantly different from those calculated assuming no creep or shrinkage. This is deceiving however, since large tensile creep strains are calculated, and large compressive shrinkage strains (about 650 x 10^{-6}) are also calculated. since the floor slab is very young (5 days old) at the time the culvert was placed (at 180 days in Figure 5.11). The calculated shrinkage strains are somewhat larger than the calculated creep strains so that the total calculated strain, including the effects from both, decreases slightly with time. Figure 5.11 also shows the calculated floor strains including the calculated creep and elastic strain but not any of the calculated shrinkage strain. These strains compare well with the lower of the two strain histories measured under the two instrumented cross sections under the high fill. The two measured strain histories were not averaged because of the large difference between them. In reality, the shrinkage in the floor slab may very well be less than the amount calculated with the BP model since each heavy rain causes substantial water flow through the culvert, and therefore rewetting of the floor slab occurs. During the first several months after construction was completed (days 229 through 320 in Figure 5.12), there were several periods when approximately six inches of wet mud lay on the floor slab for several days to weeks. Rewetting will fully or partially reverse shrinkage but no attempt has been made to include this in the CANDE model of the culvert, the number of occurrences and the extent of rewetting of the floor slab was not measured. Figure 5.11 also shows the strains calculated with the enforced displacements. Deflections and arch strains determined from the CANDE analysis with the enforced floor displacements are plotted above as noted previously. The fact that the deflections calculated with the enforced displacements agree much better with the measured values is a strong indication that the measured floor strains are representative of the average strain throughout the floor slab and are not due to a local phenomena in the floor slab near the strain gages.

No tension cracking has been observed in the floor slab and therefore a very high cracking strain was input into the CANDE model to ensure that no cracking was calculated. The elastic floor strain calculated in the analyses including the effects of creep and shrinkage (but not the enforced displacements) varied from 170 x 10^{-6} to 180 x 10^{-6}. This strain is approximately equal to the strain calculated using the 6,000 psi concrete strength of the concrete in the culvert floor slab, Equation 6.2 to calculate the direct tensile strength (760 psi), and a concrete modulus of $57{,}000(f'_c)^{1/2}$, equal to 170 x 10^{-6} in./in. Therefore the observed lack of cracking is consistent with the analysis. If less shrinkage occurred than that calculated, as hypothesized above, the calculated elastic strains would be less than 180 x 10^{-6} because the tensile creep strains would dominate compared to the compressive shrinkage strains and would cause redistribution of tensile stress from the concrete into the steel.

5.1.6 Summary of the Comparison Between Measured and Calculated Soil-Structure Interaction Parameters in the BEBO Culvert. On the whole, calculated response parameters and soil-structure interaction parameters in the BEBO culvert compare well with the measured values. The very significant long-term effects of creep and shrinkage on the culvert response are modeled well (within 10 - 20%) using the Bazant-Panula method to predict free creep and shrinkage strains in the modified version of the CANDE code. A 1.4 multiplication factor on the creep coefficient (which causes much less than a 1.4 increase in culvert response) was used to "fine-tune" the analysis and make a few calculated parameters match measured values but this caused most other calculated values to overpredict measured values. In the low fill region, the measured midspan displacement and strain near the culvert springline

match predicted values well (within 20%) throughout the 2.5 year monitoring period. This is true in spite of very unusual measured soil pressures which are modeled approximately with a reduced or effective soil density. It is thought that a relatively large nearby slope in the soil fill influences the soil pressure on the culvert in this region. In the high fill region, the measured soil pressures near the crown and springline, the measured midspan deflection, and the measured mid-thickness strains at the crown and near the springline all match measured values within 20% throughout the 2.5 year monitoring period. The measured long-term fluctuations in the soil pressure on the culvert near the springline in the high fill region are modeled well as pressures caused by temperature-induced expansion of the culvert into surrounding undrained backfill. However, the similar measured fluctuations in the soil pressure near the crown are not modeled well by this approach. This may be due to a difference between the actual and calculated soil stiffness above the culvert caused by a large difference between the actual state of stress in the soil, which may be heavily influenced by compaction-induced stresses and the calculated state of stress. It is significant that the overall good agreement noted above between measured and calculated values was attained without specific test data defining the stiffness of the soil backfill or the soil foundation and without specific information on the creep and shrinkage strains of the concrete. Approximate prediction methods were used in each case.

The two measured parameters which do not compare well with calculated values are the strain in the culvert floor under the high fill and the mid-thickness strain at the culvert crown under the low fill. In the two cases where the calculated and measured results do not match well, it is possible that factors which cannot be included in the analysis are affecting measured values. The primary reason that the measured long-term culvert floor tensile strains under the high fill are underpredicted by a large margin may be due to rewetting of the floor slab by several floods through the culvert during the first year after construction. Rewetting, which causes reversal of previous shrinkage strains and thus more apparent tensile strain, is not included in the analysis and therefore very large (compressive) shrinkage strains are calculated. The primary reason the reduction in the mid-thickness crown tensile strain in the culvert under low fill is overpredicted may be tensile creep occurring near mid-thickness not modeled by the CANDE code. Cracked concrete regions are assumed to carry no stress, and therefore undergo no creep strain, when, in fact, concrete can carry some tensile stress between tensile cracks.

5.1.7 Calculated Stresses in Soil Surrounding the BEBO Culvert. Figures 5.12 through 5.17 show soil stresses calculated with the CANDE program around the culvert under high fill at the completion of fill. Stresses are shown in psi and decimals are truncated off because of space limitations on the plot. Negative stresses are compressive. Soils #1, #2, and #3 in the plot correspond to the cement stabilized clay fill below the culvert, the pre-existing fill and consolidated soil outside the limits of the fill around the culvert, and the silty clay backfill, respectively. These soils were discussed in detail above in the section where the soil material model was discussed. Only soil #3 has self weight (128 pcf) for the analyses. For reference, the free field overburden stress is 21 psi at the culvert crown and 30 psi at the top of the culvert footing. The vertical stress over the culvert crown, where the deflection is maximum, is reduced relative to stresses in soil over stiffer portions of the culvert with more curvature. The axial stiffness of the culvert near the springline is greater than that of the soil, and consequently some vertical stress is transferred from the soil into the culvert through friction along the soil-culvert interface, which increases the thrust in the culvert. This force is transferred through the culvert, into the footing, and into the relatively stiff soil beneath culvert footing.

Significant vertical stress is transferred into soil #2 (the pre-existing soil) along the interface between soils #2 and #3 (the backfill around the culvert). This is expected since soil #3, which has self weight in the analysis, displaces relative to soil #2 which has no self weight. Below the footing this stress is transferred out of soil #2 stress into the much stiffer soil #1 along the interface between soils #2 and #1.

The lateral X-direction stresses are relatively small (20 to 30% of the vertical stresses) near the culvert. The calculated lateral stresses do not include any "locked-in" stresses created by the compaction process Therefore the soil elements with very low calculated lateral stress or negative (tensile) lateral stress probably have greater compressive stress than that calculated. This is accounted for approximately in the Duncan soil model, as it is incorporated in the CANDE code, by assuming a minimum soil confining pressure of 1.5 psi. Relatively large magnitude (15 psi to 20 psi) lateral tensile stresses are calculated in the soil fill under the floor slab. The flexural response of the culvert causes the footings to displace laterally which is resisted to some extent by the soil below the culvert. The calculated tensile stresses in the soil beneath the culvert, which is stabilized with cement, are much lower than the previously estimated tensile capacity of the soil of 50 psi. Therefore, the soil is assumed capable of resisting these relatively low tensile stresses. The tensile force in the these elements is less than 10% of the force calculated in the floor slab and therefore does not have a very significant effect on the culvert response.

Figures 5.15 through 5.17 show the soil stresses calculated by the CANDE program around the culvert under low fill (8.5 ft. over the crown). Here, the artificially low soil density for soil #3 of 75 pcf was used. Therefore, the free field overburden stress at the top of the culvert is 4.5 psi and, at the top of the footing, it is 9.6 psi. The same trends in the vertical stresses and lateral stresses discussed above for the culvert under high fill are also evident in Figure 5.16. The same tension stresses are present under the floor. Since the floor slab does not resist tension for this case, the tensile strains in the cement stabilized soil fill represent the total force resisting lateral displacement of the culvert footings. In a subsequent computer run for the culvert under low fill, an anisotropic elastic material model was used for the elements under the culvert which are in tension and had very low stiffness in the X-direction, so that almost no tensile stress developed, and a significantly greater (15%) deflection occurred. However, as mentioned above, it is thought that the cement stabilized base can tensile stresses as least as large as those calculated under the high and low fill regions of the culvert.

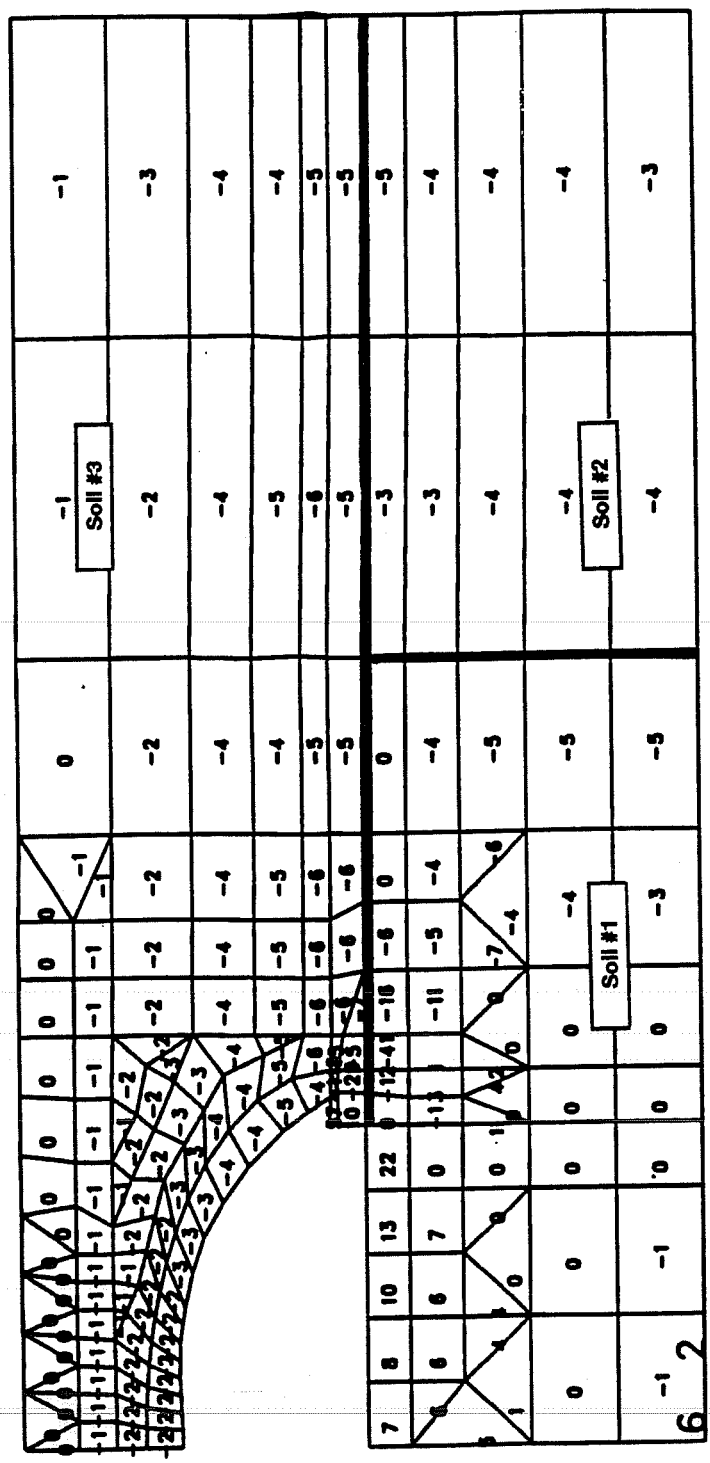

Figure 5.15 X-direction stresses in soil in low fill region

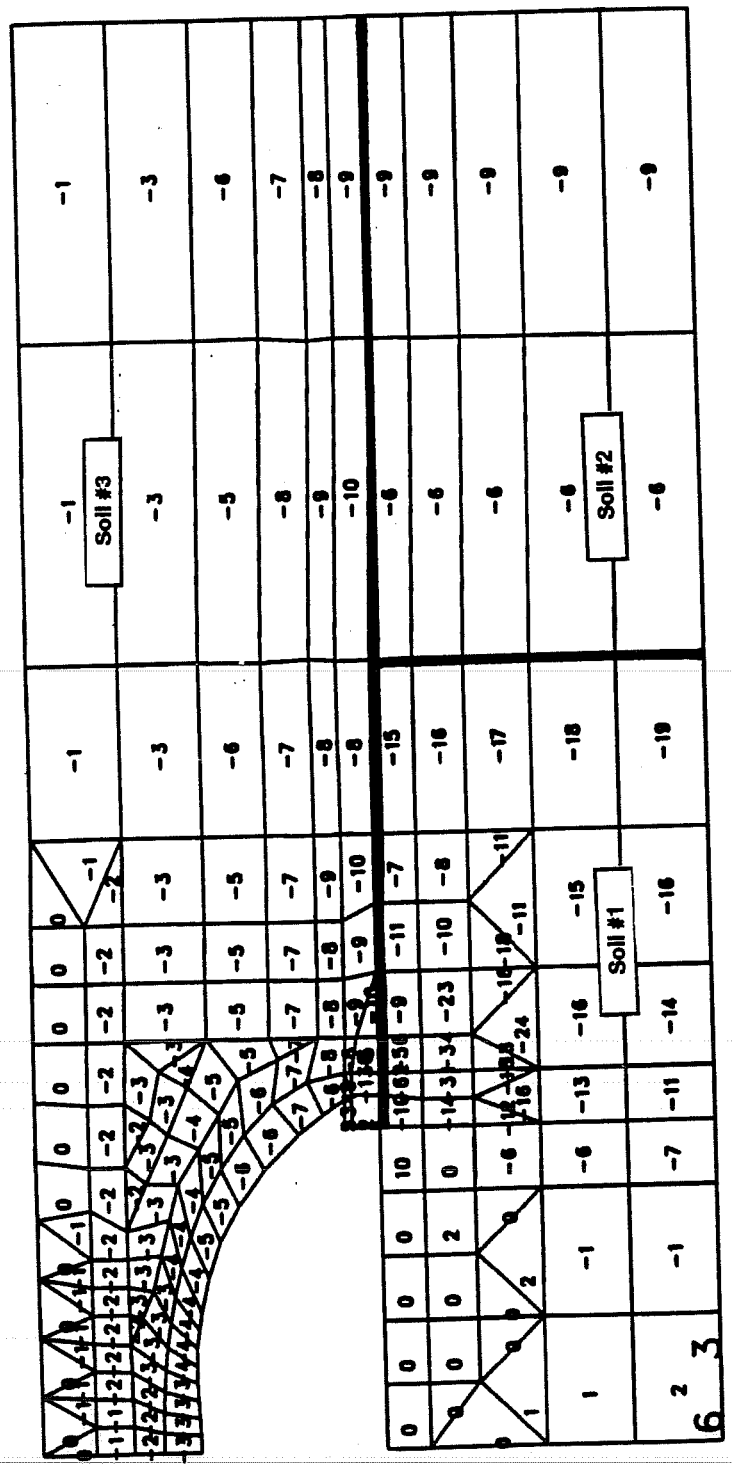

Figure 5.16 Y-direction stresses in soil in low fill region

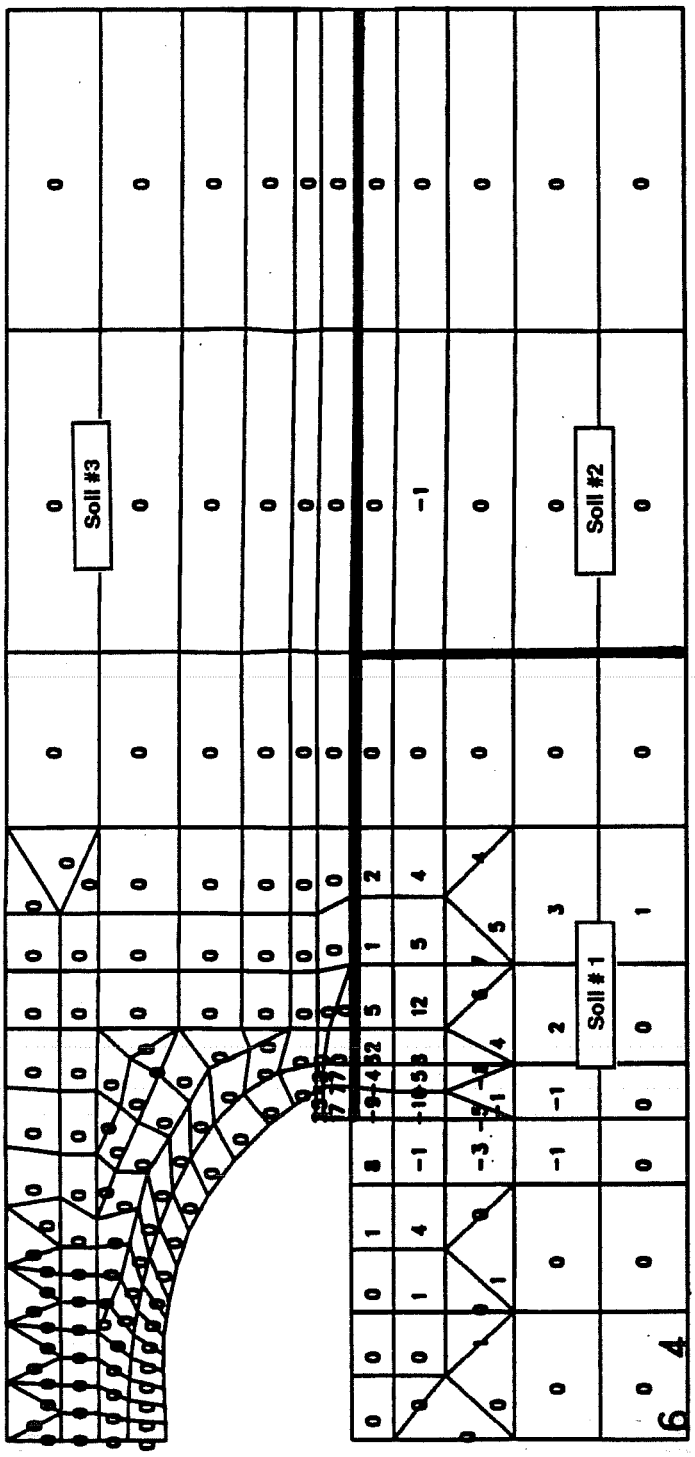

Figure 5.17 Shear stresses in soil in low fill region

CHAPTER 6

SUMMARY AND CONCLUSIONS

This is a report in three study areas: 1) the measurement of the structural response and the soil pressures against an in-service reinforced concrete culvert over a 2.5 year period; 2) finite element modeling of this culvert and the surrounding soil during the entire 2.5 year monitoring period; and, 3) use of the finite element method to investigate the design and the ultimate capacity of the culvert. A brief summary of the measurements and analyses which were performed in each of these three areas follows. Conclusions are stated following the summaries.

6.1 Summary of Field Measurements

A comprehensive set of long-term field measurements were made of the response of a low-rise reinforced concrete arch culvert in a compacted silty clay backfill. The culvert was backfilled up to a fill height of 24 ft. over the crown at two instrumented locations and up to a height of 8.5 ft. over the crown at one other instrumented location. The culvert has a 10 ft. rise, a 40 ft. span, and is 10 inches thick. Measurements began at the start of backfilling around the structure and concluded 2.5 years later. Three cross sections were instrumented, two under a high fill of 24 ft. and one under a low fill of 8.5 ft. The culvert strains and deflections were measured as well as the soil pressures on the culvert.

Measured soil pressures on the culvert under the high fill were within 15% of free-field values after the completion of fill. During backfilling, at fill heights less than 10 ft. over the culvert crown, measured soil pressures were approximately 5 psi greater than free-field values. Measured soil pressures on the culvert under the low fill were, on the average, only equal to 60% of free-field values after the completion of fill. It is hypothesized that these soil pressures were lower than expected because this instrumented cross section is located beneath the top of a slope. This hypothesis is supported by the fact that other field studies and computational studies were located in the literature where low vertical soil pressure was also measured or calculated below the top of sloped fills.

Seasonal fluctuations in soil pressure with a magnitude of approximately 15% of the mean pressure were measured. Corresponding small fluctuations occurred in the measured strains in the structure. The fluctuations were such that increased soil pressures and compressive strain occurred in summer months. It is thought that this fluctuation is due to temperature induced expansion of the culvert which is constrained by the stiffness of the surrounding soil fill.

Observed soil-structure effects were minimal. The long-term structure response was considerable (50% increase in deflection and 100% to 200% increase in mid-depth concrete strain) but the long-term change in soil pressure was very small except for seasonal fluctuations.

The measured long-term strain increases included very large tensile strains (600×10^{-6} to 900×10^{-6}) in the floor slab of the culvert, where the floor acted as a tension tie between the culvert footings.

No cracking was observed in the floor slab. It is probable that these strain increases are due to the effects of concrete creep and shrinkage.

6.2 Summary of Finite Element Analysis of the Culvert

The CANDE finite element code, which was developed and is distributed by the Federal Highway Administration for analyzing soil-structure interaction, was modified to model long-term structural response and used to predict the same parameters measured in the field study. Previously no time effects have been incorporated into the code. Specifically, the CANDE code was modified to consider the effects of concrete creep and shrinkage strains, aging of the concrete, and temperature changes. These modifications included:

1) Incorporation of several models for predicting the free creep and shrinkage of concrete into the CANDE code.
2) Modification of the CANDE code to associate the existing incremental "load steps" in the analysis method with input time steps and temperature changes.
3) Addition of logic to calculate the increase in concrete strength and modulus with time using the relationship recommended by ACI Committee 209.
4) Addition of logic to calculate the redistribution of stress within the structure cross section caused by the partial restraint of concrete creep and shrinkage by reinforcing steel.
5) Modification of the nonlinear concrete model to consider the stress redistribution within the concrete cross section caused by the effects of creep and shrinkage as well as stresses caused directly by applied loads.
6) The calculation and incorporation of the pseudo forces into the global system of equations which cause the plastic deformations from concrete creep and shrinkage and deformations from temperature strains to be included in the calculated soil-structure interaction.
7) Development of plotting software for output from the CANDE code.
8) Validation of the creep and shrinkage portion of the code with calculated values for creep and shrinkage in four different, varied structural applications published in the literature.

Also, the publicly available version of the CANDE code was only developed to consider a limited set of specific end conditions typical of many underground structures and one set of material properties per structure. Since these conditions were too restrictive for the non-typical under structure modeled in this study, the following additional modifications were made to the CANDE code.

1) Incorporation of a much fuller range of possible boundary conditions into the CANDE code including pinned end conditions, end conditions with only moment fixity, and pinned joints within the structure.
2) The capability to define a number of different sets of material properties, which can be assigned to different elements within the structure, was added.

Prior to its modification, results obtained by modeling the culvert with the CANDE code did not agree well with measured values. After the implementation of the changes discussed above, very good

agreement (within 10% in almost all cases) between the time histories of measured and predicted parameters was achieved.

The backfill was modeled with default soil model parameters in the CANDE code for a fully compacted, drained silty clay. The measured effects of compaction were modeled with temporary 5 psi surface pressures applied on soil elements during the load step they were added into the finite element mesh if they were at a fill height less than 10 ft. over the crown. This was only done for the model of the culvert under the high fill. Measured soil pressures on the culvert under the low fill were unexpectedly low as discussed above, and no pressures corresponding to 5 psi in magnitude, which could be attributed to compaction effects, were evident in the measured soil pressures.

It was found that the measured seasonal fluctuations in soil pressure could be modeled well near the springline in a separate finite element analysis when soil model parameters in the literature for an undrained silty clay were used in the CANDE code. Temperature fluctuations equal to the 7 day moving average temperature measured at the nearby San Antonio Airport were used in the code. The soil pressure fluctuations calculated near the crown with this method were significantly less than those measured. It is thought that this occurred because the actual stiffness of the soil over the crown was significantly greater than that considered by the stress-dependent soil model in the CANDE code. The low calculated compressive soil stress in this area does not include any horizontal stress locked-in during the compaction process. The need to switch to undrained soil properties to model the greater stiffness of the clay backfill to the short-term temperature induced culvert expansion meant that this type of response could not be modeled simultaneously with gradual, long-term response which did not cause significant pore pressures in the soil. Therefore, in most finite element analyses of the culvert, the measured soil pressure fluctuations were modeled in a fully drained silty clay backfill with a fluctuating surface pressure which caused fluctuations in the pressure on the culvert nearly matching measured values. The low measured soil pressures on the culvert under the low fill were modeled in the finite element analysis of this cross section by inputing a soil unit weight of only 75 pcf rather than the average measured value of 128 pcf. This caused the calculated soil pressure near the crown of the culvert to fall between the measured values.

Several different empirical models (the methods in the ACI Committee 209 Report, in the Australian Standard for Concrete Structures (AS3600-1988), and in the Bazant-Panula method) were used in the CANDE code to predict the free creep and shrinkage that would occur if there was not restraint from reinforcing steel or structural indeterminacy. The best match between the measured strain histories in the culvert, which included significant creep and shrinkage, and calculated values, was obtained when the Bazant-Panula model for predicting free creep and shrinkage strain was used in the modified CANDE code. In order to account for increased creep in cracked regions exposed to drying, which is not considered by any creep prediction method, a multiplication factor was applied in the CANDE code to the portion of the calculated creep strain attributed to drying in the Bazant-Panula model after concrete cracking was calculated. A factor of 4.0 caused the calculated strain in cracked regions to match the data well and significantly better than a factor of 2.5. This multiplication factor was only applied to cracking on the inside face of the culvert since any cracking on the soil side would presumably be exposed to less humidity.

The predicted creep and shrinkage is also sensitive to the surface area exposed to drying. The humidity, and therefore drying, on the soil side of the culvert was unknown. The strain histories, calculated for both sides of the culvert exposed to the average ambient relative humidity of 65% and for only one side exposed to the ambient humidity, varied by no more than 10%. The best match was obtained assuming both sides dried in an average ambient humidity of 65% because, in general, the calculated creep strains tend to underpredict measured values by a small amount.

As mentioned above, very large tensile strains (600×10^{-6} to 900×10^{-6}) were measured at all four strain gage locations in the floor slab of the culvert, where the floor acted as a tension tie between the culvert footings, and no tensile cracking was observed. This strain was much higher than that calculated taking into account the partially offsetting effects of shrinkage and tensile creep. It is hypothesized that extended periods when wet mud covered the culvert floor caused the actual shrinkage to be much lower than the calculated value, which did not consider this factor. The sum of only the calculated elastic and creep strain histories (assuming the shrinkage to be zero) does fall within the considerable scatter of the measured strain histories in the floor slab. The calculated stress, which is only proportional to the elastic portion of the measured strain, is slightly less than the predicted tensile strength of the concrete.

6.3 Summary of Finite Element Analysis of the Culvert Design and Ultimate Capacity

Important design parameters which were calculated with the CANDE finite element analysis at the time backfilling was completed, including the soil pressure distribution and the maximum moment and thrust in the culvert, were compared to values used for design of the culvert. The maximum unfactored moment used in the design of the culvert was approximately 15% greater than the value calculated with the finite element analysis. The design thrust was approximately 15% less than the value calculated with the finite element analysis. The design is conservative in both respects since the combined thrust and moment in the culvert under the design fill height cause the stress in the tensile steel in the maximum moment region to control the design. The unfactored soil pressure on the culvert used in the design was nearly equal to the value calculated with the finite element analysis near midspan and it was approximately 25% less than the calculated value near the springline. The design soil pressures were based on equivalent fluid densities of 120 pcf for vertical soil pressure and 40 pcf for horizontal pressure recommended in the AASHTO Specification for Highway Bridges for structures where horizontal soil pressures act to reduce the maximum moment in the structure.

It is noteworthy that the 120 pcf value used to calculate the vertical soil pressure does not account for the fact that most compacted soils have a density close to 130 pcf and that a number of previous field studies have shown that negative arching can occur over rigid reinforced concrete structures where soil pressures are 10% to 20% greater than the overburden pressure. The 15% seasonal fluctuation in soil pressure also caused the measured vertical soil pressure in this study to exceed that calculated with the 120 pcf value. Typically, differences of the magnitude referred to here will be accounted for in the 1.3 load factor that is used in load and resistance factor design or in conservative maximum allowable stresses used in allowable stress design. However, it is more consistent with the generally accepted philosophy for safe design to base unfactored design loads on realistic assumptions and generally measured values

whenever possible. The AASHTO code does not recognize that horizontal soil pressure greater than those calculated using a fluid 40 pcf density and states that a 60 pcf fluid density should be used when it causes a more conservative value. The 60 pcf value is consistent with the measured soil pressures near the springline.

The additional capacity of the culvert cross sections used under both the low fill and high fill calculated with the finite element method was much greater than that corresponding to the load and resistance factors used for design. The calculated fill heights over the culvert cross sections in the low fill and high fill regions at ultimate capacity were three to four times the design fill heights. The 1.3 load factor and 0.9 and 0.7 resistance factors, for the ultimate moment capacity and thrust capacity respectively used in the design, only account for approximately one-half of the calculated additional capacity of the culvert. The large deflections which develop as the culvert approaches its ultimate capacity cause very significant soil "arching," or redistribution of soil pressure into the soil surrounding the structure, which causes the culvert to be loaded by a lower proportion of the total overburden pressure. This response adds to the safety against structural failure provided by design safety factors.

The response of the culvert in a silty sand backfill, which has a calculated stiffness three to four times greater than that of the silty clay backfill, was investigated with the finite element method. The culvert deflection under design fill heights was not large enough to take full advantage of the tendency of the stiffer soil to cause more soil arching. At a fill height of 40 ft. over the culvert cross section used under the high fill, the calculated maximum moment was 30% less in the stiffer backfill while the thrust was relatively unchanged. At fill heights closer to the ultimate capacity of the culvert, the reduction in maximum moment caused by the stiffer backfill material was much more significant.

6.4 Conclusions Related to the Field Study

A comprehensive set of long-term field measurements were made of the response of a low-rise reinforced concrete arch culvert in a compacted silty clay backfill. The time histories of the soil pressure and concrete strain measurements over the duration of the monitoring period made at 10 out of 15 symmetrical locations matched within 15%. Also, the measured soil pressure, deflection, and strains fluctuated together, in a manner which was consistent with the physical relationships between these parameters, throughout their time histories. Therefore, the vibrating wire strain gages and total soil pressure gages used in this study produced a very consistent set of data.

The measured soil pressures at fill heights more than 10 ft. over the culvert crown matched expected free-field values well (within 15%) in an area of level fill. At fill heights less than 10 ft. over the crown, the measured soil pressures were approximately 5 psi greater than expected free-field values. Therefore, it is thought that the pore pressures induced by compaction dissipated in the two to three week period that it took to place soil up to the 10 ft. level.

The average measured vertical soil pressure on the culvert at the one instrumented cross section directly beneath the top of a slope in the backfill was 60% less than the expected free-field value. This matches the trend reported in a field study and a computation study located in the literature.

The only significant long-term change which occurred in the measured soil pressures were seasonal fluctuations which were no more than 15% of the mean stress. Very substantial long-term increases occurred in both the measured culvert deflections (50%) and strains (100% to 200%). This implies that there was minimal soil-structure interaction for this case.

6.5 Conclusions Related to the Finite Element Analysis of the Culvert Monitored in the Field Study

Poor agreement was obtained between the measured culvert response and that calculated with the CANDE finite element code distributed by the Federal Highway Administration. However, good agreement (within 15%) was obtained between results calculated with a significantly modified version of the CANDE code, which took into account concrete creep, shrinkage, and temperature strains, and the average measurements of 8 out of 10 parameters monitored in the field study over the entire 2.5 year period measurements were conducted.

It was found that the measured soil pressures could be modeled well (within 15%) with default soil model parameters in the CANDE code for a fully compacted, drained silty clay and with temporary 5 psi surface pressures applied to each group of soil elements as they were added to the finite element mesh at fill heights less than 10 ft. over the crown.

It was found that the measured seasonal fluctuations in soil pressure could be modeled well near the springline when soil model parameters in the literature for an undrained silty clay were used in the CANDE code. Temperature fluctuation equal to the 7 day moving average temperature measured at the nearby San Antonio Airport were used in the code. The soil pressure fluctuation calculated near the crown with the method were significantly less than those measured. It is thought that this occurred because the actual stiffness of the soil over the crown was significantly greater than that considered by the stress-dependent soil model in the CANDE code. The low calculated compressive soil stress in this area does not include any horizontal stress locked-in during the compaction process.

The best match between the measured strain histories in the culvert, which included a very significant amount of creep and shrinkage strain, and calculated values was obtained when the Bazant-Panula model for predicting free creep and shrinkage strain was used in the modified CANDE code. The methods recommended by ACI Committee 209 and the Australian Standard for Concrete Structures (AS3600-1988) were also used. In order to account for increased creep in cracked regions exposed to the air, which is not considered by any creep prediction method, an increase factor was applied to the portion of calculated creep strain attributed to drying in the Bazant-Panula model after concrete cracking was calculated. A factor of 4.0 caused the calculated strain in cracked regions to match the data well and significantly better than a factor of 2.5.

Also, the predicted creep and shrinkage is sensitive to the surface area exposed to drying. The humidity, and therefore drying, on the soil side of the culvert was unknown. However, the strain histories calculated for both sides of the culvert exposed to the average ambient humidity of 65% and for only one side exposed the ambient humidity varied by no more than 10%. The best match was obtained assuming both sides dried in an average ambient humidity of 65%.

Very large tensile strains (600 x 10^{-6} to 900 x 10^{-6}) were measured at all four strain gage locations in the floor slab of the culvert, where the floor acted as a tension tie between the culvert footings. No cracking was observed. This strain was much higher than that calculated taking into account the partially offsetting effects of shrinkage and tensile creep. It is hypothesized that extended periods when wet mud covered the culvert floor caused the actual shrinkage to be much lower than the calculated value, which did not consider this factor. The sum of only the calculated elastic and creep strain histories (assuming the shrinkage to be zero) does fall within the considerable scatter of the measured strain histories in the floor slab. The elastic portion of the calculated strain history is slightly less than the predicted tensile strength of the concrete.

6.6 Conclusions Related to Analysis of the Culvert Design and Ultimate Capacity

The culvert was designed based on the load factor design procedure for rigid culverts in the AASHTO Standard Specifications for Highway Bridges. The assumptions used in the design predict vertical soil pressures which are slightly less than the maximum values measured (10%) and horizontal pressures significantly greater (30%) than those measured. Because of the culvert geometry these differences have offsetting effects. The 1.3 load factor applied to the predicted soil pressures in the design is also large enough to compensate for the differences between measured and design vertical soil pressures.

The maximum moments in the culvert calculated with the finite element analysis, which compared well to measured structural and soil parameters, are 15% to 30% less than those calculated using the unfactored design pressures for the culvert cross sections used in both the high and low fill regions. This is due to the difference in the soil pressure distribution and, to a lesser extent, due to some fixity calculated at the base of the culvert in the finite element analysis. Therefore, the soil pressures and structural analysis assumptions used for design are, on the whole, conservative.

The calculated ultimate capacity of the culvert was calculated to be three to four times the existing fill heights. This occurred for several reasons. First, soil-structure interaction effects, which resulted in soil load arching over the culvert, became significant as the structural deflections approached values corresponding to the ultimate capacity of the culvert. Second, the increase in fill depth caused increase in thrust to occur simultaneously with increase in bending moment which caused the condition at cross sections of maximum moment in the culvert to approach the balanced condition where thrust acts to enhance the moment capacity. Finally, the fact that a 65% increase was added to the design steel area in the positive moment region of the culvert under the high fill prior to construction also contributed to large ultimate capacity of this culvert cross section.

REFERENCES

1. Spangler, M.G., "Long-Time Measurements of Loads on Three Pipe Culverts," Highway Research Record, 443, 1973.

2 Quigley, D.W., and Duncan, J.M., "Earth Pressures on Conduits and Retaining Walls," Report No. UCB/GT/78-06, University of California at Berkeley, September 1978.

3. Backer, A.E., and Klein, E.G., "Reinforced Concrete Arch Culvert Research by the California Department of Transportation," Transportation Research Record, 785.

4. Davis, R.E., "Structural Behavior of Concrete Arch Culvert," *Journal of Structural Engineering*, ASCE, Vol. 94, ST12, December 1969.

5. Davis, R.E., and Semans, F. M., "Rigid Pipe Prooftesting Under Excess Overfills with Varying Backfill Parameters," Transportation Research Record, 878, 1982.

6. Rude, L.C., "Computer Modeling of the Cross Canyon Culvert," Transportation Research Record, 785.

7. Krizek, R.J., and McQuade, P.V., "Behavior of Buried Concrete Pipe," *Journal of Geotechnical Engineering*, ASCE, Vol. 194, GT7, July 1978.

8. Tadros, M.K., "Cost Effective Concrete Culvert Design," Project No. HRP 83-3, Report No. NE-DOR-R-86-3, Nebraska Department of Roads, Lincoln, Nebraska, August 1986.

9. Dasgupta, A., and Sengupta, B., "Large-Scale Model Test on Square Box Culvert Backfilled With Sand," *Journal of Geotechnical Engineering*, ASCE, Vol. 117, No. 1, January 1991.

10. Kim, Y.S., "Finite Element Analysis of Centrifuged Concrete Culverts," Report No. ESL-TR-84-51, Air Force Engineering and Sciences Services Center, Tyndall AFB, Florida, February 1985.

11. Selig, E.T., et al., "Measured Performance of Newtown Creek Culvert," *Journal of Geotechnical Engineering*, ASCE, Vol. 195, GT9, September 1979.

12. McVay, M.C., and Selig, E.T., "Performance and Evaluation of a Long-Span Culvert," Transportation Research Record, 878, 1982.

13. Duncan, J.M., "Behavior and Design of Long-Span Metal Culverts," *Journal of Geotechnical Engineering*, ASCE, Vol. 105, GT3, March 1979.

14. McVay, M.C., and Papadopoulos, P., "Long-Term Behavior of Buried Large-Span Culverts," *Journal of Geotechnical Engineering*, ASCE, Vol. 12, No. 4, April 1986.

15. Brown, C.B., "Forces on Rigid Culverts Under High Fills," *Journal of the Structural Division*, Proceedings of the ASCE, Vol. 93, ST5, October 1967.

16. Katona, M.G., "Soil-Structure Analysis and Evaluation of Buried Box Culvert Designs," Computing in Civil Engineering.

17. Katona, M.G., et al., "CANDE – Modern Approach for the Structural Design and Analysis of Buried Culverts," Report No. FHWA-RD-77-5, Federal Highway Administration, Washington, D.C., October 1976.

18. Roschke, P. N., "Finite Element Analysis of Rigid Culverts Under High Soil Overfill," Proceeding of ASCE Conference.

19. Meade, B.W., and Allen, D.L., "Analysis of Loads on Top Slab of Reinforced Concrete Box Culverts," Preprint Paper No. 910390, 70th Annual Transportation Research Board Meeting, Washington, D.C., 1991.

20. Chang, C.S., et al., "Computer Analysis of Newtown Creek Culvert," *Journal of the Geotechnical Engineering Division*, ASCE, Vol. 106, GT5, May 1980.

21. Duncan, J.M., and Jeyapalan, J.K., "Deflection of Flexible Culverts Due to Backfill Compaction," Transportation Research Record, 878, 1982.

22. Instruction Manual for Model 4800E Total Pressure Cell, distributed by Geokon, Inc., Lebonon, New Hampshire, U.S.A.

23. "Calibration Tests of Special Model VSM-4000 Vibrating Wire Strain Gages for Scanrock, GMBH Gorleben Shaft I Instrumentation," Geokon, Inc., April 1989.

24. Dunnecliff, J., Geotechnical Instrumentation for Monitoring Field Performance, John Wiley & Sons, New York, 1988.

25. Private Communications with Mr. John McRae of Geokon, Inc.

26. McRae, J.B., and Simmonds, T., "Long Term Stability of Vibrating Wire Instruments: One Manufacturer's Perspective," Proceedings on the Third International Symposium on Field Measurements in Geotechnics, Oslo, Norway, Offprint published by A.A. Balkema Publishers, Brookfield, Vermont., U.S.A., September 1991, pp. 283-293.

27. Browne, R.D., "Thermal Movement of Concrete," *The Journal of the Concrete Society*, London, Vol. 6, No. 11, November 1972, pp. 51-53.

28. Wilson, W.M., "The Effect of Climatic Changes Upon a Multiple-Span Reinforced Concrete Arch Bridge," The University of Illinois Engineering Experiment Station, Bulletin No. 174, February 1928.

29. Booker, E.W., and Ireland, H.O., "Earth Pressures at Rest Related to Stress History," *Canadian Geotechnical Journal*, Vol. 2, 1965, pp. 1-15.

30. Duncan, J.M., et al., "Strength, Stress-Strain and Bulk Modulus Parameters for Finite Element Analyses of Stresses and Movements in Soil Masses," Report No. UCB/GT/78-02 to National Science Foundation, April 1978.

31. Duncan, J.M., and Seed, R.B., "Compaction-Induced Earth Pressures Under K_0-Conditions," *Journal of Geotechnical Engineering*, Vol. 112, No. 1, January 1986, pp. 1-22.

32. Lefebvre, G., et al., "Three-Dimensional Finite Element Analyses of Dams," JSMFD, Proceedings of the ASCE, Vol. 99, No. SM7, July 1973.

33. Davis, R.E., et al., "Arch Culvert Research – Phase 3," *Journal of the Structural Division*, Proceedings of the ASCE, Vol. 105, No. ST4, April 1979, pp. 739-749.

34. Ferguson, P.M., Breen, J.E., and Jirsa, J.O., Reinforced Concrete Fundamentals, John Wiley & Sons, New York, 1988.

35. Broms, B.B., and Lutz, L.A., "Effects of Arrangement of Reinforcement on Crack Width and Spacing of Reinforced Concrete Members," *Journal of the American Concrete Institute*, Proceedings, Vol. 62, No. 11, November 1965, pp. 1395-1410.

36. Bortolotti, L., "First Cracking Load of Concrete Subjected to Direct Tension," *ACI Materials Journal*, Vol. 88, No. 1, January-February 1991, pp. 70-73.

37. Katona, M.G., et al., "CANDE – 1980: Box Culverts and Soil Models," Report No. FHWA-RD-80-172, Federal Highway Administration, Washington, D.C., May 1981.

38. Duncan, J.M., and Chang, C.Y., "Nonlinear Analysis of Stress and Strain in Soils," *Journal of Soil Mechanics and Foundation Engineering*, ASCE, 96(5), 1629-1653.

39. Bortolotti, L., "Interdependence of Concrete Strength Parameters," *ACI Materials Journal*, January-February 1990.

40. Leonards, G.A., et al., "Predicting Performance of Buried Conduits," Report No. FHWA/IN/JHRP-81/3, Federal Highway Administration, Washington, D.C., June 1982.

41. McVay, M.C., "Evaluation of Numerical Modeling of Buried Conduits," Doctoral Dissertation, Department of Civil Engineering, University of Massachusetts, Amherst, Massachusetts, February 1982.

42. Wong, Kai, S., and Duncan, J.M., "Hyperbolic Stress-Strain Parameters for Nonlinear Finite Element Analysis of Stresses and Movements in Soil Masses," Report No. TE-74-3, University of California, Berkeley, July 1974.

43. Boscardin, M.D., et al., "Hyperbolic Parameters of Compacted Soils," *Journal of Geotechnical Engineering*, ASCE, Vol. 116, No. 1, January 1990.

44. Musser, S.C., "CANDE – 89 Users Manual," Report No. FHWA-RD-89-169, Federal Highway Administration, Washington, D.C., June 1989.

45. Selig, E.T., "Soil Parameters for Design of Buried Pipelines," Proceedings, Pipeline Infrastructure Conference, ASCE, 1988, pp. 99-116.

46. Herrmann, L.R., "Efficiency Evaluation of a Two-Dimensional Incompatible Finite Element," *Computers and Structures*, Vol. 3, pp. 1377-1395.

47. George, K.P., "Characterization and Structural Design of Cement-Treated Base," Preprint, 69th Annual Transportation Research Board Meeting, Washington, D.C., 1990.

48. Lambe, T.W., and Whitman, R.V., Soil Mechanics, John Wiley and Sons, Inc., New York, 1969.

49. Peck, R.B., Hanson, W.E., and Thornburn, T.H., Foundation Engineering, John Wiley and Sons, Inc., New York, 1974.

50. Norbari, E.S., and Duncan, J.M., "Effect of Reservoir Fill on Stresses and Movements in Earth and Rockfill Dams," Report No. TE-72-1, University of California at Berkeley, January 1972.

51. Katona, M.G., et al., "Structural Evaluation of New Concepts for Long-Span Culverts and Culvert Installation," Federal Highway Administration, 1979.

52. Bazant, Z.P., and Wittman, F.H., Creep and Shrinkage of Concrete Structures, John Wiley and Sons, Inc., New York, 1982.

53. ACI Manual of Concrete Practice, 1989.

54. Bazant, Z.P., and Panula, L., "Practical Prediction of Time-Dependent Deformations of Concrete," Materials and Structures, Parts I and II: Vol. 11, No. 65, 1978, pp. 307-328, Parts III and IV: Vol. 11, No. 66, 1978, pp. 415-434, Parts V and VI: Vol. 12, No. 69, 1979, pp. 169-183.

55. Bazant, Z.P., and Panula, L., "Creep and Shrinkage Characterization for Analyzing Prestressed Concrete Structures," *PCI Journal*, May-June 1990, pp. 86-123.

56. Gilbert, R.I., Time Effects in Concrete Structures, Elsevier Science Publishers B.V., Amsterdam, 1988.

57. ASCE Task Committee on Finite Element Analysis of Reinforced Concrete Structures, State-of-the-Art Report on Finite Element Analysis of Reinforced Concrete, ASCE, New York, 1982.

58. Bazant, Z.P., et al., "Effect of Cracking on Drying Permeability and Diffusitivity of Concrete," *ACI Materials Journal*, September-October 1987, pp. 351-357.

59. Neville, A.M., et al., Creep of Plain and Structural Concrete, Construction Press (Longman Group Ltd.), London, 1983.

60. Manual of Steel Construction, Ninth Edition, AISC, Chicago, 1989.

61. Bresler, B., and Selna, L., "Analysis of Time Dependent Behavior of Reinforced Concrete Structures," Symposium on Creep of Concrete, ACI Special Publication SP-9, No. 5, March 1964, pp. 115-128.

62. Selna, L., "Creep, Cracking, and Shrinkage in Concrete Frame Structures," *Journal of the Structural Division*, Proceedings of the ASCE, Vol. 95, No. ST12, December 1969.

63. Kang, Y., and Scordelis, A.C., "Nonlinear Analysis of Prestressed Concrete Frames," *Journal of the Structural Division*, Proceedings of the ASCE, Vol. 106, No. ST2, February 1980.

64. Lee, H.M., et al., "Creep Analysis of Concrete Buildings During Construction," *Journal of Structural Engineering*, Vol. 117, No. 10, October 1991.

65. Anand, S.C., and Rahman, M.A., "Numerical Modeling of Creep in Composite Masonry Wall," *Journal of Structural Engineering*, Vol. 117, No. 7, July 1991.

66. Tarantino, A.M., and Dezi, L., "Creep Effects on Composite Beams with Flexible Shear Connectors," *Journal of Structural Engineering*, Vol. 118, No. 8, August 1991.

67. Ghali, A., and Elliot, E., "Serviceability of Circular Prestressed Concrete Tanks," *ACI Structural Journal*, Vol. 89, No. 3, May-June 1992.

68. Gilbert, R.I., "Time-Dependent Analysis of Composite Steel-Concrete Sections," *Journal of Structural Engineering*, Vol. 115, No. 11, November 1989.

69. Zarghamee, M.S., et al., "Concrete Creep and Shrinkage and Wire Relaxation in Buried Prestressed Concrete Pipe," *ACI Structural Journal*, Vol. 87, No. 5, September-October 1990.

70. Lee, C., "Evaluation of Duncan's Hyperbolic Soil Model," Department of Civil Engineering, University of Notre Dame, Notre Dame, Indiana, May 1979.

Technical Report Documentation Page

1. Report	2. Government Accession No.	3. Receipient's Catalog No.
PRELIMINARY REVIEW COPY		

4. Title and Subtitle	5. Report Date
OBSERVED BEHAVIOR OF A CONCRETE ARCH CULVERT	February 1993
	6. Performing Organization Code

7. Author(s)	8. Performing Organization Report No.
Charles S. Oswald and Richard W. Furlong	Research Report 932-1

9. Performing Organization Name and Address	10. Work Unit No. (TRAIS)
Center for Transportation Research The University of Texas at Austin Austin, Texas 78712-1075	11. Contract or Grant No. Research Study 3-15D-88/2-932

12. Sponsoring Agency Name and Address	13. Typeof Report and Period Covered
Texas Department of Transportation Transportation Planning Division P.O. Box 5051 Austin, Texas 78763-5051	Final
	14. Sponsoring Agency Code

15. Supplementary Notes

Study conducted in cooperation with the Texas Department of Transportation
Research Study Title: "Monitoring Performance of BEBO Arch Culvert"

16. Abstract

Observations of soil pressures and strains in arch components over a 5-year period indicate that:

(1) The design procedure used for arch segments produced components that have supported imposed soil and environmental forces successfully.

(2) The use of tension tie reinforcement in the slabs under arches beneath high fill was a wise and proper decision, as the tension strains in the floor indicate that the bars developed significant strains.

(3) Vertical earth pressures exceeded the nominal amount determined for uncompacted density and depth. Measured vertical pressures imply a soil density in the order of 130 pcf.

(4) Creep deformations in concrete must be included in analytic procedures in order to obtain displacement responses corresponding to those measured.

(5) The redundancies associated with soil-structure interaction tend to produce favorable redistributions of resistance to soil loads against the arch.

(6) A sophisticated analytic model of the structural system was shown to produce stress and displacement values very similar to those measured. The analytic model must include specific data regarding soil properties, and creep response time effects for concrete as well as for soil.

17. Key Words	18. Distribution Statement
arch, arch components, soil pressures, strains, arch segments, tension tie reinforcement, bars, density, depth, creep deformations, displacement	No restrictions. This document is available to the public through the National Technical Information Services, Springfield, Virginia 22161.

19. Security	20.	21. No. of Pages	22. Price
Unclassified	Unclassified	238	

NOT INTENDED FOR CONSTRUCTION,
PERMIT, OR BIDDING PURPOSES

Richard W. Furlong, P.E. (Texas No. 17744)

Research Supervisor

The contents of this report reflect the views of the authors, who are responsible for the facts and the accuracy of the data presented herein. The contents do not necessarily reflect the views of the Texas Department of Transportation. This report does not constitute a standard, specification, or regulation.

There was no invention or discovery conceived or first actually reduced to practice in the course of or under this contract, including any art, method, process, machine, manufacture, design or composition of matter, or any new and useful improvement thereof, or any variety of plant which is or may be patentable under the patent laws of the United States of America or any foreign country.